Discrete Element Modeling of Rock

Pre-Peak fracturing and Dilation

by

Namkak Cho

A thesis for submitting to the Faculty of Graduate Studies and Research

in partial fulfillment of the requirements for the degree of Doctor of Philosophy

University of Alberta

Department of Civil and Environmental Engineering

Edmonton, Alberta
Spring 2008

Library and Archives Canada

Published Heritage Branch

395 Wellington Street
Ottawa ON K1A 0N4
Canada

Bibliothèque et Archives Canada

Direction du Patrimoine de l'édition

395, rue Wellington
Ottawa ON K1A 0N4
Canada

Your file Votre référence
ISBN: 978-0-494-45407-7
Our file Notre référence
ISBN: 978-0-494-45407-7

NOTICE:
The author has granted a non-exclusive license allowing Library and Archives Canada to reproduce, publish, archive, preserve, conserve, communicate to the public by telecommunication or on the Internet, loan, distribute and sell theses worldwide, for commercial or non-commercial purposes, in microform, paper, electronic and/or any other formats.

The author retains copyright ownership and moral rights in this thesis. Neither the thesis nor substantial extracts from it may be printed or otherwise reproduced without the author's permission.

AVIS:
L'auteur a accordé une licence non exclusive permettant à la Bibliothèque et Archives Canada de reproduire, publier, archiver, sauvegarder, conserver, transmettre au public par télécommunication ou par l'Internet, prêter, distribuer et vendre des thèses partout dans le monde, à des fins commerciales ou autres, sur support microforme, papier, électronique et/ou autres formats.

L'auteur conserve la propriété du droit d'auteur et des droits moraux qui protège cette thèse. Ni la thèse ni des extraits substantiels de celle-ci ne doivent être imprimés ou autrement reproduits sans son autorisation.

In compliance with the Canadian Privacy Act some supporting forms may have been removed from this thesis.

While these forms may be included in the document page count, their removal does not represent any loss of content from the thesis.

Conformément à la loi canadienne sur la protection de la vie privée, quelques formulaires secondaires ont été enlevés de cette thèse.

Bien que ces formulaires aient inclus dans la pagination, il n'y aura aucun contenu manquant.

Canada

DEDICATION

To my wife, Mekyung

Thank you for the love and understanding you have demonstrated over and over.

Thank you also for bringing us our two wonderful children;

you are the loves of my life.

ABSTRACT

In laboratory tests, the onset of dilation occurs at stress levels far below the peak strength. Yielding of the laboratory specimen is not synonymous with the onset of dilation but it is more associated with pre-peak fracturing failure observed in many underground excavation projects which also referred to as "spalling", "dog earing", and "borehole breakout" The dilation resulting from this pre-peak fracturing results in large displacements that cannot be replicated using traditional flow rules continuum mechanics and fracture mechanics.

In this study a methodology is developed for modeling dilation using DEM based particle analysis software *PFC* (particle flow code, 2D).

The findings from this study shows that when using *PFC*, adjusting the micro parameters has little effect on the macro-scale properties of compression and tension tests, and clumped-particle geometry has a significant impact on the macro-scale properties.

The clump generated PFC simulation models were applied to explore the development of shear zone in rock subjected direct shear. The PFC models showed quite good agreement with laboratory test results and revealed that fractures occurring under shear zone were the results of tension not shear.

A spalling occurring in overstressed zone in underground opening at depth was also explored using axially compressed beam bending test. A notched failure similar to the one observed in an underground opening was able to reproduce in the system and the results were compared with PFC simulation for the test. The stress path analysis using PFC revealed that notched failure mainly associated with extensile fracturing and feacture initiation.

ACKNOWLEDGEMENTS

More than a thank-you is owed to my supervisors, Dr. C. Derek Martin and Dr. Dave C. Sego. Their insights into science, constructive criticisms and relentless encouragement drove this project (and me) further than I had envisioned.

I wish to thank my supervisory and examination committee for their advice, comments and critical review of this work.

I also like to thank Steve Gamble for his consistent assistance and advice to the laboratory tests.

Thank-you to graduate students in geotech group at U of A who discussed together and stimulated me to bring ideas whenever facing difficulties during my study.

Finally, I wish to thank to NSERC (Natural Sciences and Engineering Research Council of Canada) and Swedish Nuclear Fuel and Waste Management Co. (SKB) for supporting my research.

TABLE OF CONTENTS

CHAPTER 1

Introduction, Issues and Research Focuses

1.1	Introduction	1
1.2	Dilation Process in rock fracturing	4
1.3	Modeling approaches of extensile fractrung of rock	11
	1.3.1 Continuum mechanics approach	12
	1.3.2 Fracture mechanics approaches	14
	1.3.3 DEM based modeling approach	15
1.4	Fracture under shear loading	18
1.5	Notch type failure in axially compressed beam subjected to bending	20
1.6	Resaearch objectives	23
1.7	Thesis outline	23
1.8	References	25

CHAPTER 2

Literature Review : Previous Modeling Approaches on Rock

2.1	Introduction	30
2.2	Continuum mechanics approach	31
2.3	Fracture mechanics approach	36
	2.3.1 Rock fracture model	36
	2.3.2 Extensile fracture models	42
	2.3.3 Discussion on fracture mechanics approaches	47
2.4	DEM Approach	48
	2.4.1 PFC (Particle Flow Code) : A brief Review	49
	2.4.2 Application in rock modeling	53
2.5	Summary	61
2.6	Reference	62

CHAPTER 3

Laboratory Tests

3.1	Introduction	66
3.2	Characteristics of synthetic rock	69
3.2.1	Selection of target synthetic rock	69
3.2.2	Bolt anchor sulfaset	70
3.2.3	Uniaxial compression test	72
3.2.4	Effect of curing condition	73
3.2.5	Effect of initial moisture content at mixing	76
3.3	Properties of synthetic rock	78
3.3.1	Compressive strength	78
3.3.2	Tensile strength	80
3.3.3	Deformation modulus and poisson's ratio	82
3.4	Axially compressed beam bending test	85
3.4.1	Laboratory test system design	85
3.4.2	Preparation of the beam specimen	90
3.4.3	Core strength	94
3.4.4	Test results	95
3.5	Chapter summary and conclusion	104
3.6	References	105

CHAPTER 4

A Clumped Particle Model for Rock

4.1	Introduction	107
4.2	Bonded particle model (BPM) approach	109
4.2.1	Dilation in rock	109
4.2.2	Bonded particle analogue	112
4.3	Parametric study on dilation and strength ratio (σ_t / σ_{ci})	115
4.3.1	Micro-parameters	115
4.3.2	Bond models	116

4.3.3 Effect of micro-contact parameters 119
4.3.4 Effect of geometric factors 128
4.3.5 Controlling factors of dilation and strength ratio 133
4.4 Calibration of PFC to hard rock and weak rock using clumped bonded particle 134
4.4.1 Calibration of PFC to a brittle rock 134
4.4.2 Calibration of PFC to a synthetic weak rock 141
4.5 Dilational boundary 147
4.6 Conclusion 149
4.7 References 150

CHAPTER 5

Development of a Shear zone in Brittle rock subjected to Direct shear

5.1 Introduction 153
5.2 Direct shear box test on solid synthetic rock sample 157
5.2.1 Synthetic rock sample 157
5.2.2 Direct shear box test 158
5.3 Discrete element modelling 162
5.3.1 Bonded particle model 162
5.3.2 Micro parameters for synthetic rock 165
5.3.3 Direct shear discrete element modeling 169
5.4 Results and interpretation 172
5.4.1 Strength envelope 172
5.4.2 Stress and velocity vector distribution 174
5.4.3 Local stress path 176
5.4.4 Shear zone development in clay experiments 178
5.4.5 Shear zone development in brittle synthetic rock 179
5.5 Conclusion 186
5.6 References 187

CHAPTER 6

Dilation and Spalling in axially compressed Beams subjected to Bending

6.1	Introduction	190
6.2	Experimental setup	193
6.2.1	Synthetic rock	195
6.2.2	Axially compressed beam bending system	196
6.3	Test results	200
6.4	Bonded particle analogue	206
6.4.1	Discrete element modelling	206
6.4.2	Micro parameters for synthetic rock	207
6.4.3	Modeling axially compressed bending test	209
6.5	Results and analysis	212
6.6	Discussion and conclusions	220
6.7	References	221

CHAPTER 7

Summary, Conclusion and Future Research

7.1	Summary and Conclusion	226
7.1.1	DEM modeling of rock	226
7.1.2	Modeling of Shear zone in Rock	228
7.1.3	Spalling and dilation under axially compressed beam bending	229
7.2	Future research	231
7.3	References	232

Appendix A

Appendix B

TABLE OF FIGURES

Figure 1.1	Examples of stress induced failure of rock .	2
Figure 1.2	Practical risk issues associated with the overstressed rock damage.	4
Figure 1.3	Characteristics of bonding by the mineral type that constitute the rocks and the associated failure mechanism.	5
Figure 1.4	Dilation mechanism along the grain boundary and the role of dilation to the extension of fracture.	7
Figure 1.5	Bi-linear mobilization of cohesional and frictional strength of rock.	7
Figure 1.6	Characteristics of bonding by the mineral type that constitute the rocks and the associated failure mechanism.	8
Figure 1.7	Strength of Lac du Bonnet granite compared with AE measurement.	10
Figure 1.8	Example of continuum analysis and fracture mechanics approaches.	13
Figure 1.9	Example of DEM Modeling (PFC 2D).	16
Figure 1.10	Definition of fracture pattern observed in most shear zone.	19
Figure 1.11	Typical shear zone formed in stiff soil or rock by shear loading and the illustration of the fundamental issue about the source of fractures.	19
Figure 1.12	Illustration of buckling failure mechanism under non-uniformly distributed tangential stress.	21
Figure 1.13	Experimental approaches for simulating extensile fracturing around the tunnel.	22
Figure 2.1	Examples of yield surfaces plotted on the 3D principal stress space and octahedral plane.	32
Figure 2.2	Illustration of flow rule defining post yielding of a material	35
Figure 2.3	Griffith's narrow elliptical cracks	37
Figure 2.4	Modified Griffith model by McClintock and Walsh	39
Figure 2.5	Validation of modified Griffith theory compared with actual crack yield strengths published in the literature.	41
Figure 2.6	Relationship between extension of wing crack and confinement ratio.	42
Figure 2.7	Three primary modes of fracture.	43
Figure 2.8	Shear slip model suggested by Ashby and Hallam.	44
Figure 2.9	(a) Kemeny and Cook, (b) Germanovich and Dyskin	45
Figure 2.10	Pore models for extensile fracture	47
Figure 2.11	PFC calculation cycle	50

Figure 2.12	Particle Constitutive law and bond strength principle	51
Figure 2.13	Micro parameters and the illustration of yielding process for micro bonding.	52
Figure 2.14	Development of local tensile stresses under compression in particle assembly	54
Figure 2.15	Systematic damage process of rock in particle assembly by uniaxial compressive test simulation.	55
Figure 2.16	Formation of shear rupture surface and stress strain responses of biaxial simulation of PFC.	56
Figure 2.17	Approximating irregular grain with clustered particle model.	57
Figure 2.18	PFC simulated failure envelope compared with Lac du Bonnet Granite.	58
Figure 2.19	Linear failure envelope resulted from confined direct shear test simulation.	60
Figure 3.1	General micro parameter calibration approach in PFC 2D.	67
Figure 3.2	Saw cut section of 100 x 200 mm cylinder sample of Sulfaset synthetic rock	72
Figure 3.3	Typical failure shape of the synthetic rock specimen failed under uniaxial compressive load.	73
Figure 3.4	Effect of curing condition.	75
Figure 3.5	Effect of moisture content at mixing of Sulfaset synthetic rock.	77
Figure 3.6	Triaxial Test Results of the Sulfaset synthetic rock specimens	79
Figure 3.7	(a) Brazilian test results (b)Tensile failure of the sample	81
Figure 3.8	Failure envelope of the synthetic rock.	84
Figure 3.9	Stress distribution calculated by the variation of the loading ratio.	87
Figure 3.10	Axially compressed beam bending test system setup.	89
Figure 3.11	Hydraulic ram setup with a hinge	90
Figure 3.12	Steel mould used for molding the beam specimen.	91
Figure 3.13	Wire mesh used for the reinforcement.	92
Figure 3.14	Illustration of beam specimen molding process.	93
Figure 3.15	Verification of the beam strength from the core strength compared with cylinder mold strength (uniaxial compressive test).	95
Figure 3.16	Comparison of bending behavior of the reinforced and non-reinforced beam specimen for the stresses at the notch tip.	98

Figure 3.17	Dilation due to the extensile fracture development estimated from the differences between top and bottom bending displacement measured from LVDT.	99
Figure 3.18	Final ruptured shape of beam specimen and spalled shard inside the specimen at the top center.	101
Figure 3.19	Tensile strength test of sulfaset synthetic by 4 point bending system.	102
Figure 3.20	Development of extensile fractures near the notch just before the sample rupturing.	103
Figure 4.1	An extension fracture generated in uniaxial compression in granite.	110
Figure 4.2	Illustration of dilation process by fracture initiation and growth in brittle material subjected to compressive loading.	111
Figure 4.3	Contact force chain structure in PFC and failure envelope.	114
Figure 4.4	Micro parameters and the illustration of yielding process for micro bonding.	116
Figure 4.5	Illustration of bond models provided in PFC.	118
Figure 4.6	Effect of the coefficient of friction on lateral dilatant strain and the ratio of tensile strength to uniaxial compressive strength.	122
Figure 4.7	Effect of bond stiffness on lateral dilatant strain and the ratio of tensile strength to uniaxial compressive strength.	123
Figure 4.8	Effect of bond strength ratio on lateral dilatant strain and the ratio of tensile strength to uniaxial compressive strength.	124
Figure 4.9	Relating Brazilian strength to fracture toughness.	125
Figure 4.10	Effect of Particle size on on lateral dilatant strain and the ratio of tensile strength to uniaxial compressive strength.	127
Figure 4.11 :	Clustered particles for the modeling of irregular shapes of grains in brittle rock.	129
Figure 4.12	Effect of grain shape on lateral dilatant strain and strength ratio using cluster logic.	130
Figure 4.13	Effect of particle rotation.	131
Figure 4.14	Particle rotation mechanisms in clustered and clumped particles	132
Figure 4.15	Effect of grain shape on lateral dilatant strain and strength ratio using clump logic.	133
Figure 4.16	Illustration of stamping logic to control clump size.	135

Figure 4.17	Comparison of predicted axial stress and strain response from the calibrated PFC to the measured laboratory response of Lac Du Bonnet granite	138
Figure 4.18	Predicited failure envelope from PFC compared with laboratory envelope for Lac du Bonnet granite.	140
Figure 4.19	Calibrated results in stress and strain behavior for PFC synthetic rock.	144
Figure 4.20	Failure Envelope of calibrated material compared with laboratory envelope.	145
Figure 4.21	Sample failure in uniaxial compression test for the calibrated PFC synthetic rock and Laboratory synthetic rock.	146
Figure 5.1	The discrete Riedel shear fractures (R, and R') observed in the clay.	155
Figure 5.2	Shear stress and displacement for each normal stress applied on synthetic rock.	159
Figure 5.3	Dilation features by the variation of normal stress in shear box test on synthetic rock.	160
Figure 5.4	Normal (vertical) displacement (dilation) at peak shear stress and normal stress relationship.	160
Figure 5.5	Peak shear strength envelope obtained from direct shear test.	161
Figure 5.6	Micro parameters and the illustration of yielding process for micro bonding.	164
Figure 5.7	Grain shape and size control of clump using stamping logic.	166
Figure 5.8	Calibrated results in stress and strain behavior for PFC synthetic rock.	168
Figure 5.9	Calibrated failure locus for PFC synthetic rock compared to the laboratory measured.	169
Figure 5.10	Illustration of direct shear test simulation scheme in PFC.	170
Figure 5.11	Stress measurement circle installed in the simulated model.	172
Figure 5.12	Comparison of the shear strength envelope for the laboratory direct shear test on brittle synthetic rock with the discrete element (PFC) simulation.	173
Figure 5.13	Comparison of the contact force distribution in PFC simulated model.	175
Figure 5.14	Velocity vectors during fracture development for different loading conditions.	175
Figure 5.15	Stress path measurement at the center of PFC simulated sample.	177
Figure 5.16	Fracture patterns developed at each stage of stress strain curve on	

	overconsolidated clay.	179
Figure 5.17	Development of fracture for the 1.0kPa normal stress test on PFC synthetic rock.	181
Figure 5.18	Development of fracture for the 1.85MPa normal stress test on PFC synthetic rock.	182
Figure 6.1	Spalling observed in a 600-mm-diameter borehole in massive unfractured granite.	191
Figure 6.2	Illustration of the non-uniformly distributed tangential stress near the boundary underground.	193
Figure 6.3	Illustration of the combined boundary loading conditions that were used to generate the non-uniform compressive stress conditions.	194
Figure 6.4	Failure envelope of the synthetic rock.	196
Figure 6.5	Verification of the beam strength from the core strength compared with cylinder mould strength in Uniaxial compressive test.	197
Figure 6.6	Axially compressed bending test system setup.	199
Figure 6.7	Stress concentration factor from the elastic two-dimensional finite code, Phase2D.	202
Figure 6.8	Notch tip stress calculated using the estimated stress concentration factor and the corresponding beam deflection measured at the centre of the beam.	203
Figure 6.9	Dilation due to the extensile fracture development estimated from the differences between top and bottom bending displacement measured from LVDT.	204
Figure 6.10	Final ruptured shape of beam specimen and the spalling observed at the top center.	205
Figure 6.11	Tensile fracture observed in 4 point bending system.	206
Figure 6.12	Axially compressed bending test simulation setup in PFC2D.	210
Figure 6.13	Load ratio measured during the simulation.	213
Figure 6.14	Comparison of notch tip stress between PFC and laboratory test measured.	214
Figure 6.15	Illustration of the stress paths followed at several locations as the sample is loaded and fails.	215
Figure 6.16	Stress path near the notch and fracture development by stage.	217
Figure 6.17	Number of cracks generated by stage.	219

TABLES

Table 2.1	Summary of rock yield criteria.	33
Table 3.1	Material properties of Sulfaset synthetic rock.	83
Table 4.1	Micro Parameters of LDB Granite.	121
Table 4.2	Micro Parameters used in particle size effect.	126
Table 4.3	Micro Parameters of Lac du Bonnet granite used for calibration.	136
Table 4.4	Material properties of Sulfaset synthetic rock.	142
Table 4.5	Micro Parameters used to represent the Sulfaset synthetic rock.	142
Table 5.1	Strength and deformation properties of brittle synthetic rock.	157
Table 5.2	Micro parameters used for sample calibration in PFC modeling.	167
Table 5.3	Orientation of fracture sets and maximum principal stress axis.	185
Table 6.1	Material properties of Sulfaset synthetic rock.	195
Table 6.2	Micro Parameters used to represent the Sulfaset synthetic rock.	209
Table 6.3	Micro properties obtained from the sample calibration.	209

CHAPTER 1

INTRODUCTION, ISSUES AND RESEARCH FOCUS

1.1 INTRODUCTION

Civil, mining and petroleum engineering projects involve managing rock as a geologic unit. Rock is a crucial component of underground structures or mines and it must be dealt with during both the design and construction phases.

Most rock is heterogeneous in structure containing micro and macro scale discontinuities. At low in situ stress state, most of the issues with this material are related to natural macro discontinuities such as faults or joints within the rocks. At high in situ stress states, the issues associated with rock heterogeneity change from the macro to the micro scale. Under high stress, existing macro fractures are highly compressed, thus failure processes in the rock become similar to those in intact rock (Martin et al.[1]) and micro scale fractures control the failure process. These stress induced failures are observed in deep underground excavation projects as shown in Figure 1.1.

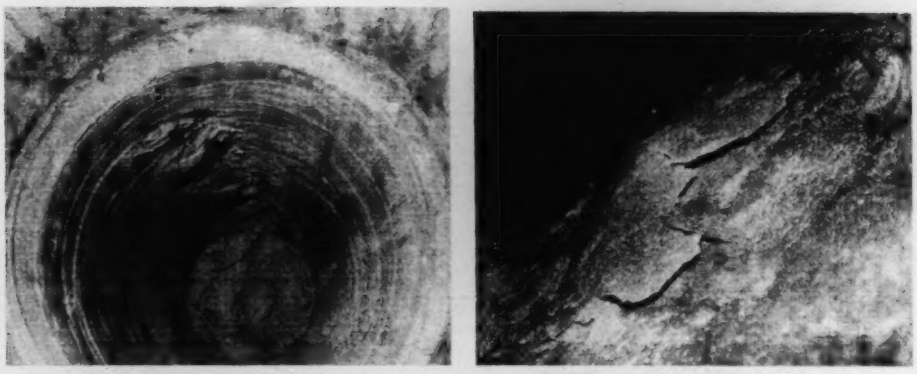

(a) (b)

Figure 1.1 : Examples of stress induced failure of rock at URL(Underground Research Laboratory), Pinawa, Manitoba, Canada, (a) Spalling observed in a 600 mm diameter borehole in a heated failure test program (reported by Read et. al[2]), (b) Spalling observed at the bottom of the tunnel notch in mine-by test tunnel (reported by Martin and Kaiser[3]).

In an underground excavation (such as a nuclear waste repository) located deeper than 300 m, in relatively undamaged rock, the major failure mode is dominated by stress induced extensile fractures. This occurs as a result of concentrated tangential stresses. While the stresses are referred to as compressive stresses the actual stresses occurring in the rock fabric are tensile (Martin[4]).

Intact rock contains pre-existing flaws and each grain has different micro properties. These micro heterogeneities cause local tensile stresses on a micro scale and micro tensile fractures form under load. If sufficient deviatoric stresses are applied, such fractures dilate and propagate to form macro scale extensile fractures. Direct observation of such fractures in overstressed rock in underground opening reveals that such fractures exhibit significant dilation. This process results in the opening of fractures associated with rock mass bulking, which produces permanent, radial deformations in

the fracture zones and at the excavation wall (Kaiser et al.[5]). Failure processes due to the dilatant extensile fracturing are often referred to as "spalling" or "dog-earing" in rock engineering while in the petroleum industry, the problem is often cast as "wellbore breakouts." One of the early descriptions in civil engineering was given by Terzaghi[6] and is referred to as "popping rock".

Rock damage due to overstressing and fracturing affects both the stability and serviceability of the underground structures and in extreme cases structures have collapsed. Figure 1.2 shows several examples of risks associated with rock damage due to overstressing. In large scale underground storage cavern, structural damage requires significant amount of concrete backfill resulting in extra construction cost (Figure 1.2 (a)) and reduced efficiency of underground storage room through leakage (Figure 1.2 (b)). In the mining industry, rock bursting may injure or kill mining workers (Figure 1.2 (c)). In a nuclear waste repository, this damage can change the hydraulic conductivity or gradient near the opening, as a result the time for ground water migration from the surface through the rock mass near the opening may be reduced causing risk of contamination due to radioactive leakage (Figure 1.2 (d)). In the petroleum industry, borehole damage via "breakout" may reduce production rates resulting in significant economic loss (Figure 1.2 (e)).

Failure mechanisms associated with rock fracturing must be understood to be predicted and prevented at the design stage. This will reduce risks to workers and loss of stored materials, and will ultimately save construction costs.

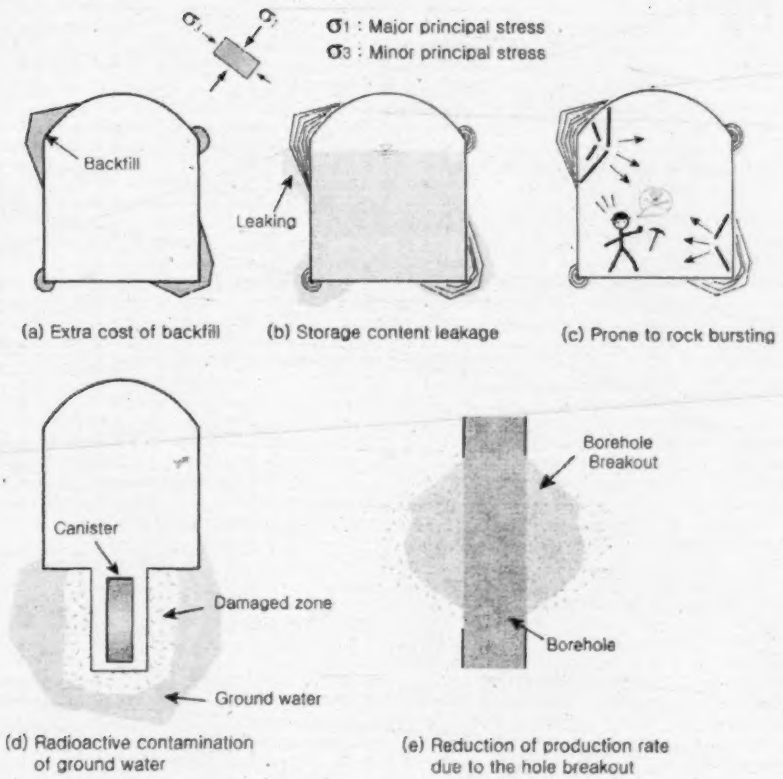

Figure 1.2 : Practical risk issues associated with the overstressed rock damage due to extensile fracturing.

1.2 DILATION PROCESS IN ROCK FRACTURING

Most rocks are composed of various minerals such as quartz, calcite, plagioclase, halite etc. The yielding of rock depends on the nature of the internal bonds within these minerals. For instance, as shown in Figure 1.3, "halite (NaCl)" has an ionically bonded mineral structure composed of large chloride anions bonded by smaller sodium cations thus forming an electrically balanced crystal lattice. Under slow loading or increasing temperature, the failure process for this type of structure is dominated by dislocation shear or lattice slip. Time dependent shear slip like creep is prevalent under a slow

loading rate and cleavage or brittle rupture dominates under more rapid loading rates. "Diamond (C)" in contrast has purely covalent bonds where boundary electrons around each atom are shared with boundary electrons of adjacent atom thus forming a strong lattice structure. In these structures, yielding can be achieved only by extensile fracturing of the lattice (Figure 1.3).

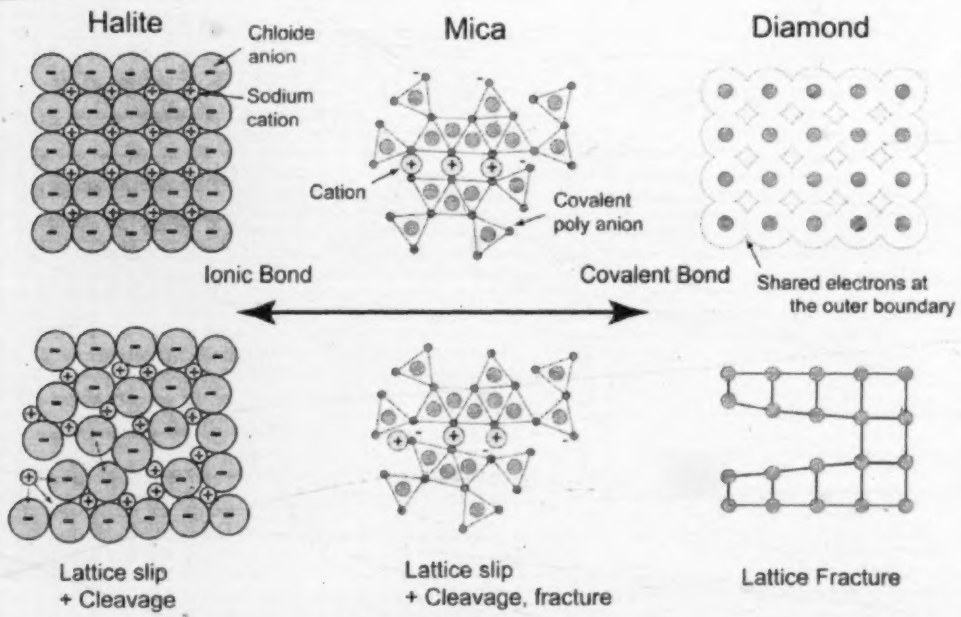

Figure 1.3 : Characteristics of bonding by the mineral type that constitutes the rock and associated failure mechanisms (modified from the compilation by Diederichs[12]).

Most rock is held together by ionic bonding of covalent complexes similar to the structure of mica (Figure 1.3). Ionic bonding is normally weaker than covalent bonding. Lattice shear slip is limited within the grains. Fractures along the grain boundary are triggered but extensile fractures of adjacent grain boundaries dominate. Hence, yield-

ing of rock can be achieved only through irreversible extensile rupture along grain boundaries.

In most rock, planar grain surfaces are rare. When fractures occur whether by shear or tensile failure between irregular boundaries of grains, dilation occurs even under small relative movement of the failing surfaces. Dilation results from a mismatch of the non-planar grain surfaces resulting in stress concentrations at the tip of the fracture that subsequently develop into extensile fractures. The newly developed fractures induce more dilation due to surface incompatibility.

The dilation process associated with extensile fractures proceeds progressively, therefore, dilation should be considered one of the most important characteristics when exploring yield processes of rock. Previous research on modeling failure processes in rock ignored this behavior. Figure 1.4 illustrates the dilation processes occurring in rock as previously discussed. These concepts of the dilation process were outlined by Lajtai[7].

Lajtai[7] developed these concepts while interpreting a series of direct shear tests using solid plaster specimens with or without artificial voids. He suggested that under low confinement, cohesion dominates the yielding of the material that might be represented by its tensile strength. As the normal stress increases, friction is mobilized; this implies that the non-planar fractures formed under low confining stresses contribute to mobilization of frictional strength as shown in Figure 1.5.

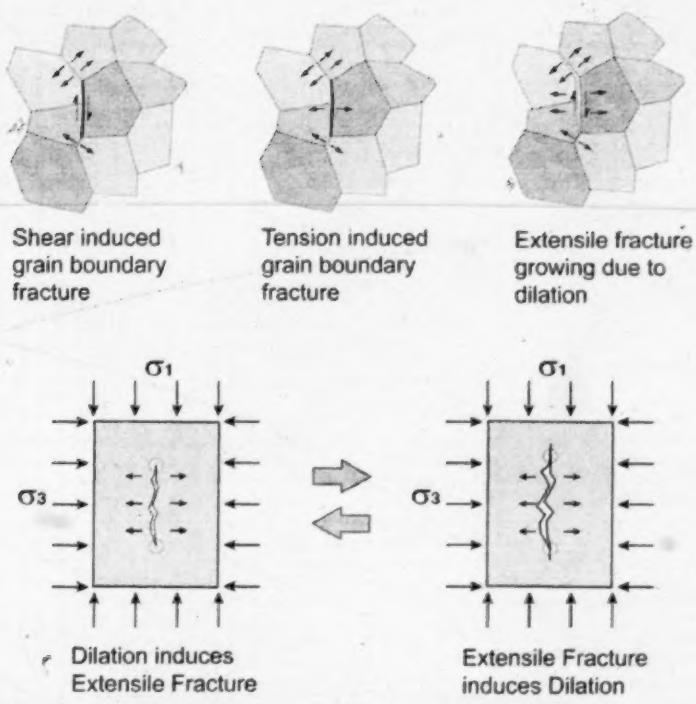

Figure 1.4 : Dilation mechanism along the grain boundary and the role of dilation in the extension of fracture.

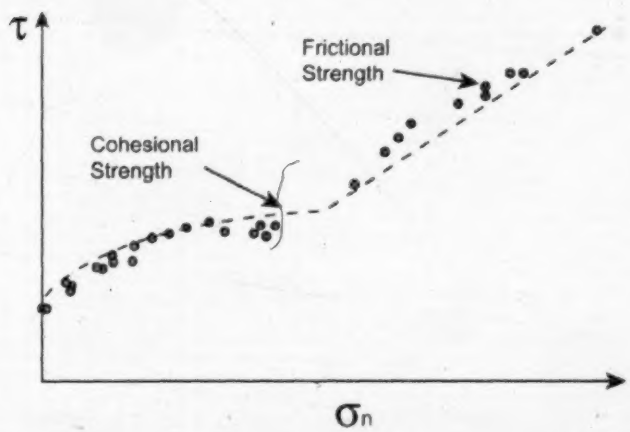

Figure 1.5 : Bi-linear mobilization of cohesional and frictional strength of rock (Results from direct shear tests on solid synthetic rock, after Lajtai[7]).

These processes contribute to micro scale fracturing along the grain boundaries as well. The stress strain response during conventional laboratory compressive tests of rock shows unique differences between lateral and axial strain behavior. Figure 1.6 shows the typical stress strain curve of Lac du Bonnet granite; this illustrates the failure process during compression of hard rock (Martin and Chandler[8]). Yielding is divided into two unique processes. The first begins at the point on the lateral strain and axial stress plane referred to as the crack initiation point which is reported as 30~50% of the uniaxial compressive strength (Brace et al.[9]). It is also reflected as the point of reversal on the crack volumetric strain curve obtained by subtracting the elastic volumetric strain from the total volumetric strain (Martin and Chandler[8]).

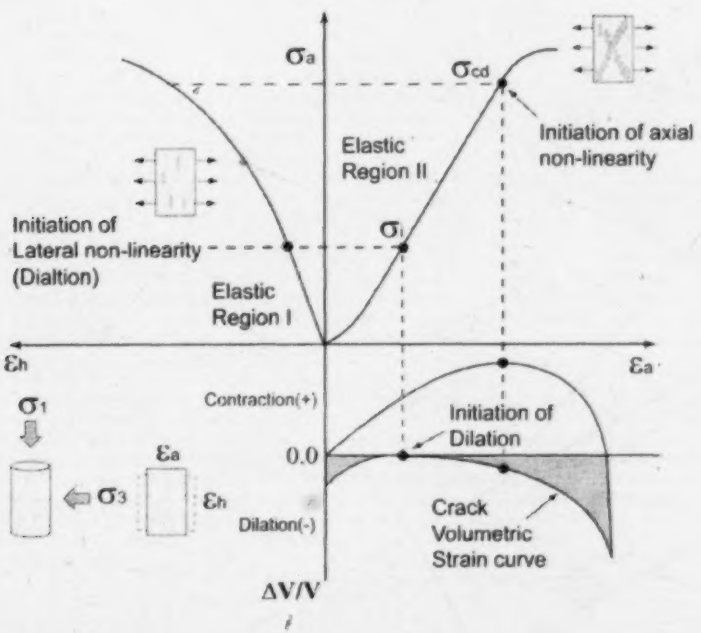

Figure 1.6 : Illustration of failure process during compression of hard rock (modified based on the illustration by Martin and Chandler[8]).

The crack dilation starts at this point (Figure 1.6) and the specimen starts to yield on this micro scale. Non-linearity results from dilation of micro fractures. This process is irreversible while the axial strain response is still elastic. Lajtai[10] noted that if an uniaxial sample is unloaded following initiation of dilation, permanent strain is recorded only in the lateral direction and no permanent axial strain is recorded. This supports the observation that the dilation is caused by cracks aligned in the axial direction and indicates that the lateral dilatancy process is not elastic.

The second stage is associated with a starting point of axial non-linearity. This point is often referred to as the rock damage initiation point; it starts at 70~80% of the uniaxial compressive strength. At this point, cracks are localized and systematically begin to form a shear band and the all-around dilation of the specimen commences. Dilation, however, does not result from axial micro fractures but from deformation by the shearing resulting from coalescence of the cracks to form a shear band.

While the micro scale yielding reflected as dilation in the lateral stress strain curve does not necessarily indicate the rock strength under normal conditions, such dilation is important when analyzing underground excavations at depth. In this situation the actual rock strength near the opening wall is more likely related to the dilation initiation stresses (see Figure 1.7). AE (acoustic emission) measurements in such cases reveal that the AE events have higher frequencies near the crack initiation stress level. This in situ strength reduction mechanism in overstressed rock near an opening was reported and explained by Pelli et al.[11], Martin et al.[1], and Diederichs[12].

Hence, such a dilation locus should be used as a lower bound strength of the rock. Models that predict overstress rock damage and dilation processes in rock must not ignore these observations.

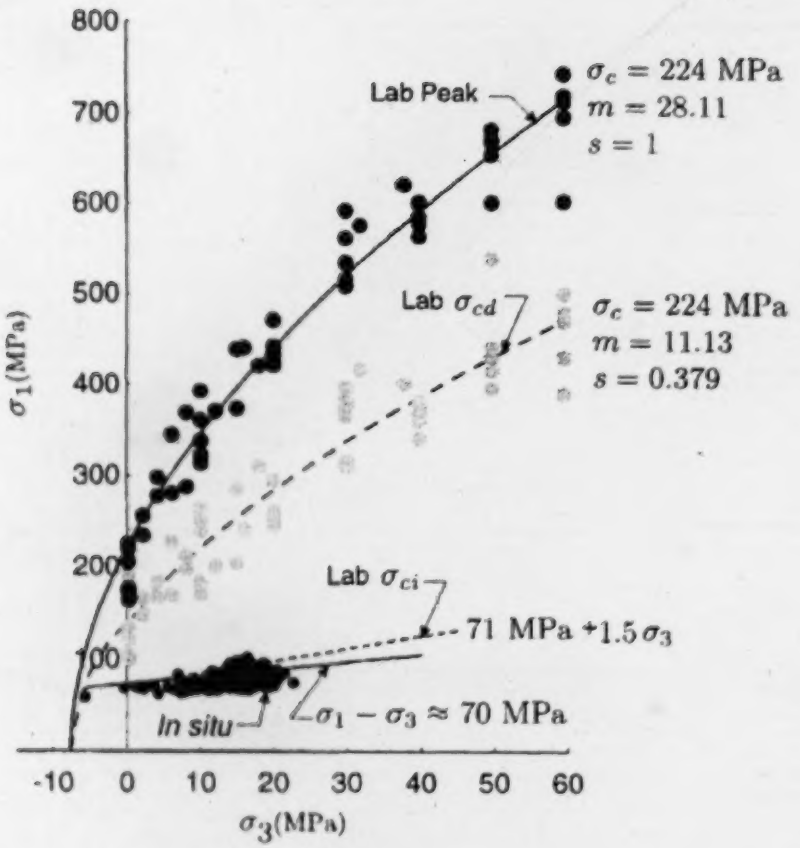

σ_c : Peak Stress

σ_{cd} : Crack Damage Stress

σ_{ci} : Crack Initiation or Dilation Initiation Stress

Figure 1.7 : Strength of Lac du Bonnet granite compared with AE (Acoustic Emission) measurement (modified from Martin et al.[1]).

1.3 MODELING APPROACHES TO EXTENSILE FRACTURING OF ROCK

Since Griffith's[13, 14] time, there have been efforts to mimic extensile fracturing in rock. Many studies have been carried out using analytical or numerical methods; these studies are classified into the following groups:

- Continuum Mechanics Approach
- Fracture Mechanics Approach
- Discrete Element Method-Based Approach.

The development of modern computer technology has allowed these approaches to evolve but each has limitations. Shortcomings of these models will be discussed in chapter 2 and the approach used in this thesis will be presented.

1.3.1 CONTINUUM MECHANICS APPROACH

Continuum mechanics models use the following fundamental assumptions;

- Material is CHILE (continuous in displacement field, homogeneous, isotropic, linear elastic),
- Stress strain and yielding are all based on the macro responses of these materials as measured using conventional material testing methods.

Under the CHILE assumption, actual tensile stresses allowed in DIANE (discontinuous, inhomogeneous, anisotropic and non-elastic) rock fabric when the stress state is all- round compression (Figure 1.8 (a)) are difficult to model (Hudson and Harrison[15]). To overcome this limitation Tang and Kaiser[16] and Tang et al.[17] resorted to use of the weakest link model. In this approach, the fracture process is identical to that of a chain, the links of which would be formed by elements and the fracture is controlled by the local strength of the weakest element which is randomly chosen based on a probabilistic distribution such as Weibull's law. Following this approach tensile stresses can be generated even under an all-around compressive stress state but this approach cannot overcome the intrinsic characteristics of continuum mechanics such as not considering the dilation or non-linearity reflected via lateral strains presented in Figure 1.6.

Simulating the fracture process that causes an open fracture (Figure 1.4) is problematic due to the need to maintain continuity of the displacement field across the fracture; since the fracture is open, this requirement is violated.

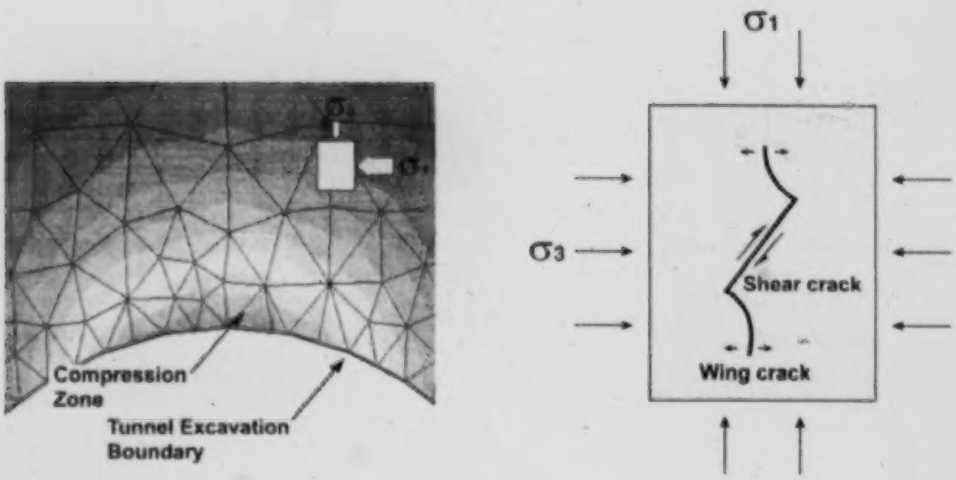

(a) *(b)*

Figure 1.8 : Example of continuum analysis and fracture mechanics approaches. (a) Example of continuum analysis (Phase2D) (b) Example of Fracture mechanics approach.

In most continuum approaches the stress strain response and yield models of a material rely on measurements of the axial macro response. Such approaches normally adopt specific flow rules such as the associated or non-associated flow rules to define the displacement field after yield. However, since such rules have been established to define the displacement field in the post peak region, they cannot evaluate the process of micro yielding in the initial loading stage (Figure 1.6).

1.3.2 FRACTURE MECHANICS APPROACHES

Since Griffith (1921, 1924) first formulated his energy balance theory on pre-existing flaws to the tension (i.e., modified to the compression later), many fracture mechanics based models have been developed. They were used to understand extensile fracture mechanisms in rock-like materials.

The most common assumptions embedded in these fracture mechanics approaches are:

- Initial flaw is always present and should be inclined,
- Failure commences by shearing and the shear surfaces are always planar,
- Fractures have zero width,
- Control of the fracture growth depends on fracture toughness (K_{IC}).

Existence of the initial flaw and inclination is restrictive as most rocks are DIANE material. However, fracture orientation is physically wrong and this limitation has been argued by many researchers (Tapponnier and Brace[18], Vallejo[19], Lockner[20], Martin[4], Cai et al.[21], etc.).

In fracture mechanics, shearing along the inclined flaw under the stress field is the approach used to generate a "wing-cracks" (Figure 1.8). This approach results in a fundamental and physical discrepancy that requires rocks to be weaker in shear than in tension. This is at odds with one of the most important characteristics of rocks as noted by Neveille Cook[22] that rocks are fundamentally weaker in tension than in shear.

While incorporating physical phenomena into analytical models is indispensable, the fracture models do not account for the lateral dilation resulting from open fractures

because they require fractures to have zero width. Models that violate fundamental physical characteristics have little chance of properly modeling the yield processes in rock.

1.3.3 DEM BASED MODELING APPROACH

Since the mid 1990s there has been growing interest in discrete element modeling. As noted by Cundall[23], one of the major advantages of this numerical method is that a flow rule does not need to be specified. Among the many DEM codes developed for micro mechanics modeling of rock, PFC (Particle Flow Code) is widely used and commercially available codes have been used to simulate tensile rupture as shown in Figure 1.9. This code is based on the following assumptions (Potyondy and Cundall[24]) as,

- The particles are circular or spherical rigid bodies with a finite mass.
- The particles move independently with one another and can also rotate.
- The particles interact only at their contacts because the particles are circular or spherical and a contact exists between two particles only.
- The particles are allowed to overlap one another, and all overlaps are small in relation to particle size such that contacts occur over a small region (i.e., at a point).
- Bonds of finite stiffness can exist at a contact, and these bonds carry load and can break. The particles at a bonded contact need not overlap.

- Generalized force-displacement laws at each contact relate relative particle motion to force and moment at the contact.

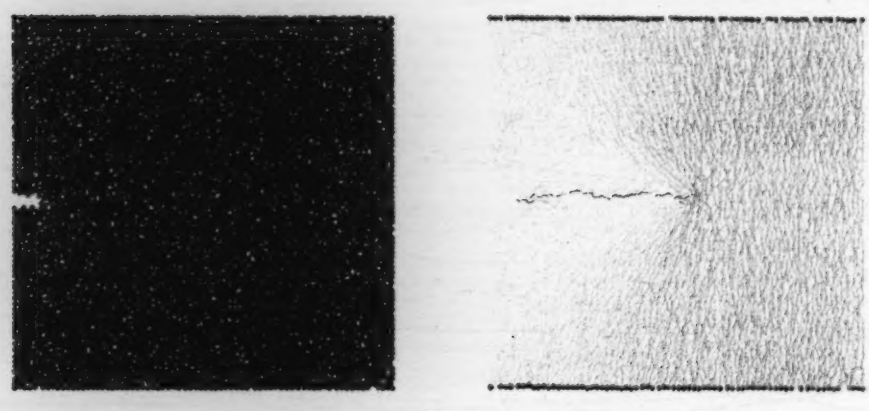

(a) *(b)*

Figure 1.9 : Example of DEM modeling (PFC 2D), Mode I tensile rupture simulation (after Cundall[23]), (a) Notch installed particle assembly, (b) Mode I tensile fracture propagation.

One of the challenges in modeling extensile fracturing based on the concept shown in Figure 1.4 is that the rigid particle elements are either circular disks or spherical. These circular particles save calculation time but, as noted by Jensen et al.[25], Thomas and Bray[26] and Guo and Morgan[27], such particles may not adequately capture geometry dependent properties such as dilation and interlocking friction. Shortcomings that arise from these circular particle modeling rocks have been outlined by Diederichs[12] and Potyondy and Cudall[24]. They indicated that fabrics assembled by circular disks are not able to generate extensile fracture growth because forces associated with particle contacts do not create stresses activated at the fracture tip in rock. As a result, such a model predicts high macro tensile strength (i.e. about 25% of laboratory uniaxial compressive strength compared with an actual laboratory tensile strength of

around 3 ~ 5% of UCS) and low dilation compared with observations of laboratory specimens.

The modeling approaches described above include many intrinsic postulations - some are acceptable but some are not supported by actual observations. Ignoring the dilatancy effect associated with extensile fracturing while trying to explain the physical behavior of rock results in underestimation of strength (Figure 1.7).

The first goal of this thesis is to develop an improved approach to model of extensile fracturing induced by dilation. More specifically, the limitations (i.e., high tensile strength and low dilation effect) of extensile fracture modeling associated with the DEM code PFC2D will be solved. This process is explored and is verified using laboratory specimens.

1.4 FRACTURE UNDER SHEAR LOADING

Most rocks and soils when deformed in shear, form a narrow shear band. Such shear bands are often observed along faults, bedding plane, landslide and have been observed in conventional laboratory tests (i.e., direct shear test or triaxial compression specimen).

Hence the fracture patterns found in these zones are all similar and are independent of scale.

Investigations of fracture types formed in such shear zones have been undertaken by Riedel[28], Cloos[29], Skempton[30], Morgenstern and Tchalenko[31], and Tchalenko[32]. They mapped and sketched the fracture patterns formed in the shear band using laboratory specimens subjected to shear loading. They suggested that the fractures observed in most shear zones follow a unique pattern (see the definition by Skempton[30] in Figure 1.10). These fractures are observed in laboratory specimens and natural shear zones and mostly agree with a failure plane direction estimated using Coulomb theory (i.e. $\phi/2$ to the axis of shearing, Figure 1.11). This conclusion implies that the source of such a fracture is predominately the shear process.

Vallejo[19] however argued that the actual source was due to fractures resulting from tension. He disputed observations that specimens under elastic conditions are subjected to the pure shear condition. Under this condition, tensile stresses dominate thus fracture initiation is induced not by shearing but by tension. Moreover, the major principal stresses inevitably rotate under such stress condition thus tensile fractures are usually aligned with the σ_1 direction as it rotates, and once fractures are initiated the

specimen is no longer continuous. Since Coulomb's theory is based on a continuum it should not be applied to this problem.

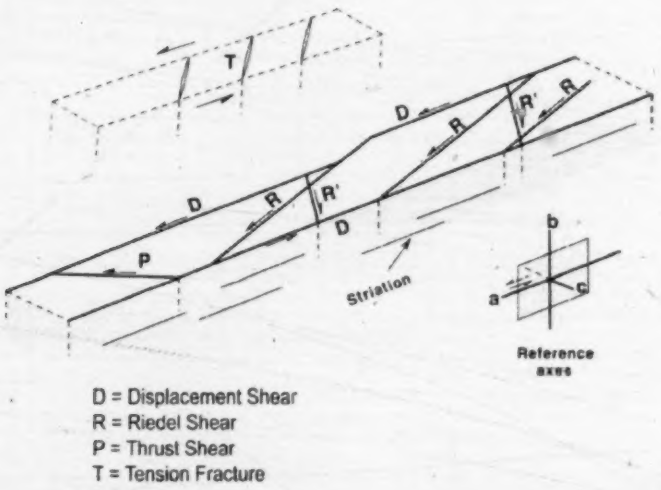

Figure 1.10 : Definition of fracture pattern observed in most shear zones (reproduced by author from Skempton[30].

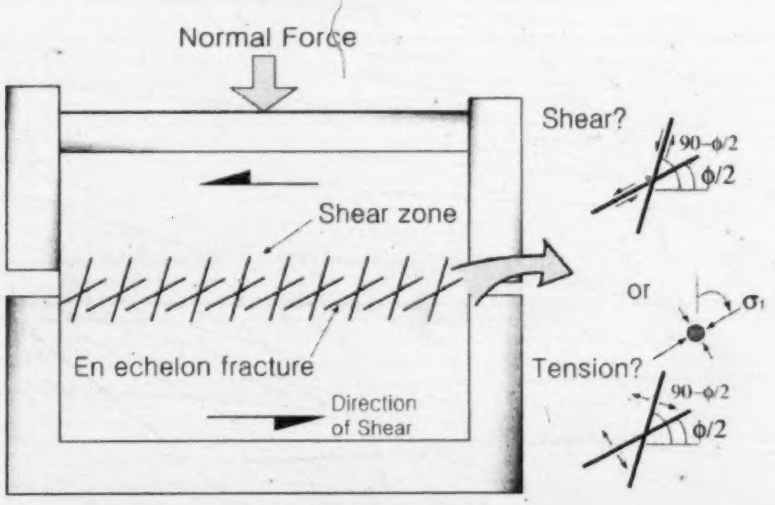

Figure 1.11 : Typical shear zone formed in stiff soil or rock by shear loading and an illustration of the fundamental issue about the source of fractures (i.e. "ϕ" denotes internal friction angle of material).

While Vallejo's argument is sound and reasonable, no clear evidence to support his notion was available so his ideas did not draw much attention from other researchers.

In this study, a goal is to reveal the actual source of the fracture mechanism within the shear zone. It will be investigated through the DEM (Discrete Element Method) model modified during this research. By taking this approach, it will be possible to identify whether the fracture source is shear induced or tension induced because the DEM yielding mechanism adopted in this thesis is not based on macro yielding but on the micro yielding process. Thus once fractures (identified as individual cracks) are formed the DEM model will confirm if the crack resulted from shear rupture or tensile rupture. The DEM based logic established in this thesis assists in understanding these mechanisms and it will thus be of practical assistance in the design of underground excavation supports and will aid evaluation of landslide hazards, slope stability, and other shear induced loading design issues.

1.5 NOTCH TYPE FAILURE IN AN AXIALLY COMPRESSED BEAM SUBJECTED TO BENDING

As shown in Figure 1.8 (a), in overstressed rock near a deep underground opening, extensile fracturing develops under a compressive stress state which results from tangential stresses. While confinement is low in such a stress zone, direct comparison with a conventional uniaxial compression test or a triaxial test is not possible since the two stress states are different. In both cases axial stresses dominate but the tangential stress distribution near the boundary is non-uniform when compared to a laboratory test car-

ried out under a uniform stress state. Once factures are initiated, the rock acts like a beam subjected to bending moment as shown in Figure 1.12. Instability against buckling failure due to the moment proceeds progressively until the stress state in the zone is stabilized by a notch type failure.

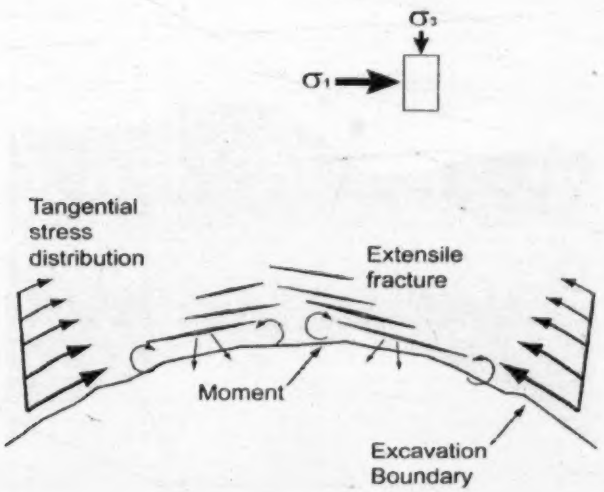

Figure 1.12 : Illustration of a buckling failure mechanism under non-uniformly distributed tangential stress.

Experimental approaches to simulate such a zone around a hole or tunnel excavation boundary have been explored during the past few decades (Hoek[33], Gay[34], Santarelli and Brown[35], Ewy and Cook[36], Haimson and Song[37], Lee and Haimson[38], Dzik[39], Sellers and Klerck[40]). However, most of the tests were limited to small scale circular holes (6~110mm in diameter) made in cubic or cylindrical specimens as shown in Figure 1.13(a). These small scale specimens are not free from scale dependency associated with the actual rock strength (Martin[4]).

It is difficult to perform large scale tests because a larger sample involves larger equipment and higher costs. For this reason, axially compressed beam bending tests were undertaken in this thesis as shown in Figure 1.13 (b).

This concept was borrowed from testing associated with pre-stressed concrete beams and eccentrically loaded beam columns, one of the most frequently used loading elements in structural engineering.

Under this setup, the beam specimen is subjected to bending but tensile failure at the bottom fiber is suppressed by horizontal axial compressive stresses imposed via the axial load.

Hence, the specimen is subjected to a compressive stress state that is non-uniformly distributed; this is similar to the tangential stress distribution imposed around a deep underground opening (Figure 1.12).

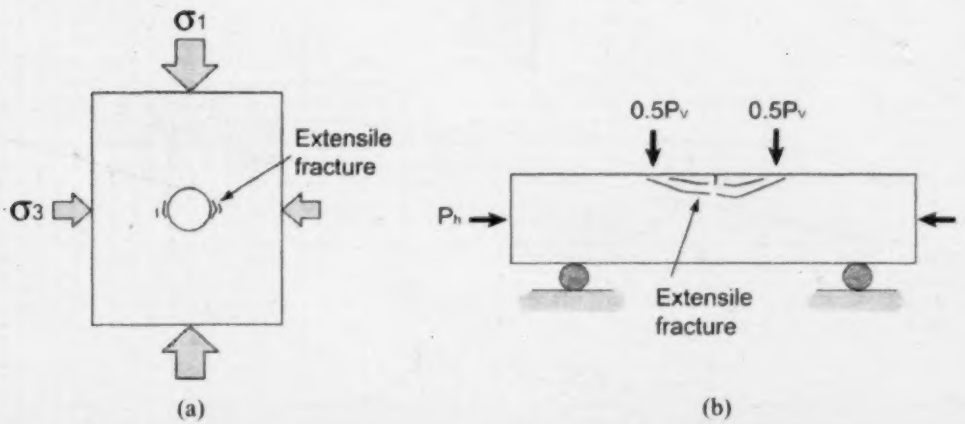

Figure 1.13 : Experimental approaches for simulating extensile fracturing around the tunnel. (a) Conventional circular hole test, (b) Axially compressed beam bending test.

Using the axially compressed beam bending test, mechanisms of excavation induced extensile fracture will be explored.

1.6 RESEARCH OBJECTIVES

The research objectives of this thesis are summarized as below

(1) DEM modeling of dilation of extensile fracturing of brittle rock and application to actual rock behavior,

(2) DEM modeling of shear zone development in brittle rock: emphasis on the mechanism controlling formation of fractures in the shear zone

(3) DEM simulation of dilation and spalling type failure in brittle rock: simulation of axially compressed beam bending test.

1.7 THESIS OUTLINE

This thesis is subdivided into seven chapters. Chapters 4, 5, and 6 were originally produced as journal manuscripts, thus these chapters are formatted for publication and some sections may be repetitious.

Chapter 1 introduces the background, motivation, issues, and research objectives and outlines the organization of the thesis.

Chapter 2 reviews previous modeling approaches of extensile fracturing and dilation of rock, it includes a discussion of the limitations of each modeling approach.

Chapter 3 provides the laboratory test program including results of the conventional laboratory test of synthetic rock and the axially compressed beam bending test. Test results are compared with the PFC simulation results in Chapters 4, 5, and 6.

Chapter 4 gives a brief introduction of the bonded particle analogue and the exploration of dilation in extensile fracturing. The chapter includes techniques to model these processes and calibration of the process to the actual laboratory response.

Chapter 5 describes the modeling of shear zone development in brittle rock. DEM simulation procedures of this zone are included and comparison with the laboratory direct shear test results is presented. The chapter compares the fracture pattern in the shear zone as previously presented in the literature with results simulated using PFC modeling, the actual source of such fractures are revealed through the simulation results.

Chapter 6 provides the PFC simulation procedure of the axially compressed beam bending test. The results are compared with the laboratory test results.

Chapter 7 presents a summary of the results of this research and indicates the contributions of this work to the field. Suggestions for future studies are outlined in this chapter.

Appendix A includes additional figures associated with the laboratory tests for the synthetic rock used in this study. Appendix B illustrates the "FISH" functions used in the PFC simulation of the laboratory tests presented in Chapter 4, 5, and 6.

1.8 REFERENCES

[1] Martin, C. D., Kaiser, P. K., McCreath, D. R. 1999. Hoek-Brown Parameters for Predicting the Depth of Brittle Failure around Tunnels. Can. Geotech. J. 36:136-151.

[2] Read, R. S., Martino, J. B., Dzik, E. J., Oliver, S., Falls, S., Young, R. P. 1997. Analysis and Interpretation of AECL's Heated Failure Tests. Tech. Rep. 06819-REP-01200-0070 R00.Ontario Hydro, Nuclear Waste Management Division.

[3] Martin, C. D., Kaiser, P. K. 1996. Mine-by Experiment Committee Report Phase 1: Excavation Response Summary and Implications. AECL. AECL-11382, COG-95-347

[4] Martin, C. D. 1997. Seventeenth Canadian Geotechnical Colloquium: The Effect of Cohesion Loss and Stress Path on Brittle Rock Strength. Can. Geotech. J. 34:698-725.

[5] Kaiser, P. K., Diederichs, M. S., Martin, C. D., Sharp, J., Steiner, W. 2000. Underground Works in Hard Rock Tunneling and Mining. Geo2000, An International Conference on Geotechnical & Geological Engineering.

[6] Robert, V. P., Thomas, L. W., Terzaghi, K. 1946. Rock Tunneling with Steel Supports. Youngstown, Ohio. [The Commercial shearing & stamping co.], 271p.

[7] Lajtai, E. Z. 1969. Strength of Discontinuous Rocks in Direct Shear. Geotechnique. 19:218-233.

[8] Martin, C. D., Chandler, N. A. 1994. The Progressive Fracture of Lac du Bonnet Granite. Int. J. Rock Mech. Min. Sci. Abstr. 31:643-659.

[9] Brace, W. F., Paulding, B., Scholz, C. 1966. Dilatancy in the Fracture of Crystalline Rocks. J. Geophys. Res. 71:3939-3953.

[10] Lajtai, E. Z. 1998. Microscopic Fracture Process in a Granite. Rock Mech. and Rock Eng. 31:237-250.

[11] Pelli, F., Kaiser, P. K., Morgenstern, N. R. 1991. An Interpretation of Ground Movements Recorded during Construction of the Donkin-Morien Tunnel. Can. Geotech. J. 28:239-254.

[12] Diederichs, M. S. 2000. Instability of Hard Rock Masses : The Role of Tensile Damage and Relaxation. Ph.D. thesis. Dept. of Civil Eng., University of Waterloo. 567pp.

[13] Griffith, A. A. 1921. The Phenomena of Rupture and Flow in Solids. Philos. Trans. Roy. Soc. London, Series A, Math. Sci. 221:163-198.

[14] Griffith, A. A. 1924. The Theory of Rupture. In Proc. First International Congress for Applied Mechanics, pp. 55-63.

[15] Hudson, J. A., Harrison, J. P. 1997. Engineering Rock Mechanics: An Introduction to the Principles. Elsevier, Oxford.

[16] Tang, C. A., Kaiser, P. K. 1998. Numerical Simulation of Cumulative Damage and Seismic Energy Release During Brittle Rock Failure - Part I : Fundamentals. Int. J. Rock. Mech. Min. Sci. 35:113-121.

[17] Tang, C. A., Xu, X. H., Kou, S. Q., Lindqvist, P.-A., Liu, H. Y. 2001. Numerical Investigation of Particle Breakage as Applied to Mechanical Crushing - Part I : Single-Particle Breakage. Int. J. Rock. Mech. Min. Sci. 38:1147-1162.

[18] Tapponnier, P., Brace, W. F. 1976. Development of Stress-Induced Microcracks in Westerly Granite. Int. J. Rock Mech. Min. Sci. Abstr. 13:103-112.

[19] Vallejo, L. E. 1982. Development of a Shear Zone Structure in Stiff Clays. 4th International conference on numerical methods in geomechanics, Eisenstein, Z. editor, pp. 255-262.

[20] Lockner, D. A., Moore, D. E., Reches, Z. 1992. Microcrack Interaction Leading to Shear Fracture. 33rd U.S. Rock Mechanics Symposium, Tillerson, J.R.,Wawersik, W.R. editors, Balkema, Rotterdam, pp. 807-816.

[21] Cai, M., Kaiser, P. K., Martin, C. D. 1998. A Tensile Model for the Interpretation of Microseismic Events near Underground Openings. Pure and Applied Geophysics. 153:67-92.

[22] Cook, N. G. W. 1995. Why Rock Mechanics? : Muller lecture. 8th International Congress on Rock Mechanics, Tokyo, Japan, Fujii, J. editor, pp. 975-994.

[23] Cundall, P. A. 2000. A Discontinuous Future for Numerical Modelling in Geomechanics. Geotech. Eng. 149:41-47.

[24] Potyondy, D. O., Cundall, P. A. 2004. A Bonded-Particle Model for Rock. Int. J. Rock. Mech. Min. Sci. 41:1329-1364.

[25] Jensen, R. P., Bosscher, P. J., Plesha, M. E., Edil, T. B. 1999. DEM Simulation of Granular Media - Structure Interface : Effects of Surface Roughness and Particle Shape. Int. J. Num. and Anal. Meth. in Geomech. 23:531-547.

[26] Thomas, P. A., Bray, J. D. 1999. Capturing Nonspherical Shape of Granular Media with Disk Clusters. J. of Geot. and Geoenv. Eng. 125:169-178.

[27] Guo, Y., Morgen, J. K. 2004. Influence of Normal Stress and Grain Shape on Granular Friction: Results of Discrete Element Simulations. J. Geophys. Res.-SOLID EARTH. (B12): Art. No. B12305:

[28] Riedel, W. 1929. Zur Mechanik geologischer Brucherscheinungen. Centralbl. f. Mineral. Geol. u. pal. v. 1929 B:354-368.

[29] Cloos, E. 1955. Experimental Analysis of Fracture Patterns. Bull. of Geol. Soc.of America. 66:241-256.

[30] Skempton, A. W. 1967. Some Observations on Tectonic Shear Zones. In: Proceedings of the First International Congress on Rock Mechanics, Lisbon. v1:pp. 329-335.

[31] Morgenstern, N. R., Tchalenko, J. S. 1967. Microstructural Observations on Shear Zones from Slips in Natural Clays. In: Proceedings of Geotechnical Conference on Shear strength of Natural Soils and Rocks, Oslo, Norwegian Geotechnical Institute. v1:pp. 147-152.

[32] Tchalenko, J. S. 1970. Similarities between Shear Zones of Different Magnitudes. Geol. Soc. of American Bull. 81:1625-1640.

[33] Hoek, E. 1965. Rock Fracture under Static Stress Conditions.CSIR Report. National Mechanical Engineering Research Institute, Council for Scientific and Industrial Research. MEG383.

[34] Gay, N. C. 1973. Fracture Growth around Openings in Thick walled Cylinders of Rock Subjected to Hydrostatic Compression. Int. J. Rock Mech. Min. Sci. Abstr. 10:209-233.

[35] Santarelli, F. J., Brown, E. T. 1989. Failure of Three Sedimentary Rocks in Triaxial and Hollow Cylinder Compression Tests. Int. J. Rock. Mech. Min. Sci. 26:401-413.

[36] Ewy, R. T., Cook, N. G. W. 1990. Deformation and Fracture around Cylindrical Openings in Rock - I. Observations and Analysis of Deformations. Int. J. Rock Mech. Min. Sci. Abstr. 27:387-407.

[37] Haimson, B. C., Song, I. 1993. Laboratory Study of Borehole Breakouts in Cordova Cream : A Case of Shear Failure Mechanism. Int. J. Rock Mech. Min. Sci. Abstr. 30:1047-1056.

[38] Lee, M., Haimson, B. 1993. Laboratory Study of Borehole Breakouts in Lac Du Bonnet Granite : A Case Extensile Failure Mechanism. Int. J. Rock Mech. Min. Sci. Abstr. 30:1039-1045.

[39] Dzik, E. J. 1996. Numerical Modeling of Progressive Fracture in the Compression Loading of Cylindrical Cavities. PhD. Department of Civil and Geological Engineering, University of Manitoba. 173pp.

[40] Sellers, E. J., Klerck, P. 2000. Modelling of the Effect of Discontinuities on the Extent of the Fracture Zone Surrounding Deep Tunnels. Tunnelling and Underground Space Technology. 15:463-469.

CHAPTER 2

LITERATURE REVIEW : PREVIOUS MODELING APPROACHES ON ROCK

2.1 INTRODUCTION

Rock is naturally complex. Its flaws and pores give it variable grain stiffness and strength and is often classed as discontinuous, inhomogeneous, anisotropic and non-elastic (DIANE) material as noted by Hudson and Harrison[1]. Because of this complexity, many rock models inevitably introduce various hypotheses. There are three general approaches in rock modeling depending on their hypotheses,

(1) Continuum mechanics,

(2) Fracture mechanics, and

(3) Particle mechanics.

These approaches are briefly reviewed in this chapter and shortcomings in applying such approaches to simulate the brittle rock fractures are discussed.

2.2 CONTINUUM MECHANICS

According to Desai and Siriwardane[2], assuming that a rock can be represented as a continuous, homogeneous, isotropic, linear elastic (CHILE) continuum, generally yield models in which rock or rock masses can be expressed as a function of principal stresses:

$$f(\sigma_1,\ \sigma_2,\ \sigma_3)=0, \tag{2.1}$$

or as a function of stress invariants:

$$f(I_1,\ I_2,\ I_3)=0, \tag{2.2}$$

$$I_1=\sigma_{kk},\ I_2=\frac{1}{3}(\sigma_{ik}\sigma_{ki}-\sigma_{mm}\sigma_{nn}),\ I_3=\frac{1}{6}(\varepsilon_{ijk}\varepsilon_{rst}\sigma_{ir}\sigma_{js}\sigma_{kt})$$

If hydrostatic stress does not affect yield condition yield function can be expressed as a function of second and third deviatoric stress invariants:

$$f(J_2,\ J_3)=0, \tag{2.3}$$

$$S_{ij}=\sigma_{ij}-\frac{1}{3}\sigma_{kk}\delta_{ij},\ J_2=\frac{1}{2}S_{ij}S_{ij},\ J_2=\frac{1}{3}S_{ij}S_{jk}S_{ki},$$

where, S_{ij} is deviatoric stress components and δ_{ij} is the Kroneker delta. When such yield functions are plotted in three dimensional principal stress space, various types of yield surfaces are formed. Such yield locus shapes are represented as either cylinder type (Von Mises, Tresca, Figure 2.1(a)) or cone type (Drucker-Prager, Mohr-Coulomb, Figure 2.1(b)). Numerous variations of yield locus for geo-materials were reviewed by Desai and Siriwardane[2] and Cividini[3]. Various failure criteria used for rock were summarized by Hudson and Harrison[1] (Table 2.1).

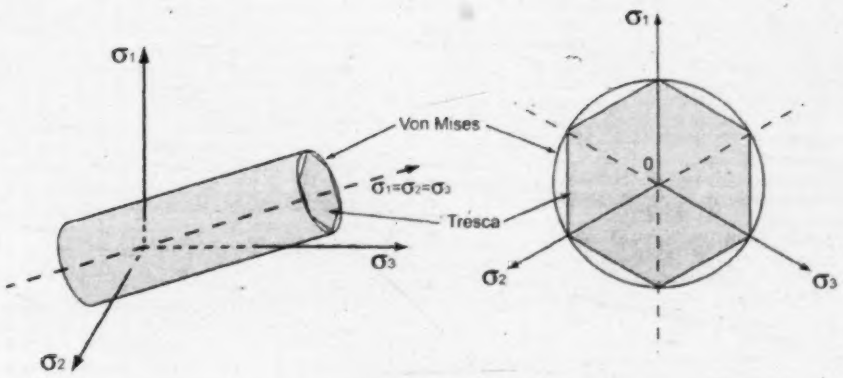

(a)

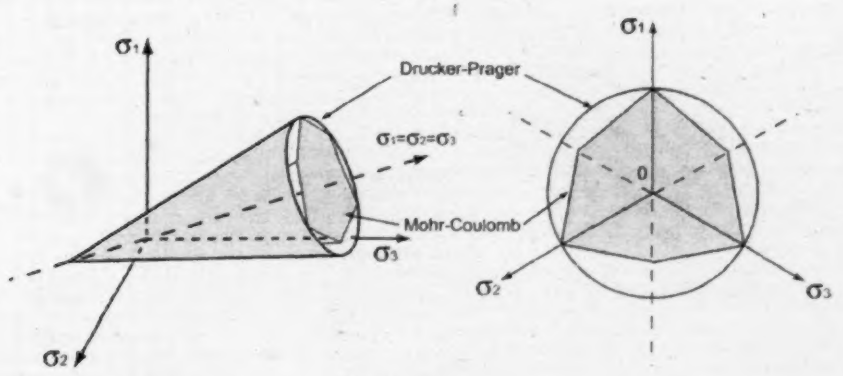

(b)

Figure 2.1 : Examples of yield surfaces plotted on a 3D principal stress space and octahedral plane (a) Cylinder type yield surface, Von Mises and Tresca, (b) Cone type yield surface, Drucker-Prager and Mohr-Coulomb.

Table 2.1 : Summary of rock yield criteria (modified from Hudson and Harrison[1])

Authors	Criteria	Constants	Development of criteria
Murrel (1963)	$\tau_{oct}^2 = 8T_o\sigma_{oct}$ or $J_2 = 4T_oI_1$	One constant (3D criterion)	Extended 3D Griffith theory.
Fairhurst(1964)	if $m(2m-1)\sigma_3 + \sigma_1 \geq 0$: $\sigma_3 = K$ if $m(2m-1)\sigma_3 + \sigma_1 < 0$: $\frac{(\sigma_1 - \sigma_3)^2}{(\sigma_1 + \sigma_3)} =$ $-2(m-1)^2 K\left[1 + \frac{2K}{(\sigma_1+\sigma_3)}\left\{\left(\frac{m-1}{2}\right)^2 - 1\right\}\right]^2$	Two constants (2D criterion)	Empirical generalization of 2D Griffith theory for intact rock.
Hobbs(1966)	$\sigma_1 = B\sigma_3^b + \sigma_3$ or $r = K_2\sigma_a^n$	Three parameters (2D criterion)	Empirical test data fitting for intact rocks.
Hock(1968)	$\sigma_1 - \sigma_3 = 2C + A(\sigma_1 + \sigma_3)^B$ or $\tau_{max} = \tau_{max\,0} + A\sigma_m^b$	Two constants (2D criterion)	Empirical curve fitting for intact rock.
Franklin(1971)	$\sigma_1 - \sigma_3 = \sigma_c^{1-B}(\sigma_1 + \sigma_3)$	Two constants (2D criterion))	Empirical curve fitting for 500 rock specimens
Bienlawski(1974)	$\sigma_1 = K'\sigma_3^A + \sigma_c$ or $\tau = B'\sigma_n^r + 0.1\sigma_c$	Three constants (2D criterion))	Empirical curve fitting for 700 rock specimens (5 types).
Yoshinaka and Yamabe(1980)	$\sigma_1 - \sigma_2 = \alpha K(q)(\sigma_1 + \sigma_2 + \sigma_3)^B$	Three parameters (3D criterion)	Empirical test data analysis for soft rocks(mudstone. etc.)
Hock and Brown(1980)	$\sigma_1 - \sigma_3 = \sqrt{m\sigma_c\sigma_3 + s\sigma_c^2}$ or $\tau = A(\sigma_n + B)^2$	Three parameters (2D criterion for rock and rock masses)	Appl. of Griffith theory and empirical curve fitting for rock and rock masses.
Johnston(1985)	$\frac{\sigma_1}{\sigma_c} = \left[\frac{M}{B}\frac{\sigma_3}{\sigma_c} + 1\right]^B$	Three parameters (2D criterion)	Empirical curve fitting for soft rock specimens.
Desai and Salami(1987)	$J_2' = \left(-\frac{\alpha}{\alpha_0}(I_1)^n + \gamma(I_1)^2\right)(1 - \beta S_r)^m$	More than six parameters (3D criterion)	Polynominal expansion in terms of stress invariants to curve fitting.
Michelis(1987)	$\ln\left(\frac{q^2}{f_0^2} + a_1 p\frac{q}{f_0} + a_2 p^2\right) =$ $a_4 \ln\left(\frac{2q/pf_0 + a_1 - a_3}{2q/pf_0 + a_1 + a_3}\right) + \ln a_5$	Four constants (2D criterion)	Analytical and experimental examination on yield surface(true triaxial test)
Hock and Brown(1998)	$\sigma_1 - \sigma_3 = \sigma_c\left(m_b\frac{\sigma_3}{\sigma_c} + c\right)^a$	Three parameters (2D criterion for rock and rock masses)	Modified criteria by the GSI introduction.
Martin et al.(1999)	$\sigma_1 - \sigma_3 = \sigma_c s^a$	Two constants (2D criterion)	Lower-bound rock strength criteria.

Such yield models are useful for defining the boundary between the elastic and plastic regions. Deformations occurring in the elastic region, i.e, below the yield threshold

depend only on the final stress state and not on the stress path. However, in the plastic region deformations depend on the stress path, and for many rocks the stress-strain relationships are non-linear.

In continuum models, the plastic deformations follow specific "flow rules" that are specified a priori by the user. Flow rules define the relationship between the plastic strain and stress and can be expressed in general form as (Desai and Siriwardane[2]):

$$d\varepsilon_{ij}^{p} = \frac{dq}{d\sigma_{ij}} d\lambda, \qquad (2.4)$$

where, $d\varepsilon_{ij}^{p}$ is the incremental plastic strain rate, q is the plastic potential function, and λ is an undetermined positive constant of proportionality.

According to Eqn. (2.4) the plastic strain rate is a gradient vector and thus is normal to the plastic potential surface, i.e., "normality rule". The plastic potential function can be either identical to or different from the yield function. The flow rule in the former case is called an "associated flow rule" while in the latter case it is called a "non-associated flow rule" (Figure 2.2).

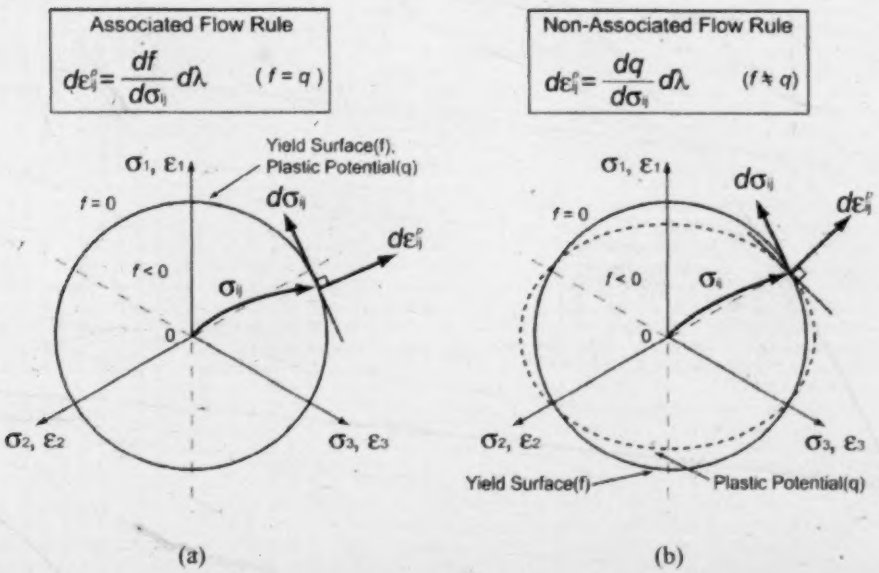

Figure 2.2 : Illustration of a flow rule defining the post yielding of a material. Flow rules are expressed as incremental plastic strain rates and also as gradient vectors normal to the plastic potential. If plastic potential function(q) is equal to the yield function(f) then is called (a) Associated flow rule otherwise (b) Non-associated flow rule.

Once the material has yielded, if the post-peak stresses are identical to the yield stress, the material behavior can be classed as elastic-perfectly-plastic behavior. In modeling such material (some metals, loose sand, normally consolidated clay), associated flow rules are often used to represent the material response. If the post-peak stresses are less than the yield stress, the material behavior can be classed as elastic-brittle or strain-weakening. In strain-weakening materials such as over consolidated stiff clay, dense sand or rock, non-associated flow rules are generally used.

Application of conventional plastic theory to represent the brittle fracturing of rock and the associated induced dilation (see Figure 1.4) is extremely problematic. For

practical applications plastic models are normally incorporated with a mesh dependant numerical method such as FEM (finite element method) or FDM (finite difference method). The fundamental hypothesis embedded in the continuum approach is that the displacement field should be continuous. In other words, under the continuum assumption, nodal points forming the mesh are always shared with other elements. For the modeling of closed cracks that have planar and smooth surfaces, such numerical approaches might be possible if interface elements are used. However, as physically observed in many rocks, actual fracture surfaces are neither planar nor perfectly smooth. Moreover, once dilatant fractures form, the continuum displacement hypothesis is no longer valid.

To overcome such shortcomings, some approaches have adopted remeshing techniques (Gerstle et al.[4, 5], Martha et al.[6]) but such approaches are limited. An extension of this approach is fracture mechanics which is discussed in the next section.

2.3 FRACTURE MECHANICS APPROACH

2.3.1 ROCK FRACTURE MODEL

Fracture models of rock date back to the early 1900s. Griffith[7] noted that that the actual tensile strength of a material is much lower than theoretically predicted. He postulated that the many submicroscopic flaws and other discontinuities in brittle materials serve as stress concentrators resulting in fracture initiation from the tip of such flaws. Using an energy balance approach, and assuming an elliptical hole in an infinite

plate subjected to uniform tension at infinity as shown in Figure 2.3(a), he proposed a relationship between fracture strength and initial flaw size, expressed as:

$$\sigma_f = \sqrt{\frac{k\gamma_s E}{a}}, \qquad (2.5)$$

$k = \frac{2}{\pi}$ For plane stress,

$k = \frac{2}{\pi}(1-\upsilon^2)$ For plane strain,

where E is Young's modulus, γ_s is the specific surface energy, i.e., the energy required to create a unit area of crack new surface as the crack increases in length: a is crack half-length and υ is Poisson's ratio.

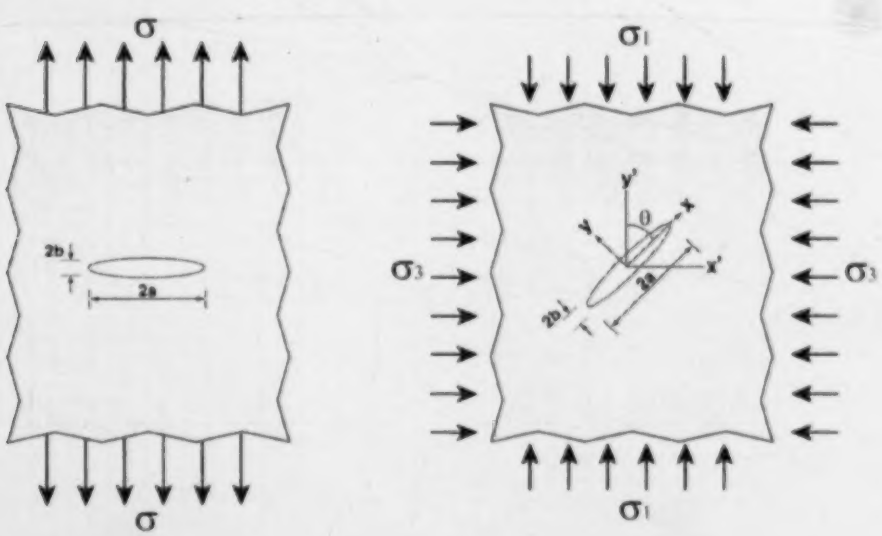

Figure 2.3 : Griffith's narrow elliptical cracks, (a) Direct tension model, (b) Compression model.

In using Eqn. (2.5) for calculating uniaxial tensile strength, it is assumed that the crack extends in its own plane. This assumption might be appropriate for the case of direct tension, however, difficulty occurs when applying Eqn. (2.5) to more complicated stress fields such as compression. Under compressive stress condition, Griffith's tension crack shown in Figure 2.3(a) can be closed. Griffith[8] proposed a fracture yield model for the inclined open elliptical crack subjected to compressive stresses as shown in Figure 2.3(b). Griffith's fracture model for compression is normally expressed as a function of principal stresses:

$$(\sigma_1 - \sigma_3)^2 = -8\sigma_t(\sigma_1 + \sigma_3) \qquad \text{when } \sigma_1 + 3\sigma_3 > 0, \qquad (2.6)$$

$$\sigma_3 = \sigma_t \qquad \text{when } \sigma_1 + 3\sigma_3 < 0.$$

If $\sigma_3 = 0$, then σ_1 becomes the uniaxial compressive strength (σ_c), given as:

$$\sigma_c = -8\sigma_t \qquad (2.7)$$

Eqn. (2.7) implies that the unixial compressive strength found in Griffith's compression theory is 8 times greater than the uniaxial tensile strength.

Griffith's approach was successful in accounting for the initiation of cracks under biaxial compressive loading. Under compressive loading conditions however, elliptical cracks may close before the tensile stress at the crack tip is sufficient to initiate a crack. Once the crack has closed, shear stresses caused by the contact friction of crack surfaces have to be overcome before tensile crack initiation can occur.

McClintock and Walsh [9] modified the Griffith's compression model using an initially inclined closed crack as shown in Figure 2.4. This modification to Griffith's compression model is expressed in terms of principal stresses as given in Eqn. (2.8):

$$\sigma_1 = \sigma_3 \left[1 + \frac{2\mu}{\sqrt{1+\mu^2} - \mu} \right] + \sigma_c, \qquad (2.8)$$

where, μ is given as the coefficient of friction on crack surfaces and σ_c is the uniaxial compressive strength.

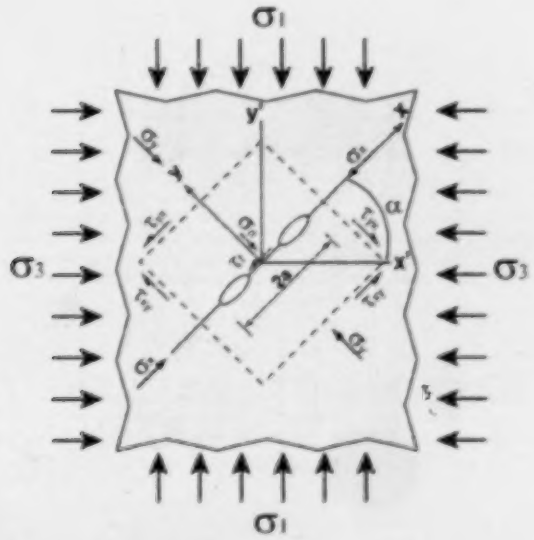

Figure 2.4 : Modified Griffith model by McClintock and Walsh[9] considering shear resistance of the closed crack.

Eqn. (2.8) also can be expressed in terms of a linear Mohr envelope:

$$\tau = \mu\sigma_n - 2\sigma_t, \qquad (2.9)$$

where σ_n is a normal stress acting on the crack surface and σ_t is the uniaxial tensile strength.

Hoek[10] extensively surveyed the published rock fracture data and presented the results in a dimensionless ratio of fracture initiation strength to uniaxial compressive strength. Excellent agreement was achieved between the actual fracture initiation strength and the yielding predicted by the modified Griffith theory: this is shown in Figure 2.5. However, inspection of Figure 2.5 reveals that the coefficient of friction can be more than unity. This is not likely to occur because a coefficient of friction greater than unity implies that the shear resistance is greater than the normal stress acting on the crack surfaces. Hoek[10] stated that such anomalous behavior implies that there must be interlocking projections on the crack faces thus propagation of the crack can occur only when these projections have been sheared off.

Cook[11] suggested modifying the Griffith shear fracture criterion to account for the energy required to overcome the frictional resistance along the crack surfaces expressed as,

$$\tau = \mu\sigma_n - \sqrt{\frac{2kE\gamma_s}{a}} \qquad (2.10)$$

where, k is the same definition as Eqn. (2.5).

During the past few decades other shear fracture models have been introduced and a detailed review of these models was carried out by Barry et al.[12]. These models assume that the fractures are elliptically thin and either open or closed. In rock it is doubtful that the yield process can be represented as single closed or open fracture.

The fracture models discussed above illustrate the initiation of fractures. In direct-tensile loading, fracture initiation immediately results in rupture of the rock specimen. Under compression loading, rock yielding is caused not by the initiation of a single-crack, but by the coalescence of individual cracks linking to form a shear band (Hallbauer et al.[13], Tapponnier and Brace[14], Lockner et al.[15], Dey and Wang[16], Du and Aydin[17]). Moreover, fracture yield models also do not capture the deformation associated with the fracture opening, i.e., dilation and extension of the fracture. In the next section, fracture extension and dilation models will be explored.

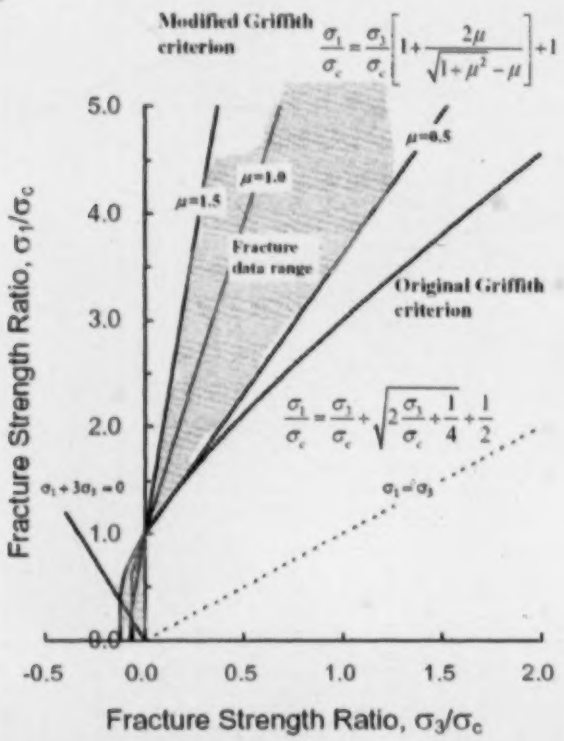

Figure 2.5 : Validation of modified Griffith theory compared with actual crack yield strengths published in the literature.

2.3.2 EXTENSILE FRACTURE MODELS

EXPERIMENTAL APPROACH

Hoek[10] carried out a series of tests on plates of glass with an inclined open flaw to examine the relationship between crack growth and the confinement stress ratio σ_3/σ_1(see Figure 2.6). The tests were carried out using 150mm square plates of annealed glass approximately 5mm thick. Hoek[10] showed that as the confining stress (σ_3) is decreased, the wing cracks start to extend. At a ratio of approximately $\sigma_3/\sigma_1 <$ 0.05 the wing cracks significantly increase in length (Figure 2.6). Figure 2.6 implies that as the ratio σ_3/σ_1 approaches zero, the length of the wing cracks approach infinity. This can only occur if the crack opening force is held constant. The inclined surface in Hoek's experiment serves as a crack-opening force to propagate mode I cracks (see definition in Figure 2.7). Usually the crack-opening force is associated with a finite stiffness, and hence the crack-opening force will decrease as the crack lengthens. Thus, crack length will not be infinite.

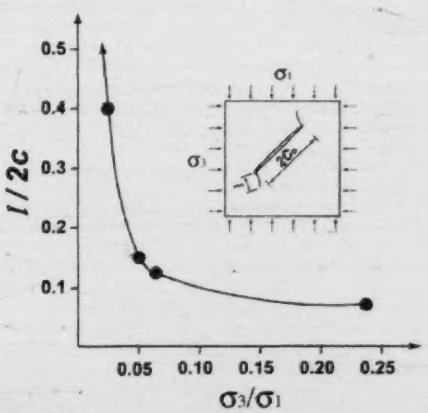

Figure 2.6 : Relationship between extension of wing crack and confinement ratio (after Hoek, 1965[10].

SHEAR SLIP MODELS

Experimental investigations for the growth of Mode I extension cracks have been reviewed by numerous researchers (Nemat-Nasser and Horii [18], Horii and Nemat-Nasser [19], Ashby and Hallam [20], Sammis and Ashby [21], Germanovich and Dyskin [22]) – all of which used an initially inclined single fracture to investigate crack growth. In this model the application of non-hydrostatic stress causes shear slippage along the existing fracture. This slippage results in the growth of tensile, "wing cracks", in the direction of maximum principal stress. In linear elastic fracture mechanics (LEFM), the fracture will propagate when the stress intensity factor K_I exceeds the fracture toughness K_{IC} (Barry et al.[12]). The maximum length of such a wing crack can be calculated from the relationship between K_I and the propagation length of the wing crack; K_{IC} can be obtained from laboratory tests.

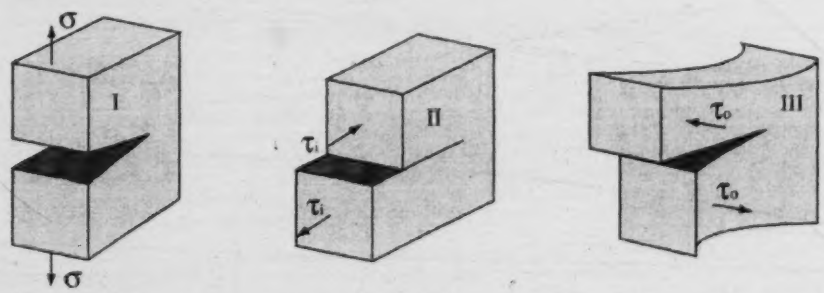

Mode I (or opening mode) ($\tau_i = \tau_o = 0, \sigma \neq 0$)

Mode II (or sliding mode) ($\sigma = \tau_o = 0, \ \tau_i \neq 0$)

Mode III (or tearing mode) ($\sigma = \tau_i = 0, \ \tau_o \neq 0$)

Figure 2.7 : Three primary modes of fracture.

Ashby and Hallam[20] investigated the propagation of mode I cracks in a compressive stress field and developed a shear slip fracture model based on the energy equilibrium concept (Figure 2.8); the model is given as:

$$K_I = \frac{\sigma_1 \sqrt{\pi c_o}}{(1+L)^{3/2}} \{1 - \lambda - \mu(1+\lambda) - 4.3\lambda L\} \times \left(0.23L + \frac{1}{\sqrt{3(1+L)}} \right), \qquad (2.11)$$

where, $\lambda = \sigma_3/\sigma_1$, $L = l/c_o$ and μ is the coefficient of friction. The orientation of the wing cracks relative to the shear fracture (θ) is related to μ by $\theta = 2\tan^{-1}(1/\mu)$.

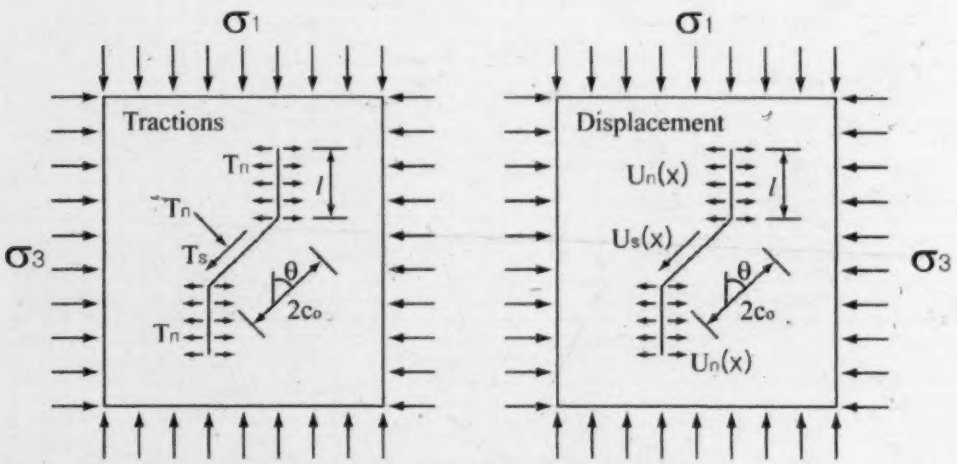

Figure 2.8 : Shear slip model suggested by Ashby and Hallam[20]

Kemeny and Cook[23] suggested a simplified shear-crack model (Eqn. (2.12), Figure 2.9 (a)) based on the solution for a straight, axially oriented crack with symmetrically opposed point forces at the crack center. This model is modified from Nasser and Horii's[18] fracture model by neglecting initial kink wing crack growth and adding a confinement term given as:

$$K_I = \frac{2c_o\tau^* \cos\theta}{\sqrt{\pi l}} - \sigma_3\sqrt{\pi l}\,, \qquad (2.12)$$

where $\tau^* = \tau_n - \mu\sigma_n$

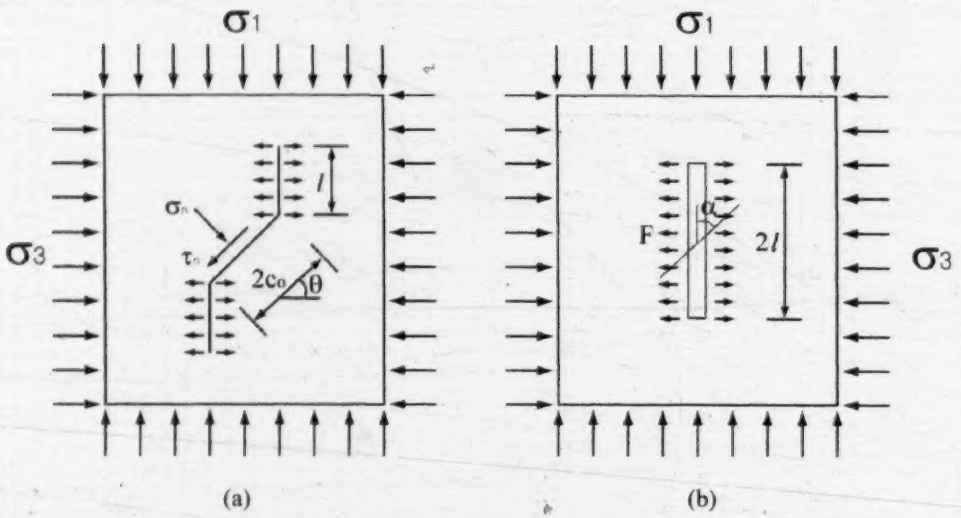

Figure 2.9 : (a) Kemeny and Cook[23], (b) Germanovich and Dyskin[24]

Germanovich and Dyskin[24] used a similar approach for their sliding crack model based on the pioneering work of Fairhurst and Cook[25]. They also proposed a relationship between crack length and the compressive stress field given by:

$$K_I = \frac{F}{\sqrt{\pi l}} - \sigma_3 \sqrt{\pi l}\,, \qquad (2.13)$$

where F = $\cos\sigma_1\beta(\alpha)$, $\beta(\alpha)=\sin^2\alpha\cos\alpha(1-\tan\alpha\tan\phi)$, and α is a shear fracture angle measured from the major principal stress axis (Figure 2.9 (b)).

PORE MODELS

When porous brittle solids are loaded under compression, small tensile cracks grow from the pores. The extent of each crack is calculated as a function of pore size and confining pressure. Sammis and Ashby[21] investigated the propagation of mode I cracks with circular pores (both cylindrical and spherical) under compression both experimentally and analytically, and suggested an analytical fracture model based on the energy concept (Figure 2.10). The two models (cylindrical and spherical) are similar to the shear slip model proposed by Ashby and Hallam[20]and are given as:

Cylindrical Model:

$$K_I = L^{\frac{1}{2}} \left\{ \frac{1.1(1-2.1\lambda)}{(1+L)^{3.3}} \right\} \sigma_1 \sqrt{\pi c_o} \,. \qquad (2.14)$$

Spherical Model:

$$K_I = L^{\frac{1}{2}} \left\{ \frac{0.62(1-1.8\lambda)}{(1+L)^{4.1}} \right\} \sigma_1 \sqrt{\pi c_o} \,. \qquad (2.15)$$

These pore models were developed based on the extensile mode of cracks in a compressive stress environment. However, it is difficult to apply these models to closed vertical or elliptical cracks.

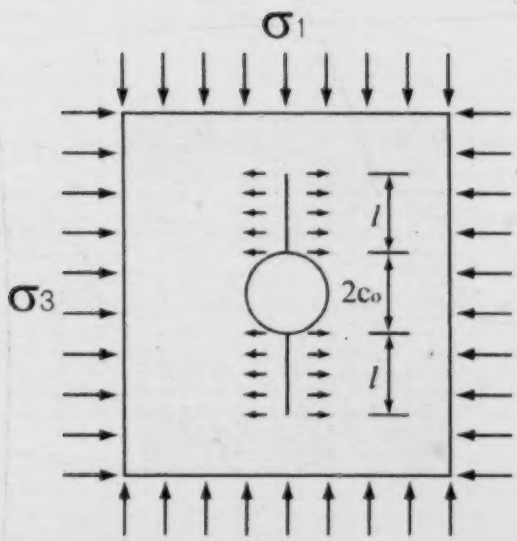

Figure 2.10 : Pore models for extensile fracture (after Ashby and Hallam[20])

2.3.3 DISCUSSION ON FRACTURE MECHANICS

Since Griffith (1921, 1924) introduced energy concepts for rupture, fracture mechanics approach have often been applied to fracturing in rock. The most commonly proposed model invokes:

1) Axially extending wing crack growth resulting from the shear slip of initially inclined flaws, and
2) Material is homogeneous within the sample

While the first assumption is one of the popular models for illustrating rock fracture, sliding microcracks in rock specimens have not been observed in numerous experiments (e. g. Brace et al.[26], Wawersik and Brace[27], Hallbauer et al.[28], Tapponier and Brace[14]) .

While fracture mechanics may have limited application for illustrating the behavior of an isolated crack, there is little evidence that rock strength is controlled by a single flaw. The limitations of fracture models to the application of rock behavior have led researchers to develop alternative approaches to simulate the heterogeneous nature of rock. Such approaches will be reviewed in the next section.

2.4 DEM APPROACH

The discrete element method (DEM) attempts to overcome the limitations of continuum and fracture mechanics in describing the behavior of rock. Cundall[29], and Cundall and Strack[30] originally proposed the DEM for modelling granular materials. Since its introduction in the 1970s, the DEM has been widely used for modeling rock and soil. In the mid-1990s the Itasca Consulting Group Inc. introduced the particle flow code (PFC[31]) based on work by Cundall[29]. Both two dimensional and three dimensional analyses are possible in PFC code and a modeling environment is provided through an internal compiler called "FISH". The DEM illustrated in this section is associated with a two dimensional bonded particle analogue using PFC. A brief review of two dimensional PFC will be illustrated in following subsection.

2.4.1 PFC (PARTICLE FLOW CODE) : A BRIEF REVIEW

The particle flow code[31] is based on the discrete element method and utilizes circular or spherical elements. Unlike other continuum codes, PFC does not require mesh generation and only requires two elements, a wall and a particle. In the two dimensional environment, particle elements are either disk shaped with finite thickness (i.e., a rod) or spherical shaped with a single layer out of the plane direction. The disk type particle model is similar to the plane strain condition and the single layered spherical model is similar to the plane stress condition in continuum mechanics.

The wall element normally acts like a loading plate or membrane that directly applies a specified velocity to the particle assembly. The fundamental assumptions embedded in PFC were illustrated in Chapter 1. Since each particle is a rigid body, the particle itself cannot be deformed. Instead, the rigid particles overlap each other when they compressed and move apart when subjected to tension. The rigid body movement of each particle is calculated by Newton's second law and the deformability between particles is defined by the specific constitutive law at the contact point as shown in Figure 2.12.

As external forces are applied to the particle assembly in equilibrium, rigid particle movement is calculated using law of motion (i.e. Newton's second law), then particle contacts, deformation, wall positions are updated and contact forces are calculated based on the constitutive law at contact points. Such contact forces impact particle movement, and cycling of the system is continued until the specified unbalanced force is reached. This process is illustrated in Figure 2.11. Hence, solving a problem using

PFC is a cyclic process of updating particle movement information and unbalanced forces caused by contact forces calculated from the updated particle motion.

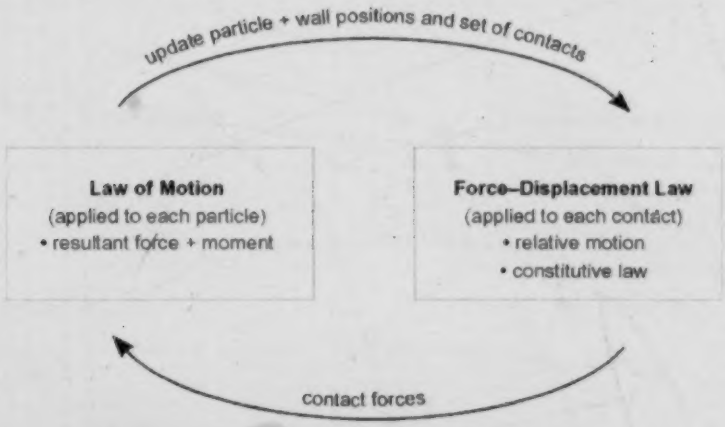

Figure 2.11 : PFC calculation cycle (Itasca, Consulting Group[31])

For the modeling of rock-like material, a bond model is implemented in PFC. Particle bonding can be specified either at the contact point (contact bond model) or some other finite area (parallel bond model). The contact bond model specifies the bond strength at the contact. While this model can resist tension or shear, it is sensitive to particle rotation, i.e., moments. The parallel bond model utilizes a beam model to resist particle rotation. A parallel-bonded contact is represented as a short length beam with a rectangular or circular cross-section as shown in Figure 2.12. A parallel-bond model can resist shear, tension, and bending moments.

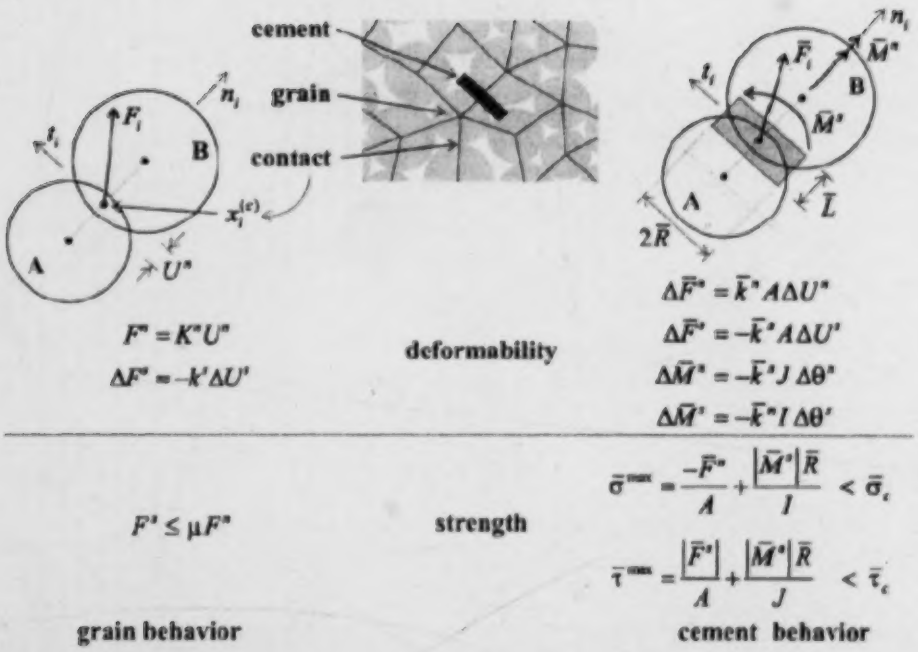

Figure 2.12 : Particle constitutive law and bond strength principle (after Potyondy and Cundall[32]).

In PFC bond rupture, a crack forms when the shear or tensile forces reach the specified bond strength. When bond-rupture is tensile the bond tensile strength immediately drops to zero. In shear bond rupture the strength reduces to a residual value that is a function of the normal stress and the coefficient of friction acting at the contact (see Figure 2.13).

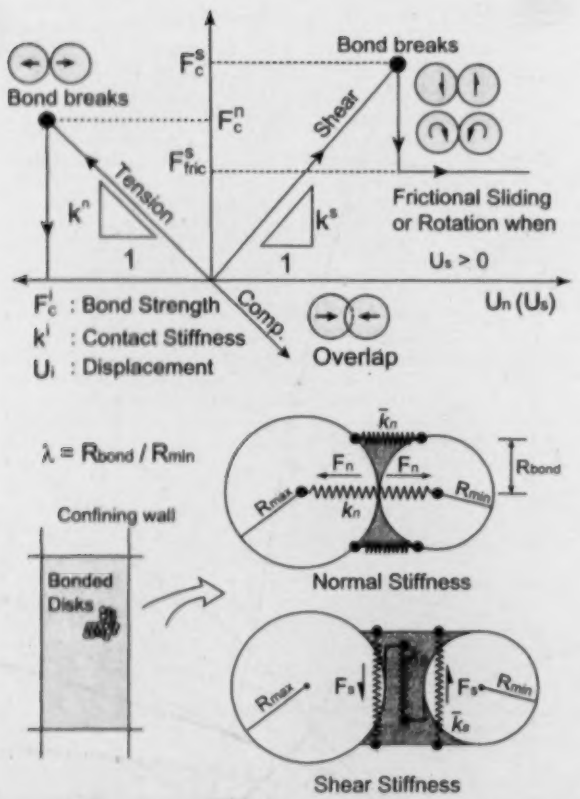

Figure 2.13 : Micro parameters and an illustration of the yielding process for micro bonding. Force and displacement logic and micro parameters at particle contact and bonding in PFC modified from Potyondy and Cundall[32]. The micro normal stiffness is contributed by both contact normal stiffness (k_n) and bond normal stiffness ($\bar{k}_n$). The micro shear stiffness is composed of contact shear stiffness (k_s) and bond shear stiffness ($\bar{k}_s$). The normal and shear bond strength are specified at the bonded area determined by minimum particle radius and bond radius ratio (λ). If the bond is broken by tension, bond strength immediately drops to zero and PFC regard this process as tension crack. Shear crack is recorded when the bond is broken by shearing or by the moment load due to particle rotation. Once the bond is broken the micro strength immediately drops to a residual value depending on the applied normal force on the particle and the coefficient of friction. Meanwhile, particle displacement by compression is reflected by particle overlap.

2.4.2 APPLICATION IN ROCK MODELING

Diederichs[33] successfully used a contact bonded model to simulate the brittle behavior of rock under compressive stresses. Using PFC he showed that the heterogeneity observed in polycrystalline rock (granite for example) can be reproduced, and that local tensile stresses were revealed when the loading conditions were all-round compression (Figure 2.14). He also found that PFC could simulate all aspects of systematic rock failure processes such as crack initiation, crack coalescence, and shear zone formation (Figure 2.15 and Figure 2.16).

Potyondy and Cundall [32] found similar results for uniaxially compressed rock. However, they indicated that under biaxially loaded rock simulation, the circular particle model resulted in a lower peak strength envelope compared with the strength envelope obtained in the laboratory. They explained that such a discrepancy was caused by lack of interlocking friction along the irregular grain boundary that was approximated as smooth surfaces in the circular particle assembly. To overcome this problem, they introduced a cluster model in which particles were grouped with infinite or finite strong bond strength such that the grouped particles acted as individual mineral grains (Figure 2.17). Using this approach they could simulate a peak strength envelope that was in closer agreement with the laboratory results (Figure 2.18).

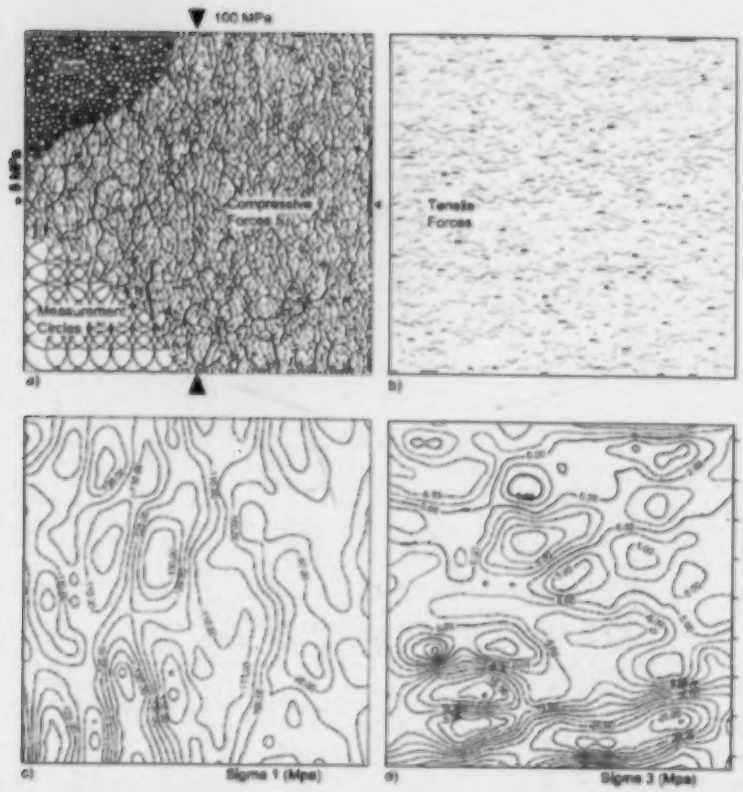

Figure 2.14 : Development of local tensile stresses under compression in particle assembly (after Diederichs[33])

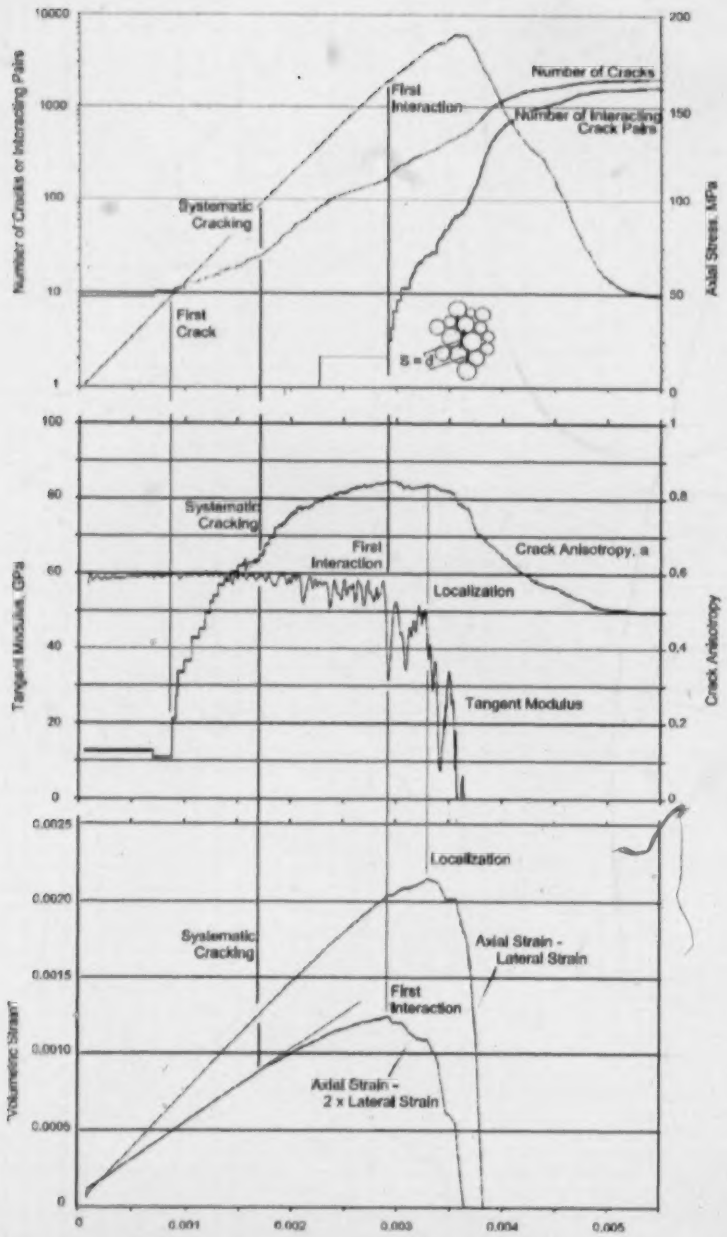

Figure 2.15 : Systematic damage process of rock in particle assembly by uniaxial compressive test simulation (after Diederichs[33]).

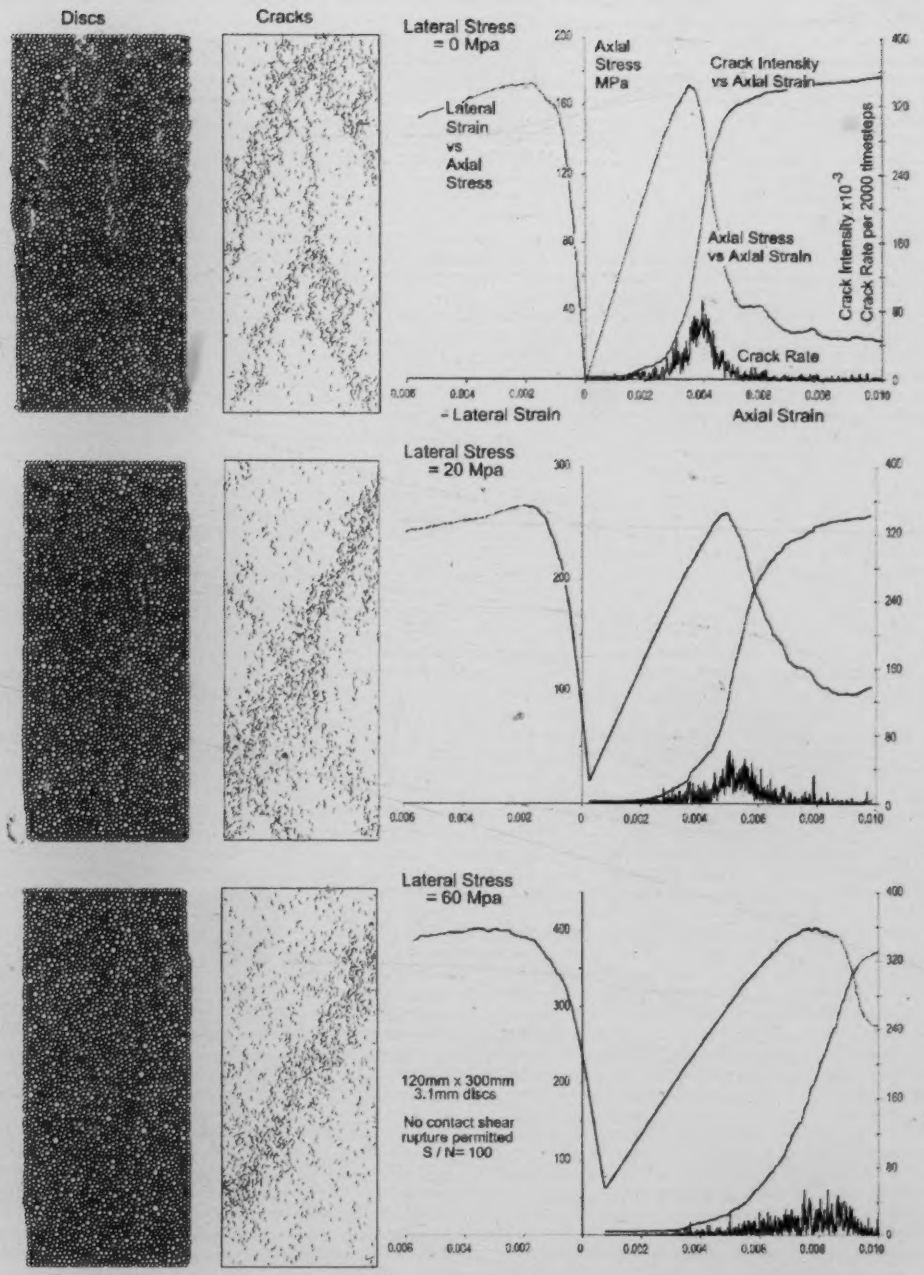

Figure 2.16 : Formation of shear rupture surface and stress strain responses of biaxial simulation of PFC (after Diederichs, 2000[33]).

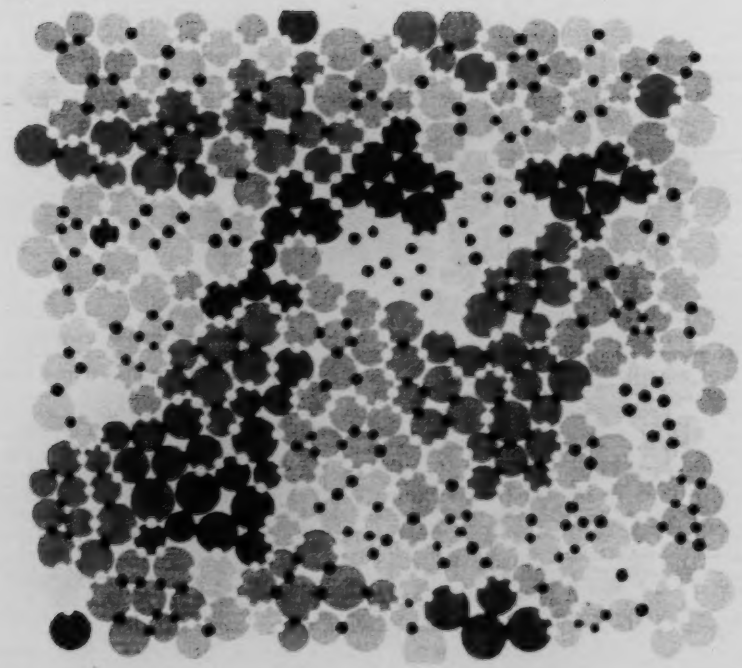

Figure 2.17 : Approximating irregular grain with a clustered particle model in PFC2D. The small black circles show intra-cluster bonds while white small white circles indicate inter-cluster bonds (after Potyondy and Cundall[32]).

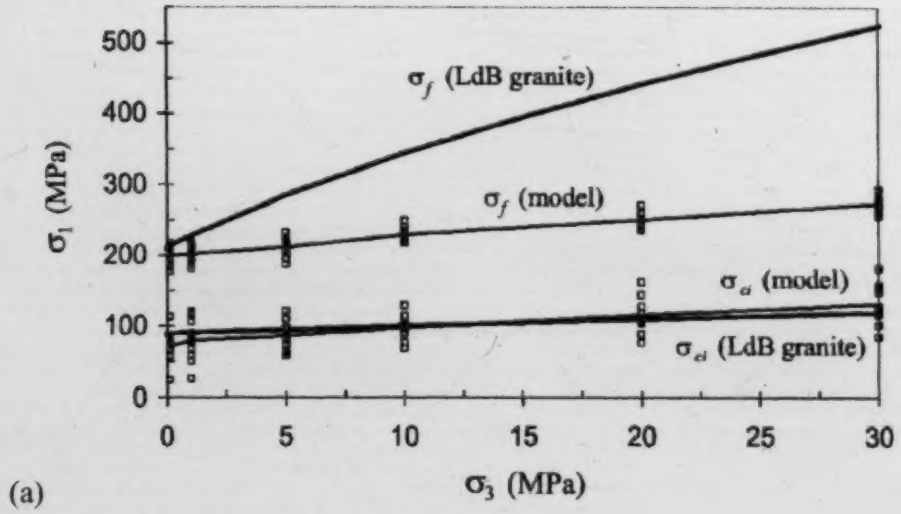

(a)

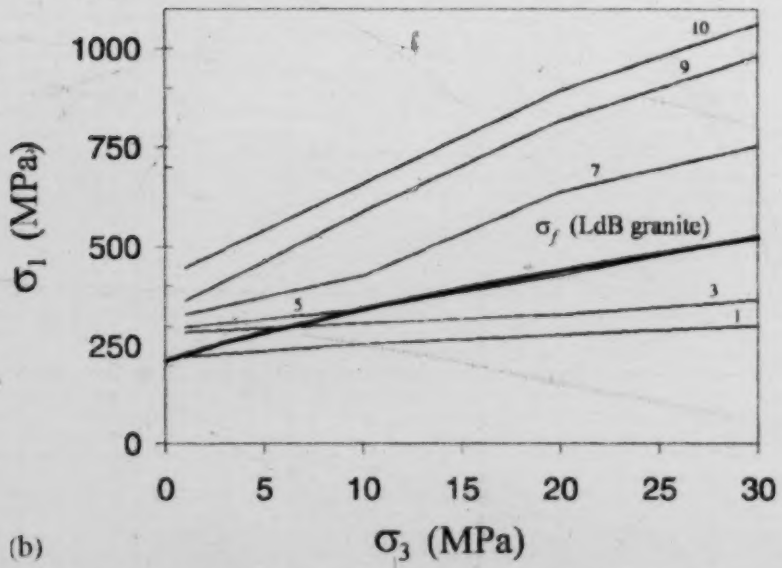

(b)

Figure 2.18 : PFC simulated failure envelope compared with Lac du Bonnet granite. (a) Circular particle assembly, (b) Clustered particle assembly (after Potyondy and Cundall[32]).

While PFC simulation of rock behavior in compression was reasonably successful, the application of PFC for tensile behavior had limited success (Diederichs[31]). Diederichs found that the tensile strength of granite obtained using PFC was approximately 1/5 of the uniaxial compressive strength. Diederichs was simulating Lac du Bonnet granite and according to Lajtai [32], the ratio of tensile to compressive strength is approximately 1/20.

Diederichs [33] concluded that the linear failure envelope in PFC resulted in significantly higher tensile strength (Figure 2.19).

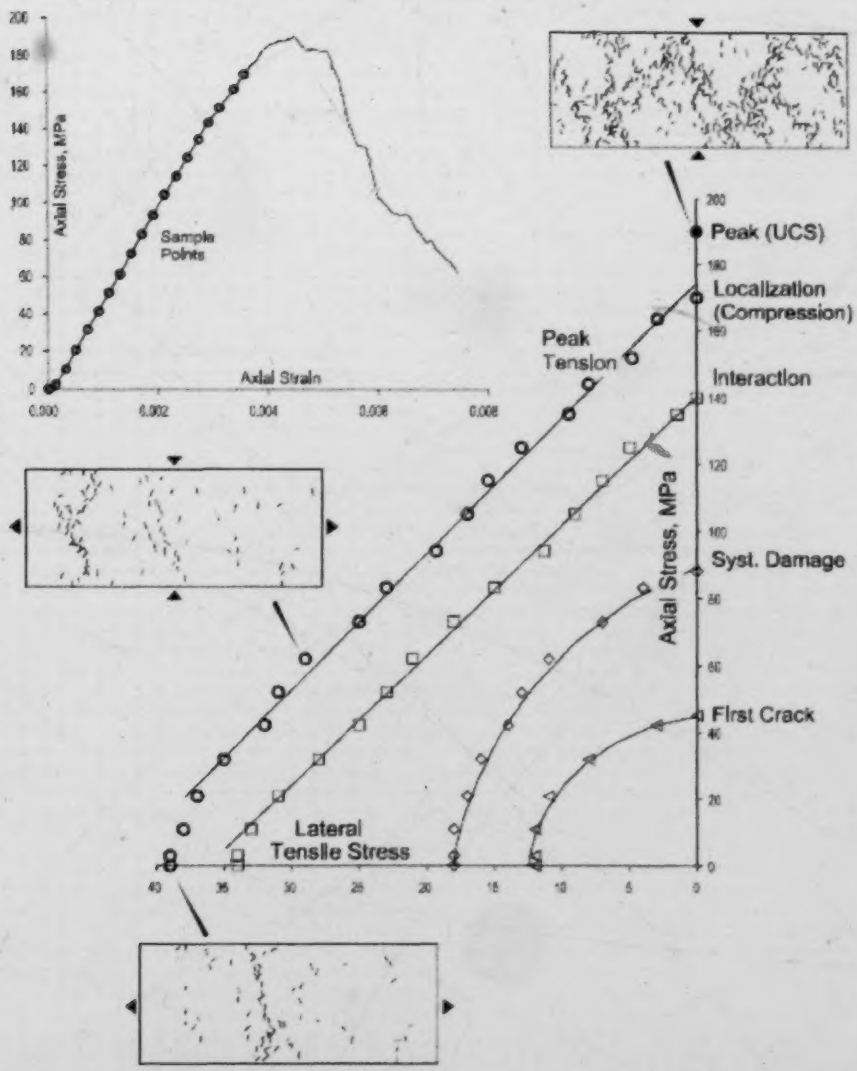

Figure 2.19 : Linear failure envelope resulting from confined direct shear test simulation (after Diederichs[33]).

2.5 SUMMARY

In this chapter, three unique modeling approaches to rock behavior were reviewed. Continuum mechanics combined with continuum numerical methods such as FEM or FDM is one of the widely used methods of modeling geo-materials. However, the fundamental CHILE assumptions made in this approach are too narrow to mimic discretely complex fracture behavior and naturally heterogeneous rock. Moreover, most continuum approaches are used to approximate macro-scale behavior. The modeling of micro-scale processes that occur prior to the peak macro-scale behaviour has met with limited success using continuum approaches.

Fracture mechanics approaches simulate discrete fracture processes and appear to approximate the the micro-scale phenomena observed in rock. Fracture mechanics has been used to illustrate the fundamental behaviour of single fractures but is not generally used to simulate the failure of rock in compression.

The DEM/PFC approach is one of the most promising approaches for simulating failure processes observed in rock. In Chapter 4 of this thesis shortcomings of the PFC identified by Diederichs[31] and Potyondy and Cundall[32] will be explored.

2.6 REFERENCE

[1] Hudson, J. A., Harrison, J. P. 1997. Engineering Rock Mechanics : An Introduction to the Principles. Elsevier, Oxford.

[2] Cai, M., Kaiser, P. K., Martin, C. D. 2001. Quantification of Rock Mass Damage in Underground Excavations from Microseismic Event Monitoring. *Int. J. Rock. Mech. Min. Sci.* 38:1135-1145.

[3] Cividini, A. 1993. Constitutive Behaviour and Numerical Modelling. Comprehensive Rock Engineering: Principles, Practice and Projects. 1:395-426.

[4] Gerstle, W. H., Ingraffea, A. R., Perucchio, R. 1988. Three-Dimensional Fatigue Crack Propagation Analysis using the Boundary Element Method. *International Journal of Fatigue.* 10:187-192.

[5] Gerstle, W. H., Martha, L., Ingraffea, A. R. 1987. Finite and Boundary Element Modeling of Crack Propagation in Two- and Three dimensions. *Engineering with Computers.* 2:167-183.

[6] Martha, L. F., Wawrzynek, P. A., Ingraffea, A. R. 1993. Arbitrary Crack RepResentation using Solid Modeling. *Engineering with Computers.* 9:63-82.

[7] Griffith, A. A. 1921. The Phenomena of Rupture and Flow in Solids. *Philos. Trans. Roy. Soc. London, Series A, Math. Sci.* 221:163-198.

[8] Griffith, A. A. 1924. The Theory of Rupture. In Proc. First International Congress for Applied Mechanics, pp. 55-63.

[9] McClintock, F. A., Walsh, J. B. 1962. Friction on Griffith Cracks in Rock under Pressure. 4th US Natl. Cogr. Appl. Mech. , Berkeley, pp. 1051-1021.

[10] Hoek, E. 1965. Rock Fracture under Static Stress Conditions.CSIR Report. National Mechanical Engineering Research Institute, Council for Scientific and Industrial Research. MEG383.

[11] Cook, N. G. W. 1965. The Failure of Rock. *Int. J. Rock. Mech. Min. Sci. Abstr.* 2:389-403.

[12] Barry, N. W., Raghu, N. S., Gexin, S. 1992. Rock Fracture Mechanics : Principles, Design and Applications. Elsevier 570p

[13] Hallbauer, D. K., Wagner, H., Cook, N. G. W. 1973. Some Observations concerning the Microscopic and Mechanical Behaviour of Quartzite Specimens in Stiff, Triaxial Compression Tests. *Int. J. Rock. Mech. Min. Sci. Abstr.* 10:713-726.

[14] Tapponnier, P., Brace, W. F. 1976. Development of Stress-Induced Microcracks in Westerly Granite. *Int. J. Rock. Mech. Min. Sci. Abstr.* 13:103-112.

[15] Lockner, D. A., Byerlee, J. D., Kuksenko, V., Ponomarev, A., Sidorin, A. 1991. Quasi-static Fault Growth and Shear Fracture Energy in Granite. *Nature.* 350(7):p. 807-816.

[16] Dey, T. N., Wang, C. Y. 1981. Some Mechanisms of Microcrack Growth and Interaction in Compressive Rock Failure. . *Int. J. Rock Mech. Min. Sci. Abstr.* 18:199-209.

[17] Du, Y., Aydin, A. 1991. Interaction of Multiple Cracks and Formation of Echelon Crack Arrays. *Int. J Num. and Anal. Meth. in Geomech.* 15:205-218.

[18] Nemat-Nasser, S., Horii, H. 1982. Compression-Induced Nonplanar Crack Extension with Application to Splitting, Exfoliation and Rockburst. *J. Geophys. Res.* 87:6805-6821.

[19] Horii, H., Nemat-Nasser, S. 1985. Compression-Induced Microcrack growth in Brittle Solids : Axial Splitting and Shear Fracture. *J. Geophys. Res.* 90:3105-3125.

[20] Ashby, M. F., Hallam, S. D. 1986. The Failure of Brittle Solids Containing Small Cracks under Compressive Stress. *Acta. Metall.* 34:497-510.

[21] Sammis, C. G., Ashby, M. F. 1986. The Failure of Brittle Porous Solids under Compressive Stress States. *Acta. Metall.* 34:511-526.

[22] Germanovich, L. N., Dyskin, A. V. 2000. Fracture Mechanisms and Instability of Openings in Compression. *Int. J. Rock Mech. Min. Sci. Abstr.* 37:263-284.

[23] Kemeny, J. M., Cook, N. G. W. 1987. Crack Models for the Failure of Rocks in Compression. In Proc. 2nd Int. Conference Constitutive Laws for Engineering Materials : Theory and Applications, Desai, C.S., Krempl, E., Kiousis, P.D.,Kundu, T. editors, Elsevier, pp. 879-887.

[24] Germanovich, L. N., Dyskin, A. V. 1988. A Model of Brittle Failure for Material with Cracks in Uniaxial Loading. *Mechanics of Solids.* 23:111-123.

[25] Fairhurst, C., Cook, N. G. W. 1966. The Phenomenon of Rock Splitting Parallel to the Direction of Maximum Compression in the Neighbourhood of a Surface. In Proc. of the 1st Congress of the International Society of Rock Mechanics, pp. 687-692.

[26] Brace, W. F., Paulding, B., Scholz, C. 1966. Dilatancy in the Fracture of Crystalline Rocks. *J. Geophys. Res.* 71:3939-3953.

[27] Wawersik, W. R., Brace, W. F. 1971. Post-failure Behaviour of a Granite and Diabase. . *Rock Mech. and Rock Eng.* 3:61-85.

[28] Hallbauer, D. K., Wagner, H., Cook, N. G. W. 1973. Some Observation Concerning the Microscopic and Mechanical Behaviour of Quartzite Specimens in Stiff, Triaxial Compression Tests. *Int. J. Rock Mech. Min. Sci. Abstr.* 10:713-726.

[29] Cundall, P. A. 1978. BALL-A Program to Model Granular Media using the Distinct Element Method. . *Technical Note: Dames and Moore Advanced Technology Group, London.*

[30] Cundall, P. A., Strack, O. D. L. 1979. A Discrete Numerical Model for Granular assemblies. *Geotechnique.* 29:47-65.

[31] Itasca Consulting Group. 2004. PFC2D(Particle Flow Code in 2 Dimensions) version 3.1.

[32] Potyondy, D. O., Cundall, P. A. 2004. A Bonded-Particle Model for rock. *Int. J. Rock. Mech. Min. Sci.* 41:1329-1364.

[33] Diederichs, M. S. 2000. Instability of Hard Rock Masses : The Role of Tensile Damage and Relaxation. Ph.D. thesis. Dept. of Civil Eng., University of Waterloo. 567pp.

CHAPTER 3

LABORATORY TESTS

3.1 INTRODUCTION

Models previously reviewed of the extensile fracturing and the micro dilation processes occurring in rock are not adequate to mimic heterogeneity induced micro processes in poly crystalline rock such as granite. The discrete element method (DEM) using the bonded particle model is a plausible approach for modeling rock because it was developed to mimic the micro processes of the particle interactions in actual rocks. It has successfully modeled the uniaxial compressive test stress path (Diederichs[1]).

DEM code such as PFC normally must adopt micro input parameters as illustrated in Figure 2.13. However, there is no direct method or test procedure to obtain these micro parameters in the laboratory, nor is this data reported in the literature (Potyondy and Cundall[2]) . Currently the only way to estimate these parameters is by a trial and error through direct comparison of the macro responses of the material from conventional laboratory tests (Figure 3.1).

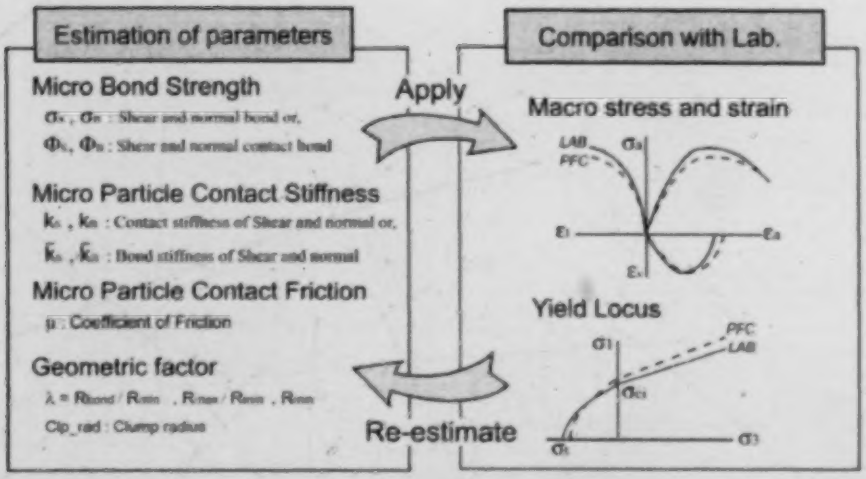

Figure 3.1 : General micro parameter calibration approach in PFC 2D.

Macro responses of numerically modeled synthetic rock with micro parameters chosen and altered are compared to actual laboratory macro responses until an adequate match is achieved. This process is laborious but there is as yet no alternative method to estimate micro parameters for a given material.

The DEM using PFC was selected to model micro processes in rock (extensile fracturing and dilation) for experiments reported in this thesis. In other laboratories, this method has been successful only when used to reproduce uniaxial compression tests. My goal was to establish the micro parameters and other factors (i.e., geometric factors) capable of simulating other conventional laboratory tests following different stress paths with the uniaxial compression test. A model that mimics these actual behaviors of a given material must be adaptable to all types of stress path.

Laboratory test data for synthetic rock chosen to calibrate a numerical model is presented in this chapter. The laboratory tests carried out using synthetic rock are:

1) Uniaxial Compression test
2) Triaxial Compression test
3) Brazilian test
4) Direct shear test
5) Axially loaded beam bending test

The first three tests were performed to select the micro parameters that allow modeling of the synthetic rock behavior. The results from these tests were compared directly with the simulation results of the tests using PFC presented in Chapter 4.

Direct shear tests were performed to explore the formation of a shear zone in the intact rock from joints, flaws, and voids. The detailed laboratory test results are compared with the PFC simulation presented in Chapter 5.

An axially compressed beam bending test was configured to simulate extensile fracturing and dilation under a compressive stress state in which Poisson's effects do not occur. The detailed test setup and results are presented in Chapter 6 and compared with the PFC simulation.

3.2 CHARACTERISTICS OF SYNTHETIC ROCK

3.2.1 SELECTION OF TARGET SYNTHETIC ROCK

Synthetic rock must have brittle characteristics and heterogeneity to mimic extensile fracturing under compression. Its strength should be an order of magnitude lower than natural brittle hard rock to minimize the size and capacity of laboratory equipment needed to carry out the extensive test program. To meet these requirements, three materials were considered - concrete, a sulfur composite, and sulfaset.

Concrete is a well known and it has been extensively studied. While its strength and stiffness varies with additives and mixing ratios, its material properties are well documented. Moreover, aggregates can be mixed with cement mortar to introduce heterogeneity that mimics natural rocks. One of the main shortcomings of concrete is that it requires considerable curing time (28 days of curing for full strength); for this reason, concrete was not selected.

A second material considered was "sulfur composite", a mixture of fly ash and sulfur. This material is often used to cap concrete cylinders prior to testing; it is easy to mold, sets quickly, and is brittle. Moreover, sulfur is inexpensive and readily available. While the uniaxial compressive strength of this material (shown in Figure A.1 (a)) is low and its stress strain curve indicates a brittle behavior, a cut section (Figure A.1 (b) of Appendix A) reveals that rapid cooling of liquid sulfur produces of gross heterogeneities. The presence of these discontinuities eliminated "sulfur composite" as a test material.

Sulafset was finally selected as the candidate synthetic rock. Its characteristics are outlined in detail in the next section.

3.2.2 BOLT ANCHOR SULFASET

"**Bolt Anchor Sulfaset**" or "**Sulfaset**" is a synthetic rock material developed as a fast setting grout for anchor bolts. Sulfaset is a yellowish powder which forms a fast setting cement mortar when mixed with water (U.S. Dept. of the Interior[3]). Sulfaset exhibits brittle behavior and requires a short curing time; it begins to set within half an hour of preparation and reaches 80% of strength within a few hours. Extensive laboratory experience with this material exists at the University of Alberta as it is used to produce samples for the laboratory teaching program.

Sulfaset specimens have pores due to trapped air bubbles formed during mixing, but the material is homogeneous compared with the heterogeneity present in most intact natural rock. Thus, direct usage of this material as synthetic rock is limited when considering heterogeneity effects found in natural rock specimens. To overcome this shortcoming, a small amount of sand (10% by weight) was added to the fresh mortar mixture. This imparted random heterogeneity while maintaining grain size, stiffness, and strength. For consistency, sand with a uniform grain size distribution was used for all specimens. The grain size distribution of the sand used is presented in Figure A.2 of Appendix A. It should be noted that the specific gravity of sand is greater than that of sulfaset powder thus without vibration or agitation the sand will separate from the powder. If the concen-

tration of the prepared mortar is too thick, pores form in the specimen where air bubbles are trapped; if the mortar is too thin it segregates (Figure 3.2 (a)). Figure 3.2 (b) is an example of a uniform mixture with sand uniformly distributed within the mortar matrix. The laboratory sample preparation procedure used in these experiments is outlined in Figure A.3 of Appendix A.

When the mixture is ready for molding it is poured into a cylinder mould coated with oil to assist with sample extraction. Once the specimen begins to set, i.e., 10 to 15 minutes later, the specimen is extracted from the mould and is then allowed to cure.

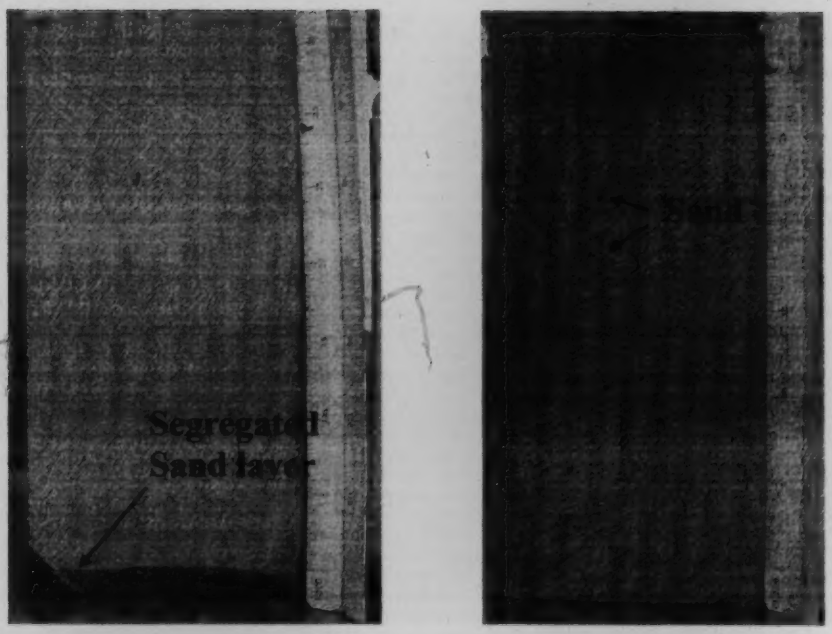

(a) (b)

Figure 3.2 : Saw cut section of a 100 x 200 mm cylindrical sample of sulfaset synthetic rock (sulfaset + water (50%) + sand (10%)), (a) Segregated layer formed due to the failure of uniform mixture (b) Uniformly mixed specimen

3.2.3 UNIAXIAL COMPRESSION TEST

Strength characteristics of the synthetic rock under different mixing and curing conditions were evaluated. Uniaxial compression tests were carried out on 100 mm by 200 mm cylinder specimens following the procedure and test conditions outlined by the International Society of Rock Mechanics (ISRM[4]). Flatness of the loading surface was ensured by placing sulfur caps on both ends of the test specimen. Axial strain was measured using

a dial gauge and the applied load was measured using a load cell connected to a data acquisition system (Figure A.4); data was recorded using a 10s capture interval.

Figure 3.3 shows a failed specimen. A typical cone shaped fracture formed near the top of the specimen and axial splitting or high angled fractures were observed. The cone fracture is associated with the frictional confinement attributed to the loading platen.

Figure 3.3 : Typical failure shape of a synthetic rock specimen which failed under uniaxial compressive load (10% sand, 50% moisture content, 7 days cured).

3.2.4 EFFECT OF CURING CONDITION

Curing conditions are important variables that may affect the behavior of the synthetic rock. Concrete strengths vary by 30%-50% depending on the curing conditions such as humidity, temperature, and time (Neville[5]). Sensitivity to curing conditions needs to be

properly understood to insure reliable data is collected. Two curing conditions were evaluated - uncontrolled and controlled.

Under uncontrolled curing, specimens were cured at normal room temperature and humidity, both of which varied with climatic conditions. Under controlled curing, specimens were cured in a room specifically designed for the preservation of undisturbed field samples; the temperature was maintained at 4°C and humidity was kept at 90%. In both cases, specimens were cured up to a maximum of 14 days. The moisture content of the mixture for all specimens was fixed to 50% and 10% sand was added to mimic heterogeneity. Uniaxial compressive strength was investigated for samples prepared under these conditions.

Figure 3.4 shows a comparison of uniaxial compressive strength obtained under controlled versus uncontrolled curing condition. Specimens cured at room temperature with ambient humidity (uncontrolled conditions, Figure 3.4 (a)) show scattering of compressive strength, while consistent strengths were obtained for specimens cured under controlled environment conditions (Figure 3.4 (b)). Uniaxial compressive strength obtained under controlled or uncontrolled curing conditions is not influenced by curing times greater than 1 day. Curing conditions have an important influence on the strength of material and must be controlled to achieve uniform behavior.

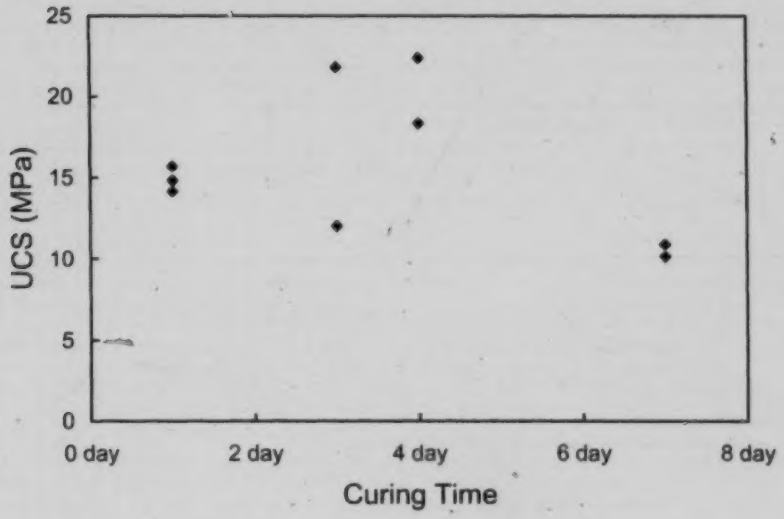

(a)

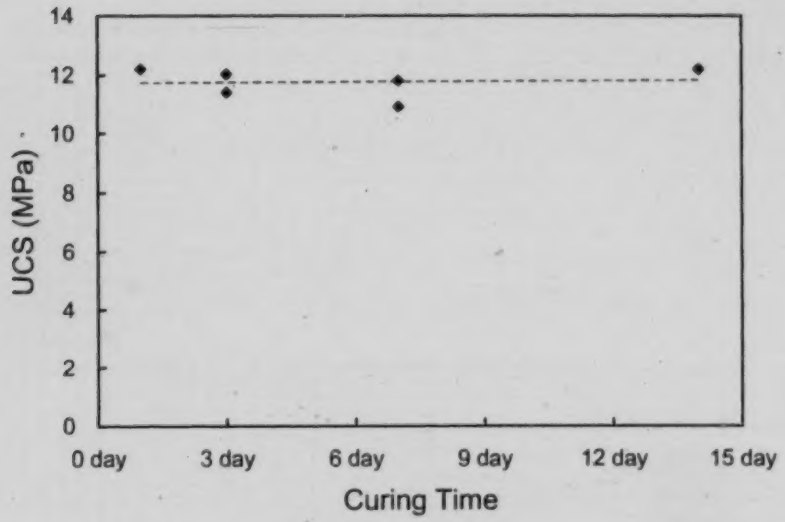

(b)

Figure 3.4 : Effect of curing conditions on uniaxial compressive strength of rock, (a) Uncontrolled curing condition (i.e., variable room temperature and humidity), (b) Controlled curing (4°C, 90% humidity).

3.2.5 EFFECT OF INITIAL MOISTURE CONTENT AT MIXING

The properties of sulfaset depend on the initial mixing contents (i.e., content of powder, water, and sand). All samples had a sand content of 10% by weight to ensure heterogeneity. Since the dry material content is fixed, the strength and stiffness of the product will depend on the initial moisture content of the prepared mixture. Sample dimensions and test setup were the same for all specimens as previously described.

Increasing the initial moisture content results in significant reduction in strength (Figure 3.5 (a)) and stiffness (Figure 3.5 (b)). Moreover, post peak behavior changes from highly brittle to ductile as moisture content increases (Figure 3.5 (b)). These results imply that controlling the moisture content of mixture controls the stiffness and strength of the prepared specimens.

Based on preliminary tests, the material strength and stiffness obtained at 50% moisture was the most favorable for the requirement of this study, thus 50% moisture was used in all sample mixtures; 10% sand based on sulfaset weight was used in all samples throughout this study. Specimens were cured for 3 days before being tested to ensure reproducible results. Strength parameters and other characteristics were measured according to the preliminary test program.

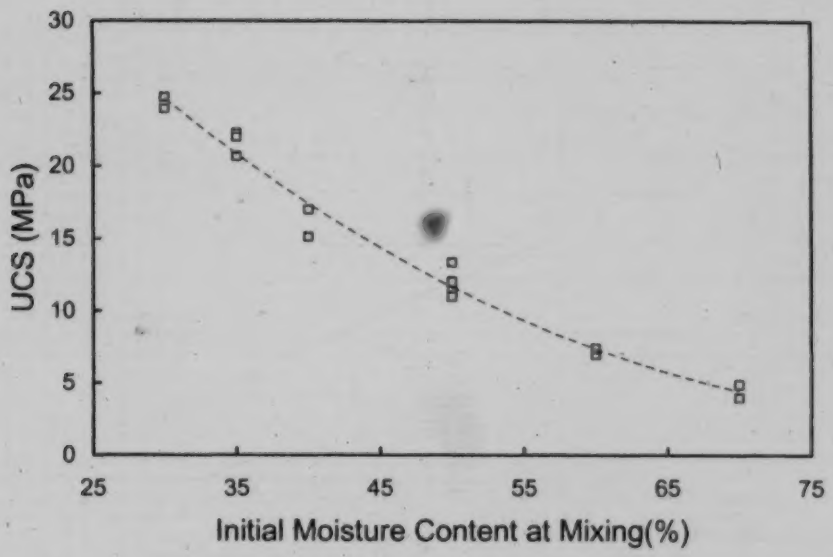

(a)

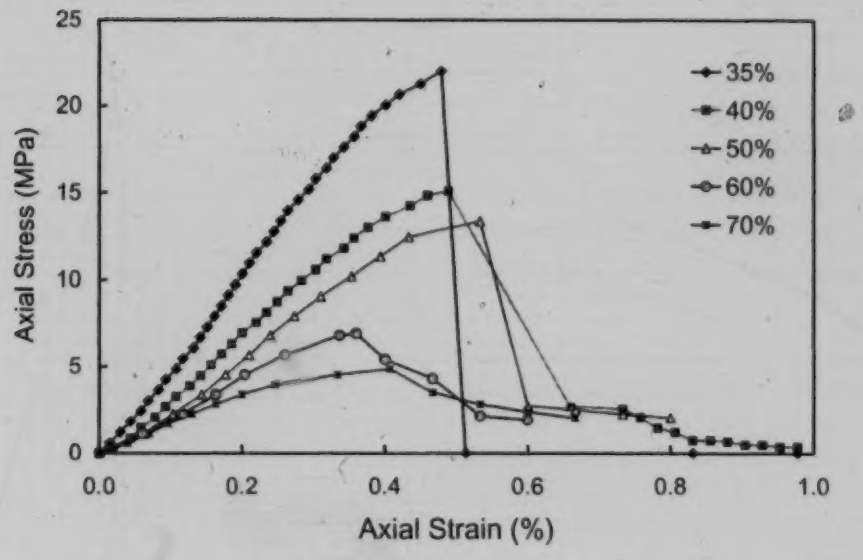

(b)

Figure 3.5 : Effect on UCS of moisture content at mixing of sulfaset synthetic rock (a). Strength, stiffness, and post peak behavior is highly influenced by the initial mixing moisture content (b).

3.3 PROPERTIES OF SYNTHETIC ROCK

Uniaxial compressive strength was measured during the preliminary test program and additional conventional tests were carried out to determine the Poisson's ratio, tensile strength, cohesion, and friction of the synthetic rock. The macro physical parameters obtained in these test results were used to calibrate the micro parameters to be used in the PFC simulation with the objective of matching the macro behavior of this synthetic rock. These micro parameters are determined in later chapters.

3.3.1 COMPRESSIVE STRENGTH

The compressive strengths of the synthetic rock specimens were measured using a Hoek cell (Hoek[6]). Compressive strength were measured for each confining stress and for the condition of no confining stress (i.e., uniaxial compressive strength).

Since the specimen size required for the cell is limited to the NX core size, the synthetic rock was remolded to a 55 mm by 110 mm cylindrical shape. At 55 mm diameter it was difficult to put a sulfur cap on the loading surface of the cylindrical specimen so care was required to meet the flatness criteria of the loading surface suggested in ISRM[4]. These surfaces were ground until the error was within the ± 0.01 mm requirement

The confining stress was applied to the cell using a hydraulic pump. (ISCO, 500D series syringe pump) with a maximum capacity of 28MPa as illustrated in Figure A.5. Axial

strain was measured using an LVDT and the applied loading was measured using a load cell.

Figure 3.6 shows both the triaxial and uniaxial compression test results. The results show the rock displays brittle behavior at low confining stress and that the material becomes more ductile as confining stress increases. Note that the initial non-linearity of each stress-strain curve is a result of closure of pores during seating of the load platen and is not a characteristic of the material. These pores resulted from trapped air bubbles formed during sample preparation.

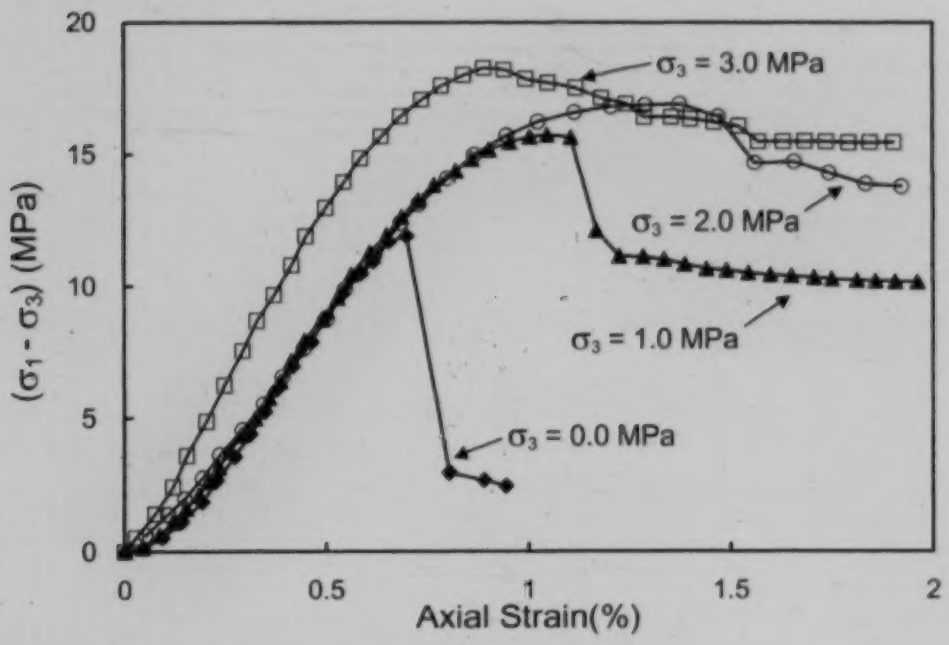

Figure 3.6 : Triaxial rest results of sulfaset synthetic rock specimens

3.3.2 TENSILE STRENGTH

Tensile strength was investigated using the conventional Brazilian test (ISRM[7]). While this test is an indirect method for obtaining tensile strength, but the test was selected because of its technical simplicity and the usual consistency of results obtained. The Brazilian test is used worldwide to determine the tensile strength of brittle materials.

Brazilian test disk specimens were prepared using the previously outlined procedure and the thickness to diameter ratio was kept at 0.5 as suggested in ISRM[7].
The cylindrical loading platen during the tests adhered to ISRM[7] specifications. A total of 7 specimens were tested following the procedure presented in ISRM[7]. Figure 3.7 presents the test results and a typical failure shape of the specimens.

The stress-strain relationship shown in Figure 3.7 (a) illustrates that the initial non-linear portion is not consistent especially for specimens Sp1, Sp2, and Sp3. The reason for this behavior is the existence of internal pores. These pores close as the applied compressive stresses develop near the platen contact. However, the platen contact and origin of each specimen differ because the synthetic rock specimen was molded using a PVC mould and the specimens expanded a small amount during the hydration process. The Brazilian disk shaped specimens were thus not perfectly circular and likely had a slight elliptical shape. This variation leads to a different contact condition for each specimen during the tests.

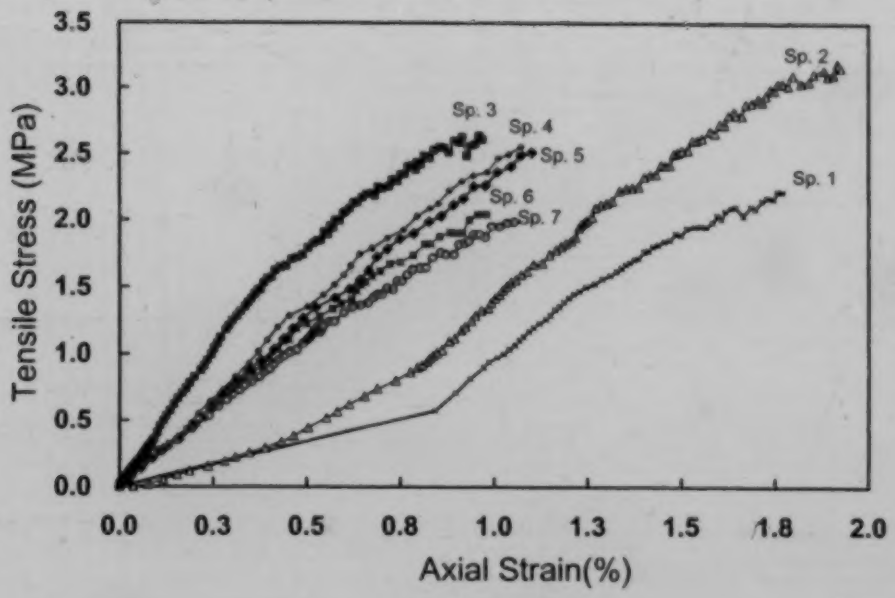

(a)

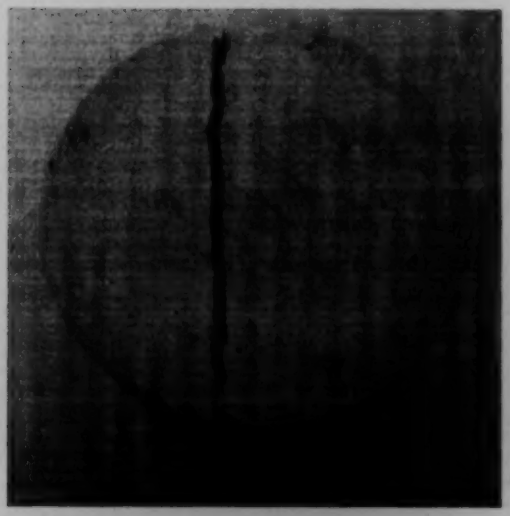

(b)

Figure 3.7 : (a) Brazilian test results, (b)Tensile failure of the sample

3.3.3 DEFORMATION MODULUS AND POISSON'S RATIO

The deformation modulus of the synthetic rock was determined using the triaxial test results. The modulus for each test was determined using the linear portion of the stress-strain curves (see Table 3.1).

Poisson's ratio characterizes the elastic quality of a material. In hard rock specimens, the Poisson's ratio is measured from the responses of strain gauges attached both vertically and laterally onto the specimen surfaces, that is, strain gauges are tightly bonded to the rock surface until fracture forms. In this synthetic rock, however, the surface of the specimen is oily due to the lubricant used during casting, and strain gauges were unable to bond. Moreover, the origin of the synthetic rock is a mortar, thus hydrated powder grains hinder attachment of the gauge to the specimen surface. Radial strain gauges were considered, but the sensitivity of these gauges was not adequate to capture the lateral strain. As a result, it was not possible to measure Poisson's ratio in the synthetic rock; it was estimated at 0.3 based on the measured deformation modulus of the synthetic rock.

As outlined in chapter 4, direct use and comparison of Poisson's ratio with PFC calibrated response is not required for micro parameter calibration. For this reason, additional efforts to measure the Poisson's ratio in laboratory specimens were not considered necessary for the successful completion of this research.

Strength and stiffness parameters were obtained from the compression and tensile strength test results. Figure 3.8 shows the failure envelope obtained from the laboratory test results along with the best fit curve using commercial software RocLab v.1.0 developed by Rocscience Inc.[8]. The Hoek-Brown constants for the synthetic rock were then

used to obtain the Hoek-Brown failure envelope and from the relationship between the Hoek-Brown and Mohr-Coulomb envelopes, cohesion and friction parameters were determined. These strength parameters and the stiffness parameters of the synthetic rock are shown in Table 3.1.

Table 3.1 : Material properties of sulfaset synthetic rock.

σ_c (MPa)	σ_t (MPa)	E (GPa)	c (MPa)	ϕ (MPa)	s	m_b
11.6 ± 1.0	2.6 ± 0.3	2.5± 0.5	2.95	35.1	1	5.07

Variables: σ_c : Uniaxial Compressive Strength, σ_t : Brazilian tensile Strength, E : Young's modulus, c : Cohesion, ϕ : Friction angle, s, m_b : H-B material constants

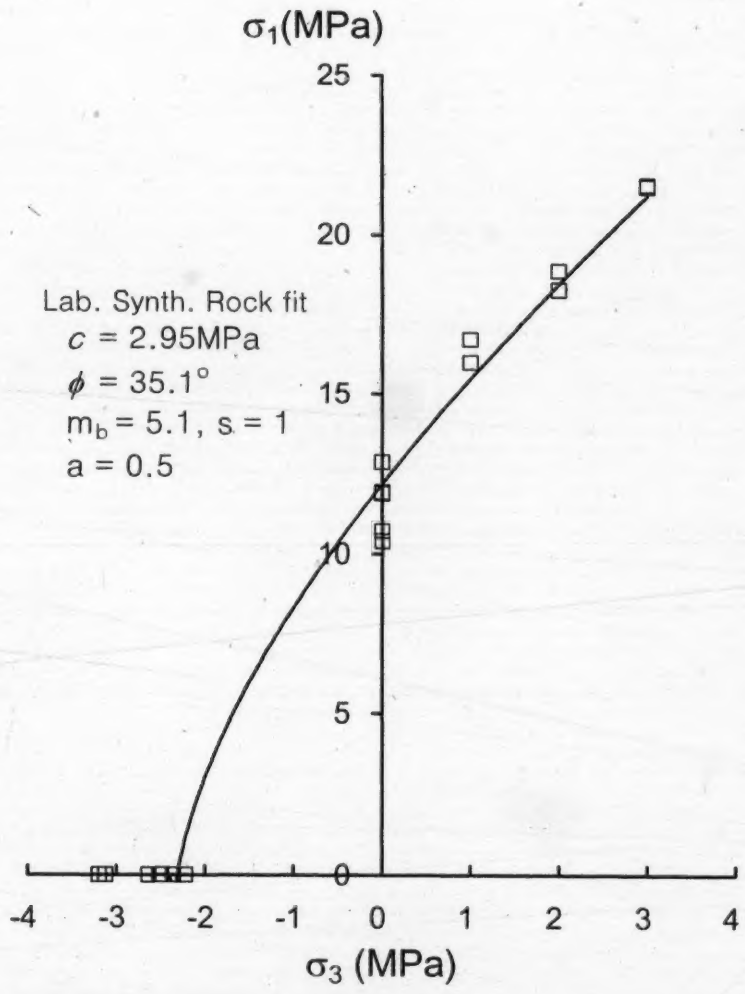

Figure 3.8 : Failure envelope of the synthetic rock. The strength parameters were estimated using RocLab ver. 1.0, RocScience Inc[8].

3.4 AXIALLY COMPRESSED BEAM BENDING TEST

3.4.1 LABORATORY TEST SYSTEM DESIGN

The axially compressed beam bending test was undertaken so that measurements of extensile fracturing and ultimate notch failure would be available for simulation. The stress state induced during this test is similar to that of the overstressed zone associated with an underground opening in which the tangential stresses are non-uniformly distributed and the zone is subjected to a bending moment as shown in Figure 1.12.

Due to the complexity of the stress state and the boundary conditions, it is difficult to simulate such a zone using conventional laboratory tests (uniaxial compression, triaxial compression) since their boundary stresses are uniformly distributed. These test setups do not include application of a moment to the specimen. The motivation to carry out this test and the background to its use were discussed in Chapter 1 and are further described in Chapter 6 where the measured laboratory results are simulated using PFC.

Extensile fracturing and dilation induced by non-uniform tangential stress were simulated at the laboratory scale with moderate scale dependency. The test results exhibited larger scale fracturing compared with previously described laboratory block tests using blocks with drilled holes.

The test system was designed based on the superposition involving combined axial compression and the 4 points bending system.

The 4 points system to apply the bending moment was chosen over the 3 points system to avoid a confining effect from the loading system on the potential zone of dilation to cause fractures to develop at the top center of the beam. Note that the main goal of this test is not to induce tensile failure but to generate extensile fractures associated with failure at the notch for both compression loads and moments.

During the design of the laboratory axially compressed bending system, it is most important to establish boundary conditions such as spacing between loading points, degrees of freedom and a ratio of axial and bending loads. The bending moment and stress state developed in the beam section depend on these conditions. The first consideration is that the bending moment should not cause initial tensile rupture at the bottom of the beam section. This was accomplished by selecting spacing between the top and bottom loading points on the beam (i.e., 150mm at top and 300mm at bottom) and ensuring adequate clearance for installation of the deformation monitoring sensors.

Once the position of point loads is determined, the axial (P_h) and vertical (P_v) load ratio (P_h/P_v) must be established to induce the appropriate stress distribution. If this ratio is too low, i.e., vertical loads are greater than axial loads, then bending moment induced stresses will govern the system and failure via tension in the bottom fiber will occur. If the ratio is too high, axial compression will govern the system and the beam may fail in a manner similar to the uniaxial compression test. The failure mode desired for this test needs to be between these two extreme states.

Figure 3.9 shows how changes in stress distribution are caused by changes in load ratio. The stress is calculated at the center section of the beam. The load ratio is determined without considering the stress concentration associated with a notch installed at the top fiber because the load ratio required must avoid tensile failure in the bottom fiber of the specimen.

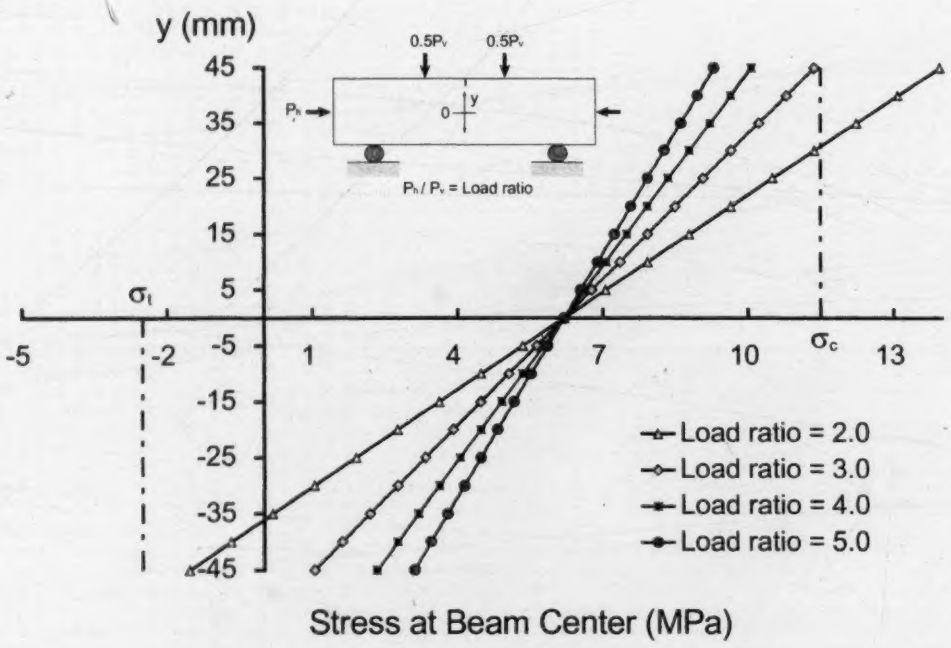

Figure 3.9 : Stress distribution calculated at different load ratio.

The load ratio should be greater than 3.0 to avoid tension in the bottom fiber of the beam when the compressive stress at the top fiber of the beam reaches the uniaxial compressive strength of the synthetic rock (Figure 3.9). When the ratio is greater than 3.0, all stress distribution remains in the compressive range, thus the beam behavior is governed by compression.

The optimum load ratio determined for the axially compressed bending test was 3.0. For application of this load ratio in the laboratory system, loads were designed to be applied using hydraulic rams and the load ratio was controlled by choosing the appropriate ram size for the given load ratio. The hydraulic pressure transmitted to the rams was then supplied using a syringe pump (ISCO 500D series). The ram sizes determined for the given ratio were 55.5 mm and 32.0 mm in diameter for the horizontal axial load and vertical point loads, respectively.

The load frame supporting the system comes in two parts. One applies the horizontal axial load and the other is the frame used to apply the vertical load. The frame must be robust and stiff to avoid excessive storage of the strain energy during application.

For this purpose the axial loading frame consists of 25 mm steel plates connected via six 30 mm diameter bolted steel rods. The vertical loading frame was provided by a U shaped steel angle beam of 10 mm thickness.

In establishing the boundary condition of the lateral point load platen application of moments must be avoided as this would induce a more complex statically indeterminate moment condition. A ball bearing, acting as a hinge, was installed between loading plates and the hydraulic ram. The final laboratory frame system setup is presented in Figure 3.10 and the hydraulic ram setup is shown in Figure 3.11.

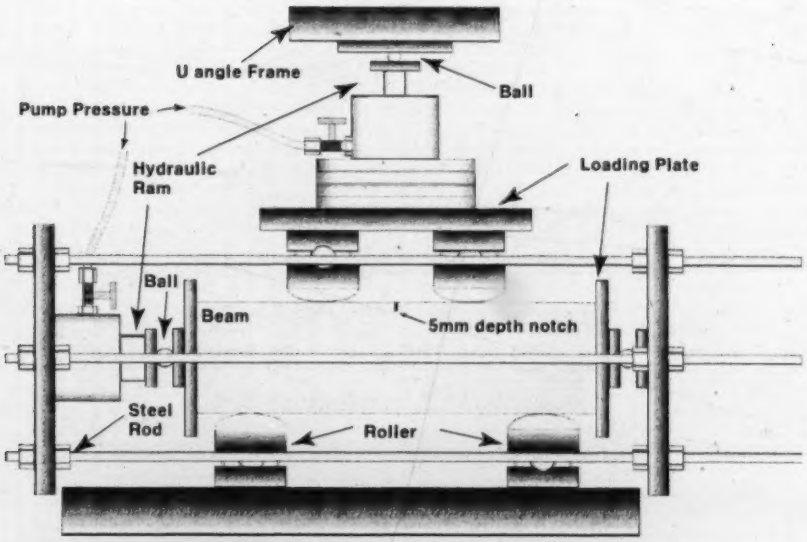

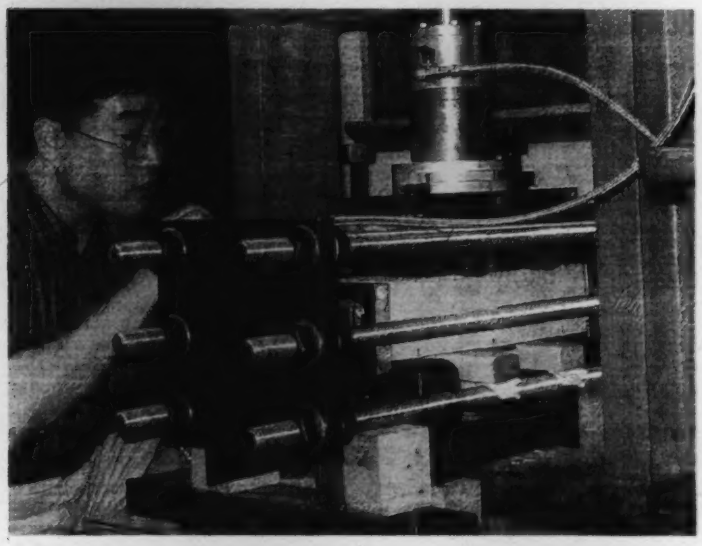

Figure 3.10 : Axially compressed beam bending test system setup.

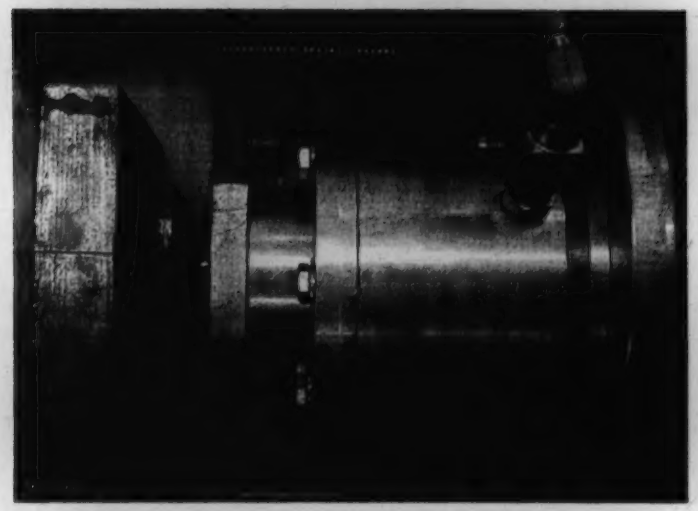

Figure 3.11 : Hydraulic ram setup with hinge.

3.4.2 PREPARATION OF THE BEAM SPECIMEN

The beam specimen was molded to 88.9 mm in height, 114.3 mm in width and 406.4 mm in length. To avoid deformation due to expansion of the specimen from hydration, a thick walled steel mould was designed and constructed. It consisted of separate thick plates (1 cm thick), each plate tightly assembled using bolts to form a prism mould (see Figure 3.12).

Two types of the specimen were prepared with the mould - one incorporated wire mesh reinforcement and the other was without reinforcement. Differences in the bending behavior of these specimens are discussed later.

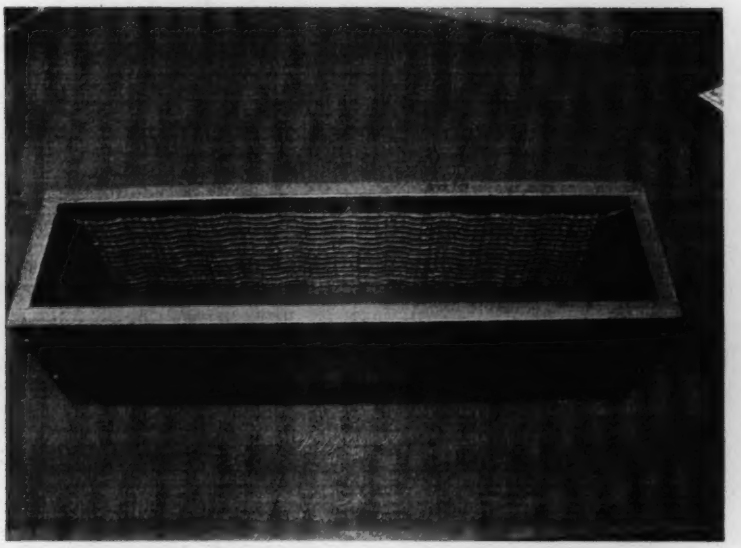

Figure 3.12 : Steel mould used for molding the beam specimens.

For the reinforced beam specimen, both 0.5 mm and 1 mm diameter wire mesh with a 5 mm grid (Figure 3.13) was installed in the bottom of the specimen. This reinforcement was provided to prevent sudden collapse of the beam due to the tensile failure in the bottom fiber as the extensile fracturing in the top fiber of the beam reduces the moment of inertia of the beam as cracks propagate thus creating tension in the bottom fiber.

Sample preparation requires a thick mortar to be poured into the steel mould overflowing the mould. The overflow is then trimmed with a steel blade before the mortar is completely set (Figure 3.14).

Once the mortar is set the bolted steel plates are dismantled and the beam specimen is preserved in a room with controlled moisture and temperature for consistent curing of the specimen.

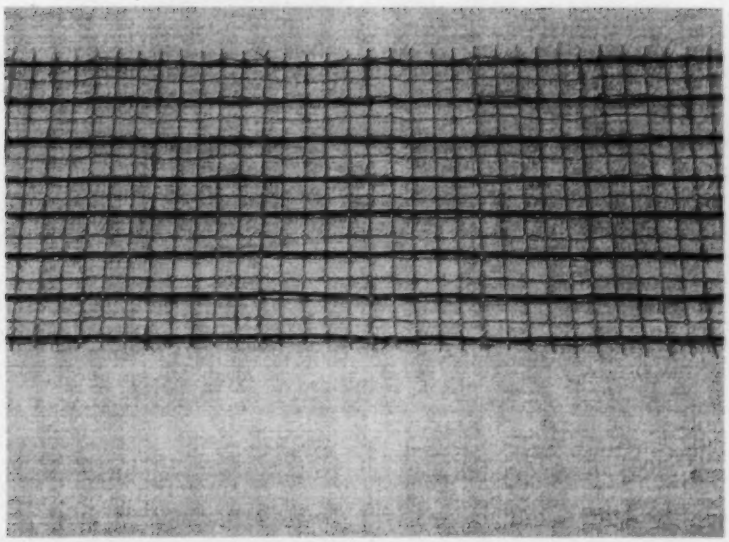

Figure 3.13 : Wire mesh used for the reinforcement (5 mm grid, 0.5 mm and 1 mm diameter mixed wire mesh) .

The procedure described above is typical of sample preparation of a beam specimen for either concrete or other mortar type synthetic material.

However, the synthetic rock beam specimens generated using this procedure were variable. The synthetic rock mortar cures quickly thus it was difficult to trim the surface to the smoothness of the other prepared faces. The trimming process caused scratches on the surface resulting in surface disturbance of the specimen (Figure 3.14). Moreover, the trimmed surface was exposed to the air during initial curing while the other surfaces were in contact with the steel plates. Under these conditions the flaws may become stress concentrators, resulting in an unbalanced corner that develops during loading as shown in Figure 3.14.

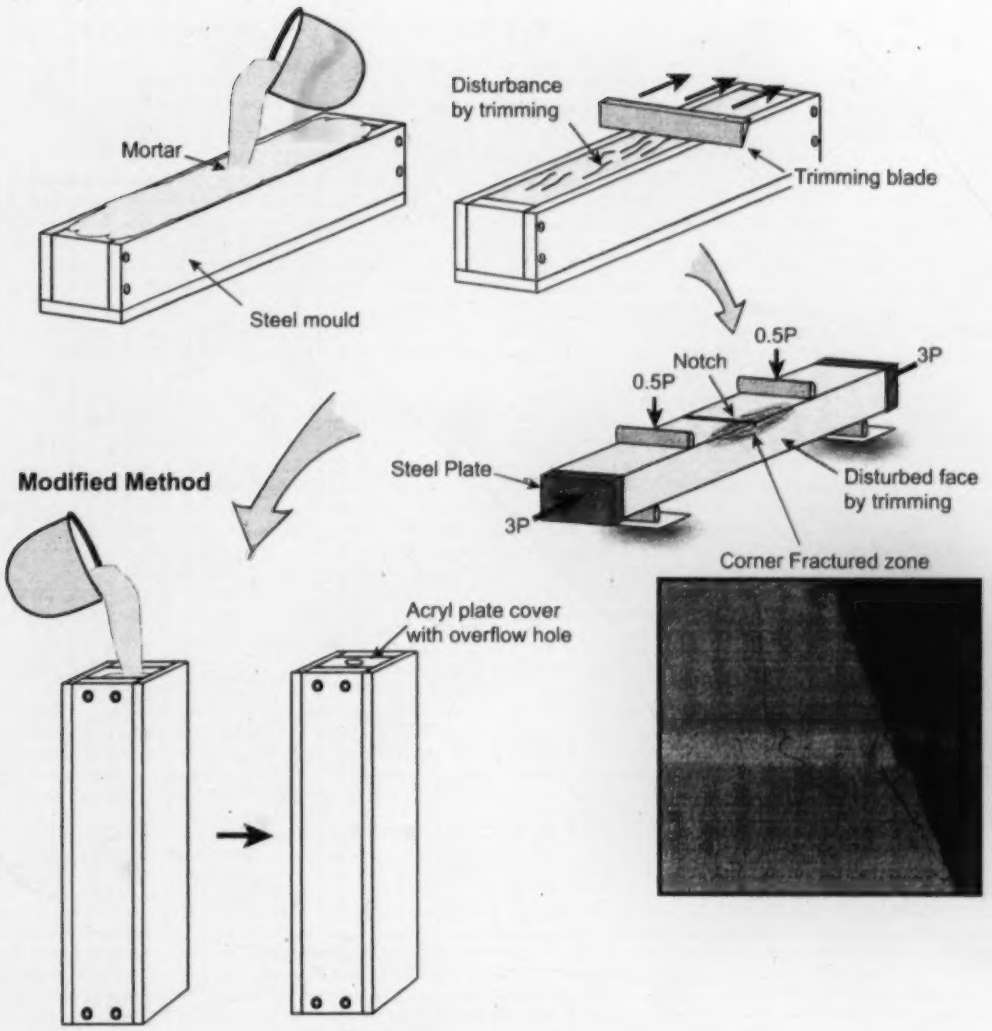

Figure 3.14 : Illustration of beam specimen molding process. Note that horizontally molded specimens may generate non-uniformly distributed corner fractures.

Figure 3.14 also illustrates an alternative preparation method for preparing the beam specimen. Using this method, local fracture zones formed at the corner of the surface were eliminated. To eliminate the previously described trimming process, an additional

edge plate was added and the mould stood vertically while a top plate wall was added. The mortar was then poured into the space opened at the top (plate removed). As the mortar filled the mould, the top plate was replaced and the mortar was allowed to overflow through a hole in this top plate. The extruded mortar from this hole was trimmed as the plates were disassembled. Thus the procedure allows for preparation of specimens having smooth surfaces, insuring less disturbances, and provides uniform identical curing conditions.

3.4.3 CORE STRENGTH

To verify the strength within the beam specimen, NX cores were taken from the molded beam and the uniaxial compressive strength was measured for comparison with the results reported earlier. Figure 3.15 shows a comparison of the stress-strain curve of the specimen cored from within the beams and the cast cylindrical specimen. No significant difference in strength is observed between specimens; this indicates the scale effect and preparation procedure had little influence on the strength of the product. However, specimens cored from the beam were less brittle. This could be attributed to the effects of water which can be absorbed into the test specimens during the coring procedure.

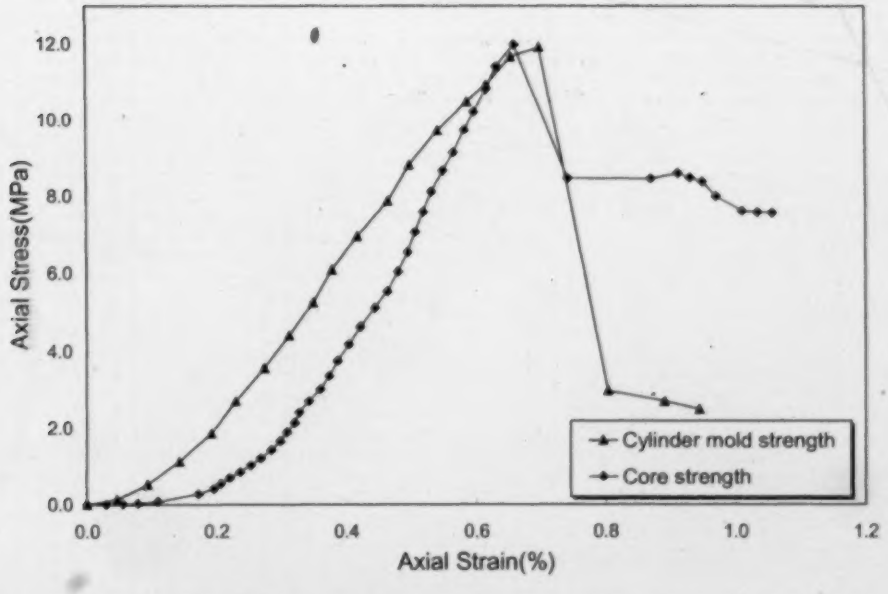

Figure 3.15 : Verification of beam strength from core strength compared with cylinder mold strength (uniaxial compressive test).

3.4.4 TEST RESULTS

Under the laboratory setup illustrated above, an axially compressed bending test was performed using a synthetic rock specimen. Based on the observations reported by Martin et al.[9], the onset of extension fracturing around a circular test tunnel was similar to that around a notch tip. To simulate this effect, a stress concentrator; (5 mm depth and 1 mm width) notch was installed in the top of the beam using a steel saw.

The stresses applied by the hydraulic ram loading system at the tip of the notch were then calculated by combining the axial stress and the well-known beam flexure induced stress by introducing a stress concentration factor:

$$\sigma_f = k\left(\frac{P_a}{A} \pm \frac{M}{I} y\right), \qquad (3.1)$$

where, σ_f is compressive stress, P_a is axial force, A is the cross section area of the beam, M is the bending moment, I is the moment of inertia, y is the centroid of the cross-section, and k is the stress concentration factor.

The stress concentration factor k varies depending on the curvature of the notch tip and the geometric ratio (Lipson and Juvinall[9]). Thus it is difficult to estimate analytically and is usually obtained using numerical analysis. According to the numerical analysis, the stress concentration factor k at the notch tip was estimated to be 3.3 (Chapter 6).

Two LVDT was installed at the center of the beam. The first LVDT was installed at the top beside the notch to measure dilation as a fracture developed and the second LVDT was installed at the bottom center of the beam to measure the beam's downward deflection while bending. To protect the LVDT at the bottom from the sudden collapse of the beam when it ruptured, timber was placed beneath the beam.

For the initial seating a 70kPa pump pressure was applied to the rams; this corresponds to 0.03 MPa stress induced in the top fiber of beam center section. The applied pressure was recorded using a pressure transducer with a 10 s capture interval on a data logger using the LABVIEW software. The applied pump pressure and LVDT measurement data were recorded for this system. The rate of pressure application was kept constant during the test at 50 kPa/min which is slow enough to not induce excessive energy into the sample through the loading system.

Figure 3.16 shows a comparison of displacements measured at the top and bottom of the beam plotted with the stress calculated at the notch of the beam using Eqn. (3.1) for two different specimens. The non-reinforced beam is compared with a reinforced beam which shows high bending stiffness attributed to the reinforcement effect. Displacement versus stress is noticeably non-linear in the reinforced beam specimen while such non-linearity was not as pronounced in the non-reinforced beam. The non-linear behavior shown in the reinforced beam could be attributed to the interaction between the synthetic rock and the wire-mesh as is observed in composite beams such as reinforced concrete.

In reinforced beam test results shown in Figure 3.16, displacements measured at the top and bottom are significantly different while similar displacements were measured for the non-reinforced case. The main purpose of measuring the displacement using LVDT at the top of the beam is to measure dilation resulting from the extensile fracturing. Since the displacements at the top and bottom of the specimen should be the same if the specimen

is homogeneous, the difference between top and bottom displacement could be the measure of the dilation due to the development of fractures in the top fiber of the specimen.

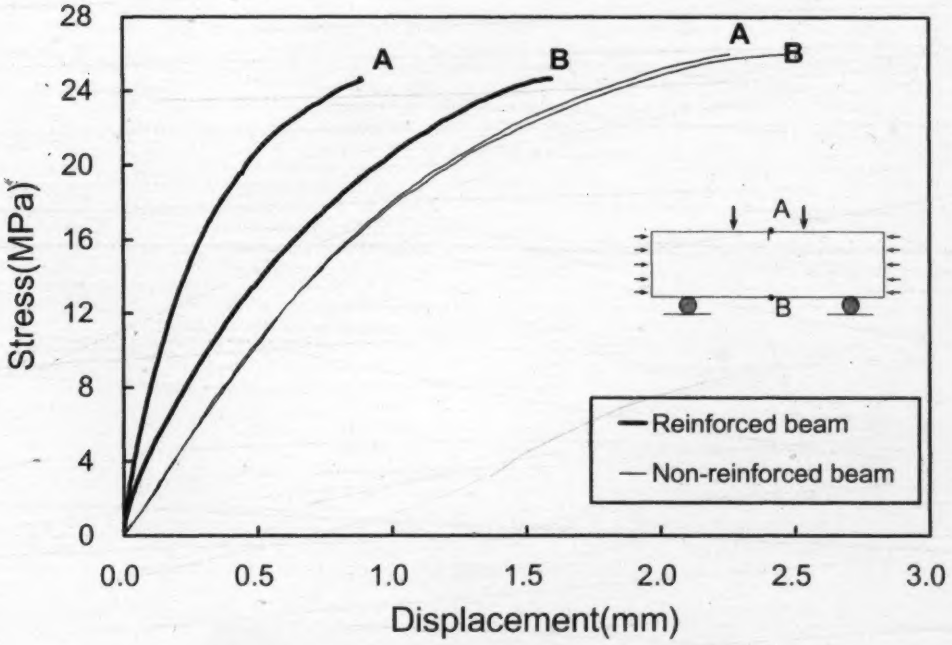

Figure 3.16 : Comparison of bending behavior of the reinforced and non-reinforced beam specimens with stresses at the notch tip.

Displacements measured in the reinforced beam specimen do not represent true dilation because displacement differences are observed even during the initial loading stage which is not associated with fracturing or yielding. However, the dilation measured from the displacement differences in the non-reinforced beam specimen is plausible.

Figure 3.17 shows the dilation calculated as the difference between point A and point B for the non-reinforced beam specimen.

Dilation is initiated near 12.5 MPa in Figure 3.17 and this is similar to the stress level where the non-linear response commences (Figure 3.16). After fracture initiation, non-linearity becomes significant but initiation of the fracture does not result in rupture of the specimen.

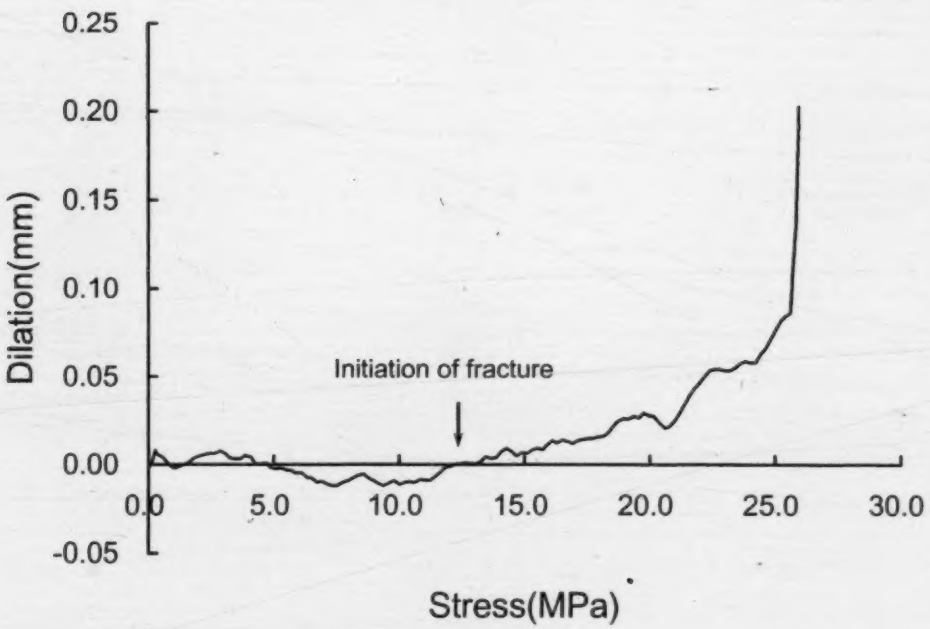

Figure 3.17 : Dilation due to the extensile fracture development estimated from differences in top and bottom bending displacements measured by LVDT.

In terms of uniaxial compressive strength, stresses shown in Figure 3.17 exceed the yield strength of the synthetic rock shown in Table 3.1. But note that the stress was calculated at the notch tip, thus, strength of the specimen should be evaluated based on the devia-

toric stress, not the uniaxial stress. More discussion associated with the dilation and yielding of the specimen will be dealt in Chapter 6.

Figure 3.18 shows the ruptured shape of the non-reinforced beam. Note the typical notch failure and spalling often observed in overstressed rock in underground openings at depth (Martin[9]). In the pure bending cases, this notch shaped failure is rarely found as shown in Figure 3.19. While a notch failure was observed in Figure 3.18, the sample eventually collapsed via tensile fracture initiated at the bottom of the beam despite the applied axial load. This was attributed to a reduction in the moment of inertia of the specimen as failure began around the notch at the top of the sample.

Figure 3.20 shows the fracture development around the notch at the top center of the beam. The grid interval drawn is 5 mm by 5 mm and digital images of fracture initiation and propagation were captured with a 5.0 mega pixel digital camera attached to a data logger; the image was captured at 10 s intervals. Noticeable fracture propagation could be observed with the naked eye at 98% of rupture stress.

The fractures developed near the tip of the notch and grew horizontally (Figure 3.20 A). Once formed, dilation occurs by shearing along the fracture surface (Figure 3.20 B) and is facilitated by fracture growth at the tip of the fracture (Figure 3.20 C).

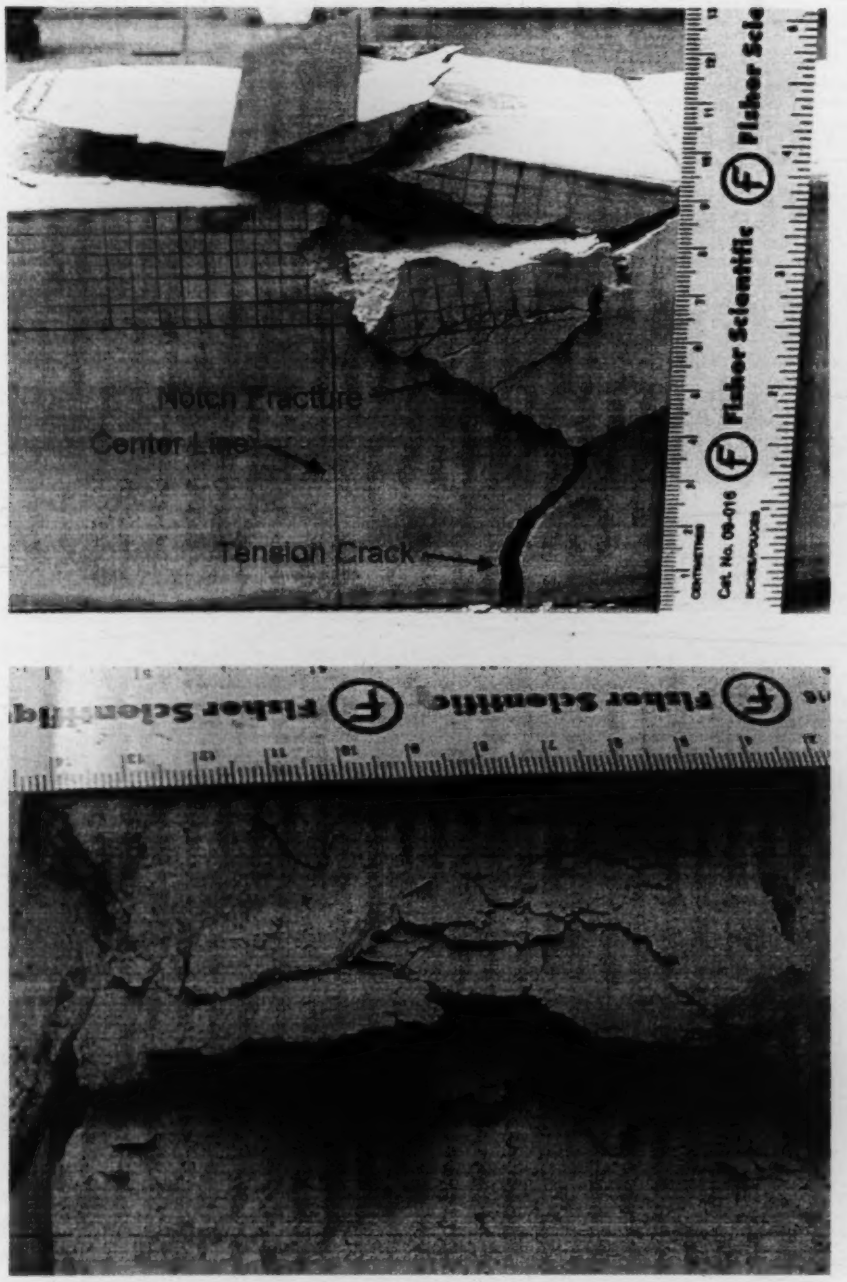

Figure 3.18 : Final ruptured shape of beam specimen and spalled shard inside the specimen at top center.

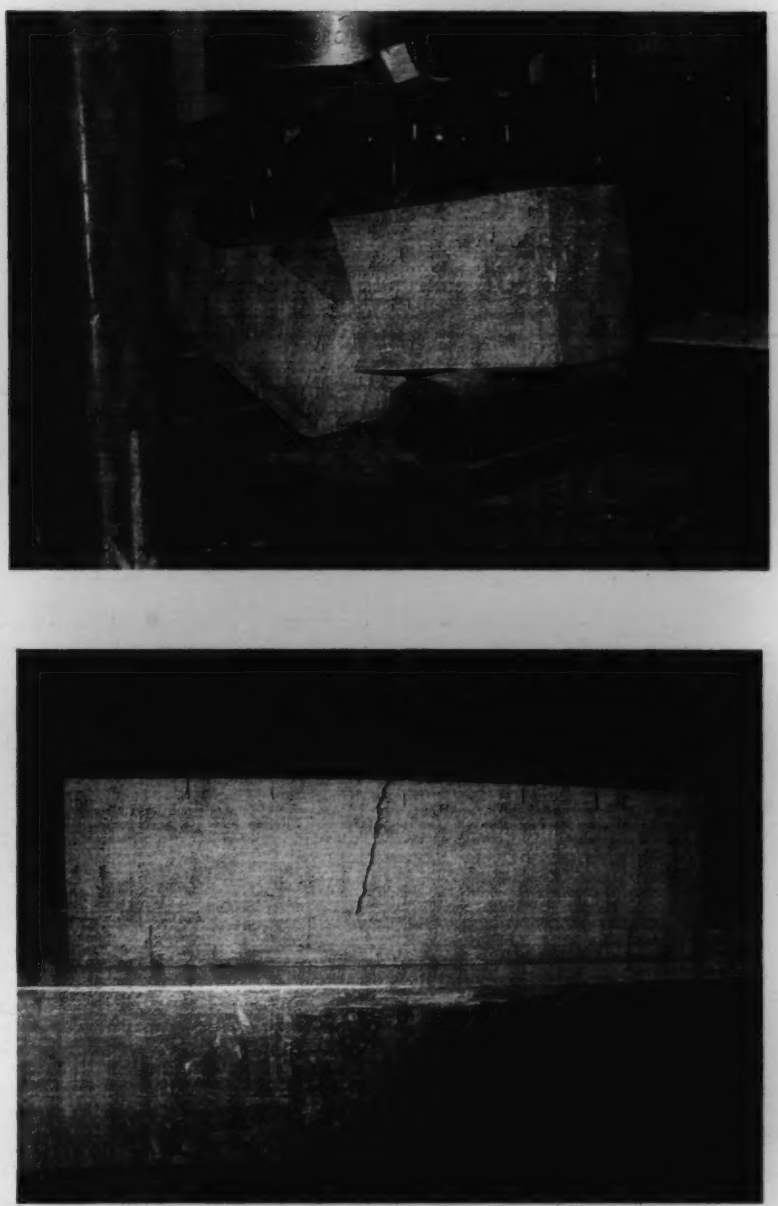

Figure 3.19 : Tensile strength test of sulfaset synthetic rock by a 4 point bending system. The tensile strength measured from this test was 1.5MPa which is 60% of the tensile strength measured in the Brazilian test shown in Table 3.1.

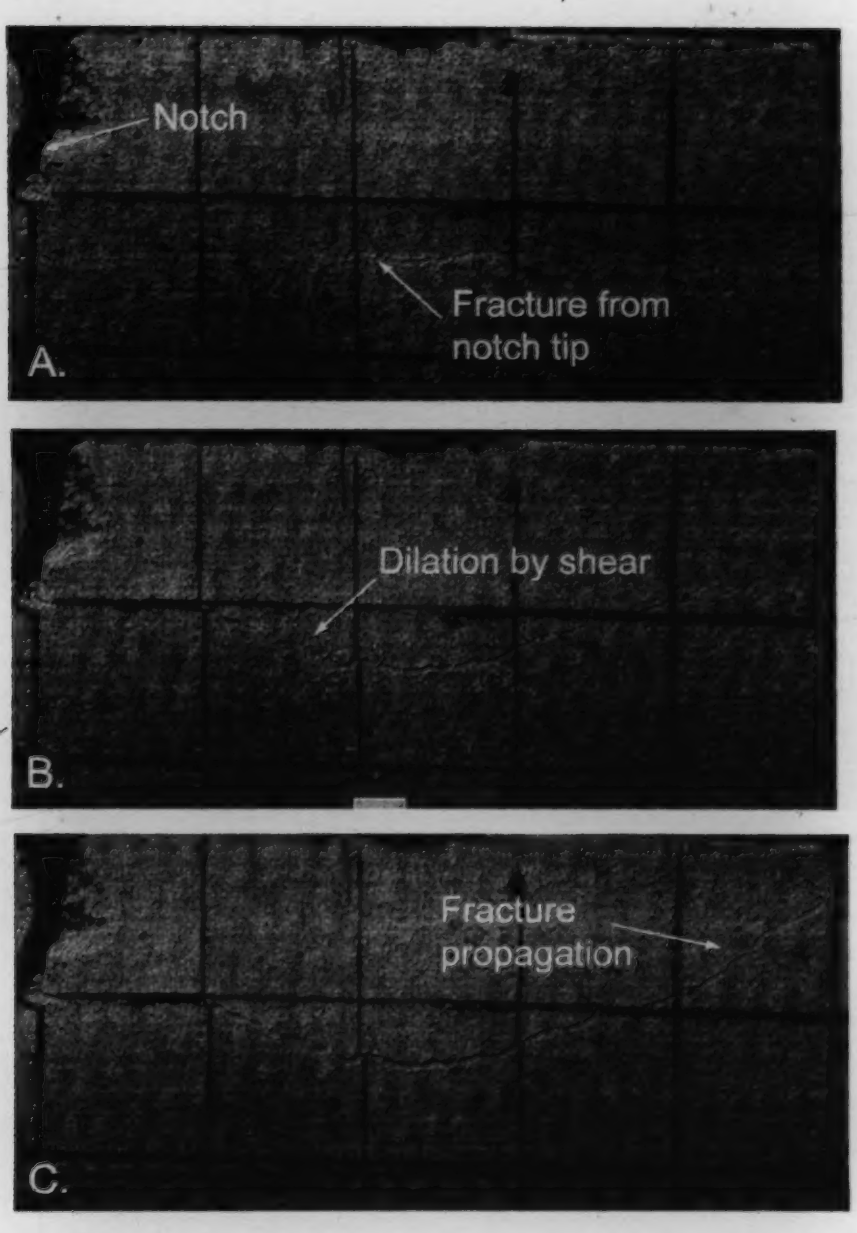

Figure 3.20 : Development of extensile fractures near the notch just before sample rupture.

3.5 CHAPTER SUMMARY AND CONCLUSION

This chapter describes conventional laboratory tests results using synthetic rock. The laboratory test setup was described in detail, especially for the axially compressed bending tests. The material properties and results of these tests are compared with PFC simulated synthetic rock in later chapters.

The synthetic rock chosen for the tests was originally referred to as "Bolt Anchor Sulfaset". This material sets quickly, requires short curing time, and develops adequate brittle responses with moderately low strength and stiffness. The strength and stiffness of the synthetic rock was sensitive to the initial mixing ratio and the curing conditions. Desirable results were obtained using 50% moisture content and 10% sand by weight of sulfaset dry powder. Each specimen was cured for 3 days at constant moisture and temperature. Characteristics measured from the conventional laboratory tests are shown in Table 3.1.

The axially compressed bending test was developed to generate extensile fracture induced notch failure and dilation similar to that observed in the tangential stress concentration zone in underground openings at depth. Tangential stresses are non-uniformly distributed and the axially compressed beam bending condition was studied to mimic this stress condition.

The test results revealed that notch failure similar to extensile fracturing and spalling is observed during the bending test. Dilation from the extensile fracturing was measured by

computing the differences of bending displacements at the top and bottom fibers of the beam using LVDT measurements. The stress level at initiation of dilation was recorded as12.5 MPa which is similar to the point of non-linear response observed in stress displacement curves for these bending tests.

3.6 REFERENCES

[1] Diederichs, M. S. 2000. Instability of Hard Rock Masses : The Role of Tensile Damage and Relaxation. Ph.D. thesis. Dept. of Civil Eng., University of Waterloo. 567pp.

[2] Potyondy, D. O., Cundall, P. A. 2004. A Bonded Particle Model for Rock. *Int. J. Rock. Mech. Min. Sci.* 41:1329-1364.

[3] U. S. Dept. of the Interior Bureau of Reclamation. 1992. Miscellaneous General Maintenace Volumes II : Fist Volume 4-10, Bolt Anchor Sulfaset.

[4] ISRM. 1983. Suggested Methods for Determining the Strength of Rock Materials in Triaxial Compression : revised version. *Int. J. Rock Mech. Min. Sci. Abstr.* 20:283-290.

[5] Neville, A. M. 1981. Properties of Concrete, 3rd ed. Pitman Publishing, London.

[6] Hoek, E. 1965. Rock Fracture under Static Stress Conditions. CSIR Report. National Mechanical Engineering Research Institute, Council for Scientific and Industrial Research. MEG383.

[7] ISRM. 1978. Suggested Methods for Determining Tensile Strength of Rock Materials. *Int. J. Rock Mech. Min. Sci. Abstr.* 15:99-103.

[8] Rocscience Inc. 2002. RocLab 1.007, http://www.rocscience.com.

[9] Martin, C. D., Martino, J. B., Read, R. S. 1997. Observations of Brittle Failure around a Circular Test Tunnel. *Int. J. Rock. Mech. Min. Sci.* 34:1065-1073.

[10] Lipson and Juvinall, 1963. Handbook of Stress and Strength, Macmillan.

CHAPTER 4

[1]A CLUMPED PARTICLE MODEL FOR ROCK

4.1 INTRODUCTION

The bonded particle model has received considerable attention over the past 10 years for its ability to simulate the behavior of intact materials using a variety of test configurations: Brazilian test, uniaxial and triaxial compression test.

Potyondy and Cundall[1] summarized the background and motivation for the development of the approach and provided an example application using the software Particle Flow Code (PFC), i.e., modeling of a tunnel in massive granite.

One of the requirements for the bonded particle model is the calibration of the micro-contact parameters to match the macro-scale response. While the approach and benefits of the bonded particle model are compelling it is not clear if the calibration of the bonded particle model to a uniaxial test is adequate for modeling any problem in that material or can only be used for modeling a uniaxial test.

[1] This chapter has been published to the Int. J. of Rock Mech. and Min. Sciences. 44: 997-1010

Diederichs[2] showed that if *PFC* was calibrated to the uniaxial compressive strength it significantly over-predicted the tensile strength.

Potyondy and Cundall[1] also showed that calibrating *PFC* to the uniaxial strength gave very low triaxial strengths and required a cluster logic to increase the friction angles to more realistic values. In order for the application of the bonded particle model to practical problems to be successful, the calibration must result in a *PFC* failure envelope and stress-strain response that matches those of the actual material, independent of stress path.

In this paper we examine the impact of the *PFC* micro-scale parameters on the macro-scale response in order to establish its sensitivity to the micro-scale parameters. A series of laboratory tests (Brazilian, uniaxial and triaxial) were used to determine the micro-scale properties for *PFC*. By developing a new clumped-particle logic one set of micro parameters was used for predicting the strength of the synthetic rock independent of stress path. The clumped-particle logic was used to predict the complete nonlinear failure envelope of Lac du granite and a weak synthetic rock. The new approach captures the major characteristics of brittle rock observed in laboratory testing, including the onset of dilation

4.2 BONDED PARTICLE MODEL (BPM) APPROACH

4.2.1 DILATION IN ROCK

All rocks are heterogeneous at the micro and macro scale. In rocks such as granite the heterogeneous nature can be readily observed with the naked eye. Laboratory testing of such rocks shows that when subjected to sufficient deviatoric loads these rocks dilate laterally indicating that axially aligned fractures are forming (Martin and Chandler[3]). The deviatoric load required to generate these opening, i.e, dilatant fractures is considerably less than the peak strength of the rock and for uniaxial compressive tests is often reported as 1/3 to 1/2 the uniaxial strength (Brace et al.[4]). Lajtai[5] noted that if the uniaxial sample is unloaded once dilation is initiated, permanent straining is only recorded in the lateral direction, while no permanent straining is recorded in the axial direction supporting the notion that the dilation is caused by axial cracks and indicating that the dilatancy process is not elastic and not uniformly distributed (Figure 4.1). One of the mechanisms that can explain this observation is illustrated in Figure 4.2.

As rock is subjected to deviatoric stresses, local tensile stress will be generated because of the heterogeneous nature of the rock. A likely location for a crack resulting from these tensile stresses is at a grain boundary (A in Figure 4.2). Because of the irregularities at grain boundaries, even a small amount of elastic distortion, once the tensile crack forms, could result in dilation. This dilation may be sufficient to induce tensile stresses at the crack tip and cause the crack to open and extend (B in Figure 4.2). Moreover, this elastic distortion may result in additional tensile stresses and when distributed to neighboring

cracks result in additional cracking and dilation (C in Figure 4.2). The coalescence or alignment of individual cracks may ultimately propagate in an unstable manner, i.e., because the region of tensile stresses grows, and form a macro fracture surface with associated dilation (D in Figure 4.2). The essential elements of this process are the deviatoric stresses required to cause the distortion once the crack forms and the nonplanar surface of the microcrack.

Figure 4.1 : An extension fracture generated in uniaxial compression in granite. The fracture is parallel to the direction of loading and the grain size is approximately 3 mm. Note the open irregular geometry of the fracture.

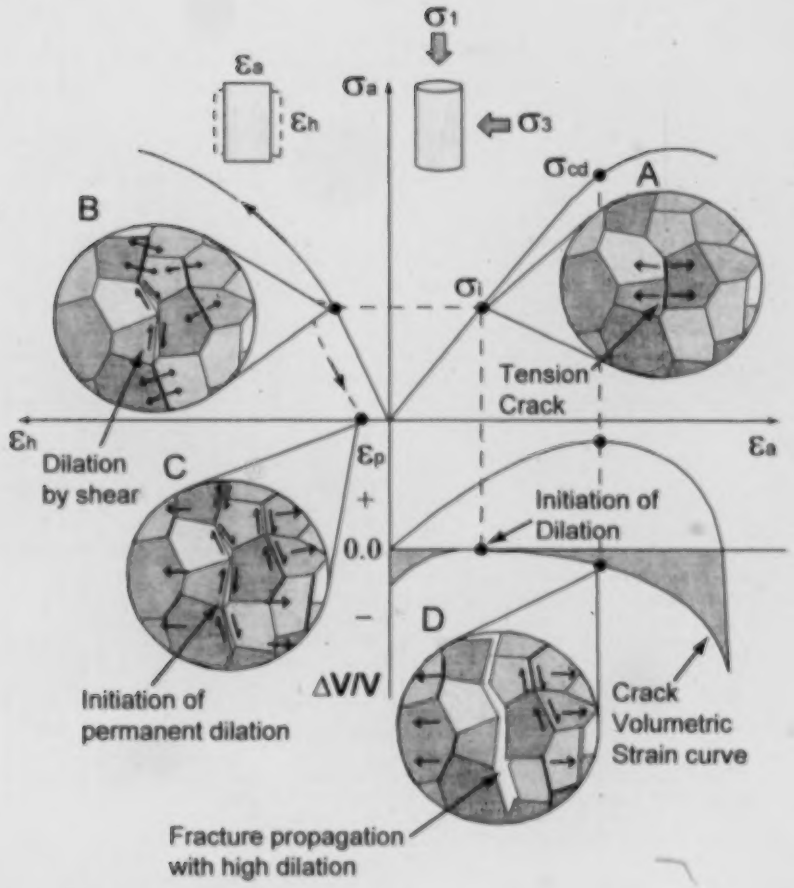

Figure 4.2 : Illustration of dilation process by fracture initiation and growth in brittle material subjected to compressive loading.

The formation of these axial dilatant cracks is a stable process since tensile stresses are required for their formation and it is difficult to create this tension when samples are loaded in compression. Once this dilation boundary has been crossed additional loading is still required to reach the peak strength of the rock. Lockner et al[6] showed using acoustic emission monitoring that cracking continues throughout the sample as the loads

are increased and failure eventually forms by a shear band developing across the confined samples. In unconfined samples, failure by axial splitting is often observed. Regardless of the failure mode a characteristic of brittle failure is an increase in dilation associated with discrete fracture growth with increasing stress (Martin and Chandler[3]).

The stress-strain behavior of Lac du Bonnet granite has been studied extensively in the laboratory. The data from Martin and Chandler[3] are used in the next section to establish the micro-parameters of the bonded particle model required to simulate the macro-scale response of Lac du Bonnet granite, bearing in mind that the particle model must capture the peak strength as well as the failure process described previously.

4.2.2 BONDED PARTICLE ANALOGUE

The bonded-particle model code used in this study was the Particle Flow Code (PFC^{2D}) developed by "*ITASCA* Consulting Group." for commercial use and widely used for many research projects since it's first distribution in 1995. *PFC*^{2D} represents a rock mass as an assemblage of circular disks that has finite thickness, connected with cohesive and frictional bonds and finite stiffness at contact and bonded area between disks. When specified bond strengths are exceeded by applied local stresses (i.e. tension, shear or moment by particle rotation), these bonds break to form a rupture surface, i.e., a crack. During these processes, *PFC* does not require any flow rule for describing the post yield response or fracture toughness to control fracture behavior, but only requires the law of

motion for particle movement, simple constitutive laws for particle deformation and yielding laws for particle bond rupture.

Diederichs[7] successfully used this approach to simulate brittle behavior of rock under compressive loading. However, as he noted that a bond rupture in *PFC* does not create the same singular stress concentration present at the tip of an extending micro crack within a continuum. The rupture in *PFC* results in stress redistribution in neighboring bonds, but this redistribution may not be adequate to rupture the adjacent contacts. As a result, the crack generating process in *PFC* is a stable process such that applied deviatoric boundary stress must be increased to generate new cracks. Therefore, *PFC* will not, without modification, model the dilation and crack generation process described in Figure 4.2.

One of the disconcerting results when using *PFC* to represent rock is that the tensile strength obtained in *PFC* is approximately 0.25 of the uniaxial compressive strength. This is disproportionately high, compared to granite and most other rocks where the ratio of σ_t/σ_{ci} is typically reported as 0.04 to 0.03 (Hoek and Brown[8]), i.e. σ_t/σ_{ci} = 1/24~1/30. Diederichs[2] showed that calibrating *PFC* to the compressive strength resulted in significantly higher relative tensile strength. He performed conventional direct tension test simulation with *PFC* and obtained a linear strength envelope without a tension cut-off as illustrated in Figure 4.3. This is clearly not in keeping with measured laboratory results. Diederichs[2] concluded that the linear tensile envelope in Figure 4.3 is attributed to the intrinsic contact force fabric structure in *PFC* known as "Trellis Cell". Under this struc-

ture, stress concentration by bond breakage is not adequate to cross the adjacent compression bridges (Figure 4.3), thus unstable fracture growth that occurs in direct tensile mode cannot occur. Potyondy and Cundall[1] also indicated that tensile strength obtained in Brazilian test simulation using *PFC* shows relatively high tensile strength. This inconsistency with laboratory tensile strength and the failure strength in compression is important to reconcile if *PFC* is to be applied to the problems where the stress path may be either tension or compression. In the following section the micro-scale parameters used to establish the contact properties in *PFC* are evaluated to assess which of these parameters control dilation and the ratio of σ_t/σ_{ci}.

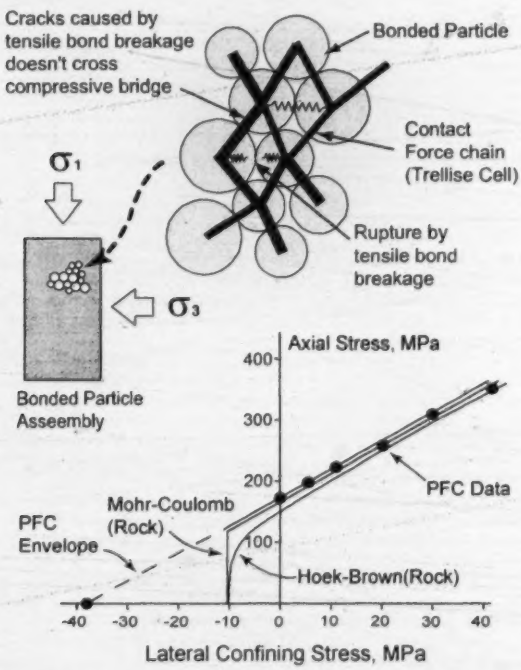

Figure 4.3 : Contact force chain structure in *PFC* and failure envelope. Note that *PFC* envelope has no tension cut-off. Modified from Diederichs[2].

4.3 PARAMETRIC STUDY ON DILATION AND STRENGTH RATIO (σ_t / σ_{ci})

4.3.1 MICRO-PARAMETERS

PFC represents a rock mass as an assemblage of circular disks confined by planar walls. In this system, the particles can move independently of one another and interact only at contacts. They are assumed to be rigid but can be overlapped at the contacts under compression. The particles can be bonded together by specifying the shear and tensile bond strength. The values assigned to these strengths influence the macro strength of the sample and the nature of cracking and failure that occurs during loading.

The micro-shear strength is mobilized when the contact bond is broken either by shear or rotation but once the bond is broken, the shear strength is set to its residual value as long as particles stay in contact, which is a function of compressive normal force and coefficient of friction (μ) at the contact. However, once a tensile bond is broken the tensile strength of particle bonding is set to zero regardless of its contact condition (i.e. particles are in contact or not) as illustrated in Figure 4.4.

After a bond breaks in *PFC*, forces are redistributed and this may then cause adjacent bonds to break. Thus, *PFC* only requires basic parameters to describe contact stiffness and contact friction, bond strength and bond radius (parallel bond model) and does not require any parameter for plastic flow rule formulation. This implies that only those parameters and geometrical factors associated with particle size and particle shape control dilation and macro-scale strength in *PFC*.

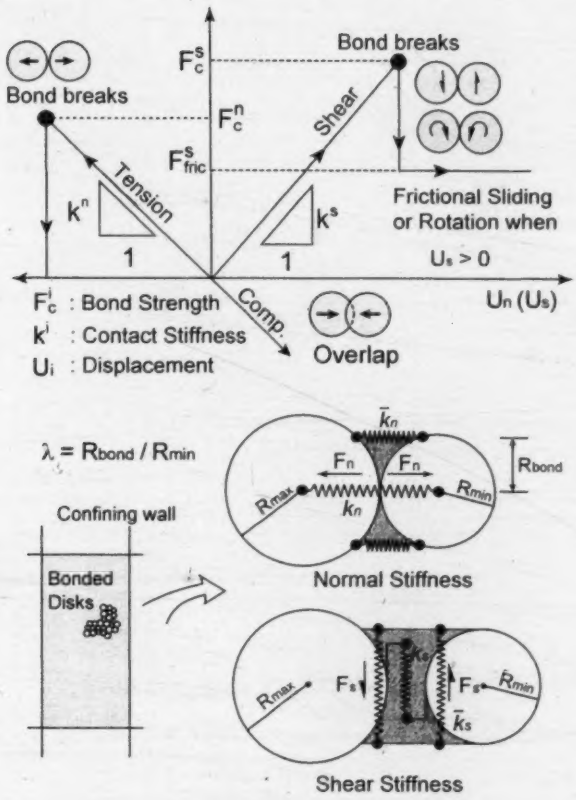

Figure 4.4 : Micro parameters and the illustration of yielding process for micro bonding. Modified from Potyondy and Cundall[1].

4.3.2 BOND MODELS

Two basic bond models are provided in *PFC*: "Contact Bond (CB) model" and "Parallel Bond (PB) model". A CB model can be envisaged as a pair of elastic springs (or point of glue) with constant normal and shear stiffness acting at a point. A PB model approximates the physical behavior of a cement-like substance joining the two particles. PB model establish an elastic interaction between particles that acts in parallel with the slip or contact-bond constitutive models. It also can be envisioned as a set of elastic springs

uniformly distributed over a rectangular cross section with constant normal bond stiffness and shear bond stiffness lying on the contact plane and centered at the contact point (Figure 4.4). Particles in *PFC* are free to move in the normal and shear direction and can also rotate between particles. This rotation may induce a moment between particles but the CB model cannot resist this moment. With the PB model however, bonding is activated over a finite area, thus this bonding can resist a moment as illustrated in Figure 4.5. In CB model, contact stiffness is still active even after bond breakage as long as particles are kept in contact. This implies that in CB model, if particle contact is maintained, bond breakage may not significantly affect the macro stiffness which is unlikely for rocks. In PB model however, stiffness is contributed by both contact stiffness and bond stiffness. Thus, bond breakage in the PB model, immediately results in stiffness reduction which not only affects the stiffness of adjacent assemblies but also affects the macro stiffness of the particle assemblage. These features are also illustrated in Figure 4.5 and in this sense, the PB model is a more realistic bond model for rock like materials whereby the bonds may break in either tension or shearing with an associated reduction in stiffness. For these reasons, the PB model was used in our study and applied to all the *PFC* modeling discussed in this paper.

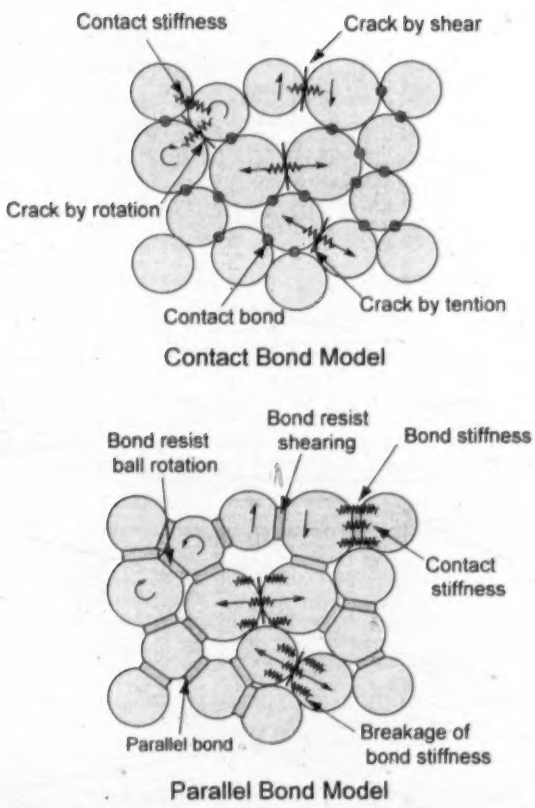

Figure 4.5 : Illustration of bond models provided in *PFC*. CB model has little resistance to the moment induced by particle rotation or shearing while PB model can resist to such particle movements since PB model is acting like a beam that resist the bending moment occurring within the bonded area. Note that in CB model, contact stiffness is still active even after the bond breaks as long as particles stay in contact. However, bond breakage in PB model immediately results in stiffness reduction since stiffness in PB model is contributed by both contact and bond stiffness. Bond stiffness is instantaneously removed when bonds breaks regardless of whether particles stay in contact or not.

4.3.3 EFFECT OF MICRO-CONTACT PARAMETERS

The *PFC* micro parameters were examined using uniaxial compressive test and Brazilian test simulation. From the uniaxial test simulation, lateral and axial strain, and peak strength were recorded. Tensile strength was obtained using the Brazilian test simulation as the Brazilian test is commonly used to evaluate the tensile strength of rock in practice. The procedure for the sample generation and loading methods are illustrated elsewhere (Potyondy and Cundall[1]) and in the *PFC* manual (Itasca Consulting Group[9]). Because of the heterogeneity introduced in *PFC* (e.g. standard deviation applied to micro strength and arbitrarily generated disk assembly with different particle radius), no two *PFC* runs produces identical results. During this parametric study, each simulation was run 10 times with same parameters and the results averaged. While this is somewhat laborious it approximates the variability encountered when testing rocks and avoids getting unique answers that may not be relevant.

The loading rate should be set sufficiently slow enough to ensure the sample remains in quasi-static equilibrium throughout the test and should be stable so as not to induce any possible strength increase or unexpected material responses within the simulated models. The loading rate applied in the parametric study and for other calibration purpose in this study was chosen to "0.2m/sec" for compression test and "0.05m/sec" for Brazilian test. One may accept this loading rate (i. e. a velocity applied on the loading wall) as significantly fast loading rate in physical world. In PFC modeling however, since the calculation logic in PFC is fundamentally based on the dynamic mode governed by Newton's second law, the time step (Δt) in each calculation cycle is chosen to be infinitely small

value (e.g. 10^{-8} sec) especially for a static analysis. In other words, the loading rate 0.2m/sec used for both uniaxial and biaxial simulation in this paper can be translated to $6.7x10^{-6}$mm/step which implies it requires more than 100,000 steps for moving a loading plate 1mm. Hence, while physically 0.2m/sec of loading rate is unreasonably high, this rate is slow enough in PFC simulation (Potyondy and Cudall[1], Diederichs[2], Itasca Consulting Group[9], Hazzard et al.[10]).

The lateral strains for the compressive test simulations were recorded up to 80% of the peak strength for the purposes of this parametric study. The lateral strain is used to gauge the amount of dilation occurring in each sample as cracks develop. All compressive samples measured 30 mm by 60 mm and consisted of about 1000 particles. The *PFC* specimen for Brazilian test simulation was taken from the uniaxial compressive test sample using the same diameter of the Brazilian sample as the width of the compressive sample. The ratio of tensile strength to compressive strength was determined for each simulation.

Lac du Bonnet granite has been extensively tested in the laboratory and several researchers (Potyondy and Cudall[1], Diederichs[2], Itasca Consulting Group[9], Hazzard et al.[10]) have conducted extensive calibration of its *PFC* micro properties. The micro parameters for Lac Du Bonnet Granite used in this study are given in Table 4.1 (see Figure 4.4 for definitions). During the simulation process for this parametric study, both contact and bond Young's modulus were all kept constant. However, this does not imply that

macro Young's modulus is also kept constant since the macro Young's modulus is affected by various micro parameters.

Table 4.1 : Micro Parameters of LDB Granite.

E_c	49GPa	$\overline{E_c}$	49Gpa
k_n / k_s	1.0	$\overline{k_n} / \overline{k_s}$	1.0
μ	0.0	$\overline{\sigma_n}$	200 ± 50MPa
$\overline{\sigma_s} / \overline{\sigma_n}$	1.0	$\overline{\lambda}$	1.0
R_{min}	0.55mm	R_{max} / R_{min}	1.65

Where, E_c is the contact modulus, $\overline{E_c}$ the parallel bond modulus, k_n / k_s the contact stiffness ratio (normal to shear), $\overline{k_n} / \overline{k_s}$ the parallel bond stiffness ratio (normal to shear), μ the coefficient of friction, $\overline{\lambda}$ the parallel bond radius ratio (defined as R_{bond}/R_{min}), $\overline{\sigma_n}$ the parallel normal bond strength, $\overline{\sigma_s} / \overline{\sigma_n}$ the parallel bond strength ratio (shear to normal), R_{min} the minimum particle radius, R_{max} / R_{min} the particle radius ratio (minimum to maximum).

EFFECT OF CONTACT FRICTION

As bond breaks either by rotation or shear in *PFC*, the force acting on the particle contact are set to a residual value that depends on the compressive normal force at the contact and coefficient of friction. The friction between particles mobilized at the contact, can suppress independent particle movement such as rotations or slippage. This process could increase the shear resistance and macro compressive strength. With increasing friction, dilation may be suppressed provided the dilation process is dominated by the micro friction parameters. Figure 4.6 shows the effect of friction between particles on dilation measured as lateral strain and the ratio of Brazilian tensile strength to uniaxial compressive strength. The coefficient of friction was varied from 0.0 to 0.9 but other micro parameters were not changed. Figure 4.6 illustrates that increasing the coefficient of friction

at the contacts only slightly suppresses the lateral strain and has no effect on the ratio of tensile strength to compressive strength. Hence, friction between particles does not effect the contact force chain structure discussed by Diederichs[2].

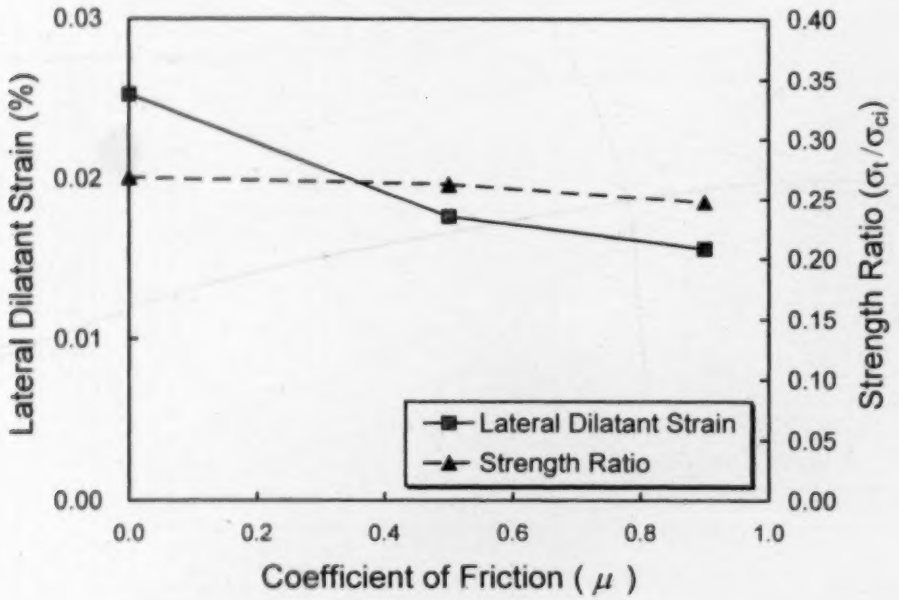

Figure 4.6 : Effect of the coefficient of friction on lateral dilatant strain and the ratio of tensile strength to uniaxial compressive strength.

EFFECT OF CONTACT STIFFNESS AND BOND STIFFNESS

Diederichs[2] and Potyondy and Cundall[1] showed that the contact normal to shear stiffness ratio (k_n/k_s) involves Poisson's ratio. As the stiffness ratio is increased, Poisson's ratio also increases and the sample becomes ductile. In this study, both contact and bond stiffness ratio was varied together from 1.0 to 10.0. Figure 4.7 indicates that as stiffness ratio is increased, the amount of dilation is also increased implying that more tension crack develops. Potyondy and Cundall[1] also reported similar results and suggested that

when the stiffness ratio is high, the stiff bonds result in increased tensile stresses and more tensile cracks. When the number of tensile cracks is increased, lateral dilation also increases. This is supported by the results in Figure 4.7 which shows a significant increase in lateral strain as the bond stiffness ratio is increased. However this ratio has little effect on the ratio of tensile to compressive strength which suggest that despite the increase in the number of bond contact broken, it was not adequate to change the strength ratio and fabric structure.

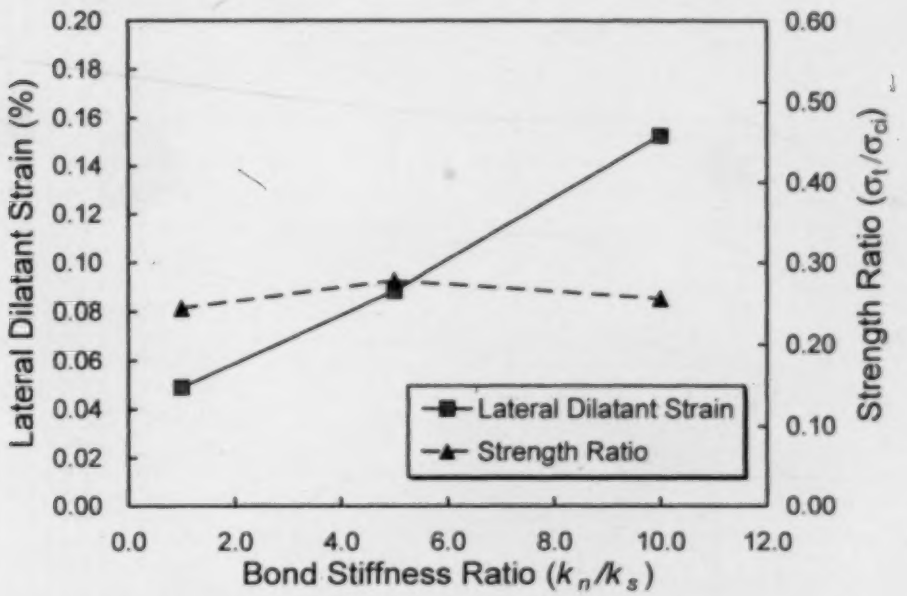

Figure 4.7 : Effect of bond stiffness on lateral dilatant strain and the ratio of tensile strength to uniaxial compressive strength. Note that increasing this ratio results in increasing the Poisson's ratio and hence apparent lateral strain.

EFFECT OF BOND STRENGTH

In *PFC*, the micro strengths must be iteratively selected to match the macro-scale strength. One of the important parameters that characterize the macro strength and micro-

fracture behavior is the bond shear to normal strength ratio ($\overline{\sigma_s}/\overline{\sigma_n}$). By increasing this ratio, the material response can be made to resemble brittle failure dominated by tensile cracking because increasing this strength ratio implies shear bond rupture is almost suppressed and only tension bond rupture is allowed. Diederichs[2] showed that this ratio could control the macro peak strength of the material. Figure 4.8 illustrates the effect on the lateral strain and ratio of tensile to uniaxial compressive strength as this micro bond strength is varied from 1.0 to 30.0. No significant increase in dilation occurs beyond a bond strength ratio of 10 and the ratio of tensile to uniaxial compressive strength is not influenced by the bond strength ratio.

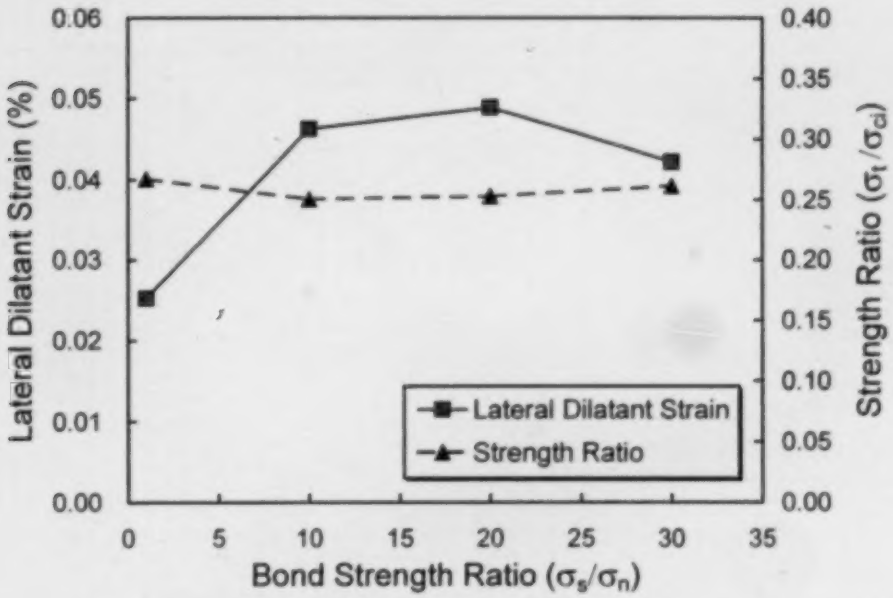

Figure 4.8 : Effect of bond strength ratio on lateral dilatant strain and the ratio of tensile strength to uniaxial compressive strength

EFFECT OF PARTICLE SIZE

Potyondy and Cundall[1] suggested that particle size could control tensile strength. They found a relationship between particle size and fracture toughness by using Brazilian test simulations. They assumed that wedge fractures occurring at the edge of the sample could initiate a single micro fracture that triggers the rupture surface (a. in Figure 4.9). For their example, the wedge shaped damage regions are replaced by edge cracks of length a (b. in Figure 4.9) and the mode-I stress intensity factor at each crack tip is then proportional to tensile stress activating across the model assembly.

$$K_I \propto \sigma\sqrt{a} \qquad (4.1)$$

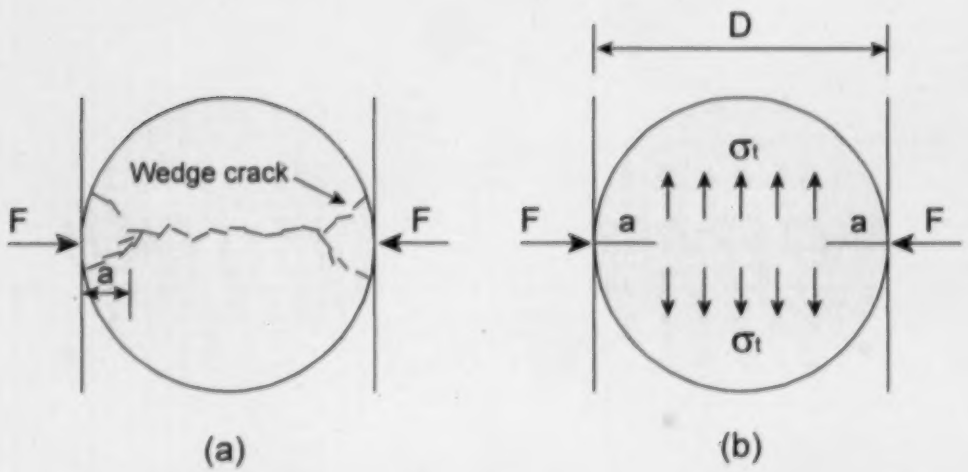

Figure 4.9 : Relating Brazilian strength to fracture toughness, modified from Potyondy and Cundall[1].

At peak load, $K_I = K_{Ic}$, $\sigma = \sigma_t$ and $a \cong 0.2D$, then

$$\sigma_t \propto \frac{K_{Ic}}{\sqrt{D}} \qquad (4.2)$$

where, σ_t is tensile strength of model assembly. Fracture toughness can be related to micro properties,

$$K_{Ic} = \beta \bar{\sigma}_t \sqrt{\pi \alpha R} \qquad (4.3)$$

where, $\alpha(> 1)$ is a non-dimensional factor that increases with packing irregularity, strength heterogeneity and bond ductility, and $\beta(< 1)$ is a non-dimensional factor that accounts for the weakening effect of the bending moment. $\bar{\sigma}_t$ is particle bond normal strength and R is particle radius. From Equation (4.2) and (4.3), Brazilian strength can be related to material micro properties by:

$$\sigma_t \propto \bar{\sigma}_t \sqrt{\frac{R}{D}} \qquad (4.4)$$

Equation (4.4) implies that particle size is proportional to the magnitude of tensile strength. Micro properties used for the particle size simulation analysis are shown in Table 4.2. In this case the same properties are used for both the Brazilian and compressive test simulation.

Table 4.2 : Micro Parameters used in particle size effect

E_c	62GPa	$\overline{E_c}$	62GPa
k_n / k_s	2.5	$\overline{k_n} / \overline{k_s}$	2.5
μ	0.5	$\overline{\sigma_n}$	157 ± 36MPa
$\overline{\sigma_s} / \overline{\sigma_n}$	1.0	$\overline{\lambda}$	1.0
R_{min}	Varies	R_{max} / R_{min}	1.66

Figure 4.10 shows that as particle size decreases, the ratio of tensile to compressive strength also decreases. The ratio tensile strength to compressive strength for Lac du Bonnet granite is about 10/200 = 0.05. Thus to achieve this strength ratio the particle size would have to get smaller and calculation time exponentially increases. The grain size for Lac du Bonnet granite was reported by Martin et al.[11] to average around 2mm in diameter. Hence Figure 4.10 would suggest that increasing the mean particle radius to 1mm would increase σ_t/σ_{ci} to 0.35, considerably more than the 0.05 measured. In terms of dilation, the smaller the particle size would also reduce the amount of dilation (Figure 4.10).

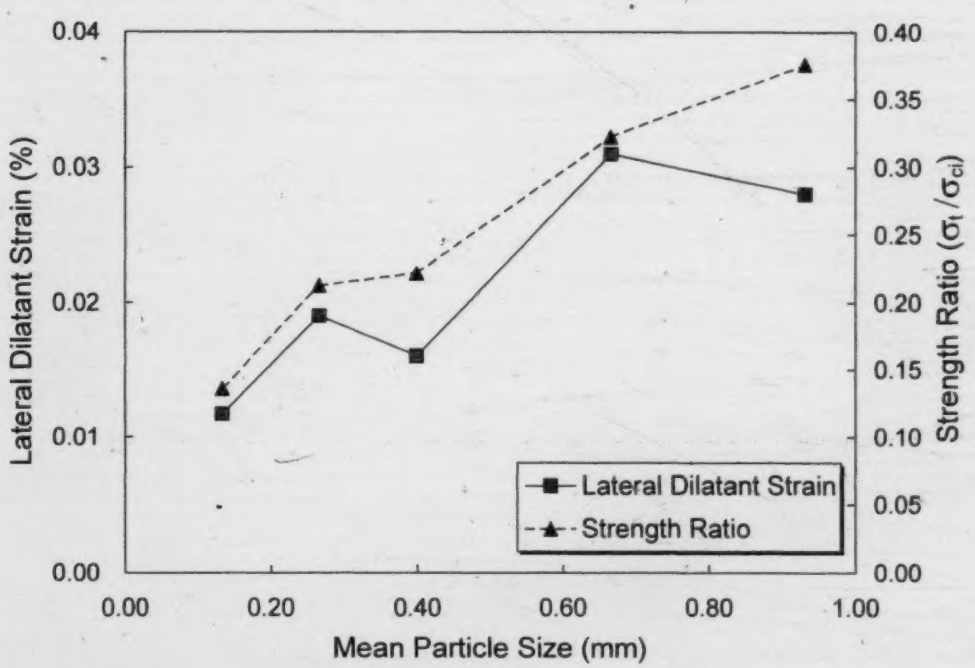

Figure 4.10 : Effect of Particle size on on lateral dilatant strain and the ratio of tensile strength to uniaxial compressive strength.

4.3.4 EFFECT OF GEOMETRIC FACTORS

EFFECT OF GRAIN SHAPE

Most rocks in nature are composed of irregular grains strongly bonded together. In *PFC* the basic element is a circular disk which significantly reduces the calculation times. However, Jensen et al.[12] and Thomas and Bray[13] suggested that circular disk elements may not adequately model geometry dependent properties such as dilation and interlocking friction. Guo and Morgan[14] also demonstrated that grain shape model using specifically grouped circular particles could significantly increase the sliding friction along shear plane.

In conventional *PFC* modeling with circular disk elements Potyondy and Cundall[1] showed that the macroscale failure envelope, resulted in unrealistically low friction angles, when compared to measured values. For example the measured friction angle for Lac du Bonnet granite was reported as more than 50 degrees based on triaxial test[3]. However, Potyondy and Cundall[1] found that *PFC* provided a macro-friction angle for Lac du Bonnet granite of approximately 30 degrees. To overcome this shortcoming, they suggested clustering the circular disks. In clustered assemblies, grains are modeled as a group of individual circular disks. The intra-cluster bond strength can be set to different value from the bond strength of boundary particles neighboring with other clusters.

The same cluster concept was used in this study to explore how grain shape could affect the strength ratio and dilation. The intra-cluster bond strength was set sufficiently high such that bond breakage could only occur at cluster boundaries. The clustered particles with this setting are considered to be a better representation of naturally irregular grains

as shown in Figure 4.11. For the comparison of previous non-clustered particle assemblies, the average cluster diameter (i.e. grain diameter) was roughly matched to the average single particle size of non-clustered assemblies. Hence for keeping the cluster size in clustered assembly to the particle size in non-clustered assembly, the particle size making up the cluster had to be decreased.

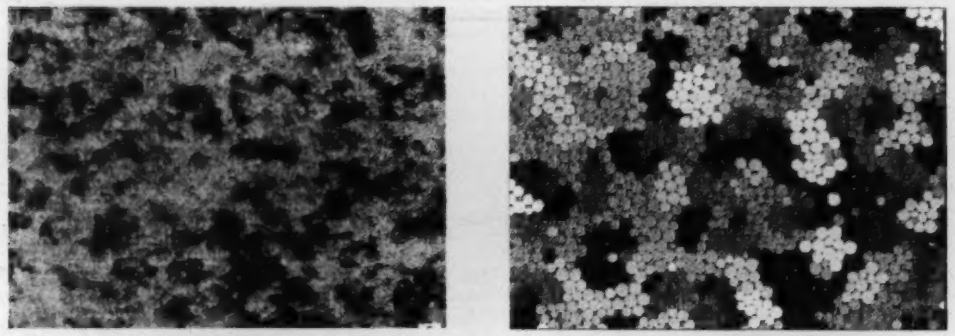

Figure 4.11 : Clustered particles for the modeling of irregular shapes of grains in brittle rock.

Using this logic dilation and σ_t/σ_{ci} strength ratio was investigated again. Figure 4.12 clearly shows that as cluster size increases, the amount of dilation is significantly increased and hence associated with the irregular cluster boundary, i.e, roughness. It is worth noting that this dilation process resembles the mechanical dilation for irregular geometry described by Lajtai[15]. Also shown in Figure 4.12 is reduction in the σ_t/σ_{ci} strength ratio as cluster size and dilation increase. However, the strength ratio shown in Figure 4.12 is still high, approximately 0.1 to 0.15, compared with the measured σ_t / σ_{ci} $\leq$ 0.05 for Lac du Bonnet granite.

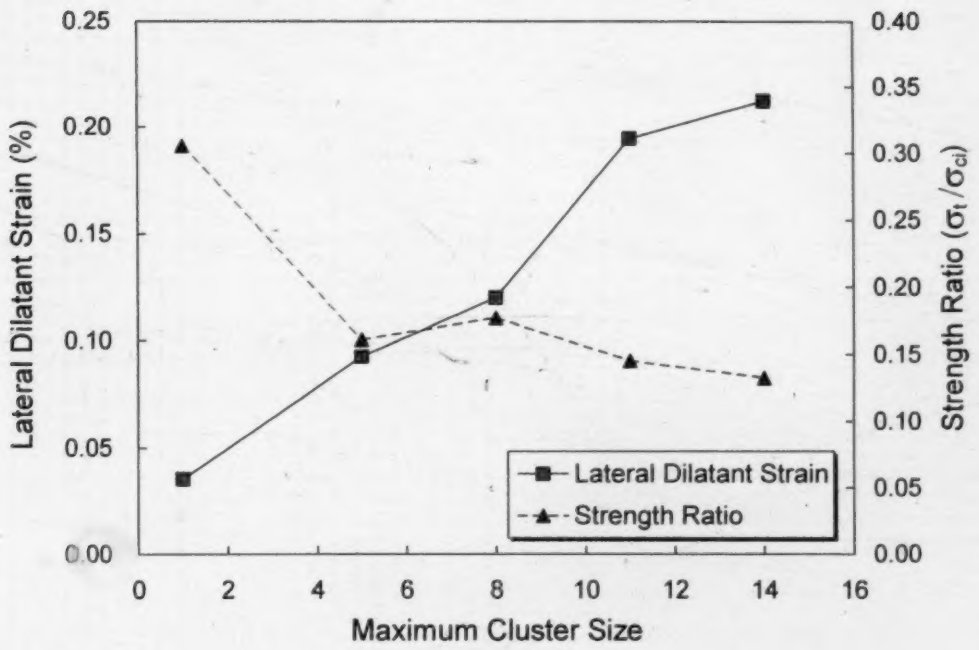

Figure 4.12 : Effect of grain shape on lateral dilatant strain and strength ratio using cluster logic.

Although bond strength between intra-cluster particles has been set an order of magnitude higher than the cluster contacts, rotation of the intra-cluster particles cannot be completely suppressed and this rotation may contribute to force chains. To illustrate the effect of particle rotation two simulations were conducted with identical micro parameters and particle assembly. The only difference between two cases is that all particle rotational velocity in case 2 was fixed to zero, in other words, moments occurring on contact beam are all set to zero. Figure 4.13 clearly shows that as particle rotation is completely suppressed, the peak strength was enormously increased (e.g. an order of magnitude). However, it is unrealistic to suppress all rotation because the force chains clearly indicate that

bending does occur. One alternative approach which reduces the effect of particle rotation within the clustered grains is to use clumped particle assembly. This approach is illustrated in next section.

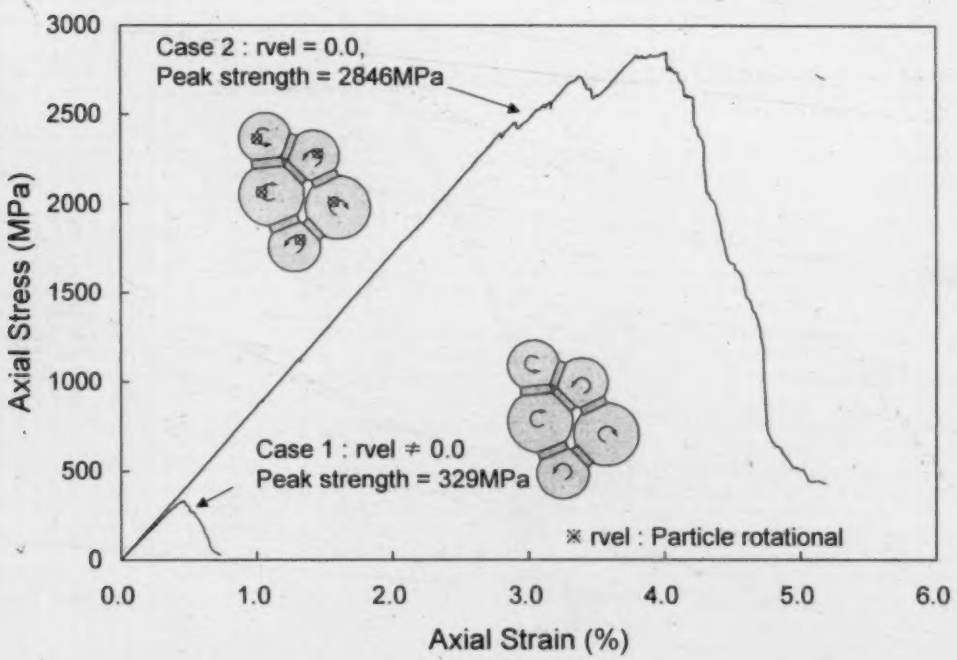

Figure 4.13 : Effect of particle rotation. Note that as particle rotation is completely suppresses, peak strength is increased an order of magnitude. The bond strength was set close to the laboratory uniaxial strength.

CLUMPED PARTICLES

The clump logic provides a means to create a group of glued particles that behave as a single rigid body in a clump. Clumped particles may overlap to any extent as a deformable body that will not break apart regardless of the forces acting upon it. Hence, clumped particles can act like a single particle that has an irregular shape yet move as a

rigid body. In this sense, a clump differs from clustered particles. However one of the big differences other than that is the particle rotation mechanism. As shown in Figure 4.14, intra-cluster particles in clustered material have rotational velocities. Whereas rotational velocities of particles in clumped assembly are fixed. Only the clumped body itself can have rotational velocities. Hence, by taking the clump logic, excessive particle rotation is restricted but moment loading can still be properly simulated.

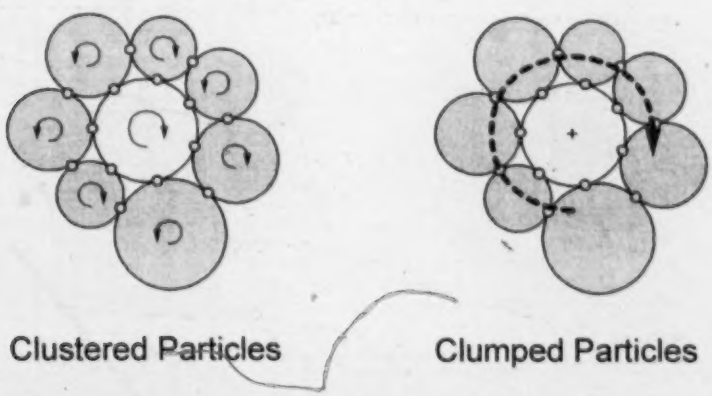

Figure 4.14 : Particle rotation mechanisms in clustered and clumped particles

The simulations used to investigate the effect of cluster size were repeated using the clump logic. The results are given in Figure 4.15 and clearly show as clump size increases, dilation is significantly increased and the strength ratio σ_t / σ_{ci} is reduced to approximately to 0.07. It is worthy to note that the amount of dilation is almost an order of magnitude larger than the other cases discussed. The strength ratio is also closer to the values measured for Lac du Bonnet granite and many other brittle rocks.

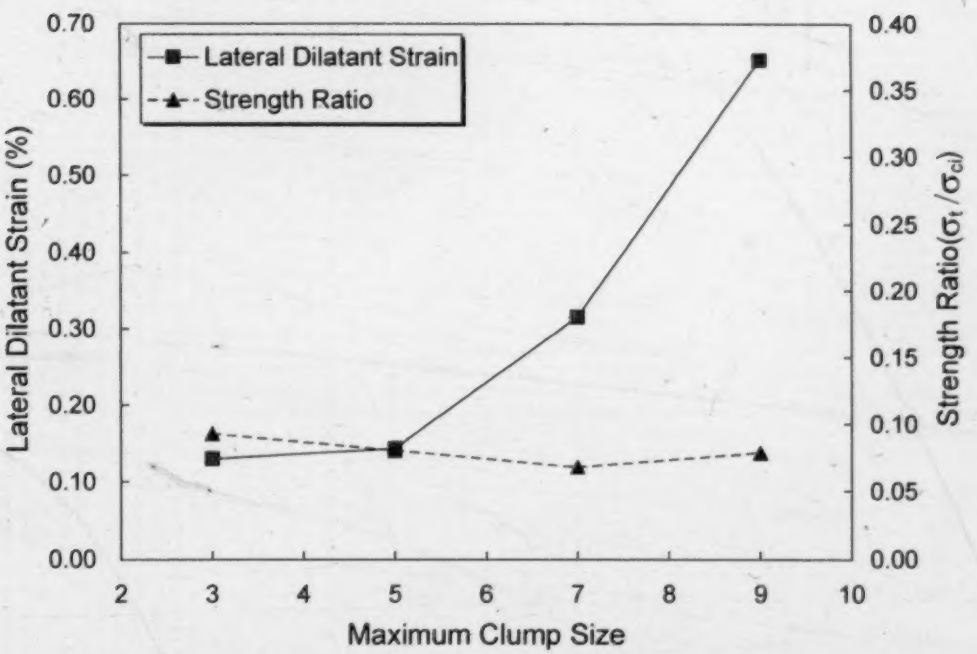

Figure 4.15 : Effect of grain shape on lateral dilatant strain and strength ratio using clump logic. Note that strength ratio is significantly reduced compared with adjusting other micro parameters.

4.3.5 CONTROLLING FACTORS OF DILATION AND STRENGTH RATIO

From the simulations discussed above, it is clear that the most important factor in controlling dilation and the strength ratio σ_t / σ_{ci} in the particle simulations is the geometrical factors rather than micro-contact parameters. The clustered and clumped material all showed an order of magnitude larger amount of dilation and lower strength ratio compared with all other cases. Thus, it is evident that geometrical factors such as cluster or

clump cases are more realistic and effective for modeling dilation and this dilation is actually controlling the strength.

The other interesting result is that rotation of particles in assemblage has a significant effect on material strength. For instance, the clumped material has more than 20 times larger compressive strength than non-clumped material with the same micro properties. Whereas, tensile strength of the clumped material only increased 2 to 3 times more than the non-clumped material. Hence this kept the strength ratio low in clumped material. In conventional *PFC* modeling, if one adjusts the micro-parameters to match the macro compressive strength the tensile strength is overestimated. The clumped logic adopted in this study may overcome this deficiency.

4.4 CALIBRATION OF *PFC* TO HARD ROCK AND WEAK ROCK USING CLUMPED BONDED PARTICLE

4.4.1 CALIBRATION OF *PFC* TO A BRITTLE ROCK

It is evident from the parametric study that introducing the geometric factors using the clump logic is more realistic and effective for modeling of rock like brittle material in *PFC*. In this section we apply the clump technique to simulate Lac Du Bonnet granite and compare the simulated results with laboratory test results.

The clump logic introduced in Figure 4.15 uses maximum clump size to form irregular grain modeling by limiting the number of particles in one clump. This type of size control is however, not adequate to consider the actual grain size since it only defines the maxi-

mum number of particles so it is difficult to account for the actual grain size in real rock. For this reason, we introduced the stamp logic for the size control of the clump. This logic is illustrated in Figure 4.16.

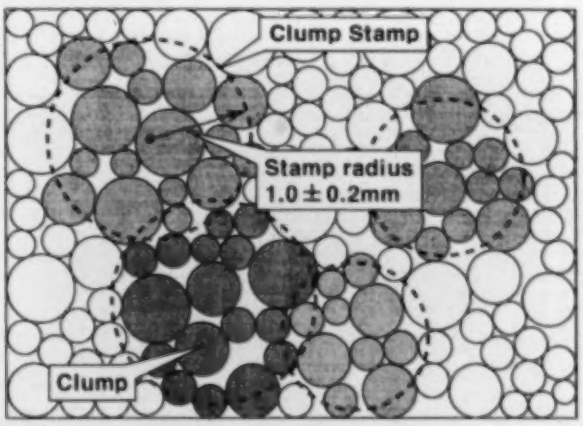

Figure 4.16 : Illustration of stamping logic to control clump size.

Using this logic, a clump can be created by stamping a circled area that corresponds to the desired grain size so that the particles within this area, if their center position is inside the stamped boundary, they can be added to a clump and grouped particles in a clump represent a grain acting as a single particle. The size of a clump is determined by specifying the radius of the stamp circle with a standard deviation (i. e. "*clp_rad*" in Table 4.3) and clump stamping is continuously activated until the 99% of the particles in the assembly are clumped.

While we were not intended to match the similarity in grain size with actual grains, the final average clump size calibrated for the simulation was 2mm in diameter which is the same average grain size as Lac du Bonnet granite reported by Martin et al.[11]. However,

no further attempts were made to match the similarity in statistical distribution and the shape of grains to actual grains.

Table 4.3 : Micro Parameters of Lac du Bonnet granite used for calibration

R_{min}	0.20mm	E_c	20.0GPa
R_{min} / R_{max}	1.5	k_n / k_s	2.5
$\overline{\lambda}$	1.0	$\overline{E_c}$	20.0GPa
μ	0.1	$\overline{k_n} / \overline{k_s}$	2.5
$\overline{\sigma_n}$	25.0 ± 3.5MPa	*Clp_rad*	1.0 ± 0.2mm
$\overline{\sigma_s} / \overline{\sigma_n}$	20.0	Unit_weight	2639kg/m^3

As discussed earlier, the stiffness ratio (i.e. normal to shear ratio for both contact and bond) directly involves Poisson's ratio. However, as Potyondi and Cundall[1] mentioned, direct comparison of Poisson's ratio in PFC^{2D} with laboratory result is not that meaningful because of the limitation in 2D analysis of PFC. The fundamental assumption for particle elements employed in *PFC*^{2D} is that particles are either disks having finite thickness or spheres having single layer toward out of plane direction. The former is similar to the plane strain condition and the latter is similar to the plane stress condition in continuum mechanics. However, unlike continuum mechanics assumption, there is no out of plane stress in plane strain and no out of plane strain in plane stress in *PFC*^{2D}. Hence, attempts to match volumetric strain or Poisson's ratio in *PFC*^{2D} material to match 3D physical material are not always successful (Potyondy and Cundall[1]).

Hence, no attempt was made for calibrating the ratio with laboratory results and only to be fixed to 2.5 which is identical value that Diederichs[2] provided using simple bonded particle assembly (i.e. no clump or no cluster particle assembly) for the same rock.

The bond normal strength (σ_n) was set to one and half to two times of actual tensile strength of Lac Du Bonnet granite. Uniaxial strength of this synthetic assembly was then calibrated by increasing clump size (*clp_rad*) and shear to normal strength ratio ($\overline{\sigma_s} / \overline{\sigma_n}$). Both parameters could increase both uniaxial strength and slope of failure envelope. As discussed earlier, increasing $\overline{\sigma_s} / \overline{\sigma_n}$ ratio implies that as the micro shear strength is set to higher values than that of normal strength only tension cracks can occur. Increasing clump size has largely two effects on the strength. First, once particles are joined to the clump, the individual particle rotation is suddenly frozen so if clump radius is larger and larger, then particle rotation is more and more suppressed and the strength will increase (i. e. note that suppressing particle rotation highly increase material strength). Secondly, increasing clump radius can geometrically increase the apparent friction along the clump boundaries thus this friction could effect both uniaxial strength and slope of failure envelope.

Figure 4.17 (a) and (b) shows the comparison of axial stress-strain and lateral strain response respectively between *PFC* synthetic rock and Lac Du Bonnet granite for 15MPa of confining stress. Although *PFC* exhibits a slightly higher strength and lateral strain shows somewhat high dilation, overall responses for axial stress strain are well matched.

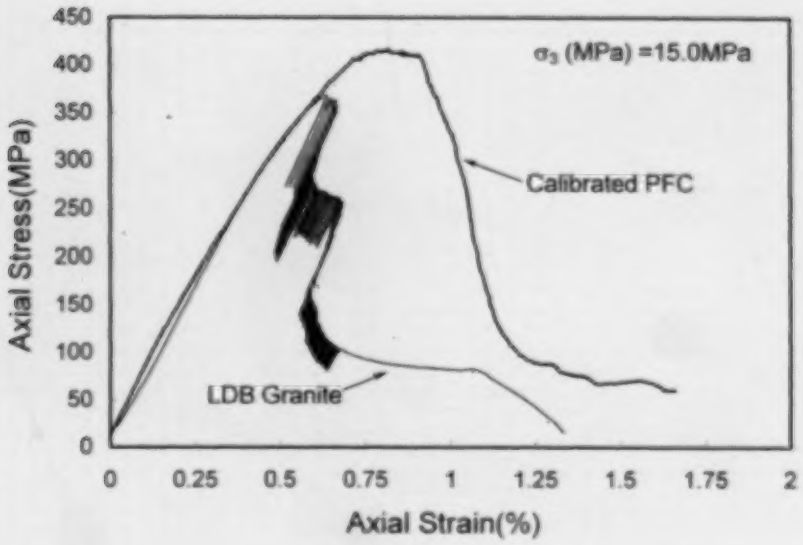

(a)

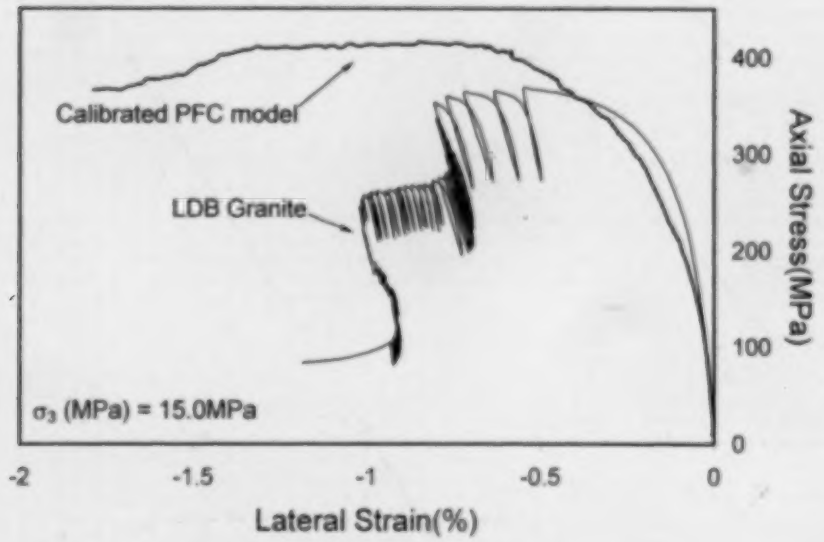

(b)

Figure 4.17 : Comparison of predicted axial stress and strain response from the calibrated *PFC* to the measured laboratory response of Lac Du Bonnet granite for σ_3=15.0MPa.

The stress-strain in *PFC* is somewhat different from the laboratory results after the post peak because the servo control of strain in laboratory test setup was not reflected in current PFC simulation. While Hazzard and Young[10] demonstrated that post peak response of Westerly granite could be captured in PFC using constant acoustic emission rate since our study was not focused on the post-peak response, this issue was not addressed in our current study.

The differences in lateral strain in post peak may be also attributed to the intrinsic features of clump logic. Since grouped particles in a clump are treated like rigid and unbreakable particles no clumped particle crushing occurs even after the post peak. Future work should consider this limitation particularly if high confining stresses are important.

Figure 4.18 compares the failure envelope of *PFC* and LDB granite. Although *PFC* shows slightly higher tensile strength and uniaxial compressive strength, the two failure envelopes generally show excellent agreement. In particular, the nonlinear strength envelope, the realistic friction angle and the correct strength ratio (tensile to uniaxial) are all captured by the new clump logic. It is also important to remember that the predicted stress-strain response and strength envelope is based on the calibration to the conventional laboratory tests (i.e. uniaxial, triaxial compressive test and Brazilian tensile test) which have different stress path respectively.

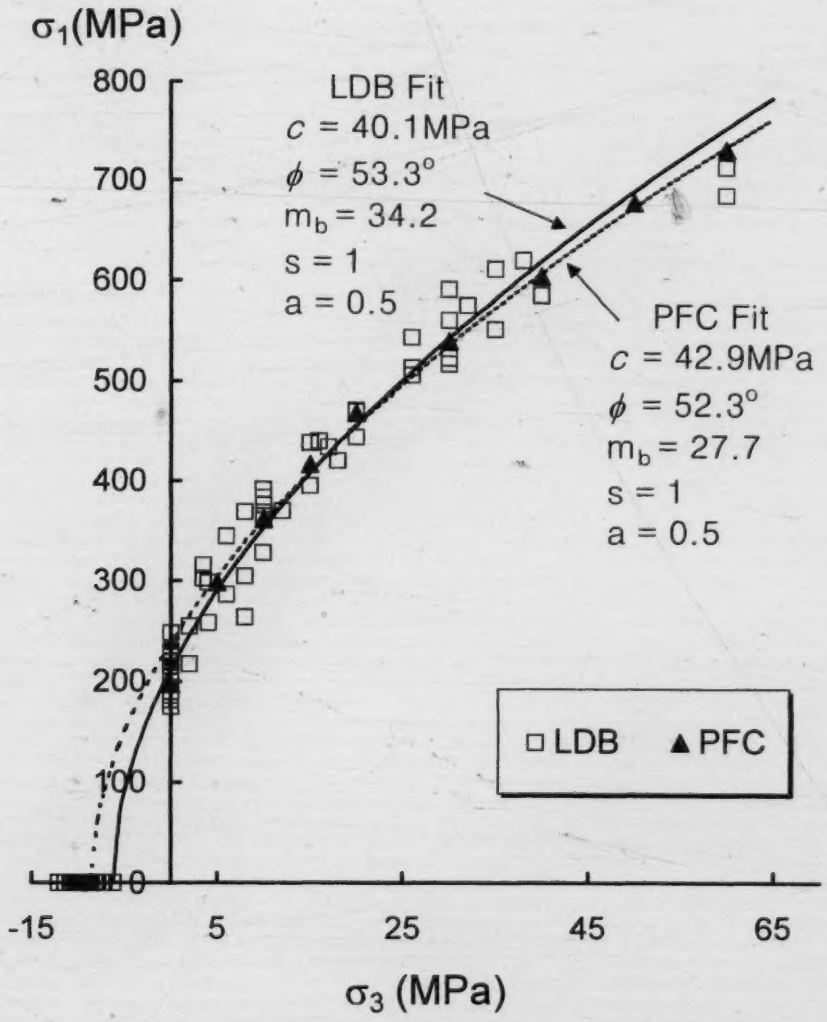

Figure 4.18 : Predicited failure envelope from *PFC* compared with laboratory envelope for Lac du Bonnet granite. The best fit in the figure was obtained using Rocklab (ver. 1.0 , Rocscience Inc.)

4.4.2 CALIBRATION OF *PFC* TO A SYNTHETIC WEAK ROCK

While the calibration of *PFC* with a hard brittle rock, Lac du Bonnet granite, described in previous section was successful, it was not known if the same logic could be applied to a weak brittle rock. In western Canada and in other parts of the world, many engineering projects are constructed on weak rocks that provide significant challenges. Weak rocks often have a uniaxial compressive strength about an order of magnitude lower than Lac du Bonnet granite. In this section, we use the same *PFC* logic applied to Lac du Bonnet granite and apply it to a brittle synthetic weak rock that has a peak strength an order of magnitude lower than Lac Du Bonnet granite.

LABORATORY SYNTHETIC ROCK PROPERTIES

The synthetic rock chosen for representing weak rock in this study is "Sulfaset" that is generally used for setting anchor bolt. This synthetic rock has brittle characteristics but a much lower compressive strength and reaches almost 80% of full strength within a few hours after molding. The strength and stiffness of the synthetic rock is highly dependent on its initial moisture content at mixing, and for the test reported here the initial moisture content has been fixed to 50% and cured for 3 days in a constant temperature and moisture room. To induce random heterogeneity in the sample, 10% sand by mass was added to all the samples. The material response and properties were obtained from conventional laboratory tests (i.e. uniaxial, triaxial and Brazilian test). The measured sample properties are shown in Table 4.4.

Table 4.4 : Material properties of Sulfaset synthetic rock.

σ_c (MPa)	σ_t (MPa)	E (GPa)	c (MPa)	ϕ (MPa)	s	m_b
11.6 ± 1.0	2.6 ± 0.3	2.5± 0.5	2.95	35.1	1	5.07

Where, σ_c : Uniaxial Compressive Strength, σ_t : Brazilian tensile Strength, E : Young's modulus, c : Cohesion, ϕ : Friction angle, s, m_b : H-B material constants

PFC CALIBRATION TO LABORATORY DATA

The *PFC* micro parameters for the synthetic weak rock we used were determined based on the macro-scale laboratory properties in Table 4.4. The chosen micro parameters for this material are tabulated in Table 4.5.

Table 4.5 : Micro Parameters used to represent the Sulfaset synthetic rock.

R_{min}	0.25mm	E_c	1.4GPa
R_{min} / R_{max}	1.5	k_n / k_s	2.5
$\overline{\lambda}$	1.0	$\overline{E_c}$	1.4GPa
μ	0.75	$\overline{k_n} / \overline{k_s}$	2.5
$\overline{\sigma_n}$	6.8± 1.7MPa	*clp_rad*	0.37± 0.2mm
$\overline{\sigma_s} / \overline{\sigma_n}$	1.0	Unit_weight	1830kg/m^3

Bond strength between one clump and another was chosen as approximately half the macro strength since the clumped grains significantly contribute to the macro strength of the assembly. Contact and bond young's modulus was also set to low value as the same reason. Thus, the cohesion of the assembly is mostly represented by the micro bond strength, and as this cohesion is lost, the rest of macro strength is contributed by friction

between particles, but this friction is mobilized by both clump geometry irregularity and particle contact friction defined by coefficient of friction.

Figure 4.19 shows the uniaxial and biaxial test simulation results from *PFC* when using the micro-scale parameters in Table 4.5 compared to the measured laboratory stress strain response. Compared with the laboratory results the initial non-linearity is not present because no initial flaws or pore effects are modeled in *PFC*. If a random distribution of pores or cracks were used, the non-linearity measured might also be recorded in *PFC*. However, it is beyond our current research focus to model this initial pore effect.

For the confining stresses examined, the agreement between *PFC* and laboratory results is excellent. It is interesting to note that no flow rule is required for modeling the stress-strain behavior in post peak region in *PFC*. The failure envelope for *PFC* is also in agreement with the laboratory failure envelope (Figure 4.20). More importantly the agreement with the tensile and compressive strength is also excellent. The shape of the failure zone in *PFC* shows the typical macro shear fractures observed in the laboratory test (Figure 4.21).

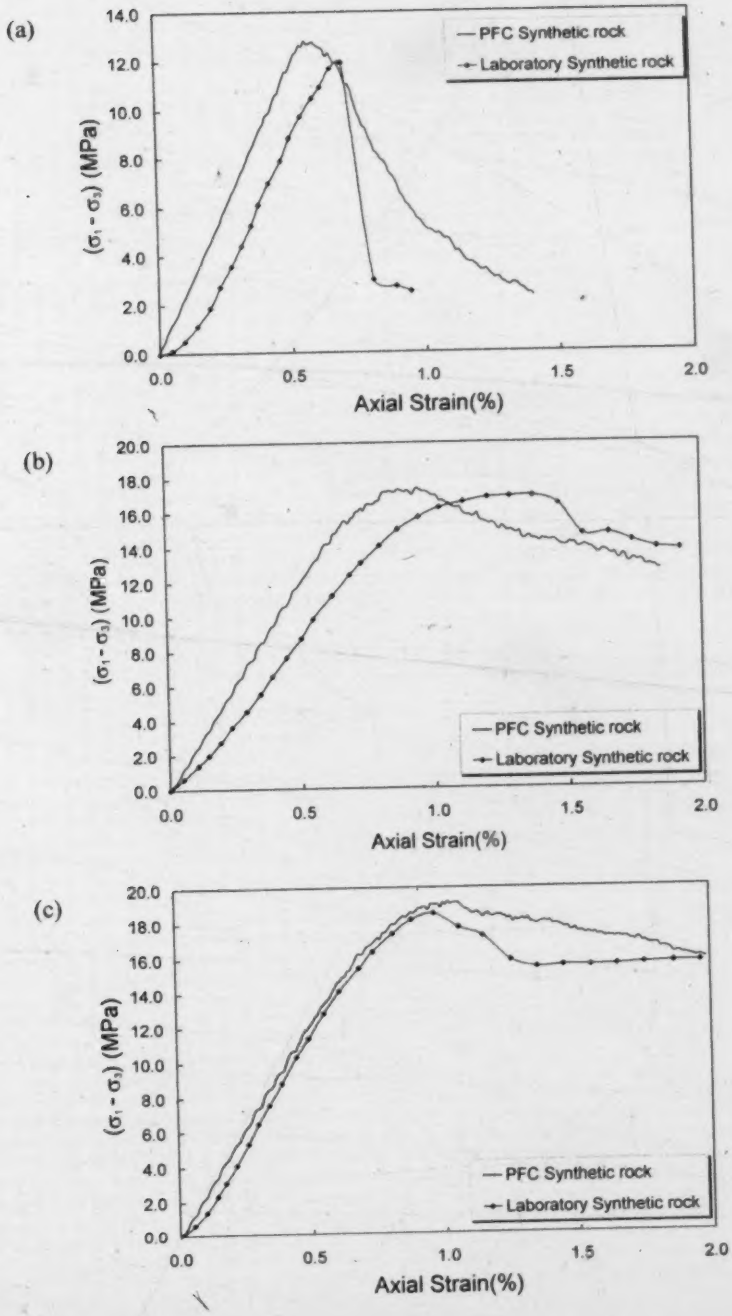

Figure 4.19 : Calibrated results in stress and strain behavior for *PFC* synthetic rock. (a) σ_3 = 0.0MPa, (b) σ_3 = 2.0MPa, (c) σ_3 = 3.0MPa.

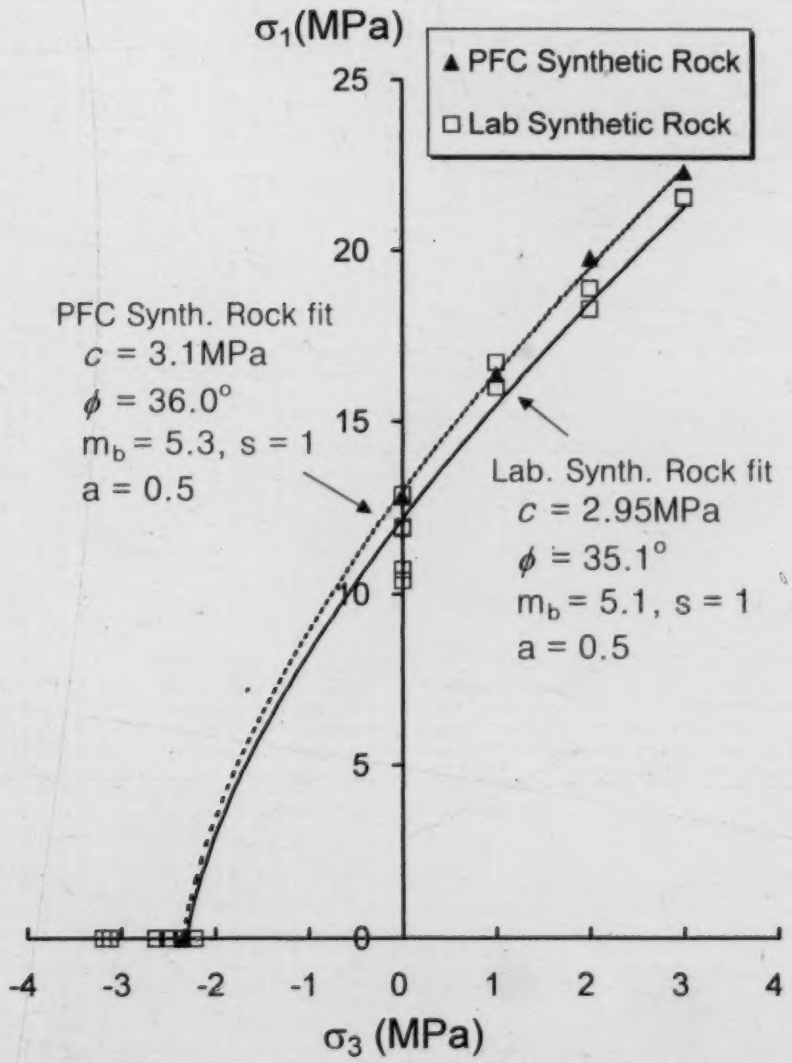

Figure 4.20 : Failure Envelope of calibrated material compared with laboratory envelope. The best fit in the figure was obtained using Rocklab (ver. 1.0 , Rocscience).

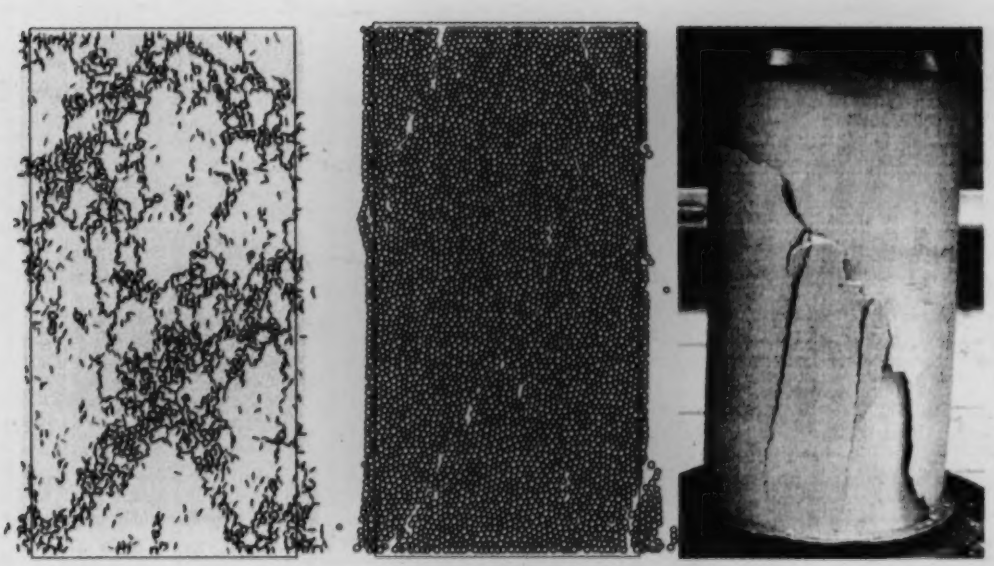

(a) (b) (c)

Figure 4.21 : Sample failure in uniaxial compression test for the calibrated *PFC* synthetic rock and Laboratory synthetic rock. (a) Crack distribution (b) Sample dilation (c) Synthetic rock failure.

4.5 DILATIONAL BOUNDARY

Numerous researchers (Martin and Chandler[3], Brace et al.[4], Lajtai[5], Hallbauer et al.[16], Martin[17], Tapponnier and Brace[18]) have reported that the onset of dilation in uniaxial tests initiates at about 1/4 to 1/2 of the peak strength. In most case the dilation is associated with the initiation of axially aligned micro-cracks. Scholz[19], Holcomb and Martin[20], Pestman and Van Munster[21] studied the crack initiation, of granite, sandstone, and marble using acoustic emission and they showed that the onset of dilation could be approximated by:

$$\sigma_1 = 0.4\sigma_c + 1.5 \text{ to } 2.0\sigma_3 \qquad (4.5)$$

A typical procedure to determine the crack-initiation stress (i. e. referred to the onset of the dilation in this study) from the results of laboratory testing is described by Martin and Chandler[3]. The onset of dilation in conventional laboratory test for granite is defined as the stress at which dilation just begins on a plot of crack volumetric strain. The crack volumetric strain is found by subtracting the elastic volumetric strains from the total volumetric strains. Although this method provides a good means to obtain an onset of dilation from laboratory tests, it is not applicable for obtaining the response from a PFC^{2D} material because as illustrated earlier the volumetric response and Poisson's ratio of the two-dimensional PFC^{2D} material cannot be compared directly with that of a three-dimensional physical material.

Potyondy and Cundall[1] suggested that the onset of dilation could be estimated by taking the stress magnitude that corresponds to the 1~2% of total number of cracks at the

peak stress for the biaxial simulation of *PFC* synthetic rock. Using this approach the dilation locus was estimated for both calibrated Lac du Bonnet granite and weak synthetic rock. By taking approximately 2% of total number of cracks at peak stress for Lac du Bonnet granite and weak synthetic rock respectively, the dilational boundary for the calibrated *PFC* models can be approximated by :

$$\sigma_1 = 0.3\sigma_{ci} + 1.6\sigma_3 \text{ (Lac du Bonnet granite)} \qquad (4.6)$$

$$\sigma_1 = 0.5\sigma_{ci} + 2.0\sigma_3 \text{ (weak synthetic rock)} \qquad (4.7)$$

Equation (4.6) and (4.7) is in good agreement with equation (4.5) and this boundary is controlled by micro strength, particle radius ratio and clump size. As observed in the laboratory tests, the dilation boundary in *PFC* signifies the beginning of crack growth and as reported by other researchers (Potyondy and Cundall[1], Diederichs[2]) these cracks are mainly axially aligned cracks created by localized tensile stresses.

4.6 CONCLUSION

During the past ten years the discrete particle codes, particularly the software *PFC*, have been used to model brittle failure. Conventional modelling of the macro-scale response using the discrete particle code requires calibration of the particle parameters. This is often achieved using the results from laboratory uniaxial compression tests. Three significant deficiencies have been identified when doing conventional *PFC* modeling: (1) the tensile strength to compressive strength ratio is considerable greater than that measured in the laboratory tests, (2) the failure envelope using *PFC* is linear, and (3) the failure envelope using *PFC* provides very low friction angles compared to measured laboratory values. The extensive sensitivity studies carried out for this study has shown that adjusting the particle parameters appears to have little effect on these deficiencies. The findings from this research indicate that by simply introducing a clumped-particle geometry these deficiencies are significantly reduced, suggesting that the shape of the particle plays a major role in the *PFC* response and perhaps the response of the actual material being simulated.

Using the clumped particle logic, excellent agreement is found between laboratory tests results and our *PFC* simulations for both the weak synthetic rock and Lac Du Bonnet granite. Currently the calibration between real materials and *PFC* is made using the simple stress paths followed in traditional laboratory testing. In order to know if the same agreement as observed in our study can be achieved using *PFC* to model engineering problems such as slopes and tunnels more complex loading paths should be evaluated.

4.7 REFERENCES

[1] Potyondy, D. O., Cundall, P. A. 2004. A bonded-particle model for rock. *Int. J. Rock Mech. Min. Sci.* 41:1329-1364.

[2] Diederichs, M.S. 2000. Instability of Hard Rock Masses : The Role of Tensile Damage and Relaxation. PhD. Thesis. University of Waterloo.

[3] Martin, C.D. and Chandler, N.A. 1993. Stress heterogeneity and geological structures. *Int. J. Rock Mech. Min. Sci. & Geomech. Abstr.* 30, 993-999.

[4] Brace, W.F., Paulding, B. and Scholz, C. 1966. Dilatancy in the fracture of crystalline rocks. *J. of Geophys. Res.* 71, 3939-3953.

[5] Lajtai, E.Z. 1998. Microscopic Fracture Process in a Granite. *Rock Mechanics and Rock Engineering.* 31, 237-250.

[6] Lockner, D.A., Moore, D.E. and Reches, Z.e.1992. Microcrack interaction leading to shear fracture. In *Proc. 34th U.S. Symp. on Rock mechanics, Santa Fe. Tillerson, J. R., Wawersik, W. R. editors. Balkema, Rotterdam*, pp. 807-816.

[7] Diederichs, M.S. 2003. Rock fracture and collapse under low confinement conditions. *Rock Mechanics and Rock Engineering.* Vol. 36 (5), 339-381.

[8] Hoek, E. and Brown, E.T. 1998. Practical estimates of Rock Mass Strength. *Int. J. Rock Mech. Min. Sci.*, 34(8), 1165-1186.

[9] Itasca Consulting Group., *PFC2D(Particle Flow Code in 2 Dimensions) version 3.1.* 2004: Minneapolis, Minnesota.

[10] Hazzard, J.F., Young, R.P. and Maxwell, S.C. 2000. Micromechanical modeling of

cracking and failure in brittle rocks. *J. of Geophys. Res.* 105(B7), 16683-97.

[11] Martin, C.D., Read, R.S. and Martino, J.B. 1997. Observations of brittle failure around a circular test tunnel. *Int. J. Rock Mech. Min. Sci.* 34, 1065-1073.

[12] Jensen, R.P., Bosscher, P.J., Plesha, M.E. and Edil, T.B. 1999. DEM Simulation of Granular Media - Structure Interface : Effects of Surface Roughness and Particle Shape. *Int. Jou. for Num. and Anal. Meth. in Geomech.*, 23, 531-547.

[13] Thomas, P.A. and Bray, J.D. 1999. Capturing Nonspherical Shape of Granular Media with Disk Clusters. *J. of Geot. and Geoenvi. Eng.* 125, 169-178.

[14] Guo, Y. and Morgen, J.K. 2004. Influence of normal stress and grain shape on granular friction: Results of discrete element simulations. *J. of Geophys. Res.-SOLID EARTH.* B12, Art. No. B12305.

[15] Lajtai, E.Z. 1969. Strength of discontinuous rocks in direct shear. *G'eotechnique.* 19, 218-233.

[16] Hallbauer, D.K., Wagner, H. and Cook, N.G.W. 1973. Some observations concerning the microscopic and mechanical behaviour of quartzite specimens in stiff, triaxial compression tests. *Int. J. Rock Mech. Min. Sci. & Geomech. Abstr.* 10, 713-726.

[17] Martin, C.D. 1997. Seventeenth Canadian Geotechnical Colloquium: The effect of cohesion loss and stress path on brittle rock strength. *Canadian Geotechnical Journal.* 34, 698-725.

[18] Tapponnier, P. and Brace, W.F. 1976. Development of stress-induced microcracks in Westerly granite. *Int. J. Rock Mech. Min. Sci. & Geomech. Abstr.* 13, 103-112.

[19] Scholz, C.H. 1968. Microfracturing and the inelastic deformation of rock in compression. *J. of Geophys. Res.* 73, 1417-1432.

[20] Holcomb, D.J. and Martin, R.J.1985. Determining peak stress history using acoustic emissions. In *proc. 26th U.S. Symposium on Rock Mechanics, Rapid City,* vol.1, E. Ashworth editor, Balkema, Rotterdam. pp. 715-722.

[21] Pestman, B.J. and Munster, J.G.V. 1996. An acoustic emission study of damage development and stress-memory effects in sandstone. *Int. J. Rock Mech. Min. Sci. & Geomech. Abstr.* 33, 585-593.

CHAPTER 5

[2] DEVELOPMENT OF A SHEAR ZONE IN BRITTLE ROCK SUBJECTED TO DIRECT SHEAR

5.1 INTRODUCTION

Most rocks and soils when deformed in shear form a narrow shear band. Detailed characterization of this band by Riedel[1] and Cloos[2] using simple-shear experiments on clay-cakes showed that the shear zone is made up of series of discrete fractures forming at various angles to the direction of shearing. These fractures are today generally referred to as the *R* and *R'* Riedel shears (Figure 5.1 (a)). Skempton[3] using detailed field mapping of shear zones in clays, siltstones, and sandstones concluded that at large deformation the Riedel shears are linked by the principal displacement fracture, i.e., the major plane of movement. Tchalenko[4] found in clay experiments that the fracture characteristics of the shear zones was similar at all scales.

---

[2] This chapter is submitted to the Int. J. of Rock Mech. and Min. Sciences on Feb. 22. 2007

There is also evidence that these characteristics are found in a wide variety of natural materials, e.g., Ahlgren[5] documented Riedel fractures in porous sandstones and Ortlepp[6] encountered similar features in a mining-induced shear zone in intact brittle quartzite in a deep South African gold mines.

b shows a tectonic shear zone in brittle diorite in southern Sweden. The diorite has a uniaxial compressive strength of 212 MPa and by comparing Figure 5.1 (b) with the results from the Tchalenko there is little doubt that there are similarities between the features observed in clay experiments and in the tectonic shear zone in brittle diorite.

Based on the observations from simple shear tests on clay Skempton[3] suggested that several distinct stages of shear zone development could be observed. The first stage was the development of the Riedel shears forming at an angle of $\phi/2$ (i.e. ϕ is internal friction angle of a material) to the axis of shearing (Figure 5.1 (a)).

Morgenstern and Tschalenko[7] and Tschalenko[4] using results from direct shear tests on clay also noted that the *R* fractures formed first with *R'* fractures developing later at an angle $90^{o}-\phi/2$. Skempton[3] showed that the principal displacement fracture was the last to form, linking the R fractures and that the final appearance of the shear zone was a function of the amount of displacement which often resulted in an undulating principle displacement fractures.

While Figure 5.1 (b) shows that there are similarities between the tectonic shear zone in brittle rock to Skempton[3]'s general description for the latter stages of shear zone development, the progressive development of the Riedel fractures within a shear zone in brittle materials is not well understood, i.e., it is not clear if the first fractures that form in brittle

materials are Riedel shear fractures or possibly extension fractures, i.e., formed by tensile stresses.

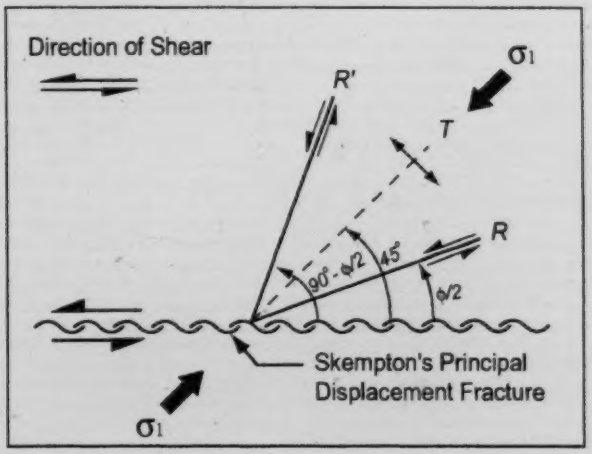

(a)

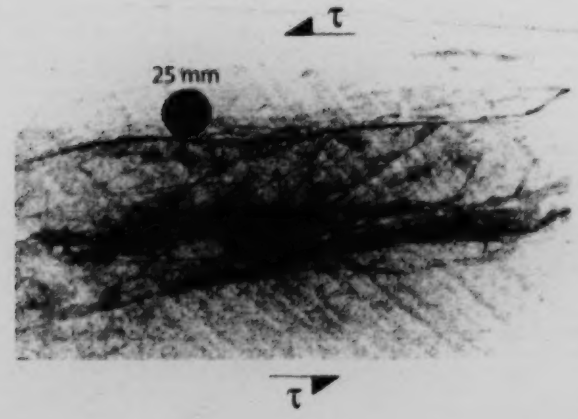

(b)

Figure 5.1 : (a) The discrete Riedel shear fractures (R, and R') observed in the clay experiments and Skempton's[3] principal displacement fracture connecting the Riedel shears modified from Barlett et al.[8]. The T fractures are thought to be tension-induced fractures. (b) Tectonic shear zone in Diorite, Uniaxial compressive strength 212MPa. It shows a natural shear zone observed in a brittle hard rock in southern Sweden.

There is ample evidence that many of the small scale fractures observed in brittle rocks subjected to deviatoric loading are extensional in origin(Diederichs[9], Lajtai[10], Stacey[11], Nye[12]). Nye[12] also suggested that the formations of crevasses in glaciers resulted from shear-induced extensile fractures and these fractures form an en echelon pattern aligned with maximum principal stress within the glacier. Lajtai[13] demonstrated using conventional shear box testing of weak synthetic rock that when the applied normal load is very low, extensile fractures dominate the failure process but that at high normal loads shear fractures were mainly observed. Kutter[14] using numerical analysis of direct shear test for brittle material showed that zones of tensile stresses developed on the edges of the shear box, as well as along the central area where final failure surfaces eventually developed. Vallejo[15] also concluded from direct shear testing of stiff clays that all the fractures, including the Riedel and principle displacement fractures, resulted from the development of tensile stresses resulting from stress rotation. More recently Cresswell and Barton[16] suggested based on shear box testing of slightly cemented iron oxide sand that inclined tensile fractures initiated before reaching the peak shear stress. Hence, while it is clear that the progressive shearing of brittle materials involves the initiation and coalescence of fractures it is not clear if the origin of these fractures is shear or tension. In this paper, the progressive failure process of a brittle synthetic rock in direct shear using laboratory tests and discrete element modeling is examined. In particular, discrete element modelling is used to evaluate the origin of the fractures from initiation through development of the principal rupture surface.

5.2 DIRECT SHEAR BOX TEST ON SOLID SYNTHETIC ROCK SAMPLE

5.2.1 Synthetic Rock Sample

The synthetic rock material used in this study is "sulfaset", a commercial product generally used for grouting anchor bolts. The synthetic rock has brittle characteristics but a much lower compressive strength and reaches almost 80% of its full strength within a few hours of being cast. The strength and stiffness of the synthetic rock is highly dependent on its initial moisture content at mixing, and for the tests reported here the initial moisture content was fixed at 50% and the cast specimens were cured in a moisture room for 3 days at a constant temperature (Cho et al.[17]). To induce random heterogeneity in the sample, 10% by weight of sand was added to all the samples. The compressive and tensile strength were measured from conventional uniaxial and Brazilian tests. Its failure envelope was obtained using triaxial compression test using a Hoek's cell. The measured properties are presented in Table 5.1. Sand was added to the sulfaset to simulate material heterogeneity at the grain scale.

Table 5.1 : Strength and deformation properties of brittle synthetic rock, data from Cho et al.[17].

σ_c (MPa)	σ_t (MPa)	E (GPa)	ν	c (MPa)	ϕ (Deg)	S	m_b
11.6 ± 1.0	2.6 ± 0.3	2.5 ± 0.3	0.31	2.95	35.1	1	5.07

Where, σ_c : Uniaxial Compressive Strength, σ_t : Brazilian tensile Strength, E : Young's modulus, ν : Poisson's ratio, c : Cohesion, ϕ : Friction angle, s, m_b : Hoek-Brown material constants

5.2.2 Direct Shear Box Test

All direct shear test samples were cast in a 50mm cubic mold to fit the shear box. The normal load was directly applied to the top of the sample via weights. The machine incorporated a load cell (44.5kN capacity) and LVDT (both shear and normal direction) to measure the shear force and displacements. The data measured were recorded using a data logger linked to a computer using a 10s capture interval.

To induce a uniform distribution of sand in each sample a new mixture was prepared for every cubic mold and cured under the same conditions (Cho et al.[17]). A total of 11 samples were tested with the normal stress ranging from 1.0kPa to 2.1MPa.

The shear stress and horizontal displacement measured are illustrated in Figure 5.2 and show that the samples have a significant brittle behavior. The initial non-linearity for some of the stress-displacement curves in Figure 5.2 is attributed to the initial seating owing to the closure of existing pores created during sample preparation. These pores were also observed in uniaxial and triaxial test carried out on this material (Cho et al.[17]).

The normal displacement, i.e., dilation, recorded during shearing for each test is shown in Figure 5.3 and illustrates that the maximum dilation occurs after peak shear resistance was achieved. Similar findings were reported by Cresswell and Barton[16].

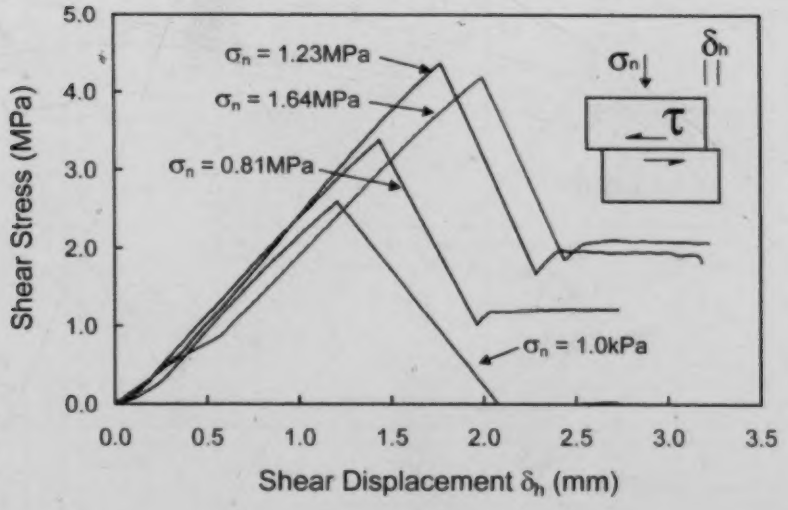

Figure 5.2 : Shear stress and displacement for each normal stress applied on synthetic rock

The dilation at peak shear stress versus normal stress plot is shown in Figure 5.4. The results clearly show that increasing normal stress reduces the dilation and also illustrates that approximately at normal stress 1.5MPa, dilation eliminated. Under the highest normal stresses the sample shows a slight negative dilation, i.e., "contraction". It is assumed that this arises from collapsing of pores in the sample during shearing however, no clear evidence of this was found.

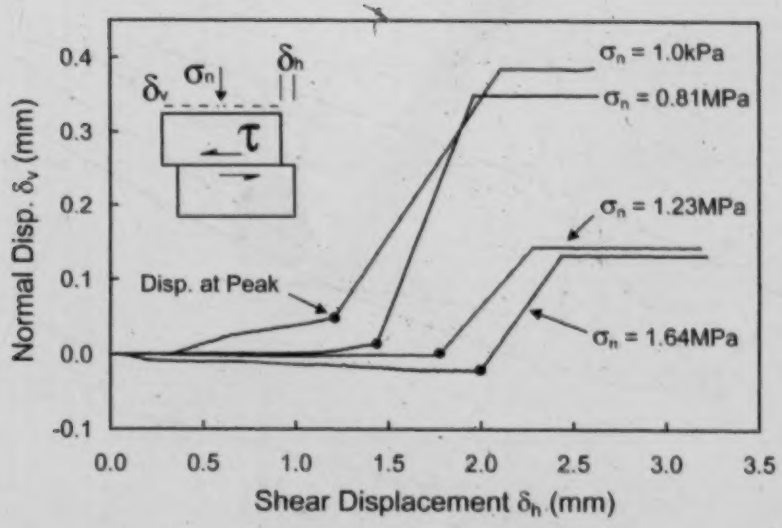

Figure 5.3 : Dilation features by the variation of normal stress in shear box test on synthetic rock

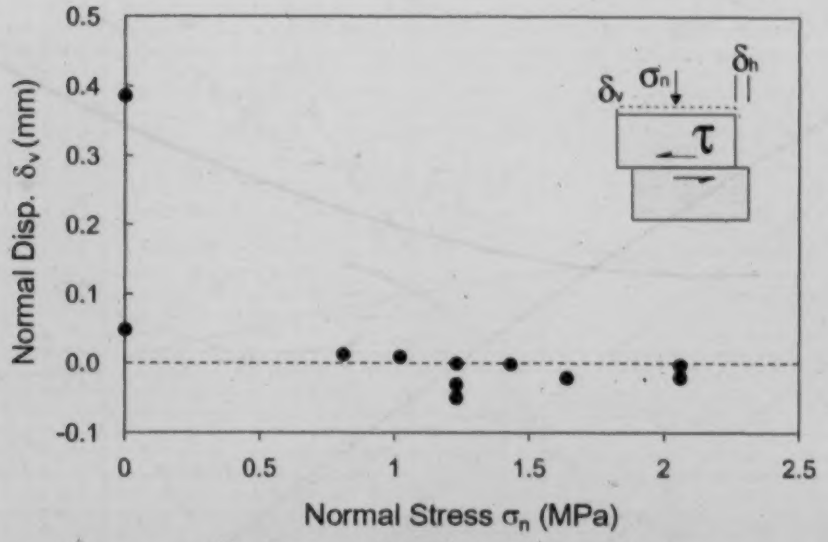

Figure 5.4 : Normal (vertical) displacement (dilation) at peak shear stress and normal stress relationship. Dilation decreases as normal stress increases and become less than zero as normal stress is greater than approximately 1.5MPa.

The peak shear strength results obtained from the direct shear tests are shown in Figure 5.5 in τ-σ_n stress space. Using linear regression ($R^2 = 0.894$), the frictional angle of the synthetic rock material is approximately 39 degrees with a cohesion intercept of 2.8MPa. The cohesive strength of 2.8MPa is approximately equal to the Brazilian tensile strength of 2.6MPa given in Table 1. This is in keeping with the findings of Lajtai[13] who demonstrated that for intact brittle material under low normal stress conditions, the shear strength could be expressed as :

$$\tau = \sqrt{\sigma_t(\sigma_t - \sigma_n)} \qquad (5.1)$$

where, σ_t = tensile strength, σ_n = normal stress. Equation. (5.1) implies that the shear strength at zero normal stress, i.e., the cohesion intercept, is equal to the tensile strength of the material.

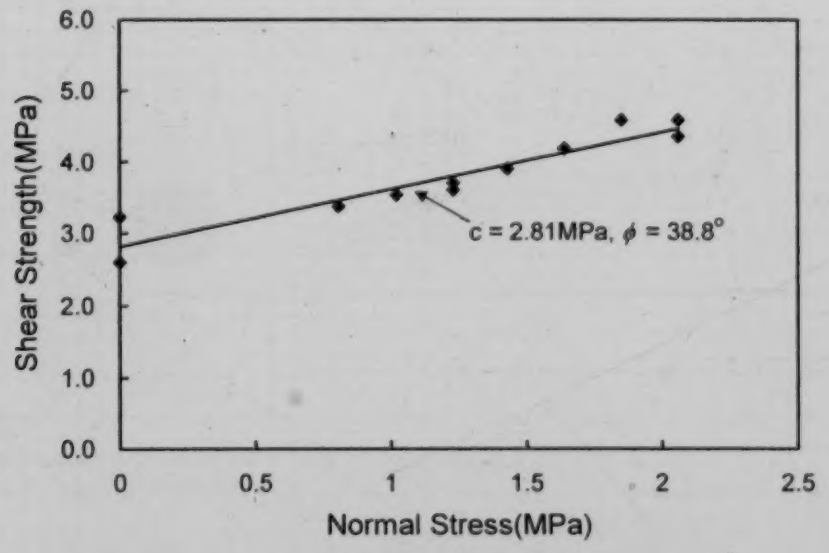

Figure 5.5 : Peak shear strength envelope obtained from direct shear test. Note that cohesion of this sample is closer to the Brazilian tensile strength.

5.3 DISCRETE ELEMENT MODELLING

5.3.1 Bonded Particle Model

Discrete element (particle) modelling is now often used to simulate the behaviour of rock (Potyondy and Cudall[18]). The method is attractive because it does not require the formulation of complex constitutive models (Cundall[19]). However, Diederichs[9] showed that the discrete element method that utilized circular particles could not accurately simulate the nonlinear failure behaviour of intact material. Cho et al.[17] used a clump bonded particle model to overcome the short comings identified by Diederichs[9]. The clumped bonded particle model was developed for the commercially available discrete element code, i.e., Particle Flow Code (PFC^{2D}) and is briefly described later.

The discrete element code (Particle Flow Code) represents a rock mass as an assemblage of bonded rigid particles. In the two dimensional version (PFC^{2D}), circular disks are connected with cohesive and frictional bonds and confined using planar walls. PFC^{2D} is based on the Discrete Element Method (DEM) developed by Cundall[20] and Cundall and Stack[21], which has been used extensively to model jointed rock masses. PFC models the forces and motions of individual particles within an assembly. Hence the particles can move independently from one another and interact only at their contacts. The particles are assumed to be rigid but can overlap at the contacts when under compression (Potyondy and Cundall[18]). Thus the particles themselves never deform as they can only undergo rigid body motion.

The particles in PFC are bonded together by specifying the shear and tensile bond strength at each contact point. The values assigned to these strengths influence the macro strength of the sample and the nature of cracking and failure that occurs during loading. Friction is activated by specifying the coefficient of friction, and is mobilized as long as particles stay in contact. Tensile cracks occur when the applied normal stress in exceeds the specified normal bond strength. Shear cracks are generated as the applied shear stress exceeds the specified shear bond strength either by rotation or by shearing of particles. The tensile strength at the contact immediately drops to zero after the bond breaks while the shear strength decreases to the residual friction value as shown in Figure 5.6. The residual shear strength depends on the coefficient of friction specified and the induced normal contact force. After a bond breaks, stress is redistributed and this may then cause adjacent bonds to break leading to localized progressive failure. For all theses microscopic behaviours, PFC does not require a plastic flow rule to govern its behaviour. It only requires selection of the basic micro parameters to describe contact and bond stiffness, bond strength and the contact friction but these micro parameters should provide the macro-scale behaviour of the material being modeled. PFC uses an explicit finite difference scheme to solve the equation of force and motion and hence one can readily track initiation and propagation of bond breakage (fracture formation) through the system (Potyondy and Cundall[18]). In addition, the user can also track the failure process at each contact and determine if the dominant mode of failure is either tensile or shear.

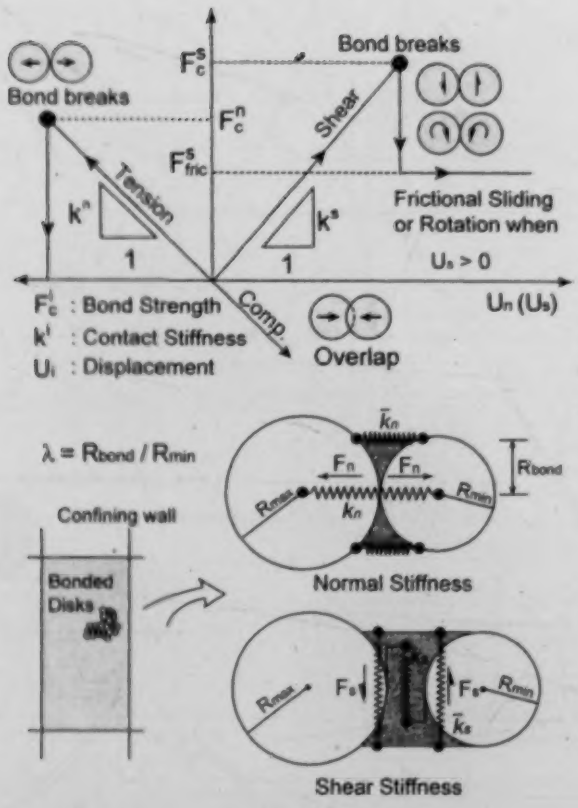

Figure 5.6 : Micro parameters and the illustration of yielding process for micro bonding. Force and displacement logic and micro parameters at particle contact and bond in PFC modified from Potyondy and Cundall[18]. The micro normal stiffness is contributed by both contact normal stiffness (k_n) and bond normal stiffness ($\bar{k}_n$). The micro shear stiffness is composed of contact shear stiffness (k_s) and bond shear stiffness ($\bar{k}_s$). The normal and shear bond strength are specified all at the bonded area determined by minimum particle radius and bond radius ratio (λ). As this bond is broken by tension, bond strength immediately drops to zero and PFC regard this process as tension crack. While shear crack is recorded when bond is broken by shearing or the moment load by particle rotation and once bond is broken then micro strength immediately drops to residual value depending on the applied normal force on the particle and the coefficient of friction. Meanwhile, the particle displacement by compression is reflected by the particle overlap.

5.3.2 Micro parameters for synthetic rock

Although *PFC* has very simple relationships to describe particle motion, it is not always easy to choose the most appropriate micro parameters to ensure that the behaviour of the model material resembles the actual behaviour of the material being tested. Because the micro parameters of the real physical material are not known directly from laboratory tests, calibrating *PFC* requires an iterative procedure (Potyondy and Cundall[18]). Cho et al.[17] calibrated the micro parameters for the *PFC* model of synthetic rock to the laboratory behaviour of the test material used for this research using biaxial and Brazilian *PFC* simulations. They found that a clumped assembly of PFC particles was required to provide the best match to the laboratory properties. In their clumped assembly, circular particles were grouped using infinite internal bond strength such that the multi-particle clump acts as a single particle. This approach allowed matching of the complete laboratory strength envelope from tensile to triaxial strength as well as the stress-strain behaviour for different confining stresses (Cho et al.[17]). Because the same synthetic rock was used for the direct shear test described in this paper, identical micro properties reported by Cho et al.[17] were also used to model these direct shear tests. Clumps that simulate irregular particle shapes can be generated using a stamp logic introduced by Cho et al.[17]. Using this logic, the clump was created by stamping a circled area, corresponding to desired grain size, over the discs. The particles within this stamped area were then clumped to represent a grain. The grain size in PFC does not necessarily represent the physical grain size but represents a methodology to introduce grain-scale induce heterogeneity. The size of each clump was determined by specifying the radius of the stamp

circle along with a standard deviation. Figure 5.7 illustrates the stamping logic used to create the clump.

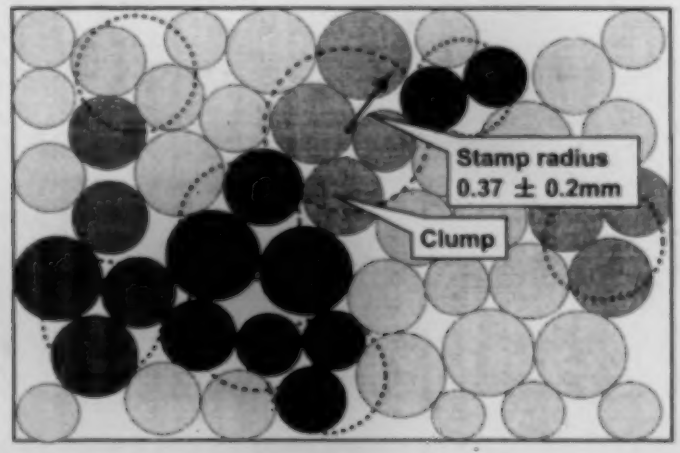

Figure 5.7 : Grain shape and size control of clump using stamping logic. Particles are clumped provided their center is within the specified circle making up the clump stamp.

The micro-parameters calibrated in PFC using this logic for synthetic rock are tabulated in Table 5.2 and taken from Cho et al.[17].

Figure 5.8 shows the stress-strain comparison for a uniaixial and triaxial test result with results from PFC using the parameters in Table 5.2. The laboratory results are in reasonable agreement for both the confined and unconfined case. Despite this agreement between the measured and modeled post peak response it is important to remember that there is no flow rule specified in PFC.

Figure 5.9 gives the strength envelope for the synthetic material and the predicted PFC strength envelope using the micro-parameters in Table 5.2. Note the excellent agreement

between the peak, uniaxial, triaxial and tensile laboratory strength and the PFC model results. In the next section, properties developed from uniaxial, triaxial and Brazilian tests are used to simulate direct shear tests.

Table 5.2 : Micro parameters used for sample calibration in PFC modeling.

R_{min}	0.25mm	E_c	1.4GPa
R_{max}/R_{min}	1.5	k_n/k_s	2.5
$\overline{\lambda}$	1.0	$\overline{E_c}$	1.4GPa
μ	0.75	$\overline{k_n}/\overline{k_s}$	2.5
$\overline{\sigma_n}$	6.8 ± 1.7MPa	*clp_rad*	0.37 ± 0.2mm
$\overline{\sigma_s}/\overline{\sigma_n}$	1.0	Unit_weight	1830kg/m^3

Where,

R_{min}	: Minimum particle radius	R_{max}/R_{min}	: Particle radius ratio
$\overline{\lambda}$	: Bond radius ratio	μ	: Coefficient of friction
$\overline{\sigma_c}$	: Normal Bond strength	$\overline{\sigma_s}/\overline{\sigma_n}$	: Bond strength ratio (shear to normal)
E_c	: Contact young's modulus	$\overline{E_c}$	: Bond young's modulus
k_n/k_s	: Contact stiffness ratio	$\overline{k_n}/\overline{k_s}$	: Bond stiffness ratio
clp_rad	: Clump radius		

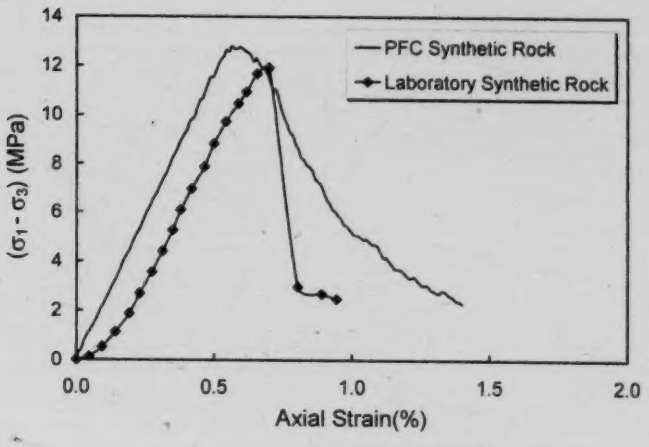

(a)

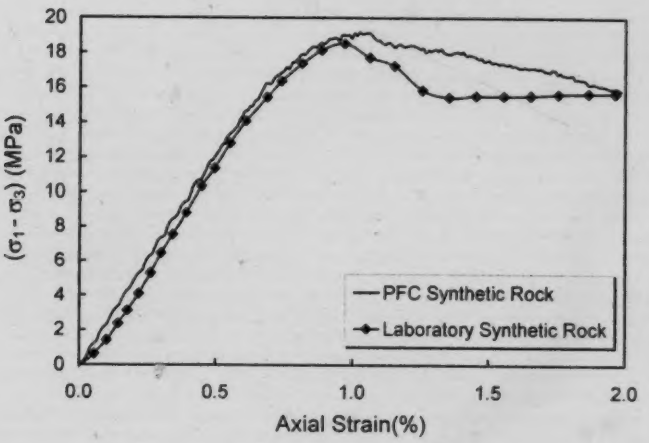

(b)

Figure 5.8 : Calibrated results in stress and strain behavior for PFC synthetic rock (a) σ_3 = 0.0MPa, (b) σ_3 = 3.0MPa.

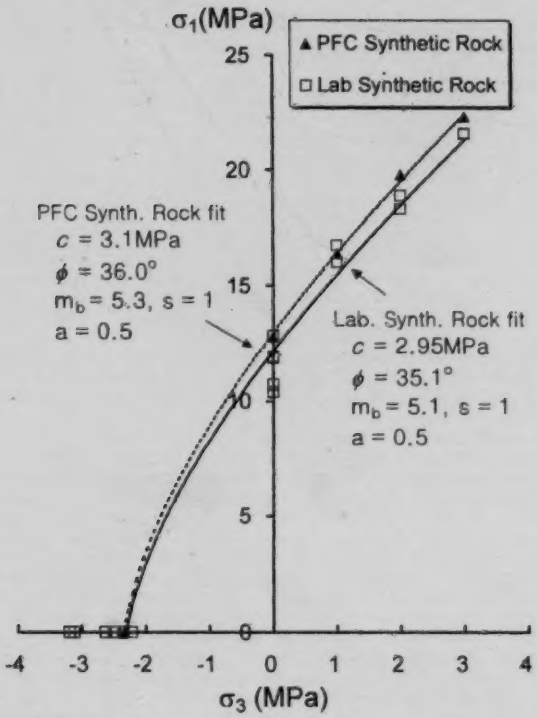

Figure 5.9 : Calibrated failure locus for PFC synthetic rock compared to the laboratory measured.

5.3.3 Direct shear discrete element modeling

The direct shear laboratory tests for the synthetic rock were numerically simulated by creating a shear box model in PFC (Figure 5.10). The PFC specimen has the same cross sectional dimensions (50.8mm x 50.8mm) as the synthetic rock sample used in the laboratory test. However, the out of plane dimension in the PFC^{2D} model is of unit thickness. A total of 7000 disks with a minimum radius of 0.25 mm were used to make up the shear box specimen and then clump particles were created using the previously described stamp logic to account for the particle shape effect.

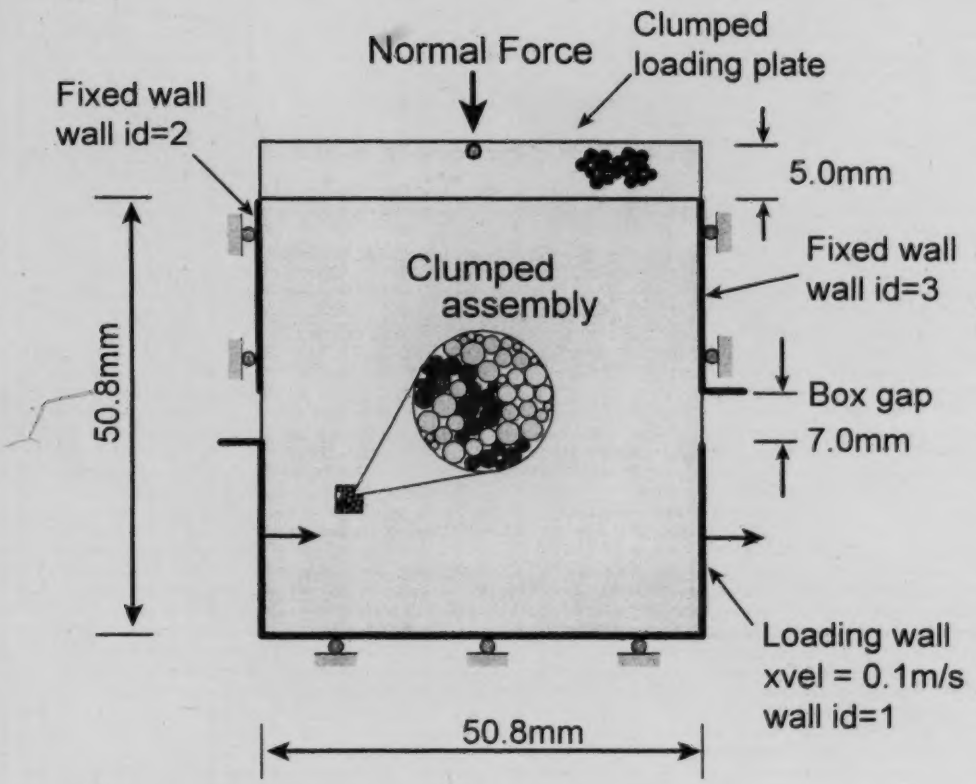

Figure 5.10 : Illustration of direct shear test simulation scheme in PFC.

For the modeling of the upper shear box, two separate walls were installed on both left and right sides while lower shear box was modelled as single 'U' type segment wall element. A 7 mm gap existed between upper and lower halves of the laboratory shear box and the same gap was applied between upper and lower shear box wall element. The upper half of the shear box was fixed while the lower half was allowed to move. To insure the uniform normal stress application, 5.0 mm thickness of plate is modeled with 1000 disks. Particles composing this plate are then all incorporated into one clump, so the plate itself can move like a rigid body transferring the boundary normal load to the sample.

Shear loading was applied to the sample by moving the lower half of the shear box while the upper half of the shear box wall velocities were fixed to zero, so no upper wall displacement could occur (Figure 5.10). The loading rate for shearing was set to "0.1 m/s", slow enough to ensure the sample remains in quasi-static equilibrium throughout the test. One may view this loading rate (i. e., a velocity applied on the loading wall) as a significantly fast loading rate if applied to laboratory tests. In PFC modeling however, since the calculation logic in PFC is governed by Newton's second law, the time step (Δt) in each calculation cycle is chosen to be infinitely small value (e.g. 10^{-7} sec) especially for a static analysis. In other words, the loading rate 0.1m/s used in this paper can be translated to approximately 1.5×10^{-5}mm/step which implies it requires more than 60,000 steps for moving a loading plate 1mm. Hence, while physically 0.1m/s of loading rate is unreasonably high, this rate is small enough in PFC simulation to minimize dynamic effects. It was found that during the study the loading rate had no effect on peak stress below 0.1m/s.

Constant normal stress was applied during the simulation by applying a normal force directly on the ball located at the top center of the clumped loading platen. Horizontal displacement was measured by tracing the horizontal wall displacement of lower shear box (wall 1, Figure 5.10). Shear stress was calculated by taking the average reaction forces on wall 3 in Figure 5.10 divided by the area of the shear surface (sample width times the unit sample thickness). An internal 10mm diameter measurement circle installed at the center of the sample was used to average the stresses at the centre of the sample as shown in Figure 5.11. The stress measurement in PFC was incorporated with such measurement

circle. The particle stresses whose centroid is within the circle are calculated by summating the contact forces for particle volume and then, summation of particle stresses within the region are averaged by the measurement circle volume. Using this measurement circle, principal stresses and their orientation could be traced during the simulation.

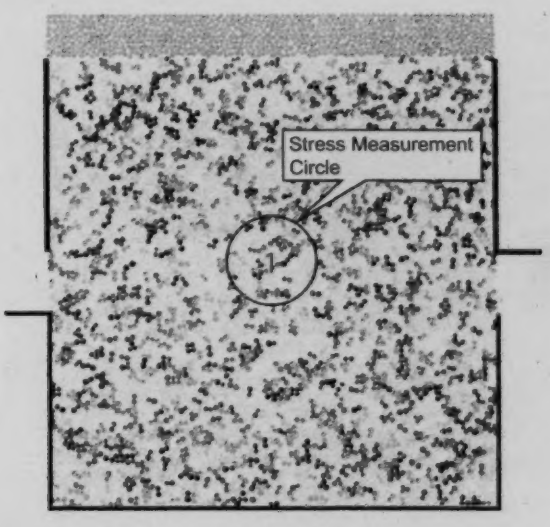

Figure 5.11 : Stress measurement circle installed in the simulated model

5.4 RESULTS AND INTERPRETATION

5.4.1 Strength envelope

Using the direct shear model configuration described in the previous section and the micro parameters outlined in Table 5.2, discrete element samples were used to simulate direct shear tests with different normal stresses. Figure 5.12 presents a comparison of the peak shear strength envelope obtained from the PFC modeling with the peak shear strength obtained from the laboratory direct shear tests.

In essence this is a blind prediction because the micro-parameters for PFC were developed from calibration with uniaxial, triaxial and Brazilian tests (see section 5.3.2). While both the cohesion intercept (3.0MPa) and friction angle (41.5 degree) obtained from the PFC envelope is slightly higher than the laboratory shear strength data (Figure 5.12), for both envelopes the data points were all within acceptable error ranges expected for laboratory tests.

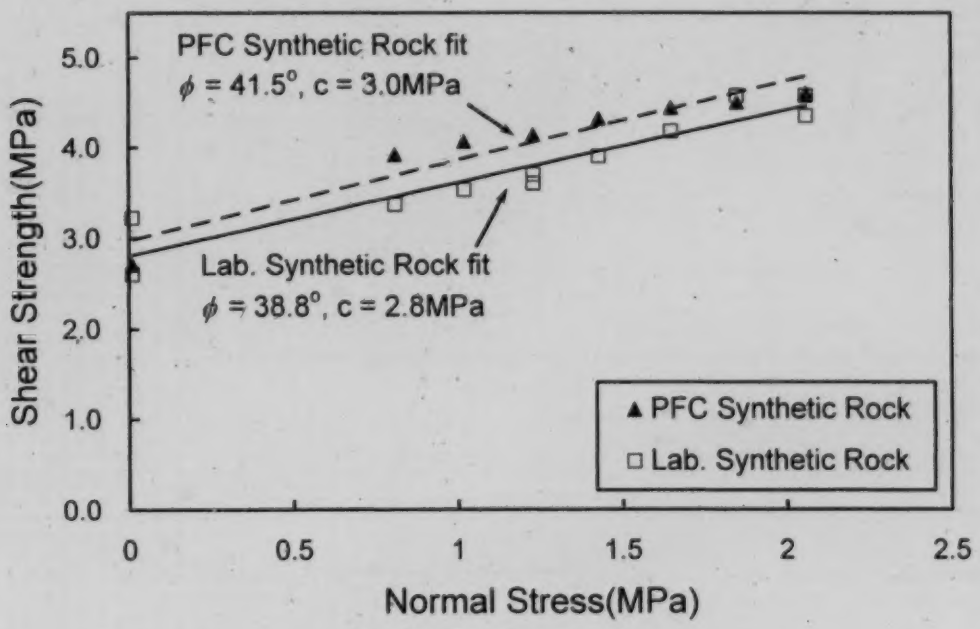

Figure 5.12 : Comparison of the shear strength envelope for the laboratory direct shear test on brittle synthetic rock with the discrete element (PFC) simulation.

5.4.2 Stress and velocity vector distribution

The contact force distribution in the PFC sample subjected to 1.2 MPa normal stress and before the peak shear strength was reached for a sample is shown in Figure 5.13 (a). It is clear from Figure 5.13 (a) that the contact forces in the sample are not uniformly distributed as the sample approaches the peak strength. For example, large force concentration occurs near the centre of both the upper and lower edges of the shear box walls. Note that in the centre of the sample, the contact forces are inclined at approximately 30 to 40 degrees to the direction of shearing. The shape of this force distribution is similar to the photoelastic image reported by Allersma[22] for the stress distribution in a direct shear test using random shaped granular glass particles (Figure 5.13 (b)).

Figure 5.14 (a) shows the particle velocity vectors as the sample is subjected to the direct shear loading with 1.0kPa normal stress. Also shown in Figure 5.14 (b) is the typical velocity vectors observed in a Brazilian tensile test simulation using the same micro parameters as the direct shear tests. The velocity vectors of the particles in a given PFC assembly illustrate how particles are moving as they are subjected to the external loading conditions. Despite the unique differences in stress paths between direct shear test and Brazilian test the velocity vectors show similar trends and in all cases the fractures display an opening phenomenon, characteristic of mode I fractures, i.e., the fracture mechanics terminology for fractures subjected to tensile loading.

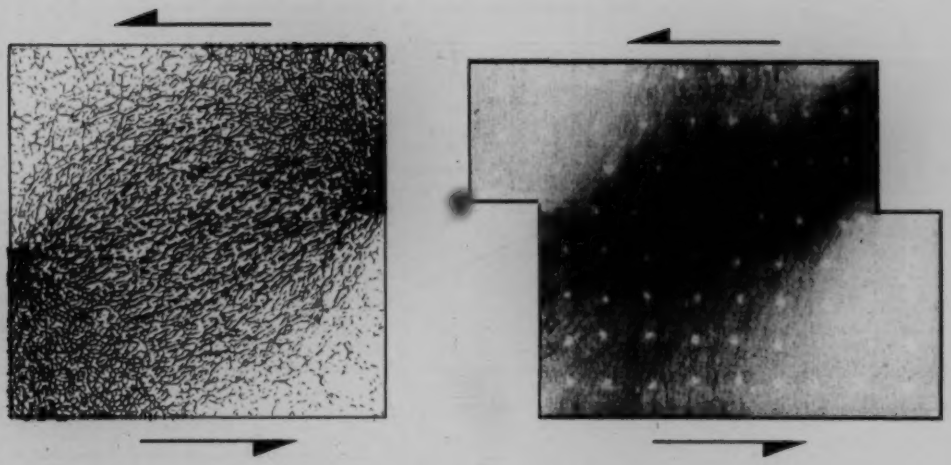

(a)Contact force distribution (b) Photoelastic image

Figure 5.13 : Comparison of the contact force distribution in PFC simulated model (a) with a photoelastic image (b) of direct shear test using randomly crushed granular glasses modified from Allersma[22]. Note that the similar orientation of the contact force distribution in the centre of both examples.

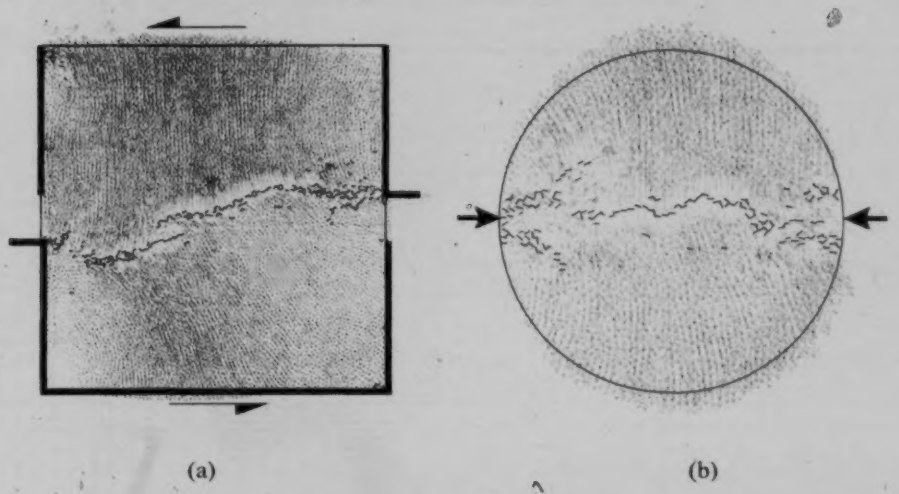

(a) (b)

Figure 5.14 : Velocity vectors during fracture development for different loading conditions. Note that the direction of velocity vectors in the direct shear tests resembles the Mode I fracture in the Brazilian test simulation. (a) σ_n = 1.0kPa, (b) Brazilian test simulation.

5.4.3 Local stress path

Using the measurement circle described in Section 5.3.3, the stress path for the direct shear test can be tracked and expressed in the σ_1 - σ_3 space. Figure 5.15 (a) shows the local stress path for the low (1kPa) and high normal stress (1.85MPa) samples. For the sample with the low normal stress, the center of the sample is subjected entirely to extension loading up to the peak strength, i.e. σ_1 is positive while σ_3 is negative. These are the same stress conditions required for the Brazilian test and hence it is not surprising that the velocity vectors for the Brazilian test and direct shear test in Figure 5.14 show such similarities.

While the stress path for the high normal stress initially starts shearing in all round compression, it also develops an extension stress state as the peak shear stress is reached. It is only after the rupture surface forms that the extension stress state returns to one of compression. From these stress paths it is clear that dilation, being a function of confinement, is suppressed in the post peak region for the high normal stress sample compared to the low normal stress sample. It is also interesting to note that the peak strength for both samples is reached when the minimum principal stress is between -0.7 and -1MPa. These data points agree reasonably well with the failure envelope given in Figure 5.9 and supports the notion that the failure envelop in the tensile region should be nonlinear.

Figure 5.15 (b) shows the development of the fracture surface in the centre of the sample for the two stress paths shown in Figure 5.15 (a). For the low normal stress sample the rupture surface develops as an approximate single surface.

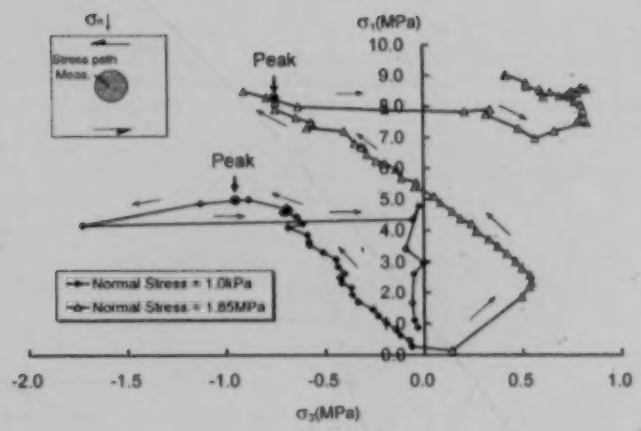

(a)

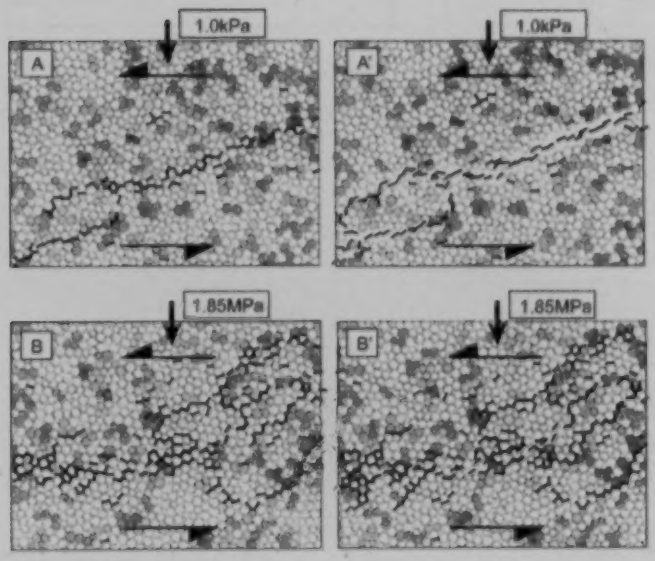

(b)

Figure 5.15 : (a) Stress path measurement at the center of PFC simulated sample. Average stresses within the circled area were traced during the simulation using the measurement circle installed in the same region. The points marked by big arrow indicate the points that correspond to the peak shear stress. (b) The fracture patterns were captured at the same stress measurement region. Note that high dilation occurs along the fracture surface due to shearing resulting in zero confinement under low normal stress condition while such dilation is significantly suppressed under high normal stress condition.

Whereas the rupture surface for the high normal stress is more complex and develops into a shear zone. It is suggested that the more complex shear zone results from the non-uniform distribution of tensile stresses in the sample as the fracture surface forms under the higher normal stress, i.e., confinement. In other words the fracture surface develops in the localized regions of tensile stresses and these are not uniformly connected or distributed.

5.4.4 Shear zone development in clay experiments

Based on Coulomb theory and observations, Skempton[3], Tchalenko[4] and Morgenstern and Tchalenko[7] described the fracture morphology that formed in the shear zone in clays when subjected to shear. According to these researchers the fracture development can be described in the following four stages, schematically shown in Figure 5.16. Before and at the peak shear stress (Stage A in Figure 5.16), en echelon Riedel shears form inclined at $\phi/2$ to the direction of shearing, where ϕ is the internal friction angle of clay. After the peak shear stress, (Stage B in Figure 5.16) as shear deformation increases, these Riedel shears extend. Before the shear stress approaches the residual strength (Stage C in Figure 5.16) these Riedel shears become kinetically impossible and a new type of fracture called Thrust shears (often called "P shear" since the material affected by this fracture is in a passive Rankine state) develop which is approximately symmetrical to the Riedel shears but in the opposite direction. As the shear stress approaches the residual strength (Stage D in Figure 5.16) the Riedel shears and P shears coalesce and further displacement forms the principal shear plane (PSP) defined by Skempton[3]. These stages are collectively called a shear band and while there is no doubt that the boundary condi-

tions create shear stresses, Vallejo[15] argued that the fracture morphology in these stiff clay experiments did not result from shear stresses but from tensile stresses.

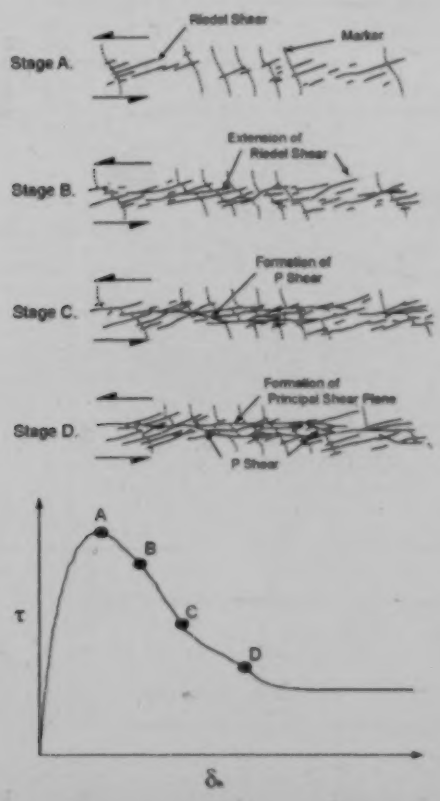

Figure 5.16 : Fracture patterns developed at each stage of stress strain curve on overconsolidated clay modified from Tchalenco[4]. (A) At peak shear strength, the first shears, Riedel shears appear with almost 12° to the horizontal. (B) Some Riedel shears are extended and a few Ridel shears are generated with about 8° to the horizontal. (C) New shears named "P shears" appear with an inclination of –10°. (D) Principal displacement surface is formed.

5.4.5 Shear zone development in brittle synthetic rock

Using the discrete element numerical simulations, it was possible to investigate the fracture pattern that occurred at various stages of loading and for various normal stresses.

The fractures occurring in the discrete element sample by either tension or shear are identified by measuring the forces mobilized in the bonds between the particles. If the mobilized shear forces in the bonds exceeds the specified micro shear bond strength, then bond breakage is counted as a shear crack while if the mobilized tensile forces in the bond exceeds the specified micro normal bond strength then bond breakage is counted as tension cracks. Using this approach it was possible to evaluate the number of shear or tensile cracks at each stage of the test.

Figure 5.17 and Figure 5.18 illustrate the fracture patterns recorded at each stage in the loading of the discrete element simulation for 1.0kPa and 1.8MPa normal stress, respectively. In each case the conditions at approximately the four stages of fracture development described in the clay experiments were recorded. Those results in Figure 5.17 and Figure 5.18 are also called Stages A, B, C and D and are described below. At each stage of the simulation the particle crack orientation and the number of shear and tension induced particle cracks were determined. However, it should be noted that a crack orientation is for the crack between two particles and not for clusters that may make up a single fracture. For this reason, clustered fractures were sketched for determining specific fracture patterns at each stage using CAD software. Orientation of these sketched fractures was plotted as rose diagrams.

The 0 degree axis in the Rose diagram is aligned to the horizontal axis in the direct shear simulation and all angles are measured counter-clockwise from the horizontal axis. The mean orientations of the sketched fractures plotted on the rose diagram were classified into three distinct fracture sets.

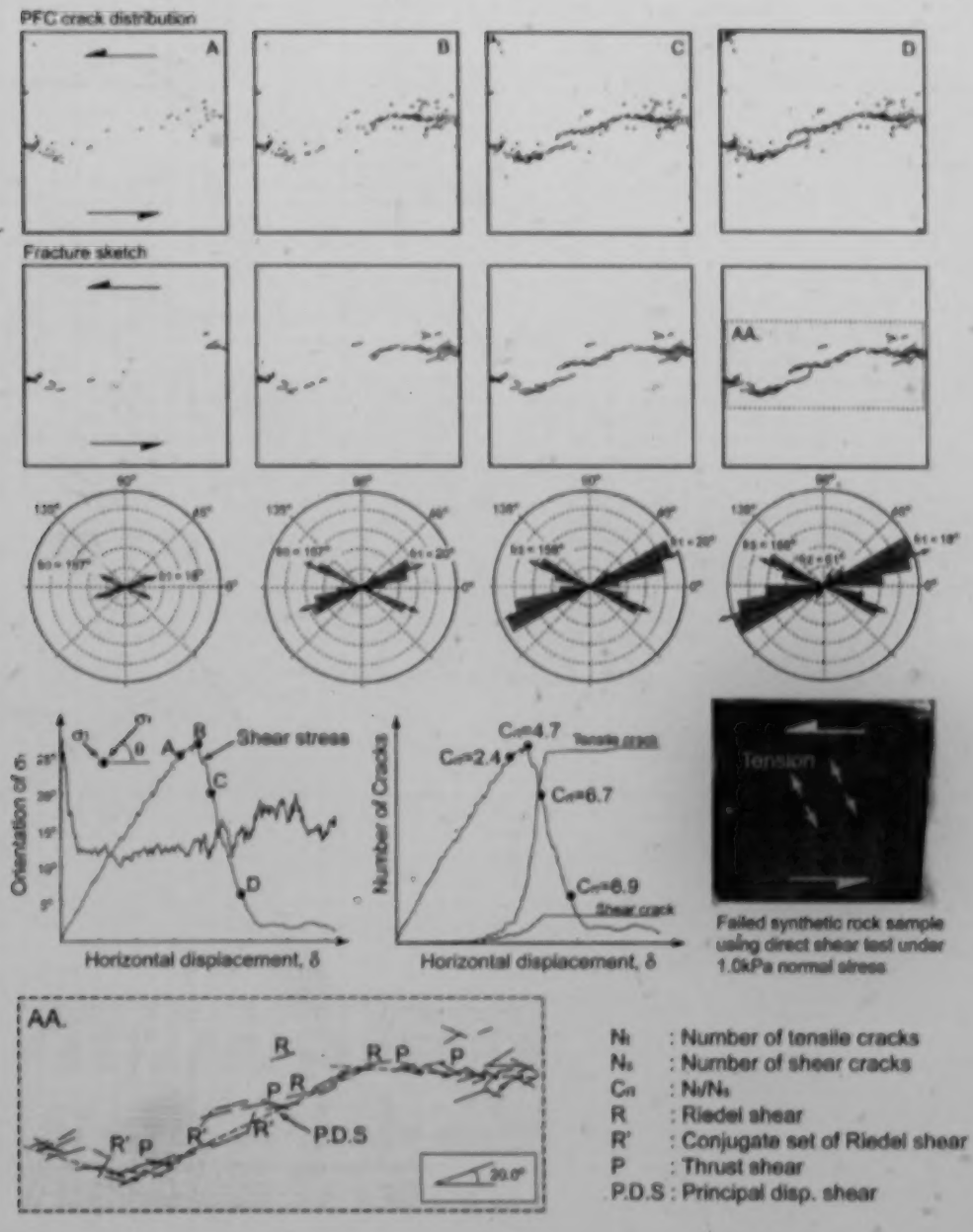

Figure 5.17 : Development of fracture for the 1.0kPa normal stress test on PFC synthetic rock.

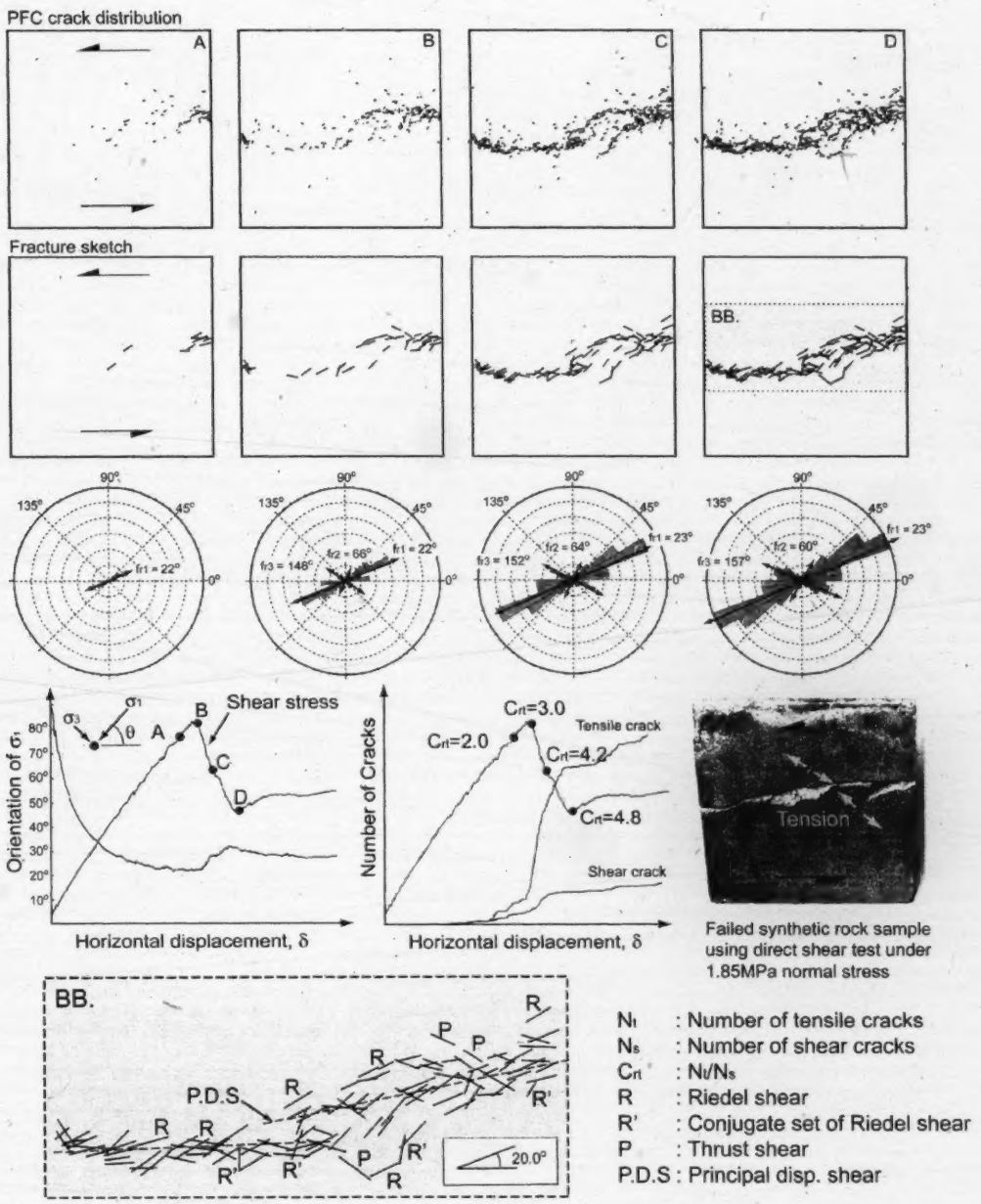

Figure 5.18 : Development of fracture for the 1.85MPa normal stress test on PFC synthetic rock.

The first fracture set (f_{r1}) was taken from 0 to 45 degree, the second fracture set (f_{r2}) was taken from 45 to 90 degree and the third fracture set (f_{r3}) was taken from 90 to 180 degree. The orientation of these fracture set can be compared with the conventional shear fracture set (i.e. R, R', P type shear) composing shear band in clay experiment. The rotation of maximum principal stress direction was also tracked in the centre of the sample and shown in Figure 5.17 and Figure 5.18. A photograph of the actual direct shear test after the shear surface has formed is also shown on the Figure 5.17 and Figure 5.18 for comparison.

STAGE A

Before the peak shear stress is reached only minor fracturing is observed in both low and high normal stress cases and these fractures were mainly concentrated near the edge of the shear box. While the fracturing was minor in both cases, mean fracture sets were identified. In the 1.0kPa test case, two distinct fracture sets f_{r1} and f_{r3} were identified with a mean orientation of 18 and 156 degree, respectively while only f_{r1} was identified in 1.85MPa test with the mean orientation of 22 degree. Interestingly, these angles are very similar to the R (=20 degree) and P (= 159 degree) type shear in clay experiment.

STAGE B

As the shear stress reaches the peak strength fractures form from the edge to near the center region of the sample. New fracture set f_{r2} and f_{r3} developed in the 1.85MPa normal

stress test. While the number of these new fracture sets is minor, the mean angle of these new fracture sets (f_{r2} = 66 degree and f_{r3} = 146 degree) is also similar to R' (=69 degree) and P shears. However, despite the similarity in orientation to R, R' and P type shear fractures, these fracture sets are mostly composed of cracks that have formed in tension. The crack ratio shown in Figure 5.17 and Figure 5.18 clearly reveal that tension cracks are considerably greater in number than shear cracks. Such differences are even more significant as shear deformation increases.

STAGE C AND D

As the shear displacement increased distinct inclined en echelon type fractures developed in both 1.0kPa and 1.85MPa test. The direction of these fractures varied from 20 to 22 degrees for both cases which is similar to the Riedel shears that also developed en echelon pattern in this early stage of deformation.. The appearance of P type fractures also increased in both tests as the principal displacement plane developed. In the low normal stress simulation the entire principal displacement plane appeared to be made up of a series of long and short en-echelon fractures with the long fractures aligned to the maximum principal stress direction. Note that in the low normal stress simulation the shear zone was relatively narrow while in the 1.8MPa normal stress simulation the zone is relatively thick. This was also observed in the laboratory tests. While the number of fractures making up set f_{r2} was relatively small, these R' type fractures were only observed in the latter stages of the test as the residual shear stress was approached.

The comparison of orientation of the maximum principal stress and the mean fracture orientation at each stage of the discrete element simulations with the predicted fracture angle using Skempton[3]'s relationships developed from the clay experiments is shown in Table 5.3. In all cases there is reasonable agreement between Skempton[3]'s predicted angles and the measured fracture angels in the discrete element simulations. In the 1.85MPa normal stress test, there is also good agreement between the orientation of the first main fracture (f_{r1}) and maximum principal stress direction suggesting extension loading was responsible for creating the first fractures. This notion is also supported by the crack ratio which showed that the dominate mode of progressive failure in the shear zone development was micro-scale tensile fracturing despite the macro-scale shear and normal stress boundary conditions. In the low normal stress test it appears that low confinement of the sample caused some of the discrepancy between the fracture and stress orientations. Nonetheless, the crack ratio also indicated that the dominate mode of fracturing was tensile.

Table 5.3 : Orientation of fracture sets and maximum principal stress axis.

Stage	Mean orientations (σ_n = 1.0kPa)				Mean orientations (σ_n = 1.85MPa)				Skempton(1967)[3]
	σ_{1r}	f_{1r}	f_{2r}	f_{3r}	σ_{1r}	f_{1r}	f_{2r}	f_{3r}	
A	12°	18°	-	157°	24°	22°	-	-	ϕ = 41.5° (PFC synth. rock)
B	14°	20°	-	157°	23°	22°	66°	146°	R = ϕ/2= 21°
C	14°	20°	-	158°	29°	23°	64°	152°	R'=90°-ϕ/2= 69°
D	14°	18°	61°	158°	30°	23°	60°	157°	P=180°-ϕ/2= 159°

σ_{1r} : Orientation of maximum principal stress measured counterclockwise from horizontal.

5.5 CONCLUSION

A series of direct shear laboratory tests were carried out using a synthetic brittle rock. These tests were then modelled using a discrete element program with a clumped logic for gluing the elements. Parameters for the discrete element simulations were obtained from calibration with Brazilian, uniaxial compression and triaxial compression tests. The numerical simulations gave excellent agreement with the direct shear laboratory test results, despite the different stress path used in the direct shear tests compared to the stress path used to establish the modelling parameters.

The discrete element simulations were used to investigate the progressive development of the shear zone at various normal stresses. In all cases examined the dominant mode of fracturing, regardless of the stage of shearing, is tension. However, the ratio of tensile to shear cracks is much lower in the early stages of shearing. Prior to the peak strength the ratio of tensile to shear cracks is approximately 2.0 and 2.4 for the 1.85 MPa and low normal stress, respectively. After the peak shear resistance is reached this ratio increased to between 4.7 and 3.0, for the 1.0kPa and 1.85MPa normal stress respectively. This is counter intuitive because at residual strength it is generally assumed that all fracturing is related to shear fracturing.

The fracture patterns observed in the numerical simulations at various stages of shearing showed similar fracture patterns to those that have been reported in direct shear and simple shear clay experiments. The laboratory tests on synthetic rock also showed similar fracture patterns to those observed in the numerical simulations. While it was possible to

identify the major fracture patterns that have been reported in the literature R, R', P and PDS, the numerical simulations showed that all of these fractures result from the formation of micro-scale tensile fracture. The progressive nature of the direct shear test leads to a stress rotation that also influences the development of the fracture pattern. This is particularly noticeable at low normal stress.

The results from this work highlight the importance of tensile fracturing in the development of a shear zone at low normal stresses. In many rock slopes stresses are relatively low and in such conditions the importance of tensile fracturing in evaluating the slope's stability may be underestimated.

5.6 REFERENCES

[1] Riedel, W. 1929. Zur Mechanik geologischer Brucherscheinungen. *Centralbl. f. Mineral. Geol. u. pal.* v. 1929 B:354-368.

[2] Cloos, E. 1955. Experimental Analysis of Fracture Patterns. *Bull. of Geol. Soc.of America.* 66:241-256.

[3] Skempton, A. W. 1967. Some Observations on Tectonic Shear Zones. *In: Proceedings of the First International Congress on Rock Mechanics, Lisbon.* v1:pp. 329 - 335.

[4] Tchalenko, J. S. 1970. Similarities between Shear Zones of Different Magnitudes. *Geol. Soc. of American Bull.* 81:1625-1640.

[5] Ahlgren, S. G. 2001. The nucleation and evolution of Riedel Shear zones as deformation bands in porous sandstone. *J. of Structural geology.* 23:1203-1214.

[6] Ortlepp, W. D. 2000. Observation of mining-induced faults in an intact rock mass at depth. *Int. J. Rock Mech. Min. Sci.* 37:423-436.

[7] Morgenstern, N. R., Tchalenko, J. S. 1967. Microstructural Observations on Shear Zones from Slips in Natural Clays. *In: Proceedings of Geotechnical Conference on Shear strength of Natural Soils and Rocks, Oslo, Norwegian Geotechnical Institute.* v1:pp. 147-152.

[8] Bartlett, W. L., Friedman, M., Logan, J. M. 1981. Experimental folding and faulting of rocks under confinfing pressure. Part IX. Wrench faults in limestone layers. *Tectonophysics.* 79:255-277.

[9] Diederichs, M. S. 2000. Instability of Hard Rock Masses : The Role of Tensile Damage and Relaxation. Ph.D. thesis. Dept. of Civil Eng., University of Waterloo. 567pp.

[10] Lajtai, E. Z. 1998. Microscopic Fracture Process in a Granite. *Rock Mechanics and Rock Engineering.* 31:237-250.

[11] Stacey, T. R. 1981. A Simple Extension Strain Criterion fro Fracture of Brittle Rock. *Int. J. Rock Mech. Min. Sci. & Geomech. Abstr.* 18:469-474.

[12] Nye, J. F. 1952. The mechanics of glacier flow. *J. of Glaciology.* 12:82-93.

[13] Lajtai, E. Z. 1969. Strength of discontinuous rocks in direct shear. *G'eotechnique.* 19:218-233.

[14] Kutter, H. K. 1971. Stress distribution in direct shear test samples. *In: Proceedings of the Symposium of the International Society of Rock Mechanics.* 1:Paper No. II6-1 - II6-12.

[15] Vallejo, L. E. 1982. Development of a shear zone structure in stiff clays. *4th International conference on numerical methods in geomechanics, Eisenstein, Z. editor*, pp. 255-262.

[16] Cresswell, A. W., Barton, M. E. 2003. Direct Shear Tests on an Uncemented, and a Very Slightly Cemented, Locked Sand. *Quarterly J. of Eng. Geol. and Hydrogeol.* 36:119-132.

[17] Cho, N., Martin, C. D., Sego, D. C. 2007. A clumped particle model for rock. *Int. J. Rock Mech. Min. Sci.* 44:997-1010.

[18] Potyondy, D. O., Cundall, P. A. 2004. A bonded-particle model for rock. *Int. J. Rock. Mech. Min. Sci.* 41:1329-1364.

[19] Cundall, P. A. 2000. A Discontinuous Future for Numerical Modelling in Geomechanics. *Geotech. Eng.* 149:41-47.

[20] Cundall, P. A. 1978. BALL-A program to model granular media using the distinct element method. . Technical Note: Dames and Moore Advanced Technology Group, London.

[21] Cundall, P. A., Strack, O. D. L. 1979. A discrete numerical model for granular assemblies. *G'eotechnique.* 29:47-65.

[22] Allersma, H. G. B. 2005. Optical analysis of stress and strain in shear zones. *Powders and Grains, Garcia-Rojo, Herrmann, McNamara editors.* Taylor & Francis Group, London, pp. 187-191.

CHAPTER 6

[3]DILATION AND SPALLING IN AXIALLY COMPRESSED BEAMS SUBJECTED TO BENDING

6.1 INTRODUCTION

The pioneering work by Fairhurst and Cook[1] showed that axial splitting, i.e., slabbing (generally referred to as spalling), is a common phenomena observed in both laboratory testing and around overstressed underground openings(Figure 6.1). As noted by Fairhurst and Cook[1] spalling in laboratory compression tests is promoted by the insertion of 'friction reducers' between the platens and the samples. However, around underground openings these friction reducers are absent; yet spalling is commonly observed when the tangential stresses on the boundary of the excavation exceed the rock mass spalling strength. In-situ experiments in crystalline rock at AECL's Underground Research Laboratory and SKB's Äspö Hard Rock Laboratory have shown that the in-situ rock mass spalling strength was approximately 50% of the laboratory uniaxial compressive strength in both

[3] This chapter is the article for submission to Rock Mechanics and Rock Engineering

massive unfractured granite and heterogeneous fractured diorite (Martin[2]; Andersson[3]). This reduction in the in-situ strength when compared to the laboratory uniaxial compressive strength has been attributed to various factors related to the excavation-induced stress path and the rotation of these stresses under low confinement near the tunnel wall (Eberhardt[4], Diederichs et al.[5]).

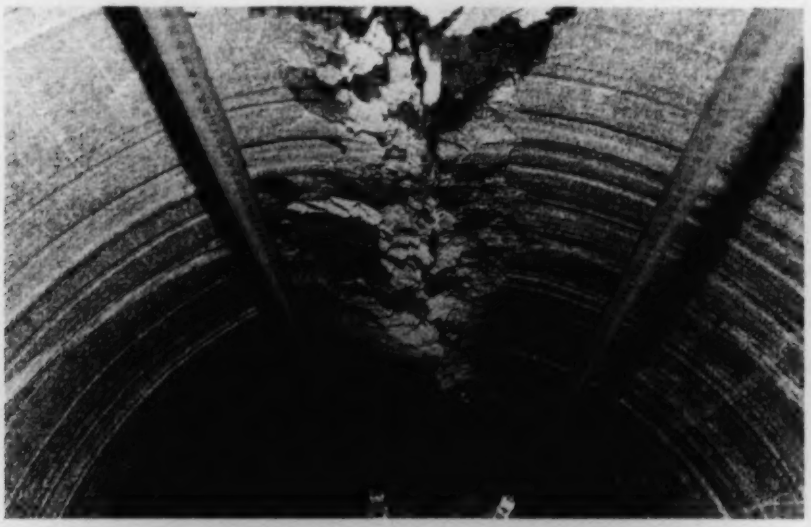

Figure 6.1 : Spalling observed in a 600-mm-diameter borehole in massive unfractured granite.

The work by Brace et al.[6] showed, using laboratory compression tests, that many rocks start to dilate at stress levels that ranged between 40% and 60% of the laboratory uniaxial compressive strength. It is now generally recognised that this dilatancy is caused by the growth of small axial cracks aligned with the direction of maximum compression, (see e.g., Lajtai[7], Tapponnier and Brace[8], Martin and Chandler[9]). Hence, as shown by Martin[2] and more recently by Andersson[3] the in-situ spalling strength is in close agreement with the onset of dilation measured in laboratory uniaxial compression tests.

The strength reduction reported by Andersson[3] and Martin[2] was observed around circular openings, however, similar strength reductions have been reported for other shaped openings in other rock types, e.g., rectangular, horse-shoe, (Martin et al.[10]). There is little doubt that the spalling rock mass strength is considerably less than the measured laboratory uniaxial compressive strength for many rocks. However, it is not clear if the agreement between the rock mass spalling strength and the onset of dilation in laboratory compression tests is fortuitous, as spalling is not observed at the onset of dilation in laboratory compression tests. To resolve this issue laboratory tests are needed that clearly capture spalling and its characteristics.

Hoek[11] experimentally explored fracturing around a circular opening using thin plates containing a hole and subjected to uniaxial and biaxial loading conditions. Since then other experimental approaches to simulate fracturing around boreholes or tunnel excavation have been explored e.g., Gay[12], Santarelli and Brown[13], Ewy and Cook[14], Haimson and Song[15], Lee and Haimson[16], Dzik[17], Sellers and Klerck[18]). Many of these laboratory tests have been restricted to small scale circular holes, ranging in diameter from 6 to 110-mm. However, as noted by Martin et al[19] there is a significant strength scale-effect observed when the diameter of these holes is less than 75-mm.

In this paper laboratory testing of rectangular beams is used to investigate the onset of dilation and spalling. Beams loaded axially in compression combined with bending provide a stress path that results in non-uniform stresses similar to those expected around an underground excavation. In addition, these tests remove the strength scale dependency

found for circular holes. Simulation of the tests was conducted using a discrete element method to investigate the progressive nature of the spalling process as the loads on the beam are applied.

6.2 EXPERIMENTAL SETUP

As schematically illustrated in Figure 6.2, the overstressed zone around an underground opening is normally subjected to both non-uniformly distributed compressive (tangential) stresses and potentially moment loading induced by formation of fractures parallel to the direction of tangential loading. Generating such stress conditions requires boundary conditions that cannot be obtained using conventional compressive laboratory test.

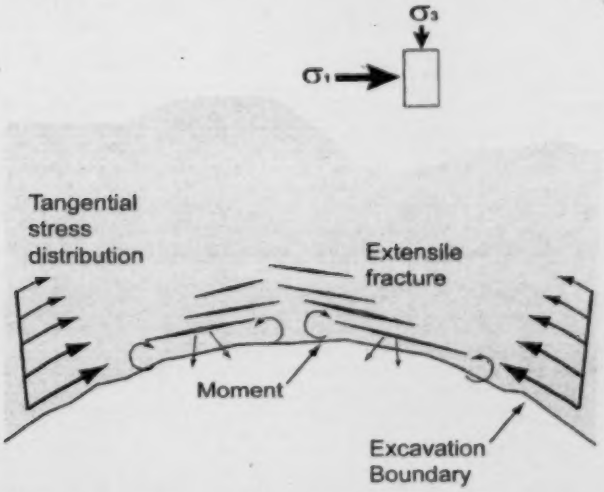

Figure 6.2 : Illustration of the non-uniformly distributed tangential stress near the boundary underground.

Pre-stressed concrete beams are frequently used structural elements due to its unique advantage of resisting tension when subjected to bending. An axially stressed beam when

subjected to bending produces non-uniformly distributed compressive stresses as illustrated in Figure 6.3. In conventional beam bending tests such as three-point or four-point bending, compression occurs at the upper section of the beam while tension occurs at the bottom. By superposing an axial stress to the bending stress the entire beam is kept in compression (Figure 6.3).

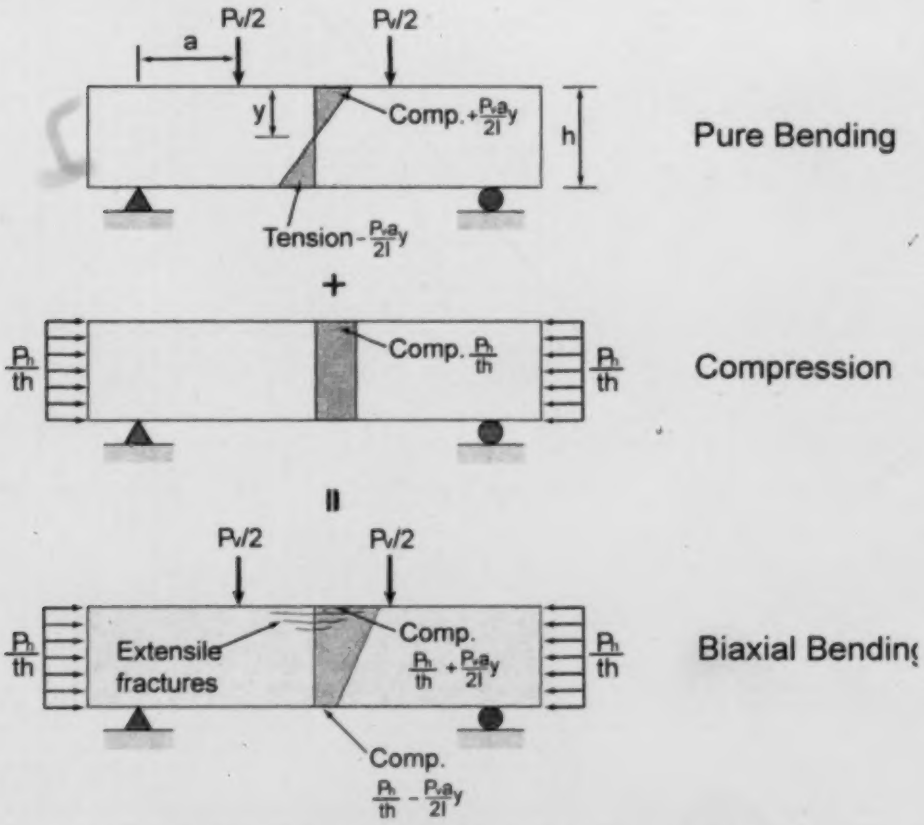

Figure 6.3 : Illustration of the combined boundary loading conditions that were used to generate the non-uniform compressive stress conditions.

To ensure reasonably uniform testing specimens a synthetic weak rock was used to create the beams. While extension fracturing around underground openings is generally associated with hard brittle rock such as granite, extension fracturing has also been reported in

weak many other rock types including claystones (Martin and Lanyon[20]). The detailed test scheme and characteristics of synthetic weak rock used in this study are presented in the next section.

6.2.1 Synthetic Rock

The synthetic weak rock used in this study was created from "sulfaset" which is generally used for setting anchor bolts. The chosen synthetic rock has brittle characteristics but a lower compressive strength that reaches approximately 80% of its maximum strength within a few hours after molding. The strength and stiffness of the synthetic rock is highly dependent on its initial moisture content at mixing, and for the tests reported here the initial moisture content was fixed at 50% and cured for 3 days in a constant temperature and moisture room. To induce random heterogeneity in the sample, 10% concrete sand by mass was added to all the samples.

Uniaxial compressive strength and tensile strength were measured from conventional uniaxial compression (55mm x 110mm cylinder sample) and Brazilian test. Shear strength parameters were obtained from triaxial compression test using Hoek's cell. The measured properties are given in Table 6.1. Though sand is added for material heterogeneity, relatively homogeneous properties were obtained.

Table 6.1 : Material properties of Sulfaset synthetic rock.

σ_c (MPa)	σ_t (MPa)	E (GPa)	c (MPa)	ϕ (MPa)	s	m_b
11.6 ± 1.0	2.6 ± 0.3	2.5± 0.5	. 2.95	35.1	1	5.07

Where, σ_c : Uniaxial Compressive Strength, σ_t : Brazilian tensile Strength, E : Young's modulus, c : Cohesion, ϕ : Friction angle, s, m_b : H-B material constants

Figure 6.4 show the failure envelope for the Synthetic rock and the fitted non-linear Hoek-Brown failure envelope.

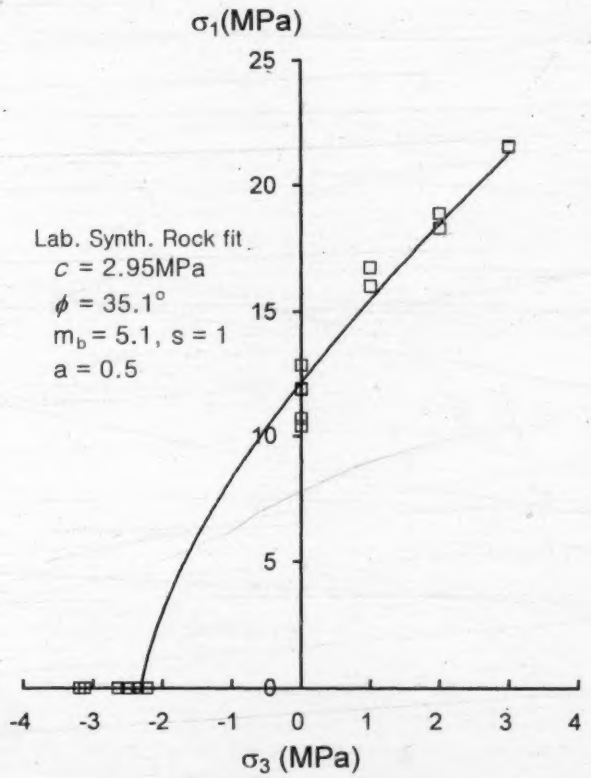

Figure 6.4: Failure envelope of the synthetic rock. The strength parameters were estimated using RocLab ver. 1.0, RocScience Inc.[21].

6.2.2 Axially compressed beam bending system

The test beam prism specimen was molded to 88.9mm in height, 114.3mm in thickness and 406.4mm in length. To provide the uniform curing condition the specimens were molded in specially devised thick walled steel mould (1cm thick), tightly bolted plates covered all sample faces until the sample set (i.e. about 20 minutes). This allowed the sample to set without being exposed to air. The mould was then removed and cured in

similar conditions as the sample used for uniaxial and triaxial testing. For the verification of beam strength, cores were taken from the molded beam and the uniaxial strength measured was compared with that from samples cast for strength tests. Figure 6.5 shows the axial stress versus axial strain for a cored sample compared with the cylindrical cast sample. No significant difference in strength was observed, however the core sample showed slightly different stress-strain response possibly related to surface damage during the coring procedure.

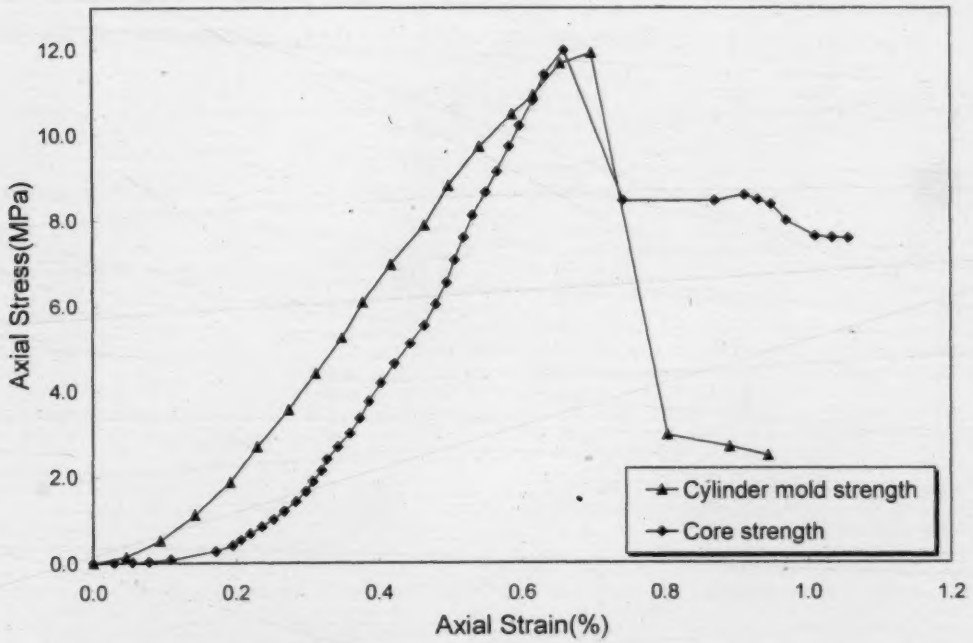

Figure 6.5 : Verification of the beam strength from the core strength compared with cylinder mould strength in Uniaxial compressive test.

Hydraulic rams were used for the application of axial load and bending load. Because the tensile stress in the bottom region of the sample needed to be suppressed, a load ratio (i.e. bending force to axial force) was determined to maintain the sample in compression

throughout the test. The load ratio determined for keeping the sample in compression was 1:3 (i.e. 1 bending force to 3 axial force). This ratio was maintained during the test by choosing appropriate diameters for the hydraulic rams. The load controls were activated by controlling the pressure via a syringe pump. The pump pressure rate was kept constant during the test at 50kPa/min which was slow enough not to induce excessive energy into specimen by the loading system. The applied pressure was recorded to the computer data logger via a transducer in 10s capture interval.

The axial load frame consisted of 25mm steel plate connected with six 30-mm-diameter steel rods. The frame supporting the vertical ram was provided by 10-mm-thick U-sections beam. To minimize the bending moment and eccentricity of the axial load ball bearings were installed between all loading plates. For the initial seating, a pump pressure of 70kPa that corresponds to 0.03MPa stress at the top fiber in the beam was applied. The specimen was then loaded until failure using this system. Based on the observations reported by Martin et al.[22] the onset of extension fracturing around a circular test tunnel was always associated with a notch tip. To simulate this notch a stress concentrator which consisted of a 5-mm-deep 1-mm wide was installed at the top center of the beam specimen using a saw. The laboratory test setup illustrated above is shown in Figure 6.6

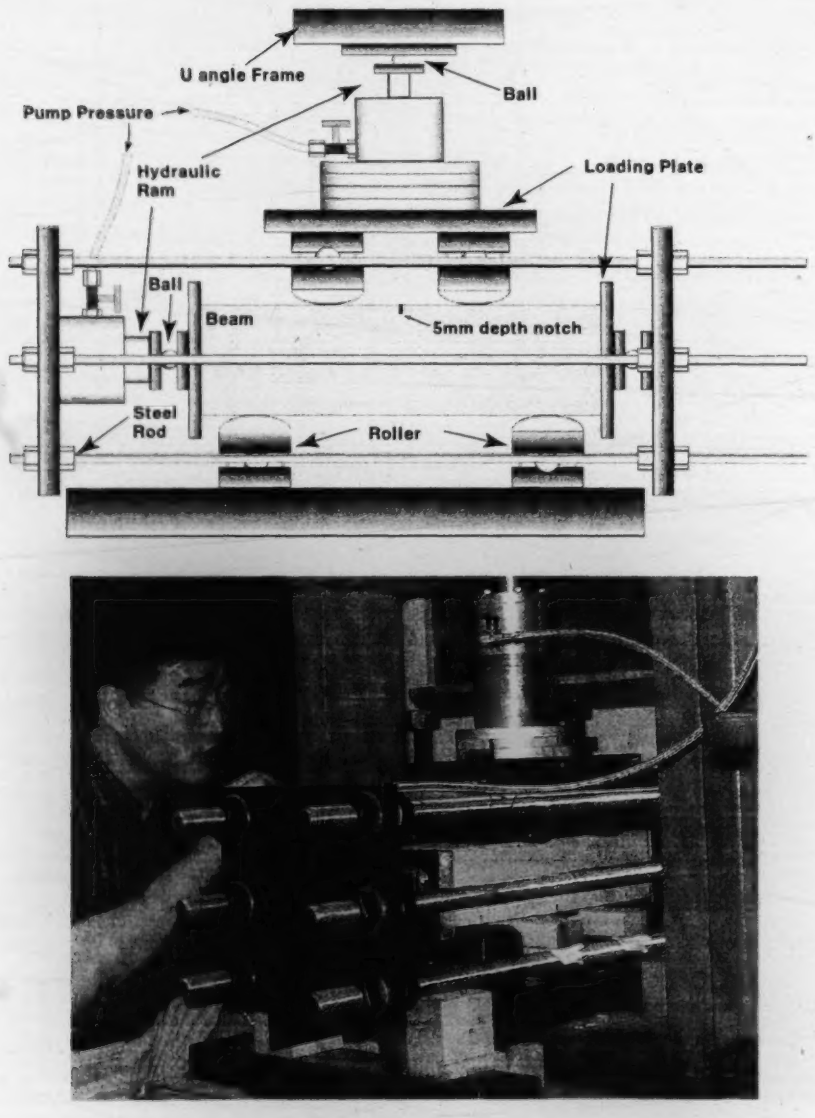

Figure 6.6 : Axially compressed bending test system setup.

6.3 TEST RESULTS

Stress applied at the top center of the beam was calculated by combining axial stress and the well-known beam flexure formula(Hibbeler[23]):

$$\sigma_f = k\left(\frac{P_a}{A} \pm \frac{M}{I} y\right) \qquad (6.1)$$

Where, σ_f =compressive stress, P_a= axial force, A =cross section area of beam, M=bending moment, I=moment of inertia, y=centroid of the cross section, k=stress concentration factor.

The stress concentration factor k depends on the curvature of the notch tip and specimen dimension (Lipson and Juvinall[24]) thus it is difficult to estimate analytically. Figure 6.7 shows the distribution of the elastic stress concentration factor estimated using a two dimensional finite element code Phase2D[25]. Based on the numerical results shown in Figure 6.7, the stress concentration factor k was estimated is 3.3.

Figure 6.8 shows the relationship between the displacements measured at the top and bottom of the beam and the stresses near the notch tip calculated using Equation 6.1 and the estimated k value. Because the k value in Figure 6.7 was estimated using elastic analysis it is only applicable for the elastic response and the actual stresses at the notch once localized yielding initiates is unknown. However from Figure 6.8 the linear portion of the stress-displacement plot appears to end at a stress of approximately 12MPa, which is

similar to the uniaxial compressive strength of the synthetic rock shown in Table 6.1. Whether this is fortuitous or is not known, as it should be noted that this represents the maximum stress measured at the notch tip and not the average stress in the region of the notch.

As noted by Andersson[3] one of the notable characteristics of spalling is the significant amount of dilation associated with the spalling process. Displacements were measured at the top and bottom of each beam using LVDT's. Since the displacement at the top and bottom of the specimen should be the same if the specimen behaviour is elastic and homogeneous, a difference between top and bottom displacement could indicate dilation associated with the fracturing/yielding in the beam. Figure 6.9 shows the dilation measured in non-reinforced beam specimen. The dilation appears to initiate at approximately 12.5MPa which also similar to the stress level where the non-linear response commences in Figure 6.8. After the fracture initiation, non-linearity become significant but initiation of the fracture doesn't appear to end up with the rupture of the specimen.

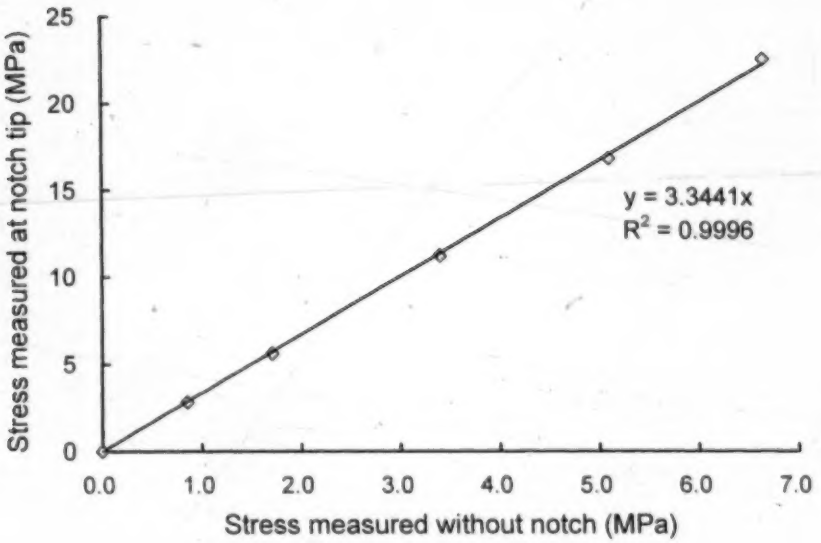

(a)

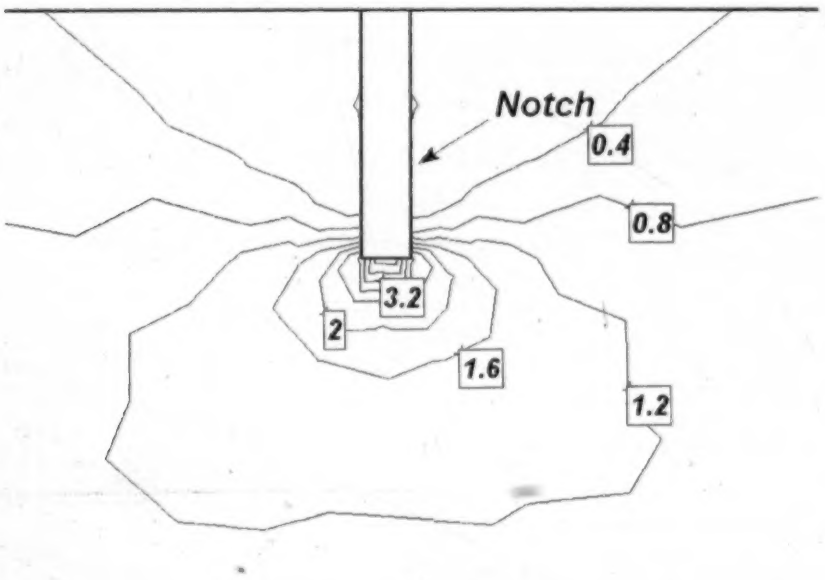

(b)

Figure 6.7 : Stress concentration factor from the elastic two-dimensional finite code, Phase2D.

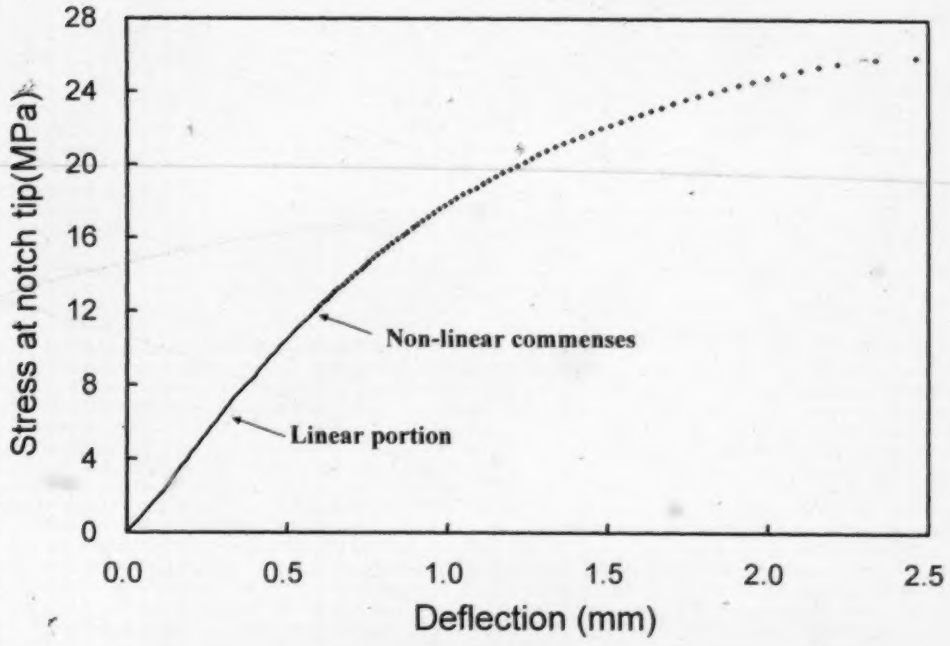

Figure 6.8 : Notch tip stress calculated using the estimated stress concentration factor and the corresponding beam deflection measured at the centre of the beam. The nonlinear portion of graph indicates the occurrence of localized yielding in the specimen.

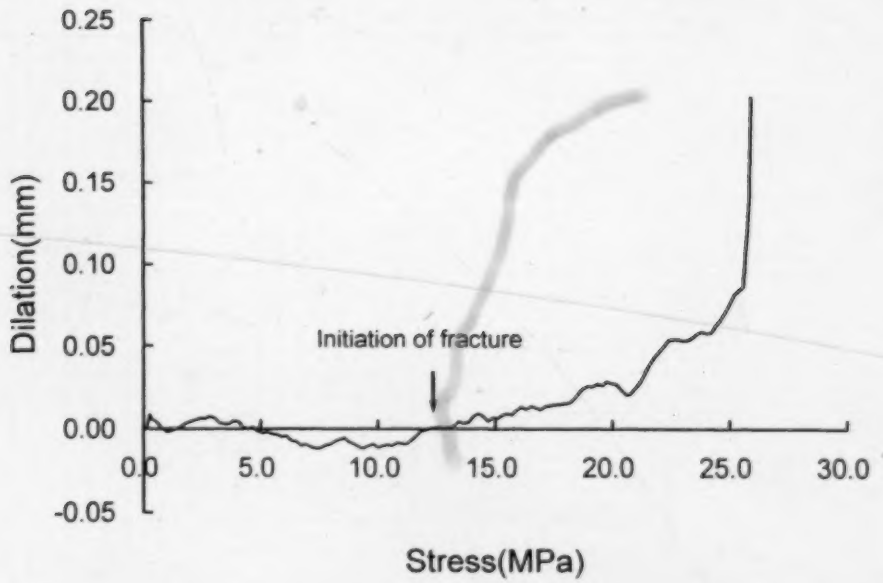

Figure 6.9: Dilation due to the extensile fracture development estimated from the differences between top and bottom bending displacement measured from LVDT.

Figure 6.10 shows the ruptured specimen shape from this test. Note that the spalling failure shown in Figure 6.1 is also observed in this test. For pure bending case spalling is not observed (see Figure 6.11). Although spalling was observed, the sample eventually collapsed by tensile fracturing despite the applied axial load. This is attributed to the reduction in the moment of inertia of the sample as failure initiated at the top of each sample and progressed downwards.

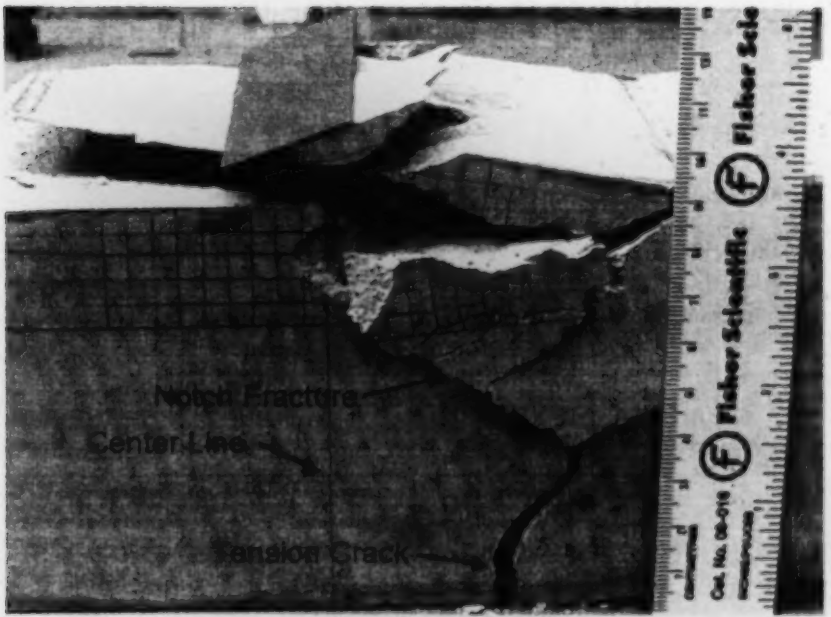

a) Beam after complete failure

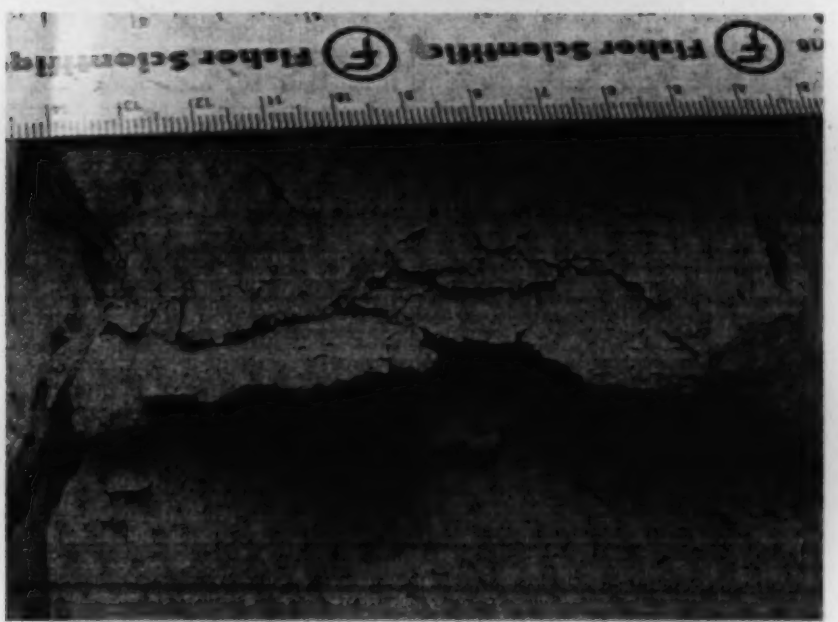

b) Spalling observed at the top of the beam after rupture

Figure 6.10 : Final ruptured shape of beam specimen and the spalling observed at the top center. Note the similarity to the spalling observed in Figure 6.1.

Figure 6.11 : Tensile fracture observed in 4 point bending system. The tensile strength measured from this test was 1.5 MPa which is approximately 60% of the tensile strength measured in Brazilian test and shown in Table 6.1.

From the test results it is concluded that the tests can adequately simulate spalling and that the onset of spalling is associated with the onset of dilation. In the next section the Discrete Element Method (DEM) is used to simulate the beam tests described above.

6.4 BONDED PARTICLE ANALOGUE

6.4.1 Discrete element modelling

The Particle Flow Code (PFC) is a discrete element code that represents a solid as an assemblage of circular disks connected with cohesive and frictional bonds. The Discrete Element Method (DEM) is used to model the forces and motions of particles within this

assembly. This method is similar to that used in explicit finite difference analysis and allows crack formation and its propagation through the system (Potyondy and Cundall[26]).

In this model, the particles can move independently with one another and interact only at their contacts. They are assumed to be rigid but they overlap at the contacts under compression. Thus, particles themselves are never deformed they only have rigid body motions. The particles can be bonded together by specifying the shear and tensile bond strength at each contact point. The values assigned to these strengths influence the macro strength of the sample and the nature of cracking and failure that occurs under load. Friction is activated by specifying coefficient of friction, and is mobilized while particles are in contact. Tensile cracks occur as the applied normal force on each contact exceeds the specified normal bond strength. Shear cracks are generated as the applied shear force either by rotation or shear of particles exceeds specified shear bond strength. The tensile strength at the contact immediately becomes zero after bond breakage while shear strength mobilized to residual value depends on specified coefficient of friction and induced normal contact force. After a bond breaks, the stress is redistributed and this may then cause adjacent inter particle bonds to break. The microscopic behavior in PFC is governed by the basic micro parameters used to describe the contact stiffness, bond stiffness, bond strength and contact friction (Potyondy and Cundall[26]).

6.4.2 Micro parameters for synthetic rock

Although *PFC* has very simple constitutive behaviors between particle motions, it is not always easy to choose appropriate micro properties so that the behavior of the resulting

synthetic material resembles that of an intended physical material. The application of PFC relies on obtaining macro-scale material behavior from the microscale interactions. While the micro properties of the real physical material are very important they are seldom known. To determine these parameters one must compare the relevant behaviors of the intended physical material with synthetic material behaviors in PFC by choosing parameters using trial and error (ITASCA[27]).

Cho et al.[28] calibrated the micro parameters in PFC on the synthetic rock used in this study by performing biaxial and Brazilian test simulations. They used a clumping technique to create irregular non-spherical particle shapes. Cho et al.[28] showed that this clumping technique removed some of known limitations in modeling brittle rock with PFC, e.g.. high tensile strength, low failure strength envelope, Diederichs[29]). Since the same synthetic rock was used in the bending test simulation the identical micro properties were used in this study.

The calibrated PFC micro parameters of synthetic rock are tabulated in Table 6.2 and the macro properties obtained from the calibrated results is shown in Table 6.3.

Table 6.2: Micro Parameters used to represent the Sulfaset synthetic rock.

R_{min}	0.25mm	E_c	1.4GPa
R_{min}/R_{max}	1.5	k_n/k_s	2.5
$\overline{\lambda}$	1.0	$\overline{E_c}$	1.4GPa
μ	0.75	$\overline{k_n}/\overline{k_s}$	2.5
$\overline{\sigma_n}$	6.8 ± 1.7MPa	*clp_rad*	0.37 ± 0.2mm
$\overline{\sigma_s}/\overline{\sigma_n}$	1.0	Unit_weight	1830kg/m^3

Where,

R_{min} : Minimum particle radius
R_{max}/R_{min} : Particle radius ratio
$\overline{\lambda}$: Bond radius ratio
μ : Coefficient of friction
$\overline{\sigma_c}$: Normal Bond strength
$\overline{\sigma_s}/\overline{\sigma_n}$: Bond strength ratio (shear to normal)
E_c : Contact young's modulus
$\overline{E_c}$: Bond young's modulus
k_n/k_s : Contact stiffness ratio
$\overline{k_n}/\overline{k_s}$: Bond stiffness ratio
clp_rad : Clump radius

Table 6.3 : Macro properties obtained from the sample calibration

σ_c (MPa)	σ_t (MPa)	E (GPa)	c (MPa)	ϕ (MPa)	S	m_b
12.27	2.24	2.51	2.9	36.1	1	5.48

6.4.3 Modeling axially compressed bending test

Axially compressed bending tests for the synthetic rock were numerically simulated using PFC2D by mimicking the laboratory configuration. Figure 6.12 illustrates the axially compressed bending model scheme used in the PFC model. It is desirable that a PFC model has the identical dimensions as the laboratory beam specimen. However this would requires more than 100000 balls to be generated with the currently calibrated PFC model.

Increasing the number of particles for composing the sample assembly not only requires a large amount of computer memory but also a longer calculation time.

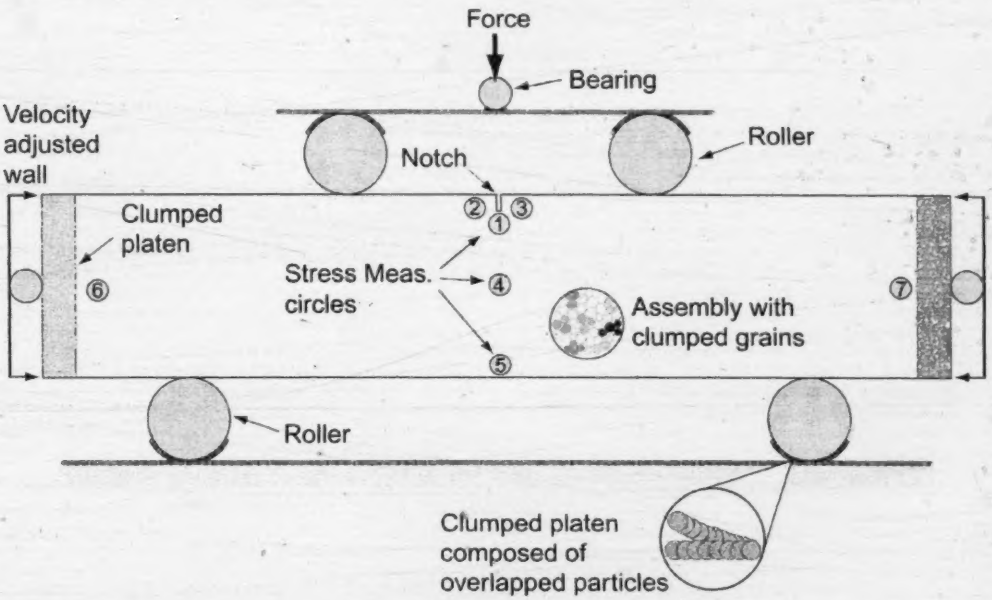

Figure 6.12 : Axially compressed bending test simulation setup in PFC2D.

Potyondi and Cundall[26] demonstrated that scale effect was not significant in rock modeling under compressive loading conditions. For this reason, PFC model used in to simulate the beam tests was downscaled to 25% of all laboratory dimensions (i.e. sample dimension, loading position, moment arm etc.). The scaled model dimension was 100mm x 22mm but out of the plane dimension was set to unit thickness since PFC2D model represents the assembly of circular disks with unit thickness. A total of 7000 disks were generated for the model.

The axial loading platen was modeled as single clumped particle so that the plate itself moved as a rigid body transferring the boundary load to the specimen. This system pro-

duces a uniform axial stress in the beam. The plate thickness was chosen as 5% of the beam length similar to the thickness applied in laboratory test. The interface layer between the specimen and the platen was created with particles with a diameter of 0.5 mm.

Bearing balls were installed on the clumped plate to mimic the laboratory test system with the friction on any contact points on these balls set to zero. These bearing balls act as a hinge to minimize the potential to create a moment or eccentricity, and also transfer the external loads to the specimen.

Four specific balls were used to mimic the rollers with the two bottom balls sitting in semi-circular platen composed of overlapped clump particles. Both the contact friction and shear stiffness of these balls were set to zero such that the balls were free to roll and rotate. The hydraulic rams were modeled by installing velocity walls on the top bearing and side bearing balls. The notch was installed at the top of beam center by eliminating balls whose center position was within the notch geometry.

Application of vertical loading to the beam was activated by applying a vertical force on the bearing ball located at top platen. Horizontal axial loads were activated by applying a specific velocity to the walls that corresponds to the force calculated from the vertical force applied to top bearing ball. The wall velocity was adjusted every iteration to maintain the specified loading ratio for bending and axial loading. This wall velocity control was developed using the wall servo control logic in "FISHTANK" of PFC (ITASCA, 2004[27]).

The stress measurement in PFC was incorporated with measurement circle. The particle stresses whose centroid is within the circle are calculated by summating the contact forces for particle volume and then, summation of particle stresses within the region are averaged by the measurement circle volume. Using this measurement circle, principal stresses and their orientation could be traced during the simulation. A total of seven measurement circles were installed in the beam. Three measurement circles were installed right below and beside the notch. Others were positioned at the centre, and bottom fibre of the beam, and just beside the axial loading platen to trace the stress path during loading.

Both axial and vertical loads were applied simultaneously in 1kPa increments per 100 cycles or when the average unbalanced force in the system was below a certain tolerance. The load increment involves a loading rate thus each load increment must be low enough to maintain a stable loading system. The loading interval was chosen based on the findings given in Cho et al.[28] and was sufficiently small to ensure the system was in equilibrium before the application of the next loading increment This logic was also developed using FISH (ITASCA, 2004[27]).

6.5 RESULTS AND ANALYSIS

Axial and vertical loads were applied to the particle assembly until the sample ultimately ruptured and Figure 6.13 shows the load ratio measured during this process. Figure 6.13 shows that a load ratio of approximately 3 was maintained until the specimen ultimately ruptured.

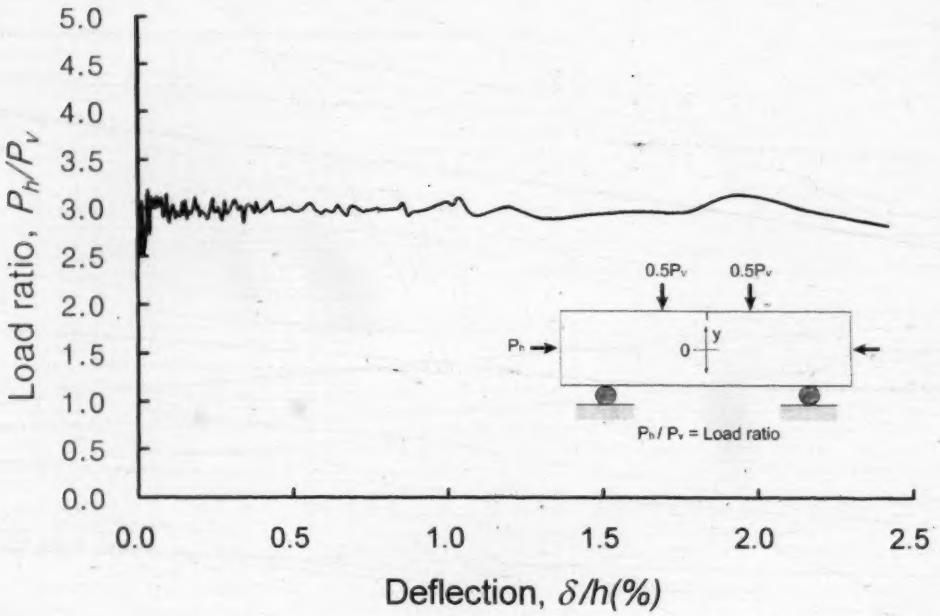

Figure 6.13 : Load ratio measured during the simulation.

Figure 6.14 compares the stress measured at the notch tip in PFC with the results from the laboratory test. Both PFC and the laboratory results are in good agreement in Figure 6.14 up to approximately 15MPa with the results showing increasing divergence above approximately 12MPa. Recall that the laboratory stresses were elastic stresses and that the onset of nonlinear behaviour and dilation in the laboratory results occurred at approximately 12MPa. This agrees reasonably well with the peak strength of approximately 15 MPa given by PFC. The slight strain hardening that occurs above 15MPa in PFC is likely related to the difficulty of maintaining a completely stable system once the sample started to fail. This rapid onset of failure once spalling initiated was also observed in the laboratory tests.

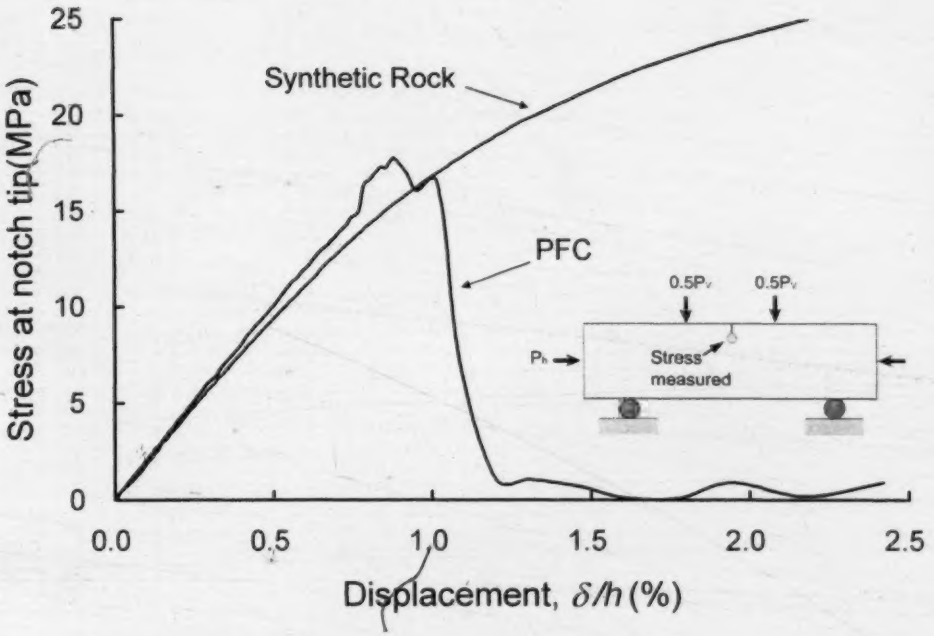

Figure 6.14 : Comparison of notch tip stress between PFC and laboratory test measured.

Figure 6.15 shows the stress path obtained from within the measurement circles during the numerical simulation. The peak failure envelope and dilation locus in Figure 6.15 for the synthetic rock was given in Cho et al.[28]. The measured stress path in Figure 6.15 illustrates that the centre of the specimen experiences several difference stress path that depends on the location of the measurement. Stress path 1 and 2 in Figure 6.15 are the stresses measured near the notch tip but they have quite different stress paths. Path 1 follows non-monotonically increasing compressive stress path while path 2 displays tensile loading similar to a Brazilian stress path.

Stress path 7 is similar to the non-monotonic stress path shown in path 1. This may be related to the confining effect of the end platen combined with non-uniformly distributed

boundary stresses. Stress path 4 is similar to the stress path 2. Path 5 shows the typical stress path observed in direct tension test but it is only observed after the notch stress reach its peak value in stress path 1.

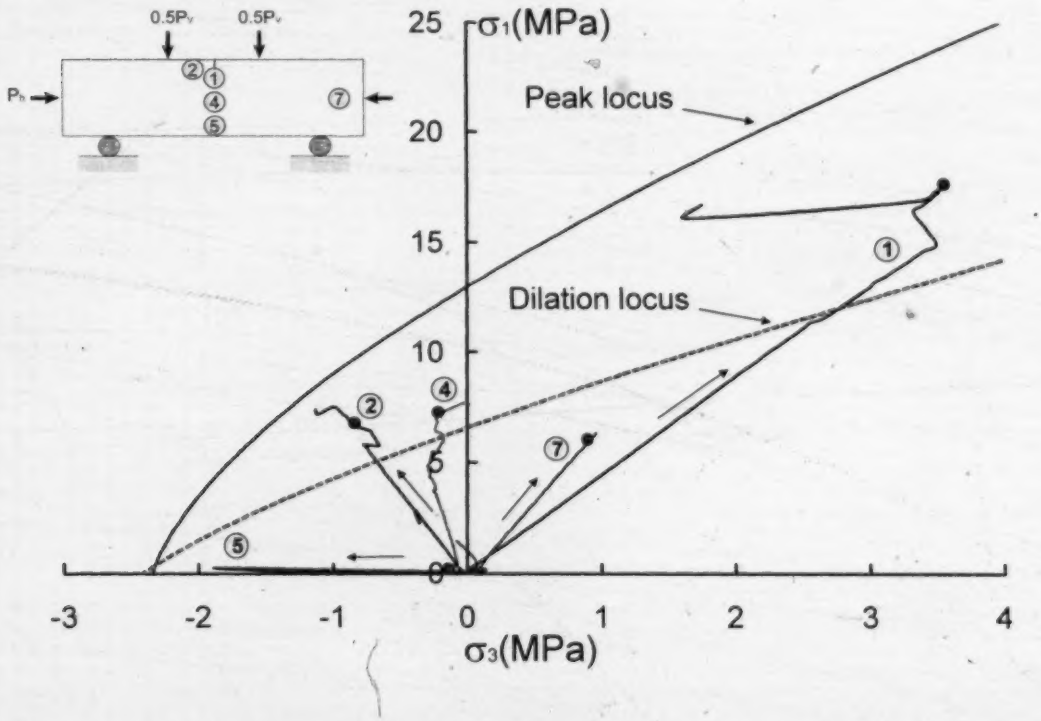

Figure 6.15 : Illustration of the stress paths followed at several locations as the sample is loaded and fails. The small red circles on each stress path show when the stress below the notch reaches its peak value.

In Figure 6.15, the red circles in each stress path show the stress level when the stress below the notch reaches its maximum value in stress path 1. Interestingly, none of stress paths shown in Figure 6.15 reach the failure envelope obtained from laboratory, Brazilian uniaxial and triaxial testing. However stress paths 1, 2 and 4 which measure the stress in the vicinity of the notch all exceed the dilation locus, i.e., the onset of extension cracking

measured in laboratory tests. This is similar to the in-situ observations reported by Martin (1997)[22].

Figure 6.16 shows the stress path evolution near the notch tip (i.e. path 1 and path 2) with the fracture development within the specimen. The subscript for each stage denotes the stress path number. As the stress path 1 reaches the dilation locus (stage A in Figure 6.16) cracks initiates near the notch and the specimen begins to experience a localised complex stress path because of the redistribution of stress associated with the crack formations. Interestingly, at this stage in stress path 2, the stresses also reach the dilation locus in the tensile region. The subsequent stress changes above the dilation locus induce more cracks and these new cracks reduce the actual confinement (stage B in Figure 6.16). This crack-induced process continues until the volume in the centre of the beam is essentially distressed.

The fractures in the PFC simulation become more distinct after the peak stress is reached. The stress-induced fracture pattern naturally evolves into a v-shaped notch that is essentially distressed (stage D in Figure 6.16). This depth of notch development is a function of the loading and boundary conditions.

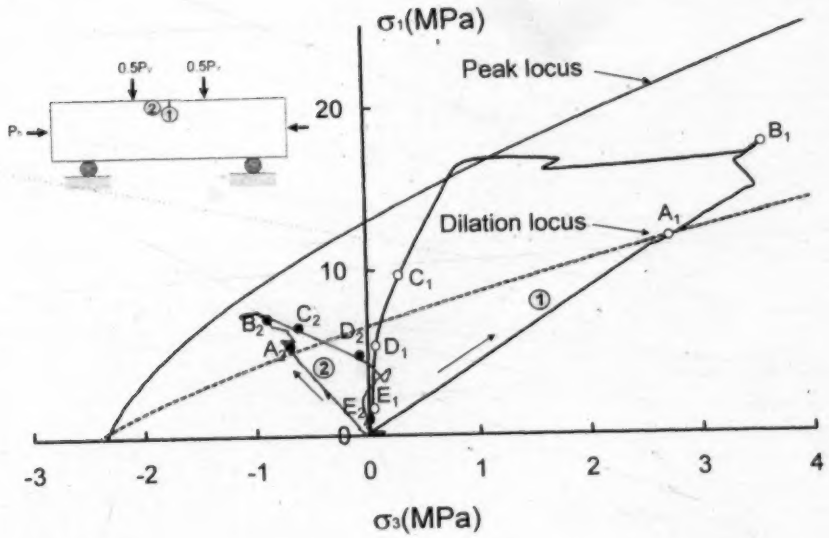

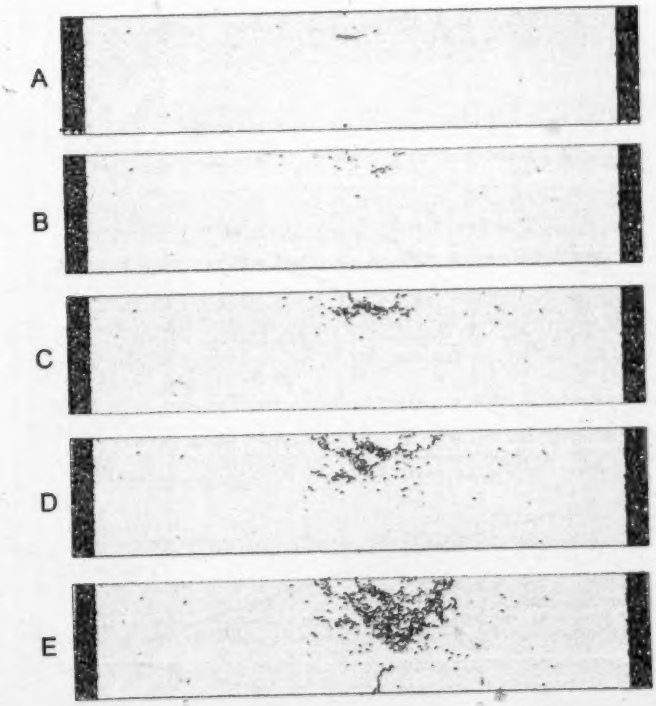

Figure 6.16 : Stress path near the notch and fracture development by stage. Note that the onset of dilation in the bending tests occurred at approximately 12MPa.

In our samples as notch development occurs the moment of inertia of beam is reduced and tensile rupture at the bottom occurs (stage E in Figure 6.16). However because of the boundary conditions around a tunnel this phenomena would not occur and the notch growth would be limited by the finite stresses around the tunnel.

Figure 6.17 compares the notch stress and the number of cracks produced by shear and tension in the PFC sample at each stage. The fractures occurring in the discrete element specimen by either tension or shear are identified by measuring the forces mobilized in the bonds between the particles. If the mobilized shear forces in the bonds exceeds the specified micro shear bond strength, then bond breakage is counted as a shear crack while if the mobilized tensile forces in the bond exceeds the specified micro normal bond strength then bond breakage is counted as tension cracks. Using this approach it was possible to evaluate the number of shear or tensile cracks at each stage of the test.

In Figure 6.17 (a), before the peak notch stress, the number of shear and tension cracks is similar. However, after the peak stress is reached and as the notch develops the number of tension cracks relative to the number of shear cracks increases significantly (see Figure 6.17). This is likely attributed to the reduction in confinement that occurs as the notch develops.

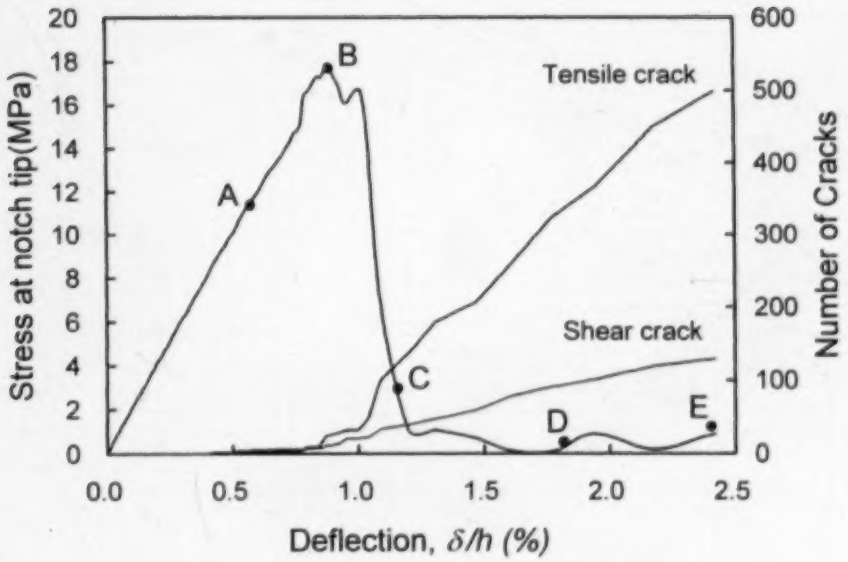

(a)

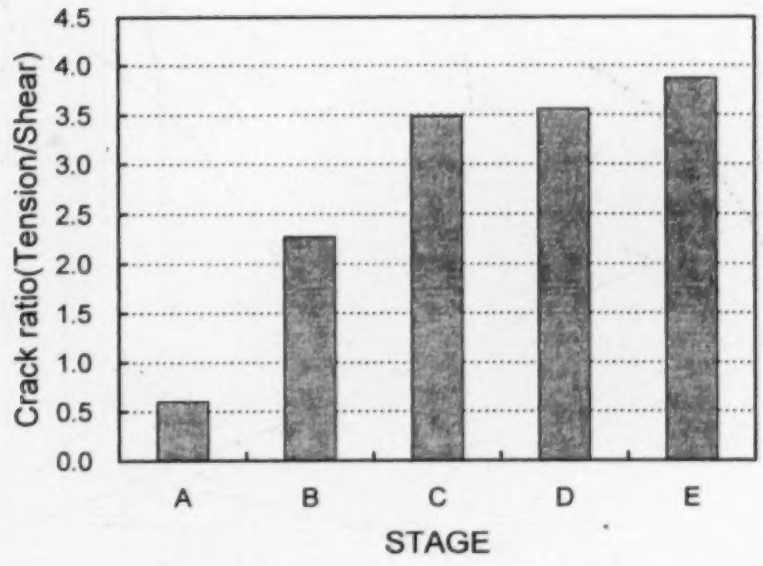

(b)

Figure 6.17 : Number of cracks generated by stage. (a) Number of cracks (b) Crack ratio.

6.6 DISCUSSION AND CONCLUSIONS

In both uniaxial and triaxial conventional laboratory compression tests researchers (e.g., Brace et al.[6], Lajtai[7], Martin and Chandler[9]) using cylindrical specimens have shown that the onset of cracking is associated with lateral dilation of the specimen. Diederichs[30] suggested that should this crack-induced dilation initiate near the boundary of the specimen these axially-aligned open cracks would increase the confinement on the interior of the sample suppressing the extension of additional cracks in the centre of the sample and preventing rupture. Hoek[31] demonstrated that open inclined cracks in compression can only propagate if the stresses near the crack tip remain tensile and Horii and Nemat-Nasser[32] showed that the crack-opening force required to create this tension was very sensitive to compressive boundary conditions. Hence, for a single open crack to grow longer the zone of tensile stress must encompass a large region and in small cylindrical samples this is difficult to achieve. Hence it appears that the size of the samples and the circular boundary condition are probable reasons for spalling not being observed in laboratory compression tests at stress level associated with the onset of dilation

In our axially compressed bending test the non-uniformly distributed stresses result in the maximum tangential stresses near the top of the beam. Once cracking begins at the notch tip spalling progressively propagates downwards towards the region of lower tangential stress. In the final stages of rupture the progressive nature of the spalling process causes the bottom portion of the beam to failure in tension.

The measurements of beam deflection showed that the onset of dilation in our beams occurred when the calculated stress beneath the notch tip reached approximately 12MPa. Numerical analysis using the distinct element method also showed that near the notch tip dilation occurred when the σ_1 stress reached approximately 12MPa. Spalling in our beam tests based on deflection and the onset on nonlinear response began at approximately the same stress level. The dilation locus based on this numerical modelling shows that the onset of dilation occurs well below the peak strength failure envelope determined from conventional laboratory tests and hence spalling in our beam tests also occurred before the peak strength was reached.

Andersson[3] and Martin[2] showed that in crystalline rock spalling occurred when tangential stresses on the boundary of circular excavations reached approximately 50% of the laboratory uniaxial compressive strength and this stress level agreed with the onset of dilation measured in conventional laboratory tests. It would appear based on their results and the results from our bending tests that the onset of dilation is a more reliable indicator for predicting the stress levels associated with spalling.

6.7 REFERENCES

[1] Fairhurst, C., Cook, N. G. W. 1966. The Phenomenon of Rock Splitting Parallel to the Direction of Maximum Compression in the Neighbourhood of a Surface. *In Proc. of the 1st Congress of the International Society of Rock Mechanics*, pp. 687-692.

[2] Martin, C. D. 1997. Seventeenth Canadian Geotechnical Colloquium : The effect of cohesion loss and stress path on brittle rock strength. *Can. Geotech. J.* 34:698-725.

[3] Andersson, J. C. 2007. Äspö Pillar Stability Experiment: Rock mass response to coupled mechanical thermal loading. PhD thesis. Royal Institute of Technology (Kungliga Tekniska Högskolan), KTH, Stockholm.

[4] Eberhardt, E. 2001. Numerical modelling of Three-Dimension Stress Rotation ahead of an advancing Tunnel Face. *Int. J. Rock. Mech. Min. Sci.* 38:499-518.

[5] Diederichs, M. S., Kaiser, P. K., Eberhardt, E. 2004. Damage initiation and propagation in hard rock during tunnelling and the influence of near-face stress rotation. *Int. J. Rock. Mech. Min. Sci.* 41:785-812.

[6] Brace, W. F., Paulding, B., Scholz, C. 1966. Dilatancy in the fracture of crystalline rocks. *J. Geophys. Res.* 71:3939-3953.

[7] Lajtai, E. Z. 1974. Brittle fracture in compression. *International Journal Fracture Mechanics.* 10:525-536

[8] Tapponnier, P., Brace, W. F. 1976. Development of Stress-Induced Microcracks in Westerly Granite. *Int. J. Rock Mech. Min. Sci. Abstr.* 13:103-112.

[9] Martin, C. D., Chandler, N. A. 1994. The progressive Fracture of Lac du Bonnet Granite. *Int. J. Rock Mech. Min. Sci. Abstr.* 31:643-659.

[10] Martin, C. D., Kaiser, P. K., McCreath, D. R. 1999. Hoek-Brown Parameters for Predicting the Depth of brittle Failure around Tunnels. *Can. Geotech. J.* 36:136-151.

[11] Hoek, E. 1965. Rock Fracture under Static Stress Conditions.CSIR Report. National Mechanical Engineering Research Institute, Council for Scientific and Industrial Research. MEG383.

[12] Gay, N. C. 1973. Fracture Growth around Openings in Thickwalled Cylinders of Rock Subjected to Hydrostatic Compression. *Int. J. Rock Mech. Min. Sci. Abstr.* 10:209-233.

[13] Santarelli, F. J., Brown, E. T. 1989. Failure of Three Sedimentary Rocks in Triaxial and Hollow Cylinder Compression Tests. *Int. J. Rock Mech. Min. Sci. Abstr.* 26:401-413.

[14] Ewy, R. T., Cook, N. G. W. 1990. Deformation and Fracture around Cylindrical Openings in Rock - I. Observations and Analysis of Deformations. *Int. J. Rock Mech. Min. Sci. Abstr.* 27:387-407.

[15] Haimson, B. C., Song, I. 1993. Laboratory Study of Borehole Breakouts in Cordova Cream : a Case of Shear Failure Mechanism. *Int. J. Rock Mech. Min. Sci. Abstr.* 30:1047-1056.

[16] Lee, M., Haimson, B. 1993. Laboratory Study of Borehole breakouts in Lac Du Bonnet Granite : a Case Extensile Failure Mechanism. *Int. J. Rock Mech. Min. Sci. Abstr.* 30:1039-1045.

[17] Dzik, E. J. 1996. Numerical Modeling of Progressive Fracture in the Compression Loading of Cylindrical Cavities. PhD. Department of Civil and Geological Engineering, University of Manitoba. 173pp.

[18] Sellers, E. J., Klerck, P. 2000. Modelling of the Effect of Discontinuities on the Extent of the Fracture Zone Surrounding Deep Tunnels. Tunnelling and Underground Space Technology. 15:463-469.

[19] Martin, C. D., Martino, J. B., Dzik, E. J. 1994. Comparison of borehole breakouts from laboratory and field tests. *Proc. EUROCK'94, SPE/ISRM Rock Mechanics in Petroleum Engineering*, Delft, A.A. Balkema, Rotterdam, pp. 183-190

[20] Martin, C. D., Lanyon, G. W. 2003. Measurement of in-situ stress in weak rocks at Mont Terri Rock Laboratory, Switzerland. *Int. J. Rock. Mech. Min. Sci.* 40:1077-1088.

[21] Rocsience Inc. 2002. RocLab 1.007, http://www.rocscience.com.

[22] Martin, C. D., Martino, J. B., Read, R. S. 1997. Observations of Brittle Failure around a Circular Test Tunnel. *Int. J. Rock. Mech. Min. Sci.* 34:1065-1073.

[23] Hibbeler, R. C. 1997. Mechanics of Material. Prentice Hall.

[24] Lipson, C., Juvinall, R. C. 1963. Handbook of Stress and Strength. Macmillan.

[25] Rocsience Inc. 2002. Phase2D, http://www.rocscience.com.

[26] Potyondy, D. O., Cundall, P. A. 2004. A bonded-particle model for rock. *Int. J. Rock. Mech. Min. Sci.* 41:1329-1364.

[27] Itasca Consulting Group. 2004. PFC2D(Particle Flow Code in 2 Dimensions) version 3.1.

[28] Cho, N., Martin, C. D., Sego, D. C. 2007. A clumped particle model for rock. *Int. J. Rock Mech. Min. Sci.* 44:997-1010.

[29] Diederichs, M. S. 2002. Keynote: stress induced accumulation and implications for hard rock engineering. *Proceedings of NARMS 2002*, Hammah R., Bawden W.F., Curran J.,Telsnicki M. editors, University of Toronto Press, pp. 3-14.

[30] Diederichs, M. S. 2003. Rock fracture and collapse under low confinement conditions. *Rock Mech. and Rock Eng.* Vol. 36 (5):339-381.

[31] Hoek, E. 1968 Brittle failure of rock Rock mechanics in engineering practice Stagg, K.G.,Zienkiewicz, O.C. ed. John Wiley & Sons Ltd.

[32] Horii, H., Nemat-Nasser, S. 1985. Compression-Induced Microcrack growth in Brittle Solids : Axial Splitting and Shear Fracture. *J. Geophys. Res.* 90:3105-3125.

CHAPTER 7

SUMMARY, CONCLUSION AND FUTURE RESEARCH

7.1 SUMMARY AND CONCLUSION

7.1.1 DEM modeling of rock

Modeling rock failure processes have been attempted by various approaches, e.g., continuum and fracture mechanics, over the past 50 years. However, in nearly all cases these approaches have brought about limited success because most previous models assumed that rock is continuous, homogeneous, and isotropic. As illustrated in Chapter 1 and Chapter 2, this assumption is fundamentally wrong. Rock is one of most heterogeneous materials in nature and this characteristic leads to failure under stress through discrete processes such as extensile fracturing and dilation.

During the past ten years the discrete element method, in combination with PFC software, has been used to model the failure of rock. This approach has been successful in modeling micro process oriented failure modes especially in uniaxial compressive test simula-

tions of brittle rock. However, two significant deficiencies have been identified in conventional PFC modeling for the application of stress paths other than uniaxial compression (Diederich[1], Potyondy and Cundall[2]); they are:

(1) The tensile strength to compressive strength ratio is considerably greater than that measured in the laboratory tests

(2) The failure envelope gives very low friction angles compared to measured laboratory values.

Adjusting micro parameters appears to have little effect on these deficiencies.

The findings from this research indicate that by introducing clumped-particle geometry these deficiencies are eliminated.

Using clumped logic, excellent agreement is found between laboratory tests results and PFC for both weak synthetic rock and Lac Du Bonnet granite. This new approach captures the major characteristics of brittle rock observed in laboratory testing, i.e., axial and lateral stress-strain behaviors including the post peak, full failure envelope, and onset of dilation.

7.1.2 Modeling of Shear zone in Rock

Most rocks and soils when deformed in shear form a narrow shear band. Many researchers (Riedel[3], Cloos[4], Skempton[5], Tchalenko[6], Morgenstern and Tschalenko[7]) have stated that the origin of the fractures developed in such shear zones is shear. They insist that the formation of the shear can be accommodated by Coulomb theory.

However, several questions arise: Can Coulomb theory, which is fundamentally a continuum model, be applicable after fracture occurs? Will the orientation of principal stresses be unchanged during the shearing? If not, what will be the origin of the fracture?

Our study of the shear zone modeling has been motivated by these questions.

In this study using DEM code PFC^{2D} , direct shear tests for solid synthetic rock were modeled and compared with direct measurements carried out on laboratory specimens.

Using the same micro parameters calibrated to the triaxial and Brazilian tests, we wanted to see whether PFC was able to match test simulation results for a stress path different from the triaxial test. Secondly, we wondered if PFC could clarify the origin of the fractures that occurred in the brittle material subjected to the shear loading, i.e., shear or tension.

The PFC based numerical simulations gave excellent agreement with the direct shear laboratory test results, despite the fact that stress paths used in the direct shear tests were different from those used to establish the modelling parameters.

The PFC simulation results for the tests also supported the theory that the source of fracture origin in shear zone development may not result from shear but may result from tension in the following aspects.

(1) While the fracture angle measured during direct shear test simulation was similar to the direction of Riedel shear $\phi/2$, the orientation of the maximum principal stresses change and the angles are similar to the principal stress direction.

(2) Velocity vectors during shearing also indirectly proved that fractures occurring during shear resemble typical mode I fractures in the Brazilian test simulation.

(3) The ratio of tensile to shear cracks is significantly high; tension cracks are 4 to 5 times greater than shear cracks.

The findings from this work emphasize the importance of tensile fracturing in the development of a shear zone, especially at low normal stresses.

7.1.3 Spalling and dilation under axially compressed beam bending

In many underground excavations at depth, the strength of rock near the boundary was reported significantly lower than conventional rock strength.

In such cases, non-uniformly distributed tangential stresses are applied to the rock near the opening. Such stress states apply both compressive stress and a moment-inducing non-monotonic stress path, while the laboratory specimen normally undergoes monotonic stress path and axial stresses are uniformly applied without any moment loads.

In this study, axially compressed bending tests were developed to simulate extensile fracturing-induced notch failure in which compressive stress and moment are both active in the system. The results show that similar extensile fracturing-induced spalling failure was

observed near the notch installed at the top of beam specimen center, and notch failure was also observed similar to the case of an underground excavation.

PFC simulation was also implemented to explore the stress effect on rock responses and the failure process. The same micro parameters and numerical setup was used for the generation of specimens used in the conventional laboratory tests.

The numerically monitored stress paths near the notch also confirm that stress paths vary depending on the position measured near the notch and the failure occurs in a highly progressive manner, particularly when the notch tip stress exceeds the dilation locus. The progressive nature of such failure is attributed to the reduction of effective confinement and the activation of moment. The stress path measured near the notch also revealed that the failure mode beside the notch resembles a typical Brazilian stress path. Hence, reduction in confinement and increasing specimen damage caused the specimen to yield before it reached peak strength and the yield stress was closer to the dilation locus (i.e., crack initiation).

The final ruptured specimen in numerical simulation was quite well matched to the notch failure observed in the laboratory test and was also similar to the notch failure observed in field.

More importantly, the source of fractures on the formation of the notch in the numerical simulation was mostly oriented by tension cracks which imply that extensile fracturing is the main source of notch failure.

7.2 FUTURE RESEARCH

In this study, discrete element modeling of rock was performed using the DEM code PFC. The clumped logic effectively generated the grain effect of rock, and has mostly shown excellent agreement between laboratory test results and PFC for both sulfaset synthetic rock and Lac Du Bonnet granite.

A deficiency in applying clump logic to the actual grain modeling of rock is that clumped particles are infinitely bonded, thus they never break apart. This may result unrealistically high dilation when compared with the laboratory test as shown in Figure 4.16 (b) because the crushing effect of grains is not considered. Modeling of considerations such as crushing effect is a good suggestion for the future research.

In underground hard rock excavations, overstressing of the excavation usually results in a phenomenon often described as spalling or slabbing. This phenomenon is observed near the unconfined boundary of the underground excavation in the region of maximum tangential stress and results in slabs forming perpendicular to the minimum principal stress, i.e., parallel to the boundary of the tunnel. Martin et al.[8] made careful observations during the construction of a granite test tunnel and demonstrated that localized stress-induced fracturing is very sensitive to confining stress. They observed that less then 1m of tunnel muck, approximately 20 kPa was sufficient to suppress stress-induced fracturing in the floor of the test tunnel.

The current study, particularly as shown in Chapter 6, has focused only on the generation of extensile fracturing induced notch failure. Effects on confinement suppressing such fractures were not considered in either the laboratory scale or the numerical simulation.

Understanding such effects would be a key factor for designing support of rock in underground openings at depth where overstressed zones are expected.

It can be predicted that such confinement effects will be studied in the near future with DEM modeling using PFC.

7.3 REFERENCES

[1] Diederich, M. S. 2000. Instability of Hard Rock Masses : The Role of Tensile Damage and Relaxation. Ph.D. thesis. Dept. of Civil Eng., University of Waterloo. 567pp.

[2] Potyondy, D. O., Cundall, P. A. 2004. A Bonded Particle Model for Rock. *Int. J. Rock. Mech. Min. Sci.* 41:1329-1364.

[3] Riedel, W. 1929. Zur Mechanik geologischer Brucherscheinungen. *Centralbl. f. Mineral. Geol. u. pal.* v. 1929 B:354-368.

[4] Cloos, E. 1955. Experimental Analysis of Fracture Patterns. *Bull. of Geol. Soc.of America.* 66:241-256.

[5] Skempton, A. W. 1967. Some Observations on Tectonic Shear Zones. *In: Proceedings of the First International Congress on Rock Mechanics, Lisbon.* v1:pp. 329 - 335.

[6] Tchalenko, J. S. 1970. Similarities between Shear Zones of Different Magnitudes. *Geol. Soc. of American Bull.* 81:1625-1640.

[7] Morgenstern, N. R., Tchalenko, J. S. 1967. Microstructural Observations on Shear Zones from Slips in Natural Clays. *In: Proceedings of Geotechnical Conference*

on Shear strength of Natural Soils and Rocks, Oslo, Norwegian Geotechnical Institute. v1:pp. 147-152.

[8] Martin, C. D., Martino, J. B., Read, R. S. 1997. Observations of Brittle Failure around a Circular Test Tunnel. *Int. J. Rock. Mech. Min. Sci.* 34:1065-1073.

APPENDIX A

ADDITIONAL FIGURES OF THE LABORATORY TESTS

FIGURE A.1 SULFUR COMPOSITE BEHABVIOR FOR SYNTHETIC ROCK

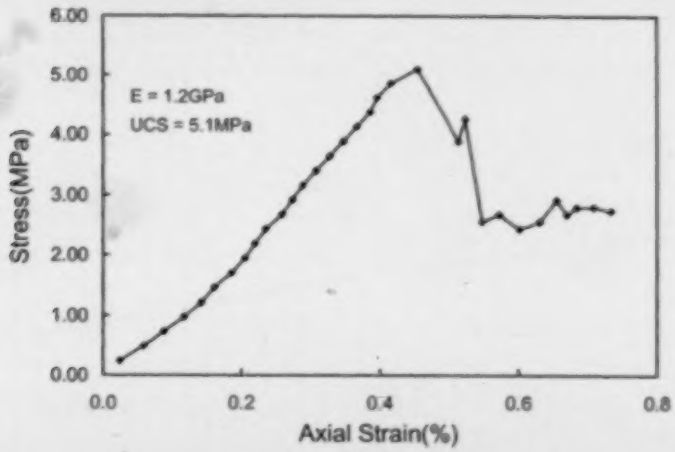

(a) Uniaxial compressive strength and stress-strain behavior of Sulfur composite

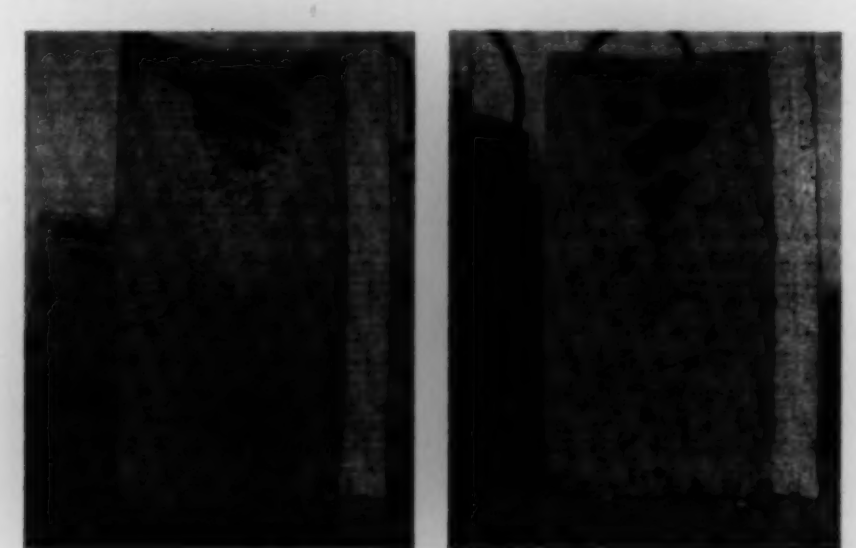

(b) Sew cut section of sulfur composite specimen. Note that significantly big pores were formed due to rapid cooling process in the air and quite large fractures were formed.

FIGURE A.2 GRAIN SIZE DISTRIBUTION OF SAND ADDED IN SULFASET SYNTHETIC ROCK

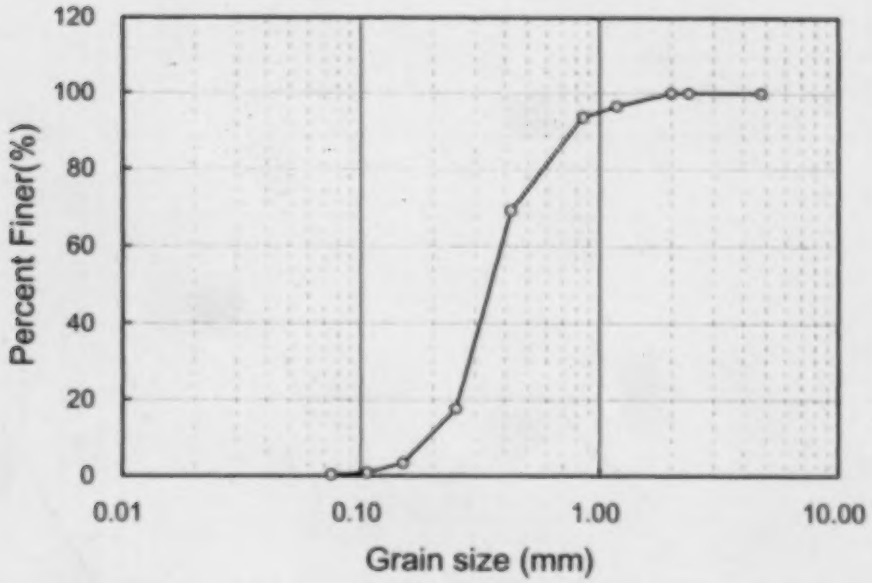

Grain size (mm)	0.075	0.106	0.150	0.250	0.425	0.850	1.180	2.000	2.360	4.750
Perc. Finer (%)	0.31	0.86	3.35	17.55	69.17	93.45	96.44	99.96	99.98	99.99

FIGURE A.3 PROCEDURE TO GENERATE UNIFORM MIXTURE OF SULFASET MORTAR

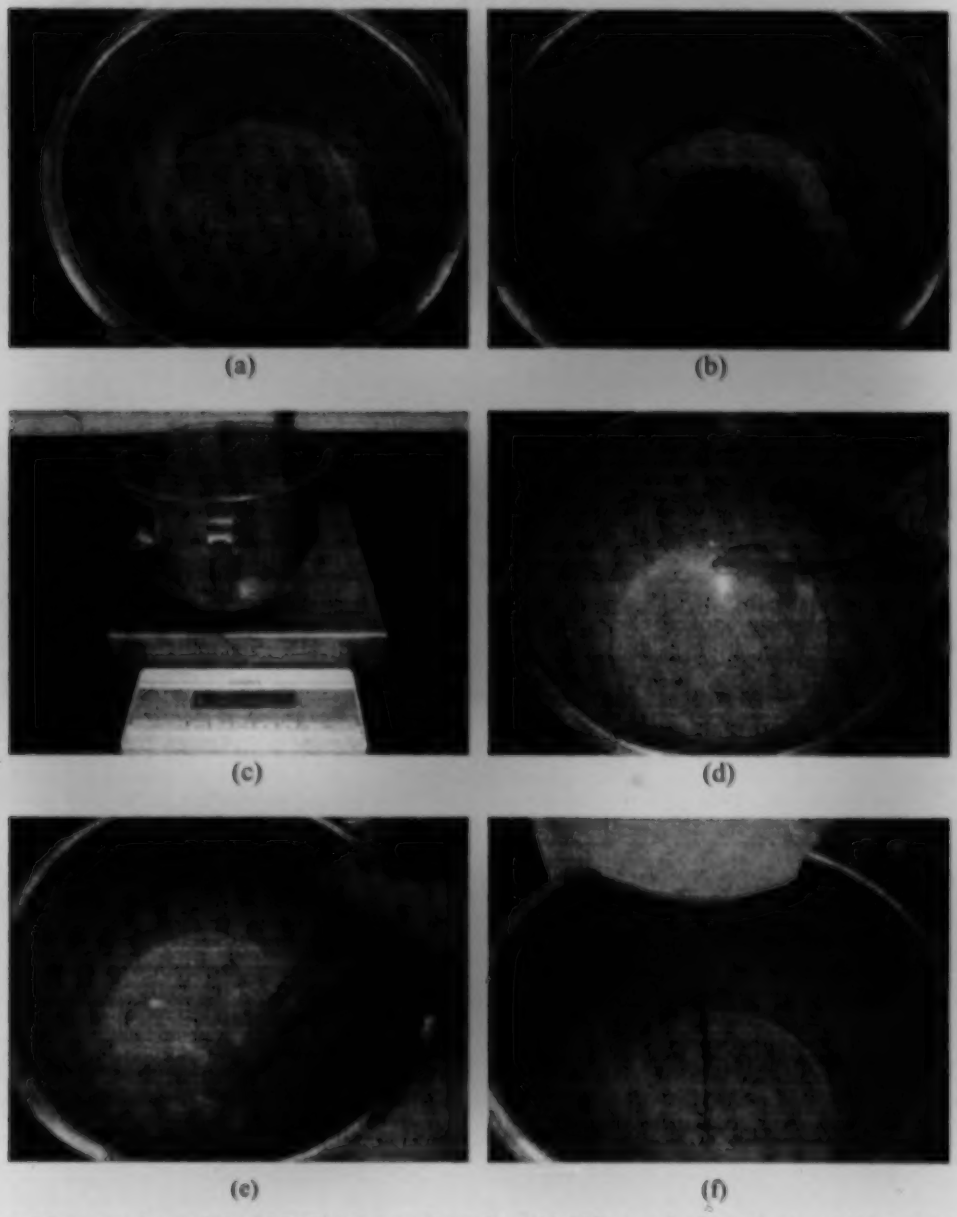

(a) Measure the weight of Suflaset poweder. (b) Add 10% sand of Sulfaset weight. (c) Add 50% water of Sulfaset weight. (d) Uniformly mix the ingredients. (e) Keep agitating manually for 20 to 25 minutes. (f) If the mortar is getting thick enough like a soup then pour it into the mould.

FIGURE A.4 DATA ACQUISITION SYSTEM

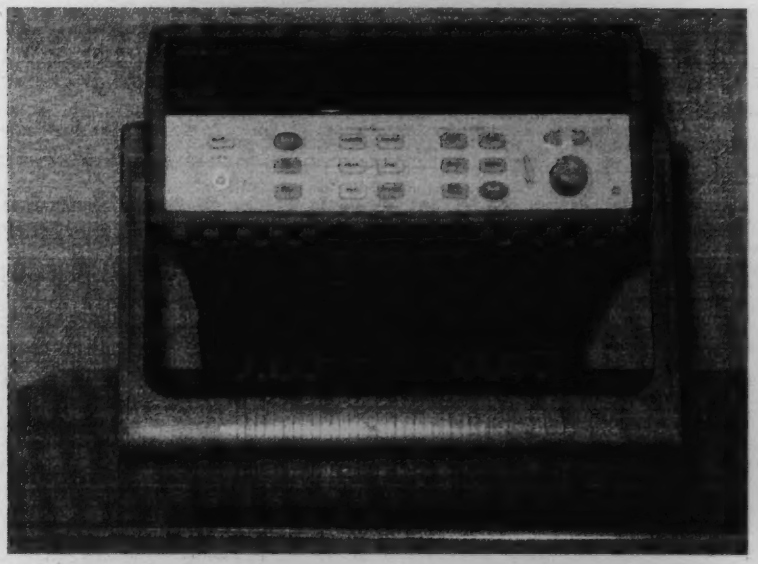

(a) Data acquisition unit, Agilent 34970A

(b) Computer incorporated data logging system

FIGURE A.5 SYRINGE PUMP

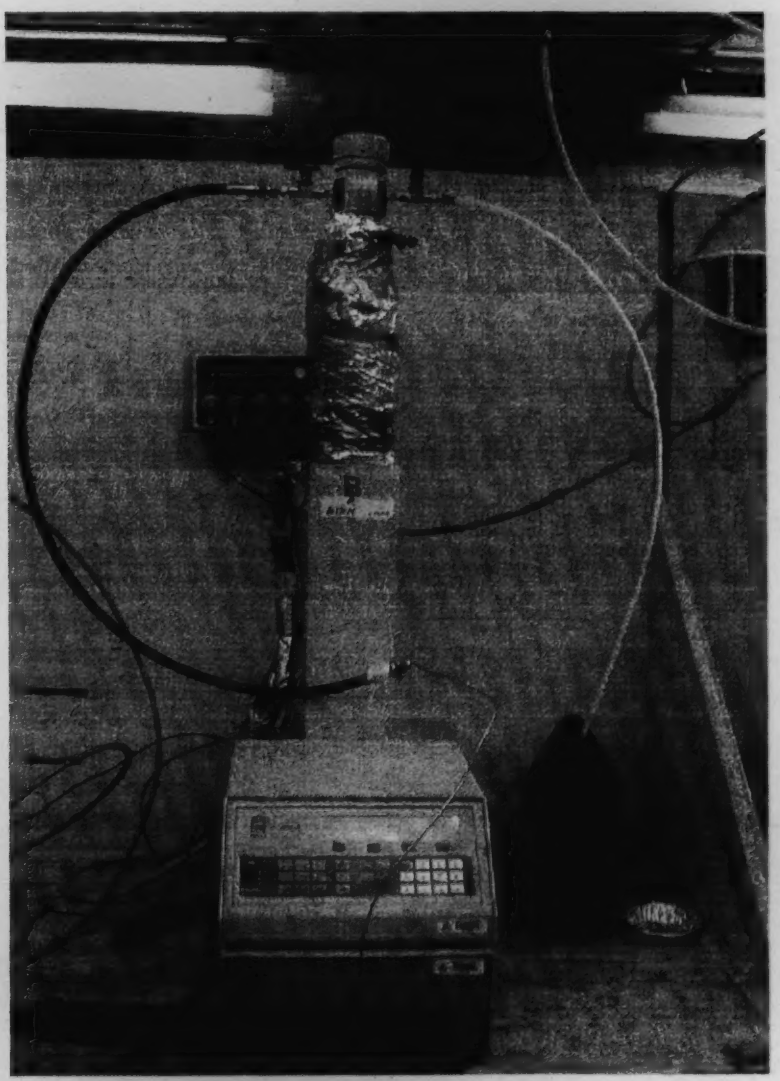

Syringe Pump : ISCO 500D Series

FIGURE A.6 DIRECT SHEAR TEST SYSTEM

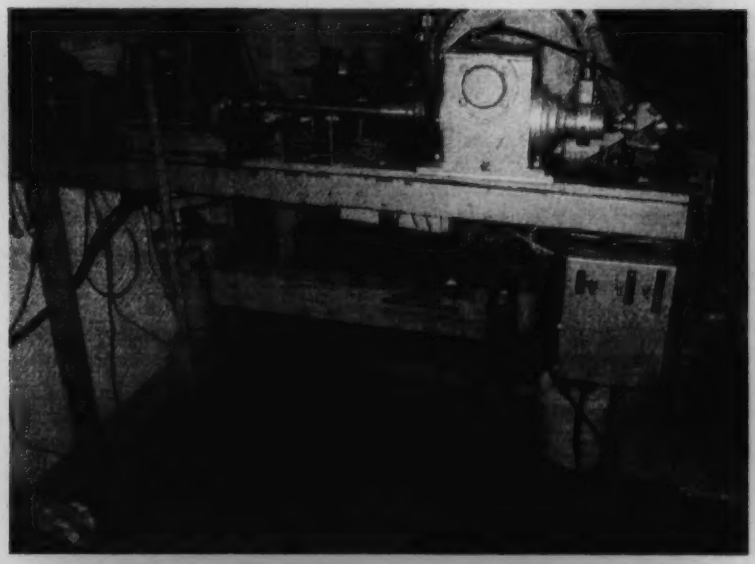

APPENDIX B

PRIMARY FISH FUNCTIONS USED IN SIMULATIONS

B.1 IRREGULAR SHAPE PARTICLE GRAIN GENERATION USING CLUMP

```
; Geotechnical Engineering Group. University of Alberta
; Developed by Namkak Cho, last updated on 2.11.2006
;=================================================================
;Purpose : Fish Function generating irregular style clumped
;          particles
;=================================================================
;
;Input : clp_rad      - clump radius
;        clp_rad_stdv - standard deviation of the clump
;                       radius
;        _clp_tol     - clump completion rate tolerance
;        _numballs    - total number of balls generated
;
def cl_clpgen
 _cli = 0
 loop while 1 # 0
  cp = contact_head
  loop while cp # null
   _cli     = _cli + 1
   clp_rad1 = clp_rad + clp_rad_stdv * urand ;; clump radius setup with stdv.
   cp1_x    = c_x(cp)
   cp1_y    = c_y(cp)
   cp1_num = 0
   bp = ball_head
   loop while bp # null
    if b_clump(bp) = null
     cp1_num = cp1_num + 1
    end_if
    bp = b_next(bp)
   end_loop
   ;;
   _clp_rate = (1 - float(cp1_num)/float(_numballs))
   ;;
   if _clp_rate >= _clp_tol then
    exit
   end_if
   command
    clump id=@_cli range circle center = (@cp1_x,@cp1_y) rad = @clp_rad1
    print _cli
    print _clp_rate
   end_command
   cp = c_next(cp)
  end_loop
 end_loop
end
;=================================================================
```

B.2 FISH FUNCTIONS FOR STRESS MEASUREMENT IN CLUMPED ASSEMBLY

```
; Filename : clp_meas.fis
; Geotechnical Engineering Group. University of Alberta
; Developed by Namkak Cho, revised in 5.10.2006
;=============================================================
; Purpose : Stress Measurement logic in clumped assembly
;=============================================================
;
def _str_init    ;; define arrays
 array _clp_pt0(2) _clp_pt1(2) _bp_str(2,2)
end
_str_init
;=============================================================
def cl_msxx
 cl_stress
 cl_msyy = cl_ms22
 cl_msxx = cl_ms11
 cl_msxy = cl_ms12
 cl_msyx = cl_ms21
end
;=============================================================
def cl_stress
;
; Average stress calculation routine for all measurement circles
; in the clumped assembly
; Input  : _mc_x, _mc_y, _mc_rad (measurement region info.)
;
 _ii = 0.0
 clp_s11 = 0.0
 clp_s22 = 0.0
 clp_s12 = 0.0
 clp_s21 = 0.0

 mp = circ_head
 loop while mp # null
  _mc_x = m_x(mp)
  _mc_y = m_y(mp)
  _mc_rad = m_rad(mp)
  clp_stress_meas
  clp_s11 = clp_s11 + _cl_s11
  clp_s22 = clp_s22 + _cl_s22
  clp_s12 = clp_s12 + _cl_s12
  clp_s21 = clp_s21 + _cl_s21
  _ii = _ii + 1
  ;;
  mp = m_next(mp)
 end_loop
 ;;
 cl_ms11 = clp_s11 / _ii
 cl_ms22 = clp_s22 / _ii
 cl_ms12 = clp_s12 / _ii
 cl_ms21 = clp_s21 / _ii
end
;=============================================================
def clp_stress_meas
;;
;; Average stress calculation routine within a specific measurement circle
;; Input  : _mc_x, _mc_y, _mc_rad (measurement region info.)
;; output : _cl_s11, _cl_s22, _cl_s12, _cl_s21
;;
 bp_force_sum
```

```
clp_force_sum
_nporous = m_poros(mp)
_mvolume = mat_vol
_cl_s11 =-1.0*((1-_nporous) / _mvolume) * (_f11sum + cl_f11sum)
_cl_s22 =  -1.0 * ((1-_nporous) / _mvolume) * (_f22sum + cl_f22sum)
_cl_s12 =  -1.0 * ((1-_nporous) / _mvolume) * (_f12sum + cl_f12sum)
_cl_s21 =  -1.0 * ((1-_nporous) / _mvolume) * (_f21sum + cl_f21sum)
end
;================================================================
def bp_cforce_meas
 ;; summation of the all contact forces acting on a particle
 ;; Input  : bp ( ball pointer)
 ;; outout : _f11, _f22, _f21, _f12
 ;;
 if md2_thick = 0.0 then
  md2_thick = 1.0
 end_if
 ;;
 _f11 = 0.0
 _f22 = 0.0
 _f12 = 0.0
 _f21 = 0.0
 ;;
 cp1 = b_clist(bp1)
 loop while cp1 # null
   _dx = c_x(cp1) - b_x(bp1)
   _dy = c_y(cp1) - b_y(bp1)
   _theta = atan2(_dy, _dx)
   _dist = sqrt(_dx^2 + _dy^2)
   if _theta < 0.0 then
    _theta = _theta + 2.0*pi
   end_if
   s_theta = pi/2.0
   if c_nforce(cp1) # 0.0 then
    if c_sforce(cp1) # 0.0 then
   _cxfor=c_nforce(cp1)*cos(_theta)+c_sforce(cp1)*cos(_theta+s_theta)
   _cyfor=c_nforce(cp1)*sin(_theta)+c_sforce(cp1)*sin(_theta+s_theta)
   ;;
   if c_pb(cp1) # null then
    pbp = c_pb(cp1)
    _pxfor=pb_nforce(cp1)*cos(_theta)+pb_sforce(cp1)*cos(_theta+s_theta)
    _pyfor=pb_nforce(cp1)*sin(_theta)+pb_sforce(cp1)*sin(_theta+s_theta)
   end_if
   ;;
   _xfor = _cxfor + _pxfor
   _yfor = _cyfor + _pyfor
   _f11 = _f11 + _xfor * _dx
   _f22 = _f22 + _yfor * _dy
   _f12 = _f12 + _yfor * _dx
   _f21 = _f21 + _xfor * _dy
   end_if
  end_if
  if c_ball1(cp1) = bp1 then
   cp1 = c_b1clist(cp1)
  else                  ;
   cp1 = c_b2clist(cp1)
  end_if
 end_loop
end
;================================================================
def clp_stress
 ;;
 ;;stress calculation acting on a clump
 ;; input : clp1
 clp_cforce_meas
 clp_ss11 = -_cf11/_cl_vol
 clp_ss22 = -_cf22/_cl_vol
```

```
 clp_ss12 = -_cf12/_cl_vol
end
;================================================================
def clp_cforce_meas
 ;; summation of the all contact forces acting on a clump
 ;; Input  : clp ( clump pointer)
 ;; outout : _cf11, _cf22, _cf21, _cf12
 ;;
 if md2_thick = 0.0 then
  md2_thick = 1.0
 end_if
 ;;
 _cf11 = 0.0
 _cf22 = 0.0
 _cf12 = 0.0
 _cf21 = 0.0
 _cl_vol = 0.0
 ;;
 bp1 = cl_list(clp1)
 loop while bp1 # null
  _cl_vol = _cl_vol + md2_thick * pi * b_rad(bp1)^2
  cp1 = b_clist(bp1)
  loop while cp1 # null
   c_dx = c_x(cp1)-cl_x(clp1)
   c_dy = c_y(cp1)-cl_y(clp1)
   _dx  = c_x(cp1) - b_x(bp1)
   _dy  = c_y(cp1) - b_y(bp1)
   _theta = atan2(_dy, _dx)
   if _theta < 0.0 then
    _theta = _theta + 2.0 * pi
   end_if
   ;;
   s_theta = pi/2.0
   _cxfor=c_nforce(cp1)*cos(_theta)+c_sforce(cp1)*cos(_theta+s_theta)
   _cyfor=c_nforce(cp1)*sin(_theta)+c_sforce(cp1)*sin(_theta+s_theta)
   ;;
   if c_pb(cp1) # null then
    pbp = c_pb(cp1)
    _pxfor=pb_nforce(cp1)*cos(_theta)+pb_sforce(cp1)*cos(_theta+s_theta)
    _pyfor=pb_nforce(cp1)*sin(_theta)+pb_sforce(cp1)*sin(_theta+s_theta)
   end_if
   ;;
   _xfor = _cxfor +  _pxfor
   _yfor = _cyfor +  _pyfor
   _cf11 = _cf11  +  _xfor * c_dx
   _cf22 = _cf22  +  _yfor * c_dy
   _cf12 = _cf12  +  _yfor * c_dx
   _cf21 = _cf21  +  _xfor * c_dy
   ;;
   if c_ball1(cp1) = bp1 then
    cp1 = c_b1clist(cp1)
   else
    cp1 = c_b2clist(cp1)
   end_if
  end_loop
 bp1 = b_cllist(bp1)
end_loop
end
;================================================================
def bp_force_sum
 ;;
 ;; calculating the summation of average contact forces acting on the balls in
 ;; the measurement region
 ;;
 _f11sum = 0.0
 _f22sum = 0.0
 _f12sum = 0.0
```

```
 _f21sum = 0.0
 ;;
 bp1 = ball_head
 loop while bp1 # null
  _dist = sqrt( (b_x(bp1) - _mc_x)^2 + (b_y(bp1) - _mc_y)^2 )
  if _dist <= _mc_rad then
   if b_clump(bp1) = null then
    bp_cforce_meas
    _f11sum = _f11sum + _f11
    _f22sum = _f22sum + _f22
    _f12sum = _f12sum + _f12
    _f21sum = _f21sum + _f21
   end_if
  end_if
  bp1 = b_next(bp1)
 end_loop
end
;=================================================================
def clp_force_sum
 ;;
 ;; calculating the summation of average contact forces acting on the clumps in
 ;; the measurement region

 cl_f11sum = 0.0
 cl_f22sum = 0.0
 cl_f12sum = 0.0
 cl_f21sum = 0.0
 ;;
 clp1 = clump_head
 loop while clp1 # null
  _cldist = sqrt( (cl_x(clp1) - _mc_x)^2 + (cl_y(clp1) - _mc_y)^2 )
  if _cldist <= _mc_rad then
   clp_cforce_meas
   cl_f11sum = cl_f11sum + _cf11
   cl_f22sum = cl_f22sum + _cf22
   cl_f12sum = cl_f12sum + _cf12
   cl_f21sum = cl_f21sum + _cf21
  end_if
  clp1 = cl_next(clp1)
 end_loop
end
;=================================================================
def _mc_porosity
 if md2_thick = 0.0 then
  md2_thick = 1.0
 end_if
 ;;
 mc_tvol = md2_thick * pi * _mc_rad^2
 ;;
 _mc_porosity = (mc_tvol - mat_vol1)/mc_tvol
end
;=================================================================
def mat_vol
 ;; calculating porosity in a specific measurement circle region
 ;;
 if md2_thick = 0.0 then
  md2_thick = 1.0
 end_if
 ;;
 mc_tvol = md2_thick * pi * _mc_rad^2
 mat_vol = ( 1 - m_poros(mp) ) * mc_tvol
end
;=================================================================
;End of File clp_meas.fis
;=================================================================
return
```

B.3 DATA FILE AND FISH FUNCTIONS FOR DIRECT SHEAR TEST SIMULATION

```
; Filename : ds_0p01.dvr
; Geotechnical Engineering Group. University of Alberta
; Developed by Namkak Cho, revised in 1.10.2007
;=============================================================
; Purpose : Direct shear test Simulation for run
;=============================================================
;
;
res com_calib-clt.sav   ;; restore clumped particle specimen
SET echo off
 call %itascaFishTank%\FishPfc2\et2\ds_shear.FIS ;; direct shear setup
 call %itascaFishTank%\FishPfc2\et2\clp_meas.FIS ;; stress measurement
SET echo on
;;
;; shear box gap and normal load plate thickness setup
SET shr_boxgap = 7.0e-3 pl_thk = 5.0e-3
;;
crk_init   ;; for crack setup
plot add fish crk_item
;;
; ===================================================================
SET md_run_name = '0p01'
title
normal stress = 0.01MPa
; ===================================================================
;;
set mc_rad_fact = 10.0 ;; measurement circle size setup
ds_sample_dimensions
create_shear_wall      ;; generate shear box
;;
set ds_wsyy_req = -1.0e2 ;; normal stress setup
ini xvel 0.0 yvel 0.0 spin 0.0
set ds_knxfac = 1.1  ;; wall stiffness setup
ds_shear_wallstiff
cycle 10
crk_init
plot add fish ds_draw_shear_sample
SET fishcall #FC_CYC_MOT ds_shear_wss ; stresses and displacements calc. setup
; ===================================================================
; Install test monitoring variables and histories
;
history reset
history nstep=100
history id=1  crk_num      ; microcracking
history id=2  crk_num_pnf
history id=3  crk_num_psf
;
history id=4  ds_wdxx      ; horizontal disp.
history id=5  ds_wdsx      ; shear stress
history id=6  ds_wsyy      ; normal stress
;
history id=7  ds1_ang
history id=8  ds1_x
history id=9  ds1_y
history id=10 ds1_xy
history id=11 ds1_ms1
history id=12 ds1_ms3
;
ds_shear_plotviews
```

```
prop xdisp=0.0 ydisp=0.0
;
; ================================================================
; Specify in calling routine:
SET p_vel=0.1 p_cyc=1000  p_stages=10
SET ds_peakfac = 0.7 ds_e_peakfac = 2.0
SET ds_save_state = 1 stress_record_pt = 2.0e6
SET ds_knxfac = 1.1 ds_save_step = 500 run_cycle = 100
ds_shear_wallstiff
ds_accel_shearwall
ds_runshear
;
SET md_tag_name='-bwl'
md_save_state
SET md_tag_name='-his'
ds_his_save
; ================================================================
; End of File ds_0p01.dvr
return
```

```
; Filename : ds_shear.fis
; Geotechnical Engineering Group. University of Alberta
; Developed by Namkak Cho, revised in 1.10.2004
;=============================================================
; Purpose : Direct shear test Simulation routines
;=============================================================
;
; ============================================================
def ds_install_meas_circles
;
; Installs a measurement circles at the center of the specimen.
; The meas. circle radius is scaled by the specimen with using
; "mc_rad_fact".
;
; INPUT:  s_height - sample height
;         s_width  - sample width
;         mc_rad_fact - measurement circle scale factor
;
  meas_rad = s_width / mc_rad_fact
;
  meas_x = 0.0
  meas_y = 0.0
  command
   measure x=@meas_x y=@meas_y rad=@meas_rad id=2
  end_command
end
; ============================================================
def ds_sample_dimensions
;
; Setting the measurement circle.
;
; Output : mp1 - measurement circle pointer
;
  ds_install_meas_circles
  ;
  mp1 = maddr(1)
end
; ============================================================
def pr_stress
;
; computes principal stresses
; Input  : _sxx, _syy, _sxy
;
; Output : pr_smax, pr_smin
;
 avg_str  = 0.5 * (_sxx + _syy)
 mohr_rad = sqrt((0.5 * (_sxx - _syy))^2 + _sxy^2)
 pr_s1 = (-avg_str + mohr_rad)
 pr_s3 = (-avg_str - mohr_rad)
 ;;
 if pr_s1 > pr_s3 then
  pr_smax = pr_s1
  pr_smin = pr_s3
 else
  pr_smax = pr_s3
  pr_smin = pr_s1
 end_if
end
; ============================================================
def ds1_ang
;
; Computes current stress path and orientation of maximum principal
; stress within a measurement circle.
;
; Input  : mp1     - measurement circle pointer
;
```

```
; Output : ds1_ms1 - maximum principal stress
;          ds1_ms3 - minimum principal stress
;          ds1_ang - direction of maximum principal stress
;
 _mc_x = m_x(mp1)
 _mc_y = m_y(mp1)
 _mc_rad = m_rad(mp1)
 mp = mp1
 clp_stress_meas
 ds1_x  = _cl_s11
 ds1_y  = _cl_s22
 ds1_xy = 0.5 * (_cl_s12 +  _cl_s21)
 ;;
 _sxx = ds1_x
 _syy = ds1_y
 _sxy = ds1_xy
 pr_stress
 ds1_ms1 = pr_smax
 ds1_ms3 = pr_smin
 ds1_ang = (180.0/pi) * 0.5 * atan2( -2.0*_sxy, (-_sxx+_syy) )
end
; ===============================================================
def ds_nload_plate
;
; platen setup for normal stress application
;
; Input  : pl_thk - platen thickness
;
; Output : _nbp - ball pointer of the particle that the normal force is
;                 applying
;          pclp - pointer of the clumped platen
;
 _y0 = 0.5 * s_height - pl_thk
 _y1 = 0.5 * s_height
 pl_id = max_clid + 1
 command
  prop col = 2 range y=(@_y0, @_y1)
  clump id=@pl_id perm range y=(@_y0, @_y1)
 end_command
 ;;
 _nbp = ball_near2(0.0, 0.5*s_height)
 b_color(_nbp) = 10
 ;;
 clp = clump_head
 loop while clp # null
  if cl_id(clp) = pl_id then
   pclp = clp
  end_if
  clp = cl_next(clp)
 end_loop
end
; ===============================================================
def create_shear_wall
; Shear box generation using wall element
;
; Input  : pl_thk     - platen thickness for normal load
;          shr_boxgap - shear box gap
;          w1_0, w2_0, w3_0, w4_0 - current wall position
;
; Output : waddi, wadd3, wadd4 - wall pointers
;
;
 cur_wy1 = w1_0 + w_y(wadd1)
 cur_wy2 = w2_0 + w_y(wadd2)
 cur_wx3 = w3_0 + w_x(wadd3)
 cur_wx4 = w4_0 + w_x(wadd4)
 ;
```

```
command
 del wall 1 2 3 4
end_command
;;
_x0 = -0.6 * s_width
_y0 = -0.5 * shr_boxgap - 0.5 * pl_thk
_x1 =  cur_wx3
_y1 = -0.5 * shr_boxgap - 0.5 * pl_thk
command
  wall id=1  nodes (@_x0,@_y0) (@_x1,@_y1)
end_command
;;
_x2 =  cur_wx3
_y2 =  cur_wy1
command
  wall id=1  nodes (@_x2,@_y2)
end_command
;;
_x2 =  cur_wx4
_y2 =  cur_wy1
command
  wall id=1  nodes (@_x2,@_y2)
end_command
;;
_x2 =  cur_wx4
_y2 = -0.5 * shr_boxgap - 0.5 * pl_thk
command
  wall id=1  nodes (@_x2,@_y2)
end_command
;;
;;
_x0 =  cur_wx3
_y0 =  0.5 * s_height - pl_thk
_x1 =  cur_wx3
_y1 =  0.5 * shr_boxgap - 0.5 * pl_thk
command
  wall id=3  nodes (@_x0,@_y0) (@_x1,@_y1)
end_command
;;
_x0 =  0.6 * s_width
_y0 =  0.5 * shr_boxgap - 0.5 * pl_thk
_x1 =  cur_wx4
_y1 =  0.5 * shr_boxgap - 0.5 * pl_thk
command
  wall id=4  nodes (@_x0,@_y0) (@_x1,@_y1)
end_command
;;
_x2 =  cur_wx4
_y2 =  0.5 * s_height - pl_thk
command
  wall id=4  nodes (@_x2,@_y2)
end_command
;;
wadd1 = find_wall(1)
wadd3 = find_wall(3)
wadd4 = find_wall(4)
;;
ds_nload_plate
_y0 = 0.5 * s_height - pl_thk - 0.5 * (et2_rlo*2.5)
_y1 = 0.5 * s_height - pl_thk + 0.5 * (et2_rlo*2.5)
command
 prop col = 10 fric=0.0 ks=0.0 pb_n=1e-1 pb_s=1e-1 range y=(@_y0, @_y1)
end_command
end
; ================================================================
def ds_shear_wallstiff
;
```

```
; Shear box wall stiffness setup
;
; Input : ds_knxfac - stiffness scale factor

 md_wEcfac = ds_knxfac
 md_wid = 1
 md_wallkn
 md_wid = 3
 md_wallkn
 md_wid = 4
 md_wallkn
 ;;
 command
  wall id=1 ks=0.0 fric=0.0
  wall id=3 ks=0.0 fric=0.0
  wall id=4 ks=0.0 fric=0.0
 end_command
end
; ===================================================================
def ds_shear_wss
;
; Compute shear stress, normal stress and horz. Disp.
;
; Input : wadd1, wadd4 - wall pointer
;         md2_thick    - particle disk thickness
;                        if "set disk on" then md2_thick = 1
 ds_wdxx  = abs(w_x(wadd1)) * 1000
 ds_wsyy  = abs(w_yfob(wadd1)) / (s_width * md2_thick)
 ds_wdsx  = abs(w_xfob(wadd4))/ (s_width * md2_thick)
 ;
 ds_wdsx_max = max( ds_wdsx_max, abs(ds_wdsx) )
end
; ===================================================================
def ds_accel_shearwall
;
;
 b_xfap(_nbp) = 0.0
 b_yfap(_nbp) = ds_wsyy_req * s_width *  md2_thick
;
 _delvel = p_vel / p_stages
 _niter  = p_cyc / p_stages
 _vel = 0.0
 loop ap_ii (1,p_stages)
  _vel   =  _vel + _delvel
  _fvel  =  _vel
  command
   wall id=1  xvel= @_fvel
   cycle @_niter
  end_command
 end_loop
end
; ===================================================================
def ds_crk_ang_norm
;
; Computes the tension induced orientation of crack based on the
; information from the "crk.fis"
;
;
; Input : _crk_x, _crk_y         - position of the current crack
;         _crk_normx, _crk_normy - crack normal vector
;         _crk_rad               - size of the crack
;
; Output : _crk_ang - orientation of the current crack
;
 crkp = crk_head
 loop while crkp # null
  crk_getdata
```

```
 ds_crk_x0 = _crk_x - _crk_rad * _crk_normy
 ds_crk_y0 = _crk_y + _crk_rad * _crk_normx
 ds_crk_x1 = _crk_x + _crk_rad * _crk_normy
 ds_crk_y1 = _crk_y - _crk_rad * _crk_normx
 _cdist_x = ds_crk_x1 - ds_crk_x0
 _cdist_y = ds_crk_y1 - ds_crk_y0
 if _cdist_x # 0.0 then
   _crk_slope = _cdist_y / _cdist_x
  nn_ang = (180.0 / pi)*atan2(abs(_cdist_y), abs(_cdist_x))
 else
   nn_ang = 90.0
 end_if
 _crk_ang = nn_ang
 if _crk_slope < 0 then
  _crk_ang = -_crk_ang
 end_if
 ;;
 if _crk_fail = 3 then  ;; crack by tension
  command
   print _crk_ang
  end_command
 end_if
 ;;
 crkp = mem(crkp+crk_NEXT)
end_loop
end
; ===================================================================
def ds_crk_ang_shr
;
; Computes the shear induced orientation of crack based on the
; information from the "crk.fis"
;
; Input : _crk_x, _crk_y          - position of the current crack
;         _crk_normx, _crk_normy - crack normal vector
;         _crk_rad               - size of the crack
;
; Output : _crk_ang - orientation of the current crack
;
 crkp = crk_head
 loop while crkp # null
  crk_getdata
  ds_crk_x0 = _crk_x - _crk_rad * _crk_normy
  ds_crk_y0 = _crk_y + _crk_rad * _crk_normx
  ds_crk_x1 = _crk_x + _crk_rad * _crk_normy
  ds_crk_y1 = _crk_y - _crk_rad * _crk_normx
  _cdist_x = ds_crk_x1 - ds_crk_x0
  _cdist_y = ds_crk_y1 - ds_crk_y0
  if _cdist_x # 0.0 then
   _crk_slope = _cdist_y / _cdist_x
   nn_ang = (180.0 / pi)*atan2(abs(_cdist_y), abs(_cdist_x))
  else
   nn_ang = 90.0
  end_if
  ;;
  _crk_ang = nn_ang
  if _crk_slope < 0.0 then
   _crk_ang = -_crk_ang
  end_if
  ;;
  if _crk_fail = 4 then   ;; crack by shear
   command
    print _crk_ang
   end_command
  end_if
  ;;
  crkp = mem(crkp+crk_NEXT)
 end_loop
```

```
end
; ================================================================
def ds_runshear
 run_cycle = run_cycle
 ds_wdsx_max = -1.0e-20
 loop while 1 # 0  ; infinite loop
  command
   cycle @run_cycle
  end_command
  ;;
  if abs(ds_wdsx) =  ds_wdsx_max then
   ds_wdxx_peak = ds_wdxx
  end_if
  ;;
  if abs(ds_wdsx) <=  (ds_peakfac * ds_wdsx_max) then
   if abs(ds_wdxx) > abs(ds_e_peakfac * ds_wdxx_peak) then
    exit
   end_if
  end_if
  ;;
  if ds_save_state = 1 then
   if ds_wdsx >= stress_record_pt then
    tg_cycle = tg_cycle + run_cycle
   end_if
   if tg_cycle = ds_save_step then
    md_run_name = string(md_run_name)
    cycle_num   = string(cycle)
    _fname = md_run_name + string('-') + cycle_num + string('.sav')
    command
     save @_fname
    end_command
    p_fname = md_run_name + string('-') + cycle_num + string('.nom')
    command
     set log on
     set logfile @p_fname
     print ds_wdsx
     ds_crk_ang_norm
     set log off
    end_command
    ;;
    p_fname = md_run_name + string('-') + cycle_num + string('.shr')
    command
     set log on
     set logfile @p_fname
     print ds_wdsx
     ds_crk_ang_shr
     set log off
    end_command
    ;;
    tg_cycle = 0
   end_if
  end_if
 end_loop
end
; ================================================================
def ds_shear_plotviews
;
; Defines a set of useful plot-views for the direct shear test.
;
  command
    plot create shear_stress_disp
    plot set title text 'Shear and normal stress vs. horizontal disp'
    plot add his 5 6 vs 4
    ;
    plot create prmax_orient
    plot set title text 'Orientation of sigma 1'
    plot add his 7 vs 4
```

```
  end_command
end
; ===================================================================
def ds_his_save
;
; Defines history set to save
;
 h_fname = md_run_name + md_tag_name + string('.dat')
 command
  his write 1 2 3 4 5 6 7 8 9 10 11 12 file @h_fname
 end_command
end
; ===================================================================
def ds_draw_shear_sample
;
; Plots specimen boundary
;
 array cord_1(2) cord_2(2)
 plot_item
 cord_1(1)=-0.5*s_width
 cord_1(2)=-0.5*s_height
 cord_2(1)= 0.5*s_width
 cord_2(2)= 0.5*s_height - pl_thk
 stat = draw_rect(cord_1,cord_2)
end
;===================================================================
;End OF File ds_shear.fis
; ===================================================================
return
```

B.4 DATA FILE AND FISH FUNCTIONS FOR AXIALLY COMPRESSED BENDING TEST SIMULATION

```
; Filename : beam_set.dvr
; Geotechnical Engineering Group. University of Alberta
; Developed by Namkak Cho, last updated in 7.16.2007
;=================================================================
; Purpose : Biaxial Bending test setup
;=================================================================
res bm_calib-clt.sav
SET echo off    ; load support functions
  call %itascaFishTank%\FishPfc2\et2\clp_meas.FIS
  call %itascaFishTank%\FishPfc2\et2\beam_set.FIS
SET echo on
;;
set t_dist          =  37.5e-3     b_dist      =   75e-3
set load_ball_rad   =   5.0e-3     hb_rad      =   2.0e-3
set pl_thk          =   4.0e-3


set st_gauge_rad    = 1.0e-3       notch_h     =   1.25e-3
set pl_dens         = md_dens      pl_fric     =   0.0
set pl_fac          = 1            ks_fac      =   0.0
;;
loading_setup
;;
SET md_run_name = 'beam_calib'
;;
set md_tag_name = '-rset'
md_save_state
;;;;
Return
;;
;; End of the file beam_set.dvr
```

```
; Filename : beam_set.FIS
; Geotechnical Engineering Group. University of Alberta
; Developed by Namkak Cho, last updated in 7.16.2007
;=================================================================
;Purpose : Biaxial Bending test setup
;=================================================================
;
;
; ================================================================
def loading_setup
 ;;
 command
  del wall 1 2 3 4
 end_command
 ;;
 pl_dens = pl_dens
 pl_kn   = _kn * pl_fac
 pl_ks   = pl_kn * ks_fac
 pl_fric  = pl_fric
 ;;
 notch_install
 ;;
 bm_hplate_setup
 hball_set
 ;;
 bm_vball_set
 bm_seating_plate
 bm_pl_addclump
 bm_genwall
 install_mcircle
end
; ================================================================
def bm_genwall
 ;;
 ;;*****************************************************************
 ;; Generate the horizontal frame wall
 ;;*****************************************************************
 _x0 =  b_x(hbp1) - b_rad(hbp1)
 _y0 =  0.5 * s_height
 _x1 =  b_x(hbp1) - b_rad(hbp1)
 _y1 = -0.5 * s_height
 command
  wall id=2  nodes (@_x0,@_y0) (@_x1,@_y1)
 end_command
 ;;
 _x0 =  b_x(hbp2) + b_rad(hbp2)
 _y0 = -0.5 * s_height
 _x1 =  b_x(hbp2) + b_rad(hbp2)
 _y1 =  0.5 * s_height
 command
  wall id=3  nodes (@_x0,@_y0) (@_x1,@_y1)
 end_command
 ;;
 command
  wall id=2 kn=@pl_kn ks=@pl_ks fric=@pl_fric
  wall id=3 kn=@pl_kn ks=@pl_ks fric=@pl_fric
 end_command
 ;;
 wadd2 = find_wall(2)
 wadd3 = find_wall(3)
end
; ================================================================
def bm_pl_addclump
 _clid1 = cl_id(clp_lh)
 _clid2 = cl_id(clp_rh)
 ;;
```

```
 clid1 = max_clid + 1
 clid2 = clid1 + 1
 command
  clump id=_clid1 perm range col=3
  clump id=_clid2 perm range col=4
  ;;
  clump id=clid1 perm range col=12
  clump id=clid2 perm range col=13
 end_command
end
; ================================================================
def bm_seating_plate
 ;;
 ;;*****************************************************************
 ;; Generate the platen for the two top point loading rollers
 ;;*****************************************************************
 _pball_rad = et2_rlo
 _npballs   = 200
 _bleng     = 1.4 * t_dist
 _npseg     = _bleng / float(_npballs)
 bm_plate   = 1
 _x0        = b_x(vbp5)
 _y0        = b_y(vbp5) - b_rad(vbp5)- et2_rlo
 _bcol      =  12
 bm_plate_gen
 ;;
 ;;*****************************************************************
 ;; Generate the platen for the two bottom point loading rollers
 ;;*****************************************************************
 _pball_rad = et2_rlo
 _npballs   = 400
 _bleng     = 1.4 * b_dist
 _npseg     = _bleng / float(_npballs)
 bm_plate   = 1
 _x0        = 0.0
 _y0        = b_y(vbp4) - b_rad(vbp4)- et2_rlo
 _bcol      =  13
 bm_plate_gen
end
; ================================================================
def bm_plate_gen
 loop _i (1, _npballs+1)
  if bm_plate = 1
   _x1 = _x0 - 0.5*_bleng + _npseg * (_i - 1)
   _y1 = _y0
  else
   _x1 = _x0
   _y1 = _y0 - 0.5*_bleng + _npseg * (_i - 1)
  end_if
  _bid = max_bid + 1
  command
   ball rad = @_pball_rad x=@_x1 y=@_y1 id=@_bid
   prop  col=@_bcol  den  =  @pl_dens  fric=@pl_fric  kn=@pl_kn  ks=@pl_ks  range
id=@_bid
  end_command
 end_loop
end
; ================================================================
def bm_vball_set
 _ball_rad =  load_ball_rad
 ;;
 ;;*****************************************************************
 ;; Generate the top left roller for point load
 ;;*****************************************************************
 _x0 = -t_dist * 0.5
 _y0 =  s_height*0.5 + _ball_rad
 _sgn = 1.0
```

```
bm_vlball_gen
v_bid1 = v_bid
vbp1 = find_ball( v_bid1)
;;
;;*************************************************************************
;; Generate the top right roller for point load
;;*************************************************************************
_x0 =  t_dist * 0.5
_y0 =  s_height*0.5 + _ball_rad
_sgn = 1.0
bm_vlball_gen
v_bid2 = v_bid
vbp2 = find_ball( v_bid2)
;;
;;*************************************************************************
;; Generate the bottom left roller for point load
;;*************************************************************************
_x0 = -b_dist * 0.5
_y0 = -s_height*0.5 - _ball_rad
_sgn = -1.0
bm_vlball_gen
v_bid3 = v_bid
vbp3 = find_ball( v_bid3)
;;
;;*************************************************************************
;; Generate the bottom right roller for point load
;;*************************************************************************
_x0 =  b_dist * 0.5
_y0 = -s_height*0.5 - _ball_rad
_sgn = -1.0
bm_vlball_gen
v_bid4 = v_bid
vbp4 = find_ball( v_bid4)
;;
;;*************************************************************************
;; Generate the bearing roller for vertical ram
;;*************************************************************************
_ball_rad = b_rad(hbp2)
b_gencond = 1
_x0 =  0.0
_y0 =  s_height*0.5 + 2.0*load_ball_rad + _ball_rad + et2_rlo * 2.0
_sgn = 1.0
bm_vlball_gen
v_bid5 = v_bid
vbp5 = find_ball( v_bid5)
;;
bm_vball_seating
end
; ===========================================================================
def bm_vball_seating
;;*************************************************************************
;; Generate the seating for each bearing an roller
;;*************************************************************************
_nballs  = 60
_bangle  = 60.0 * degrad
_nangle  = (2.0 * _bangle) / float(_nballs)
_pball_rad = et2_rlo
;;
;; Top point loading roller
;;
_x0   = b_x(vbp1)
_y0   = b_y(vbp1)
_brad = b_rad(vbp1)
_bcol = 12
_sgnx = -1.0
_sgny =  1.0
bm_plate_arc
```

```
_x0    = b_x(vbp2)
_y0    = b_y(vbp2)
_brad  = b_rad(vbp2)
_sgnx  = -1.0
_sgny  =  1.0
bm_plate_arc
;;
;;
;; Bottom point loading roller
;;
_x0    = b_x(vbp3)
_y0    = b_y(vbp3)
_brad  = b_rad(vbp3)
_bcol  = 13
_sgnx  = -1.0
_sgny  = -1.0
bm_plate_arc
_x0    = b_x(vbp4)
_y0    = b_y(vbp4)
_brad  = b_rad(vbp4)
_bcol  = 13
_sgnx  = -1.0
_sgny  = -1.0
bm_plate_arc
;;
;;
;; Vertical ram bearing
;;
_nballs  = 30
_bangle  = 30.0 * degrad
_nangle  = (2.0 * _bangle) / float(_nballs)
_pball_rad = et2_rlo
_x0    = b_x(vbp5)
_y0    = b_y(vbp5)
_brad  = b_rad(vbp5)
_bcol  = 12
_sgnx  =  1.0
_sgny  = -1.0
bm_plate_arc
end
; ===================================================================
def bm_plate_arc
 loop _i (1, _nballs+1)
  _x1 = _x0 + _sgnx * (_brad + _pball_rad )* sin(- _bangle + _nangle * (_i - 1))
  _y1 = _y0 + _sgny * (_brad + _pball_rad )* cos(- _bangle + _nangle * (_i - 1))
  _bid = max_bid + 1
  command
   ball rad = @_pball_rad x=@_x1 y=@_y1 id=@_bid
   prop col=@_bcol den=@pl_dens fric=@pl_fric kn=@pl_kn ks=@pl_ks range id=@_bid
  end_command
 end_loop
end
; ===================================================================
def bm_vlball_gen
 if b_gencond = 0 then
  vbp = ball_near2(_x0,_y0)
  ii = cl_rel(b_clump(vbp), vbp)
  _x0    = b_x(vbp)
  _y0    = b_y(vbp) + _sgn * (b_rad(vbp) + _ball_rad)
 end_if
 ;;
 v_bid  =  max_bid + 1
 command
  ball rad=@_ball_rad x=@_x0 y=@_y0 id=@v_bid
  prop col=6 den=@pl_dens fric=@pl_fric kn=@pl_kn ks=@pl_ks range id=@v_bid
 end_command
end
```

```
; ================================================================
def bm_hplate_setup
 _x0    = -0.5*s_width
 _x1    = -0.5*s_width + pl_thk
 _pclid = max_clid + 1
 command
  prop col=2 fric=@pl_fric kn=@pl_kn ks=@pl_ks range x=(@_x0, @_x1)
  clump id = @_pclid perm range x = ( @_x0, @_x1 )
 end_command
 ;;
 clp = clump_head
 loop while clp # null
  if cl_id(clp) = _pclid then
   clp_lh = clp
  end_if
  clp = cl_next(clp)
 end_loop
 ;;
 _x0    =  0.5*s_width - pl_thk
 _x1    =  0.5*s_width
 _pclid = max_clid + 1
 command
  prop col=2 fric=@pl_fric kn=@pl_kn ks=@pl_ks range x=(@_x0, @_x1)
  clump id = @_pclid perm range x=(@_x0, @_x1)
 end_command
 ;;
 clp = clump_head
 loop while clp # null
  if cl_id(clp) = _pclid then
   clp_rh = clp
  end_if
  clp = cl_next(clp)
 end_loop
end
; ================================================================
def hball_set
 _int_rad = et2_rlo * 1.0
 _ball_rad = hb_rad
 _lb_rad   = _ball_rad
 _x0 = -0.5 * s_width - _ball_rad
 _y0 =  0.0
 _bid = max_bid + 1
 _bcol=6
 bm_hlball_gen
 h_bid1 = _bid
 ;;
 _ball_rad = hb_rad
 _lb_rad   = _ball_rad
 _x0 =  0.5 * s_width + _ball_rad
 _y0 =  0.0
 _bid = max_bid + 1
 bm_hlball_gen
 h_bid2 = _bid
 ;;
 hbp1 = find_ball(h_bid1)
 hbp2 = find_ball(h_bid2)
 ;;
 bm_interface
 bm_hball_seating
end
; ================================================================
def bm_hlball_gen
 command
  ball rad=@_ball_rad x=@_x0 y=@_y0 id=@_bid
  prop col=@_bcol den=@pl_dens fric=@pl_fric kn=@pl_kn ks=@pl_ks range id=@_bid
 end_command
end
```

```
; ================================================================
def bm_interface
 _x0 = -0.5*s_width + pl_thk
 _x1 = -0.5*s_width + pl_thk + et2_rlo * 2.5
 command
  prop col=99 pb_n = 1e20 pb_s = 1e20 ks=1e3 fric = 0.01 &
       range x = (@_x0, @_x1)
 end_command
 ;
 _x0 = 0.5*s_width - pl_thk - et2_rlo * 2.5
 _x1 = 0.5*s_width - pl_thk
 command
  prop col=99 pb_n = 1e20 pb_s = 1e20 ks=1e3 fric = 0.01 &
       range x = (@_x0, @_x1)
 end_command
end
; ================================================================
def bm_hball_seating
 _nballs    = 30
 _bangle    = pi/2 - 30.0 * degrad
 _nangle    = (2.0 * (_bangle-pi/2)) / float(_nballs)
 _pball_rad = _int_rad
 ;;
 _bcol = 3
 _brad = b_rad(hbp1)
 _x0   = b_x(hbp1)
 _y0   = b_y(hbp1)
 _sgnx = -1.0
 _sgny =  1.0
 bm_plate_arc
 ;;
 _bcol = 4
 _brad = b_rad(hbp2)
 _x0   = b_x(hbp2)
 _y0   = b_y(hbp2)
 _sgnx = 1.0
 _sgny = 1.0
 bm_plate_arc
end
; ================================================================
def hcont_plcontact
 command
  prop col=8 range x=(@_x0, @_x1)
 end_command
 ;;
 _ct_radl = _ct_rad
 ;;
 bp = ball_head
 loop while bp # null
  if b_color(bp) = 8 then
   _x1 = b_x(bp) - _sgnx * (b_rad(bp) + _ct_radl)
   _y1 = b_y(bp)
   h_bid = max_bid + 1
   command
    ball rad=@_ct_radl x=@_x1 y=@_y1 id=@h_bid
    prop col=9 den=@pl_dens fric=@pl_fric kn=@pl_kn ks=@pl_ks range id=@h_bid
   end_command
   b_color(bp) = 0
  end_if
  bp = b_next(bp)
 end_loop
 ;;
 bp = ball_head
 loop while bp # null
  if b_color(bp) = 9 then
   clp = cl_add (clp, bp)
   b_color(bp) = 2
```

```
 end_if
 bp = b_next(bp)
end_loop
end
; ===================================================================
def install_mcircle
meas_rad = st_gauge_rad
meas_x =  0.0
meas_y =  0.5 * s_height - notch_h - st_gauge_rad
command
 measure x=@meas_x y=@meas_y rad=@meas_rad id=1
end_command
;;
meas_x = -st_gauge_rad - 1.0 * notch_thk
meas_y =  0.5 * s_height - st_gauge_rad
command
 measure x=@meas_x y=@meas_y rad=@meas_rad id=2
end_command
;;
meas_x =  st_gauge_rad + 1.0 * notch_thk
meas_y =  0.5 * s_height - st_gauge_rad
command
 measure x=@meas_x y=@meas_y rad=@meas_rad id=3
end_command
;;
meas_x =  0.0
meas_y =  0.0
command
 measure x=@meas_x y=@meas_y rad=@meas_rad id=4
end_command
;;
meas_x =  0.0
meas_y = -0.5 * s_height + st_gauge_rad
command
 measure x=@meas_x y=@meas_y rad=@meas_rad id=5
end_command
;;
meas_x = -0.5*s_width + pl_thk * 1.5 + meas_rad
meas_y =  0.0
command
 measure x=@meas_x y=@meas_y rad=@meas_rad id=6
end_command
;;
meas_x =  0.5*s_width - pl_thk * 1.5 - meas_rad
meas_y =  0.0
command
 measure x=@meas_x y=@meas_y rad=@meas_rad id=7
end_command
end
; ===================================================================
def notch_install
;;
notch_thk = 3.0 * et2_rlo
_x0 = -0.5 * notch_thk
_x1 =  0.5 * notch_thk
_y0 = s_height * 0.5 - notch_h
;;
bp = ball_head
loop while bp # null
 if b_y(bp) >= _y0 then
  if b_x(bp) >= _x0 then
   if b_x(bp) <= _x1 then
    b_color(bp) = 14
   end_if
  end_if
 end_if
 bp = b_next(bp)
```

```
 end_loop
 ;;
 command
  clump rel range col = 14
  del ball range col = 14
 end_command
end
; ================================================================
def draw_specimen
 array scorn_1(2) scorn_2(2)
 plot_item
 scorn_1(1)=-0.5 * s_width + pl_thk
 scorn_1(2)=-0.5 * s_height
 scorn_2(1)= 0.5 * s_width - pl_thk
 scorn_2(2)= 0.5 * s_height
 stat = draw_rect(scorn_1,scorn_2)
end
; ================================================================
return
;;
;; End of file beam_set.FIS
```

```
; Filename : beam_run.dvr
; Geotechnical Engineering Group. University of Alberta
; Developed by Namkak Cho, last updated in 7.16.2007
;=================================================================
; Purpose : Biaxial Bending test Simulation
;=================================================================
res beam_calib-rset.sav
SET echo off   ; load support functions
 call %itascaFishTank%\FishPfc2\et2\beam_run.fis
SET echo on
;;
crk_init
plot add fish crk_item
plot add fish draw_sample
plot add fish draw_specimen
;;
bm_ini
;
plot show assembly
;;
history reset
history nstep = 100
history id=1   bd1_ms1
history id=2   bd1_ms3
history id=3   bd2_ms1
history id=4   bd2_ms3
history id=5   bd3_ms1
history id=6   bd3_ms3
history id=7   bd4_ms1
history id=8   bd4_ms3
history id=9   bd5_ms1
history id=10  bd5_ms3
history id=11  bd6_ms1
history id=12  bd6_ms3
history id=13  bd7_ms1
history id=14  bd7_ms3
;;
history id=15  bm_fratio
;;
history id=16  crk_num
history id=17  crk_num_pnf
history id=18  crk_num_psf
;;
history id=23  top_bdisp
history id=24  bot_bdisp
history id=25  bm_stress
history id=26  bm_wsxx_req
history id=27  _errorx
history id=28  _errory
;;
plot show bm_plotviews
plot show 15
;;
set sp_stress = 20e6 str_rec_pt = 4.0e6 str_rec_inc = 5e5 error_tol = 0.1
set run_cycle = 100 load_incre = -1e3  bm_ratio=3.0 bm_sxx_req = -1e4
;;
bm_runbending
;;
set md_tag_name = '-his'
his_save_state
set md_tag_name = '-bm'
md_save_state
;;;;
;; End of the file beam_run.dvr
;;
;;
;;
```

```
; Filename : beam_run.fis
; Geotechnical Engineering Group. University of Alberta
; Developed by Namkak Cho, last updated in 7.16.2007
;=================================================================
;Purpose : Biaxial Bending test run
;=================================================================
;
;
; ================================================================
; ================================================================
def bm_arrays
 array bm_ms1(8) bm_ms3(8) rbp_str(2,2)
end
bm_arrays
; ================================================================
def lvdt_setup
 tbp  =  ball_near2( 0.0,  0.5*s_height )
 bbp  =  ball_near2( 0.0, -0.5*s_height )
 ;;
 b_color(tbp) = 8
 b_color(bbp) = 8
 top_ini = b_y(tbp)
 bot_ini = b_y(bbp)
end
; ================================================================
def top_bdisp
 if bm_scale = 1 then
  top_bdisp = (b_y(tbp) - top_ini)*1000
 else
  top_bdisp = 100* (b_y(tbp) - top_ini)/s_height
 end_if
end
; ================================================================
def bot_bdisp
 if bm_scale = 1 then
  bot_bdisp = (b_y(bbp) - bot_ini)*1000
 else
  bot_bdisp = 100*(b_y(bbp) - bot_ini)/s_height
 end_if
end
;================================================================
def bm_adjust_wvel
 bm_wsxx = bm_wfxx/(s_height * md2_thick)
 bm_wsxx_req = (bm_wfyy * bm_ratio)/(s_height * md2_thick)
 ;;
 _sgn = sgn(bm_wsxx - bm_wsxx_req)
 if bm_wsxx # 0.0 then
  w_xvel(wadd2) = bm_SG * (bm_wsxx - bm_wsxx_req)
 else
  w_xvel(wadd2) = _sgn * _vmax
 end_if
 if abs(w_xvel(wadd2)) > _vmax then
  w_xvel(wadd2) = _sgn * _vmax
 end_if
 w_xvel(wadd3) = -w_xvel(wadd2)
end
;================================================================
def bm_error_chk
 _bm_error_chk = 1
 _errorx = abs((bm_wfxx - bm_fxx_req)/bm_fxx_req)
 _errory = abs((bm_wfyy - bm_fyy_req)/bm_fyy_req)
 ;;
 section
 ;;
 if _errorx > error_tol then
  _bm_error_chk = 0
  exit section
```

```
 end_if
 if _errory > error_tol then
  _bm_error_chk = 0
  exit section
 end_if
 end_section
 ;;
 bm_error_chk = _bm_error_chk
end
;=====================================================================
def bm_wvel_prep
 if relax_fac = 0 then
  relax_fac = 0.5
 end_if
 _vmax = 1e0
 wadd = wadd2
 bm_wkn1 = bm_wkn
 wadd = wadd3
 bm_wkn2 = bm_wkn
 bm_awkn = (bm_wkn1 + bm_wkn2) * 0.5
 ;;
 if bm_awkn # 0 then
  bm_SG = relax_fac*(s_height * md2_thick)/(bm_awkn*tdel)
 else
  bm_SG = 0
 end_if
end
;=====================================================================
def bm_wkn
 ii=pre_cycle  ; insure that all contact info. is updated
 sum_kn = 0.0
 cp = w_clist(wadd)
 loop while cp # null
  if md_virtual = 0 then
   sum_kn = sum_kn + c_kn(cp)
  end_if
  cp = c_b2clist(cp)
 end_loop
 bm_wkn = sum_kn
end
; ====================================================================
def bm_ini
 lvdt_setup
 ;;
 command
  free x y spin
  fix x y spin range col 13
  set fishcall 0 bm_adjust_wvel
 end_command
end
; ====================================================================
def bm_runbending
 ;;
 run_cycle = run_cycle
 ;;
 loop while 0 # 1
  bm_wvel_prep
  ;;
  bm_sxx_req = bm_sxx_req + load_incre1
  bm_fxx_req = bm_sxx_req * (s_height * md2_thick)
  bm_fyy_req = bm_fxx_req / bm_ratio
  b_yfap(vbp5) = bm_fyy_req
  ;;
  command
   cycle @run_cycle
  end_command
  ;;
```

```
 if bm_error_chk = 1 then
  load_incre1 = load_incre
  command
   solve
  end_command
 else
  load_incre1 = 0.0
 end_if
 ;;
 if abs(bm_stress) >= abs(str_rec_pt) then
  md_run_name = string(md_run_name)
  _fname = md_run_name + string('-') + string(-str_rec_pt/1e6) + string('.sav')
  command
   save @_fname
  end_command
  str_rec_pt = str_rec_pt + str_rec_inc
 end_if
 ;;
 if abs(bm_stress) >= abs(sp_stress) then
  exit
 end_if
end_loop
end
; ===================================================================
def bm_stress
 _mom_arm  = ( b_dist - t_dist ) * 0.5
 _fmom     = 0.5  *  bm_fyy_req * _mom_arm
 _int_mom  = ( md2_thick * s_height^3 ) / 12.0
 _yy       = 0.5 * s_height
 bm_stress = bm_sxx_req + _fmom * _yy / _int_mom
end
; ===================================================================
def bm_fratio
 if bm_wfyy # 0.0 then
  bm_fratio = abs(bm_wfxx / bm_wfyy)
 else
  bm_fratio = 0.0
 end_if
end
; ===================================================================
def bm_wfxx
 bm_wfxx  = 0.5 * (w_xfob(wadd2) - w_xfob(wadd3))
end
; ===================================================================
def bm_wfyy
 bm_wfyy  = -b_yfob(vbp5)
end
; ===================================================================
def principal_stress
 avg_str  = 0.5 * (_cl_s11 + _cl_s22)
 shr_str  = 0.5 * (_cl_s12 + _cl_s21)
 mohr_rad = sqrt((0.5 * (_cl_s11 - _cl_s22))^2 + shr_str^2)
 pr_s1 = -1.0 * avg_str + mohr_rad
 pr_s3 = -1.0 * avg_str - mohr_rad
 ;;
 pr_smax = max(pr_s1, pr_s3)
 pr_smin = min(pr_s1, pr_s3)
end
; ===================================================================
def _mc_str
 _mc_x = m_x(_mp)
 _mc_y = m_y(_mp)
 _mc_rad = m_rad(_mp)
 mp = _mp
 clp_stress_meas
 principal_stress
 _ms1 = pr_smax
```

```
 _ms3 = pr_smin
end
; ===================================================================
def bm_stress_cal
 loop _m (1, 7)
  _mp = maddr(_m)
  _mc_str
  bm_ms1(_m) = _ms1
  bm_ms3(_m) = _ms3
 end_loop
end
; ===================================================================
def bd1_ms1
 bm_stress_cal
 bd1_ms1 = bm_ms1(1)
 bd1_ms3 = bm_ms3(1)
 bd2_ms1 = bm_ms1(2)
 bd2_ms3 = bm_ms3(2)
 bd3_ms1 = bm_ms1(3)
 bd3_ms3 = bm_ms3(3)
 bd4_ms1 = bm_ms1(4)
 bd4_ms3 = bm_ms3(4)
 bd5_ms1 = bm_ms1(5)
 bd5_ms3 = bm_ms3(5)
 bd6_ms1 = bm_ms1(6)
 bd6_ms3 = bm_ms3(6)
 bd7_ms1 = bm_ms1(7)
 bd7_ms3 = bm_ms3(7)
end
; ===================================================================
def bm_plotviews
  command
    plot create gauge_1
    plot set title text 'Maximum Principal Stress vs. Minimum Principal Stress'
    plot add his 1 vs 2
    ;
    plot create gauge_2
    plot set title text 'Maximum Principal Stress vs. Minimum Principal Stress'
    plot add his 3 vs 4
    ;
    plot create gauge_3
    plot set title text 'Maximum Principal Stress vs. Minimum Principal Stress'
    plot add his 5 vs 6
    ;
    plot create gauge_4
    plot set title text 'Maximum Principal Stress vs. Minimum Principal Stress'
    plot add his 7 vs 8
    ;
    plot create gauge_5
    plot set title text 'Maximum Principal Stress vs. Minimum Principal Stress'
    plot add his 9 vs 10
    ;
    plot create gauge_6
    plot set title text 'Maximum Principal Stress vs. Minimum Principal Stress'
    plot add his 11 vs 12
    ;
    plot create gauge_7
    plot set title text 'Maximum Principal Stress vs. Minimum Principal Stress'
    plot add his 13 vs 14
    ;
    plot create flexura_stress_vs_top_disp
    plot set title text 'flexura_stress vs. Top. Disp.'
    plot add his -25 vs -23 ymin 0.0
    ;
    plot create flexura_stress_vs_bottom _disp
    plot set title text 'flexura_stress vs. Bot. Disp.'
    plot add his -25 vs -24 ymin 0.0
```

```
    ;
    plot create Foce_ratio
    plot set title text 'Force ratio'
    plot add his 15 ymin 0.0 ymax 5.0
    ;
    plot create Comparison
    plot set title text 'Comparison'
    plot add his -25 -26 1 11 13 vs -24 ymin 0.0
    ;
    plot create error
    plot set title text 'error'
    plot add his 27 28 ymin 0.0
  end_command
end
; ================================================================
def his_save_state
 h_fname = md_run_name + md_tag_name + string('.dat')
 command
  his write 1 2 3 4 5 6 7 8 9 10 11 12 13 14 &
            15 16 17 18 23 24 25 file @h_fname
 end_command
end
; ================================================================
Return
;;
;; End of File beam_run.fis
```